CHEMICAL REVIEWS

pubs.acs.org/CR

Review

Advanced Electrocatalysts with Single-Metal-Atom Active Sites

Yuxuan Wang,[▽] Hongyang Su,[▽] Yanghua He,[▽] Ligui Li,[▽] Shangqian Zhu,[▽] Hao Shen, Pengfei Xie, Xianbiao Fu, Guangye Zhou, Chen Feng, Dengke Zhao, Fei Xiao, Xiaojing Zhu, Yachao Zeng, Minhua Shao,* Shaowei Chen,* Gang Wu,* Jie Zeng,* and Chao Wang*

Cite This: *Chem. Rev.* 2020, 120, 12217−12314

Read Online

ACCESS | Metrics & More | Article Recommendations

ABSTRACT: Electrocatalysts with single metal atoms as active sites have received increasing attention owing to their high atomic utilization efficiency and exotic catalytic activity and selectivity. This review aims to provide a comprehensive summary on the recent development of such single-atom electrocatalysts (SAECs) for various energy-conversion reactions. The discussion starts with an introduction of the different types of SAECs, followed by an overview of the synthetic methodologies to control the atomic dispersion of metal sites and atomically resolved characterization using state-of-the-art microscopic and spectroscopic techniques. In recognition of the extensive applications of SAECs, the electrocatalytic studies are dissected in terms of various important electrochemical reactions, including hydrogen evolution reaction (HER), oxygen evolution reaction (OER), oxygen reduction reaction (ORR), carbon dioxide reduction reaction (CO2RR), and nitrogen reduction reaction (NRR). Examples of SAECs are deliberated in each case in terms of their catalytic performance, structure−property relationships, and catalytic enhancement mechanisms. A perspective is provided at the end of each section about remaining challenges and opportunities for the development of SAECs for the targeted reaction.

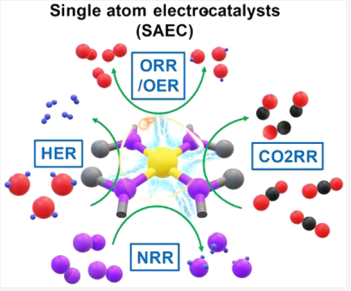

CONTENTS

Special Issue: Heterogeneous Single-Atom Catalysis

Received: June 11, 2020
Published: November 2, 2020

https://dx.doi.org/10.1021/acs.chemrev.0c00594
Chem. Rev. 2020, 120, 12217−12314

1. INTRODUCTION

The pursuit for renewable energy stimulates the development of advanced catalytic materials for electrochemical reactions. Such reactions as CO_2 and N_2 reduction, oxygen reduction, and evolution, etc., are important chemical transformation processes that carry on renewable energy conversions, in which the activity, selectivity, and/or stability of electrocatalysts play a vital role in determining the energy efficiencies and system performance. State-of-the-art catalytic chemistry for these reactions extensively relies on precious metals, such as platinum (Pt), palladium (Pd), rhodium (Rh), iridium (Ir), ruthenium (Ru), and gold (Au).[1,2] The scarcity and high costs of precious metals, however, cast doubts on economic viability of the corresponding electrochemical energy technologies.[3] How to reduce the content of precious metals in electrocatalysts, or find their earth-abundant replacements, thus represents a grand challenge for the development of renewable energy technologies.

In a report by Zhang and co-workers in 2011, single-atom catalysts (SACs) are defined as catalysts consisting of only atomically isolated active sites.[4] In principal, SACs have all the metal atoms exposed on the surface and thus can achieve 100% efficiency of atomic utilization, which is particularly attractive for lowering the cost of precious-metal-based catalytic materials (Figure 1). SACs are also featured with the uniformly distributed undercoordinated active sites, providing a model system to bridge the gap between heterogeneous and homogeneous catalysis.[5] Since the concept was introduced to the catalysis community about a decade ago, SACs have attracted great attention and have been demonstrated in a broad range of thermochemical reactions with superior activity and/or selectivity to their cluster or nanoparticulate counterparts.[5−9]

https://dx.doi.org/10.1021/acs.chemrev.0c00594
Chem. Rev. 2020, 120, 12217−12314

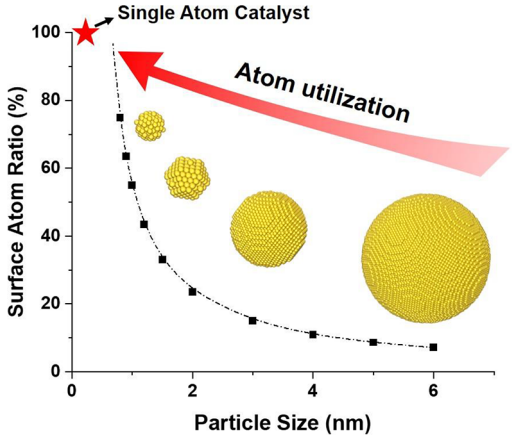

Figure 1. Ratio of surface atoms at different particle sizes.

Almost in parallel (or even prior) to its rise in thermocatalysis, the concept of SAC has been introduced to the electrocatalysis community, albeit in the name of platinum group metal (PGM)-free electrocatalysts.[10] In search of replacements of Pt for the oxygen reduction reaction (ORR), earth abundant 3*d* transition metals, such as manganese (Mn), iron (Fe), cobalt (Co), and nickel (Ni), are dispersed as single atoms on carbon-based conductive substrates, which are usually stabilized via bonding with nitrogen dopants or other heteroatomic species. It is the covalently coordinated transition metal centers that find promising adsorption properties and stability, with the latter probably even more critical in acid electrolytes, of such nonprecious elements for electrocatalytic applications.

Albeit the initial focus on the ORR, the footprint of SACs has extended to other territories of electrocatalysis, with demonstrated applications in the hydrogen evolution reaction (HER), oxygen reduction/evolution reaction (ORR/OER), and CO_2 and N_2 reduction reaction (CO2RR and NRR) (Figure 2).[5,11−13] Meanwhile, the structure of SACs in electrocatalysis has been generalized, ranging from coordinated metal atoms[14−16] to diluted surface alloys[12,17] and oxide-supported metal atoms,[6,18] with various 3*d*−5*d* transition metals being investigated as the active centers (Figure 2). Some efforts also look into the immobilization of molecular catalysts on conductive substrates to derive single-atom electrocatalysts.[19,20] In addition to the enhanced specific (high turnover rates) and mass (high metal utilization efficiency) activities, more attention has been devoted to tailoring the catalytic selectivity by taking advantage of the atomic-scale confinement of adsorption for reaction intermediates, which has given rise to distinct catalytic behaviors from their counterparts expressing continual active sites on the surface.[21]

This review aims to summarize the progress made over the past decade on the development of single-atom electrocatalysts. In recognition of their unique structures and properties, our focus is placed on their distinct catalytic

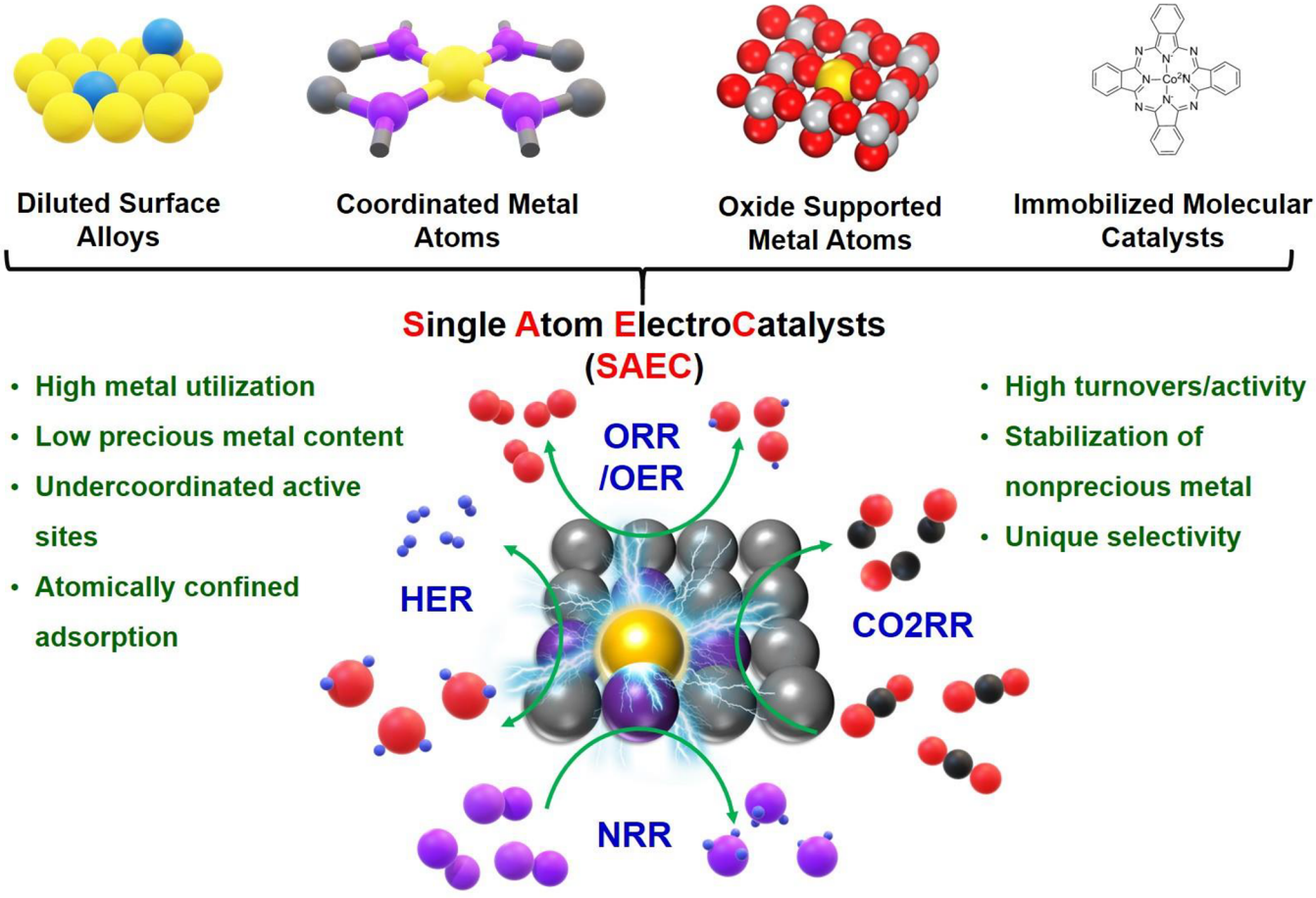

Figure 2. Single atom electrocatalysts (SAEC) tackles challenging electrochemical reactions.

https://dx.doi.org/10.1021/acs.chemrev.0c00594
Chem. Rev. 2020, 120, 12217−12314

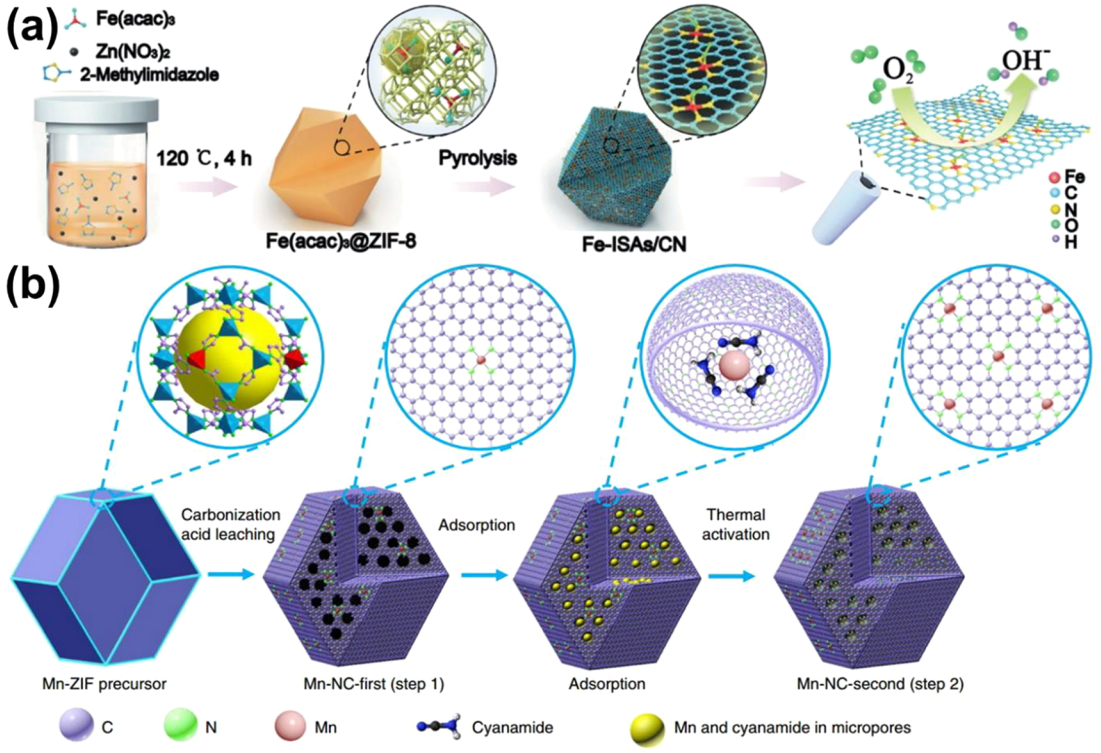

Figure 3. Synthesis routes of single-atom electrocatalysts using ZIF-8 as hard templates. (a) Formation of Fe SAECs by pyrolysis of ZIF-8 impregnated with metal precursors. Reproduced with permission from ref 36. Copyright 2017 John Wiley and Sons. (b) Preparation of Mn SAECs via the combination of adsorption and pyrolysis. Reproduced with permission from ref 42. Copyright 2018 Nature Publishing Group.

performance in various electrochemical reactions and the corresponding mechanistic studies. Considering the importance of synthesis and characterization in understanding the structure−property relationships, we also provide a brief overview of the various synthetic methodologies to control the atomic dispersion of metal sites on various substrates and state-of-the-art microscopic and spectroscopic techniques capable of depicting such atomic structures. We would like to direct the readers to the summaries concentrating on the synthetic chemistry and material science of single atoms if they are specifically looking for those perspectives.[22,23] To distinguish our topic of electrocatalysis from the previous reports on thermocatalysis, we denote single-atom electrocatalysts as "SAECs" in this discussion. A number of review articles can be found in the literature dedicated to the single-atom catalysts for thermochemical reactions.[5,8,24] We also underline that the SAECs hereby refer to the electrocatalysts with atomically dispersed active sites, which are usually a transition metal in its cationic or metallic state. As can be seen from the below discussion, such single-atom active sites would only exist if stabilized via covalent or metallic bonding to an appropriate substrate.

2. SYNTHESIS OF SINGLE-ATOM ELECTROCATALYSTS

It represents a grand challenge for catalyst preparation to achieve single-atom dispersion of metals. This usually means creation of thermodynamically un/metastable phases or structure motifs that requires exotic control of the synthetic conditions to prevent the metal atoms from aggregation, agglomeration, and cluster/nanocrystal growth.[6,25,26] Alternatively, it is plausible to disperse metal atoms via dilution in alloys,[12,17] coordination with organic ligands,[27,28] and supporting on metal oxide or other substrates with strong binding to the metal atoms.[4] While the dispersed single atoms remain metallic in alloys, the other two means rely on the formation of covalent bonds and often result in metal sites in a cationic nature. This task becomes even more challenging for electrocatalysts (as compared to, e.g., catalysts for thermocatalytic reactions[29,30]), as it typically requires relatively high loadings of metal sites to deliver measurable electric currents.[11] Moreover, the substrates used in SAECs need to be conductive, although semiconductors (such as C_3N_4 and TiO_2[30]) are also commonly used. This requirement represents a major difference from the single-atom catalysts for thermochemical reactions, where nonconductive oxides such as zeolites[31−33] and ceria[6,34,35] have been commonly used as supporting substrates. Instead of requiring thermal stability, SAECs are demanded to be stable under electrochemical reaction conditions, which usually involve acid/alkaline electrolytes, oxidizing or reducing reactants (e.g., O_2 and H_2), and cathodic/anodic potentials. In the following discussion, we aim to summarize the recent literature efforts on synthesis of SAECs, with an emphasis on addressing these three issues pertinent to electrocatalysis.

2.1. Anchoring Single Atoms via Coordinative Pyrolysis

Metal−organic frameworks (MOFs) represent a new type of porous materials with well-defined channel structure, high surface area, structural diversity, and facile functionalization at the molecular level, which are built upon coordination between inorganic metal-containing nodes and polyfunctional organic ligands.[36−38] MOFs contain high abundance of anchoring sites and allow for incorporation of single-atom metals with uniform dispersions via additional coordination, adsorption, and/or ion exchange (Figure 3). Moreover, the various amine sites can

https://dx.doi.org/10.1021/acs.chemrev.0c00594
Chem. Rev. 2020, 120, 12217−12314

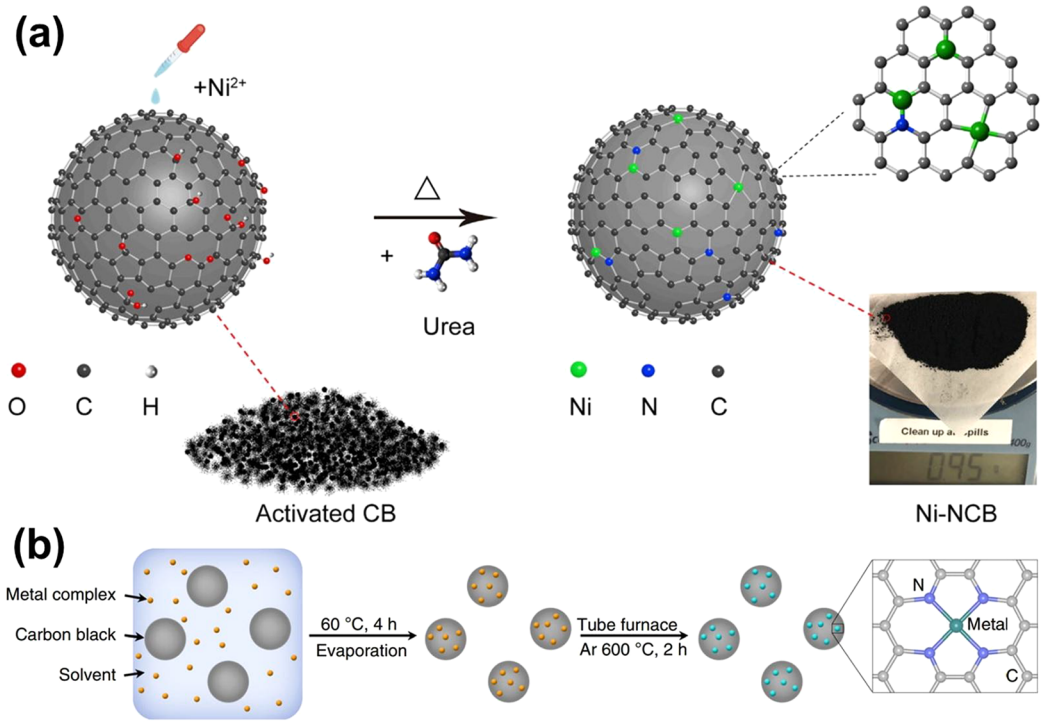

Figure 4. Schematic synthesis of SAECs with carbon black as the support. (a) Synthesis procedure of Ni SAECs. Reproduced with permission from ref 47. Copyright 2018 Elsevier. (b) Universal synthesis process for SAECs. Reproduced with permission from ref 48. Copyright 2019 Nature Publishing Group.

stabilize metal atoms during high-temperature pyrolysis due to the formation of strong metal−nitrogen bonds, giving rise to atomically dispersed metal sites in the derived SAECs (Figure 3).[39−41]

Zeolitic imidazolate frameworks (ZIFs), a typical subclass of MOFs composed of M $(MeIm)_2$ (e.g., M = Zn(II) in ZIF-8, M = Co(II) in ZIF-67; MeIm = 2-methylimidazole), are the most widely used precursors for preparing SAECs, which are advantageous owing to their facile synthesis, large surface area, and high porosity.[43−47] In this class of materials, ZIF-8 is of particular interest for SAECs synthesis, with the high content and reducing nature of Zn often being utilized to achieve high loading of the second metal. Another advantage of ZIF-8 as sacrificing templates for SAECs preparation is the facile vaporization of Zn during typical thermal pyrolysis, leaving no impurity metal in the derived catalysts. In a typical report of this approach, Chen et al. synthesized Fe SAECs via pyrolysis of ZIF-8 impregnated with iron acetylacetonate $(Fe(acac)_3)$ (Figure 3a).[36] They first dissolved $Zn(NO_3)_2 \cdot 6H_2O$ and $Fe(acac)_3$ in methanol under sonication, which was then added into another methanol solution of 2-methylimidazole. ZIF-8 encapsulating $Fe(acac)_3$ was derived via solvothermal growth and further pyrolyzed at 900 °C under an Ar atmosphere to obtain SAECs. During pyrolysis, which is usually necessary to convert the ZIF template into conductive substrates, Zn species vaporized and Fe atoms were found to bind to the nitrogen (N) sites in the obtained N-doped porous carbon products. Owing to the high content of N in ZIF-8, the loading of atomically dispersed iron achieved 2.16 wt %.

Alternative to impregnation, second metals can be introduced via ion exchange.[14] More recently, Li et al. reported a two-step doping and adsorption method to further increase the loading of metal single atoms.[42] As shown in Figure 3b, they first prepared Mn-impregnated ZIF-8 and pyrolyzed it to make a Mn−N−C composite and then applied acid leaching to this composite to obtain a porous nanostructure. Subsequently, they added Mn precursor and cyanamide, a nitrogen source, into this porous nanostructure by impregnation. After a second thermal activation, single-atom Mn catalysts were obtained at a loading of 3.03 wt %. It is interesting to point out that, as indicated by this work, high-surface area, porous carbon substrates (as what is derived after the first step of pyrolysis by Li et al.) may also be used as templates for the synthesis of SAECs.

Despite extensive studies and successful synthesis of SAECs with various metals, the method of pyrolyzing MOFs-based templates is still limited by the relatively low yields and the use of expensive organic linkers. Direct use of high-surface area carbon and other readily available conductive materials as substrates to incorporate metal precursors thus becomes a more appealing approach toward scalable synthesis of SAECs. For instance, Zheng et al. reported a simple and scalable method for the synthesis of Ni SAECs by using carbon black as the support.[47] As shown in Figure 4a, Ni^{2+} ions were adsorbed onto water-soluble carbon black, most likely by binding to the oxygen-containing functional groups or defect sites. With urea added as the nitrogen source, the obtained composite was then pyrolyzed to produce Ni−N−C SAECs. This method was further reported to be universal for SAECs by using 1,10-phenanthroline as the coordinating ligand, with the single-atom metal sites including Ni, Mn, Fe, Co, Cr, Cu, Zn, Ru, and Pt (Figure 4b).[48] The direct use of carbon black and organic ligands to form composite for pyrolysis bypasses the intermediate step of growing MOFs and allows for scaling up the synthesis of SAECs to the kilogram scale.

Other reports have used metal−ligand complexes adsorbed on graphene[49] or carbon nanotubes[50] to derive SAECs. Without the addition of high-surface area carbon, it is also

https://dx.doi.org/10.1021/acs.chemrev.0c00594
Chem. Rev. 2020, 120, 12217−12314

plausible to directly pyrolyze metal−organic composites to derive SAECs. In this way, urea,[26] dicyandiamide,[51,52] and copolymer of pyrrole and thiophene[49] have been reported as sacrificing ligands. During pyrolysis, the organic ligands are turned into conductive, N-doped carbon, with the metal single atoms anchored on the nitrogen sites. It is noted that coordination in the metal−ligand complex may play an important role in determining the atomic structures of the SAECs derived from pyrolysis. In their effort on the synthesis of Fe-SAECs using hemin (ferric chloride heme) as the precursor, Zhang et al. compared the cases with or without melamine as additional ligands.[53] As shown in Figure 5, direct

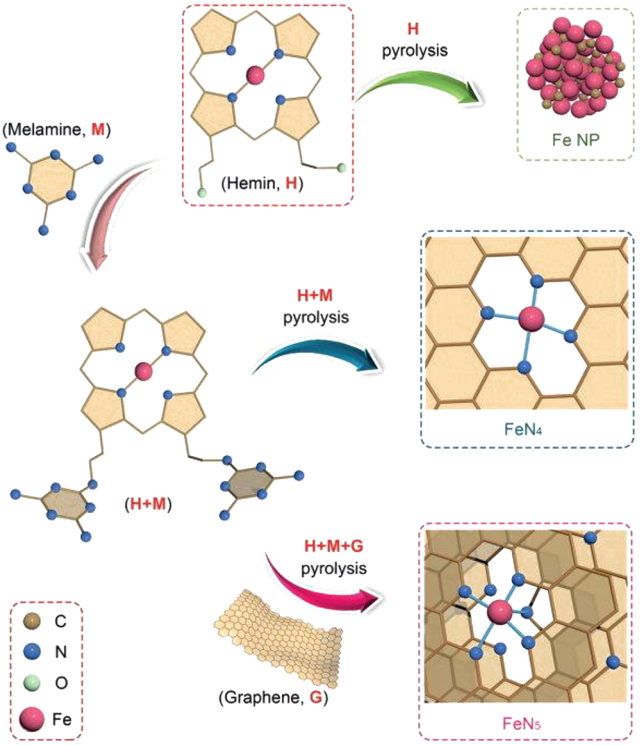

Figure 5. Synthetic routes toward FeN_4 and FeN_5 SAECs. Reproduced with permission from ref 53. Copyright 2019 John Wiley and Sons.

pyrolysis of hemin led to the formation of iron nanoparticles, with the aggregation of Fe atoms being attributed to the rather small coordination number (CN = 2) between Fe and N in the hemin molecule. When melamine was introduced to form a molecular complex with hemin, it provided an additional local N source and somehow facilitated formation of additional metal-N bonds, favoring the dispersion of the metal as isolated FeN_4 motifs. They further found that pyrolysis of hemin and melamine coadsorbed on graphene gave rise to FeN_5 SAECs. Albeit the lack of mechanistic understanding for the molecular transformation via pyrolysis, this work does suggest the potential of controlling the atomic structures of SACEs by tailoring the coordination of the metal−ligand complex precursors.

2.2. Anchoring Single Atoms via Defects

Besides coordinative pyrolysis, defects on oxides, hydroxide, or carbon substrates have also been utilized to anchor single metal atoms. The use of oxide substrates is more commonly seen in the thermocatalysis community (Figure 2).[4,9,24,54,55] Single atoms can be stabilized on oxide surfaces by taking advantage of strong metal−oxygen interactions, especially at coordinatively unsaturated step or vacancy sites. Such interactions can be further tailored to enhance the catalytic activity, selectivity, and/or durability.[5,8,11] However, oxides usually have limited conductivity that is not appealing for electrocatalytic applications, and thus much less work has been done for oxide-supported SAECs. One of such rare examples is Cu single atoms supported on CeO_2 nanorods (Cu-CeO_2-4%).[56] The Cu-CeO_2-4% SAEC was synthesized by wet impregnation of Cu^{2+} onto CeO_2, followed by annealing in a forming gas (5% H_2). During the pyrolysis, the as-reduced Cu monomers was believed to be captured and stabilized by the oxygen vacancies on CeO_2. The CeO_2 nanorods preferentially expose the (110) facet on the surface, which could accommodate the single-atom Cu via association with three oxygen vacancies. The derived Cu SAECs were used for electroreduction of CO_2.

As a two-dimensional carbon material, graphene is one of the most studied substrates to host SAECs, taking advantage of its high specific surface area and high electron mobility.[57] However, it is challenging to immobilize single atoms directly on ordered, defect-free graphene, as the small migration barrier for metal atoms easily leads to aggregation and formation of clusters or nanoparticles.[23,58] Therefore, many research efforts have been dedicated to the design and engineering of defects on graphene to stabilize single-atom active centers.[59−62] For example, Yao and co-workers reported a strategy to trap Ni single atoms in graphene defects.[59] The defects on graphene were constructed by annealing graphene with melamine at 700 and 1050 °C for 2 h in a nitrogen atmosphere. Then Ni clusters were loaded on the as-synthesized defective graphene (DG) by annealing deposited Ni hydroxide at 750 °C. Further acid leaching was applied to remove aggregated Ni and leave single-atom Ni anchored on the defect sites. The association of Ni atoms with vacancies on the graphene substrate was verified HADDF-STEM measurements (Figure 6).

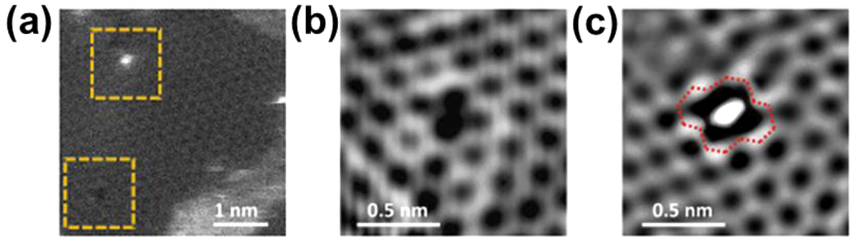

Figure 6. (a) HADDF-STEM image of A-Ni@DG. (b) Zoom-in image of the defective area (vacancy) marked with the yellow dashed frames in the bottom left of (a). (c) Zoom-in image of the defective area (with atomic Ni trapped) marked with the yellow dashed frames in the top left of (a). Divacancy is marked with the red dashed line. Reproduced with permission from ref 59. Copyright 2018 Cell Press.

https://dx.doi.org/10.1021/acs.chemrev.0c00594
Chem. Rev. 2020, 120, 12217−12314

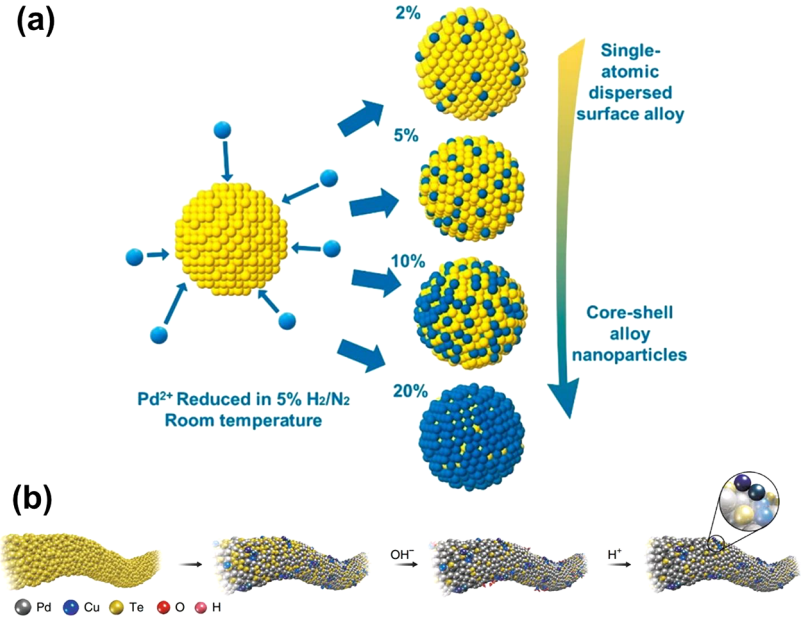

Figure 7. (a) Synthetic scheme for single Pd atoms deposit on Au nanoparticles surface. Reproduced with permission from ref 17. Copyright 2019 American Chemical Society. Schematic construction of single-atom surface alloys at atomic level. (b) Fabrication procedures of copper atom-pair catalyst. Reproduced with permission from ref 33. Copyright 2019 Nature Publishing Group.

2.3. Diluted Surface Alloys

Alloying represents a common but robust strategy toward tailoring the geometric (e.g., via strain[50,63]) and/or electronic (via ligand effects[64,65]) structures of catalyst surfaces. The coexistence of heterogeneous metal atoms on the surface can also enable synergistic effects that stabilize key reaction intermediates or facilitate multistep reactions.[66] When the content of one alloying element is reduced to the dilution limit, atoms of this metal could become atomically dispersed within the lattice of the other metal and form single atoms embedded in or supported on the surface of the host metal. In practice, this is more commonly achieved via dosing one metal at low atomic ratios onto another metal substrate, with single-atom sites constructed on the diluted alloy surfaces (Figure 2). Compared to the coordinative pyrolysis strategy discussed in the above section, this means does not rely on high-temperature thermal treatments to obtain atomic dispersion and allows for more robust control over the atomic dispersions.

Using the diluted surface alloy strategy, Wang et al. synthesized bimetallic Pd@Au electrocatalysts with Pd atomically dispersed on Au nanoparticles.[17] As shown in Figure 7a, a series of Pd@Au electrocatalysts were synthesized by decorating Au nanoparticles (supported on carbon black) with Pd at controlled doses, via low-temperature reduction of palladium chloride ($PdCl_2$) with hydrogen. By varying the loading of Pd from 2 to 20 atom %, they were able to tune the ensemble size of Pd atoms from single atoms to a continuous shell. Jiao et al. reported a copper atom-pair catalyst by simultaneous introduction of Pd and Cu onto Te nanowires via galvanic replacement (Figure 7b).[33] After dilute alkaline and acid washing, the derived nanostructures were believed to contain copper atom pairs of different charges (Cu_1^0–Cu_1^{x+}) anchored on $Pd_{10}Te_3$ alloy nanowires, with the formation probably ascribable to the unique crystal structures of the substrate. Duchesne et al. synthesized a series of Pt/Au surface alloy by coreduction of Pt and Au precursors.[12] They discovered that Pt atoms were isolated on Au nanoparticle surface at 4 wt % Pt loading, yielding Pt single atoms on Pt/Au alloy surface. The dispersed Pt sites were found to be highly active for formic acid oxidation by suppressing CO poison effect on continuous Pt surface.

2.4. Atomic Layer Deposition

Atomic layer deposition (ALD) is an emerging technique for preparing single-atom catalysts.[13,67] In a typical ALD process, metal precursor, in gas form, is flown to the reaction chamber and exposed to a second gas reactant to form an atomic layer onto a prestanding substrate. The size and thickness of the deposition are precisely controlled by simply adjusting the number of ALD cycles. Sun and co-workers introduced a synthetic method that prepared Pt single atoms on a graphene nanosheet (GNS) through ALD.[68] First, the Pt precursor, (methylcyclopentadienyl)-trimethylplatinum ($MeCpPtMe_3$), was exposed to GNS and reacted with adsorbed oxygen (either on GNS or Pt), to form CO_2, H_2O, and hydrocarbon fragments (eq 1). The subsequent oxygen exposure forms a new adsorbed oxygen layer on the Pt surface (eq 2). The two steps complete one cycle of ALD. After 50 cycles, they found the formation of highly dense Pt single atoms, in addition to some Pt NPs and clusters.

$$\mathrm{Pt-O^*} + \mathrm{MeCpPtMe_3} \rightarrow \mathrm{Me_2Pt(MeCp)^*} + \mathrm{CO_2\uparrow} + \mathrm{H_2O\uparrow} + \text{fragments} \quad (1)$$

$$\mathrm{Me_2Pt(MeCp)^*} + \mathrm{O_2} \rightarrow \mathrm{Pt-O^*} + \mathrm{CO_2\uparrow + H_2O\uparrow} + \text{fragments} \quad (2)$$

2.5. Perspectives about the Synthesis of Single-Atom Electrocatalysts

It remains a great challenge to precisely control the coordination of single-atom sites in the synthesis of SAECs. The derived single atoms usually possess a diversity of coordination number with the support, with only a small

https://dx.doi.org/10.1021/acs.chemrev.0c00594
Chem. Rev. 2020, 120, 12217−12314

portion of them being active or stable under electrochemical reaction conditions. One of the major hurdles is the lack of mechanistic understanding of the molecular transformations during high-temperature pyrolysis, which is usually used for deriving metal−nitrogen bonding in the M−N−C type of composite catalysts. The use of high-temperature annealing also limits the loading of metal single atoms, as high metal content would usually lead to the growth into nanoclusters or nanoparticles. So far, most SAECs have a typical metal loading of ∼1−5 wt % or even lower for the single-atom component, which has limited the mass- or volume-specific electrocatalytic activities. New synthetic methods, substrates and ligands need to be developed in order to yield higher single-atom loadings.

In SAECs, the substrate plays an important role, not only for anchoring and stabilization of the metal single atoms, but also in determining the catalytic activity, selectivity, and/or stability. Sometimes synergy between the metal site and the substrate is the key to enable reaction pathways and overcome kinetic barriers. Carbon-based materials such as carbon black, carbon fibers, carbon nanotubes, and graphene, are commonly employed as conductive substrates in SAECs. The key to synthesize stable SAECs thus becomes tailoring the coordination between the metal atoms and the substrate, with pertinent parameters including coordination number, heteroatomic intermediates, and density/loading of metal atoms. In this aspect, doping the carbon substrate with heteroatoms such as N, O, and S, or prechelating the metal atoms with ligands involving such heteroatoms, is often found to be an effective strategy to ensure the binding and dispersion of single metal atoms during high-temperature pyrolysis process.[48,69−72] Similar strategies can also be seen in the use of MOFs- or covalent organic frameworks (COFs)-based precursors for pyrolytic synthesis of SAECs. In this case, M−N−C type of structures are usually derived, which have been extensively studied for electrocatalytic applications.[23]

Beyond single atoms, it is interesting to explore more robust control over the dispersion of metal sites. Ensemble effect has been shown to play an important role in electrocatalysis.[12,17,73] Dimeric metal sites have also been reported to own unique catalytic properties in thermochemical[74] and electrochemical[33,40] reactions. Homo-, or even hetero-, nuclear dimers can be desirable for catalyzing multistep, complex reactions that involve molecular association/dissociation as the rate-limiting or product-determining steps (e.g., CO_2 reduction toward C_2 products; see the following discussion in section 7). Great potentials are thus envisioned for further studies of atomically dispersed electrocatalysts beyond single atoms.

Diluted surface alloys can circumvent some of the drawbacks of M−N−C type SAECs derived from coordinative pyrolysis and principally allow for controlling the metal ensembles beyond single atoms, but its random nature of surface structures undermines the robust controllability and require more comprehensive studies to uncover the physical/chemical principles governing the growth and surface structure of such SAECs. For example, surface segregation may lead to the enrichment and aggregation of the dilute element on the surface or migration of the dosed metal single atoms away from the surface into the bulk host metal due to diffusion.[50] In this case, intermetallic alloys (or compounds) may shed new lights on the development of SAECs. This type of long-range-ordered alloy has been used for electrocatalytic applications such as ORR,[75−79] but so far the studies have been focused on the enhanced electrochemical stability. Unique catalytic selectivities of single-atom sites on the surface of intermetallic alloys have been seen in thermocatalytic reactions. It remains an open question if similar mechanisms can be reproduced in electrocatalytic processes.

Molecular catalysts, such as metal porphyrins and metal phthalocyanines, has raised emerging research interest in recent years. Inherited from predefined chemical structure, molecular catalysts featured chemical stability, homogeneous active sites, and unique electronic property (Figure 2).[80] However, high impedance of molecular catalysts poses a challenge to incorporate them in the electrochemistry systems. Different conductive support and electrode preparation protocols may lead to totally different catalytic performance. For example, by depositing a single layer of Co-phthalocyanine (Co-Pc) on carbon nanotube (CNT), Wang and co-workers found its great potential to produce methanol from CO2RR, a product rarely seen from other CO2RR catalysts, including Co-Pc prepared in other methods.[81] Support effect is a new frontier in molecular catalyst. Further research of the design and engineering of effective supports is strongly desired to unveil the full potential of molecular catalysts.

3. CHARACTERIZATION OF SINGLE-ATOM ELECTROCATALYSTS

SAECs possess atomically dispersed metal atoms supported on another substrate. Among the different types of substrates, N-doped carbon is probably the most friendly for characterization of the single atoms, owing to its relatively low electron contrast, as compared to the metal sites or other substrates such as alloys and oxides. Accompanying the synthetic efforts, considerable progress has also been made on characterizing the atomic structures of single-atom catalysts in the past decade by using techniques such as scanning tunneling microscopy (STM), transmission electron microscopy (TEM), X-ray photoelectron spectroscopy (XPS), X-ray absorption spectroscopy (XAS), diffuse reflectance infrared Fourier transform spectroscopy (DRIFTS), temperature-programmed desorption and reduction (TPD/TPR), etc.[5,11,13,82] As for SAECs, it is more common to use electron microscopic and X-ray spectroscopic techniques, whereas DRIFTS and TPD/TPR techniques are more often used in the thermocatalysis community. In the following discussion, we aim to present some exemplary studies for each of the five selected techniques, instead of comprehensively reviewing all the work on SAECs.[82] We place our emphasis on portraying the dispersion and coordination of the metal sites and note that multiple techniques are usually combined in practice to obtain a comprehensive picture of the material structures.

3.1. Structural Characterizations of Single-Atom Electrocatalysts

3.1.1. Scanning Tunneling Microscopy. STM utilizes an atomically sharp metallic tip to scan the atomic structures of surfaces based on quantum tunneling of electrons.[83] It is commonly used in surface science studies to examine model catalysts such as single crystals with well-defined surface structures.[84,85] While we are unaware of any particular studies using STM for SAECs, we note that it has been used in the thermocatalysis community to characterize single atoms supported on single crystals. For example, Boucher et al.[86] studied the aggregation process of Pd atoms supported on Cu(111) at increasing loading. In this work, the collected STM images revealed isolated Pd atoms at surface coverages up to

https://dx.doi.org/10.1021/acs.chemrev.0c00594
Chem. Rev. 2020, 120, 12217−12314

0.01 monolayer (ML), whereas Pd/Cu alloy, Pd clusters and ad-islands start to form at higher doses (Figure 8a–d). It was

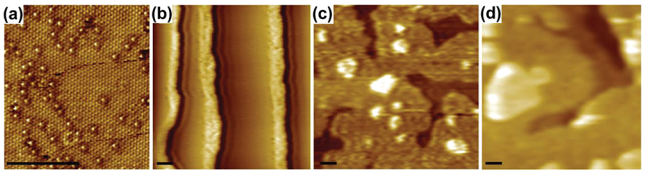

Figure 8. STM images of Pd/Cu(111) alloy surfaces with a varying coverage of Pd: (a) 0.01 ML, (b) 0.1 ML, (c) 1 ML, and (d) 2 ML. Scale bars: (a) 5 nm, (b) 5 nm, (c) 5 nm, and (d) 5 nm. Pd/Cu alloys were formed at 380 K. Reproduced with permission from ref 86. Copyright 2013 Royal Society of Chemistry.

further claimed that STM in combination with TPD/TPR can be used to study the dissociative adsorption of H_2 on the Pd single-atom sites.[7] We believe similar techniques can also be used to study electrocatalysts, especially those made of diluted surface alloys. It is potentially advantageous for STM to acquire electronic structure information on the single-atom sites and probe molecular adsorbates associated with them.

3.1.2. Transmission Electron Microscopy. Nowadays, TEM techniques are widely employed to characterize catalytic materials involve single-atom active sites. It should be pointed out that, to our best knowledge, the first microscopic image of single uranium (U) atoms was acquired by Crewe et al. using scanning transmission electron microscope (STEM) in the early 1970s, long before single atoms became a hot research topic in catalysis.[87] They developed a cold-field emission electron apparatus that allows for the construction of a subnanometer electron beam for scanning at high spatial resolutions and an annular dark-field (ADF) detector that substantially improves the signal-to-noise ratio. Imaging contrast of such ADF-STEM methods depends on both atomic number and crystallographic orientation of the object, which becomes a limitation for distinguishing small metal particles or clusters from crystalline substrates, a combination commonly seen in catalytic materials.[88] Howie's group at Cambridge University proposed to increase the inner collection angle of the ADF detector to suppress the diffraction contrast of crystalline materials and thus recover the atomic number contrast of the supported noble metal particles/clusters.[89] The new imaging mode, denoted as high-angle ADF (i.e., HAADF-STEM), proved to be highly valuable for characterizing supported single-atom catalysts.[4,17,90]

In HAADF-STEM, the higher the Z value of the single-atom element, the more electrons are scattered at higher angles due to greater electrostatic interactions between the nucleus and the scanning electron beam. As a result, a higher Z contrast of the metal than the substrate gives rise to better images of the single atoms. In 1996, Nellist et al. observed "occasional two-atom features" in their effort on using high-resolution STEM to image ultradispersed Rh on γ-Al_2O_3 support (Figure 9a).[90] Later on, more explicit images of isolated Pt atoms were obtained by Qiao et al. on an iron oxide substrate by using HAADF-STEM (Figure 9b). In both cases, the single atoms of noble metals appear as bright dots in the images, as they have much higher Z contrast than the oxide substrates. The Z-contrast strategy works particularly well for the M–N–C type SAECs, due to the drastic difference in atomic weight between the metal center and underlying elements. For example, Huang

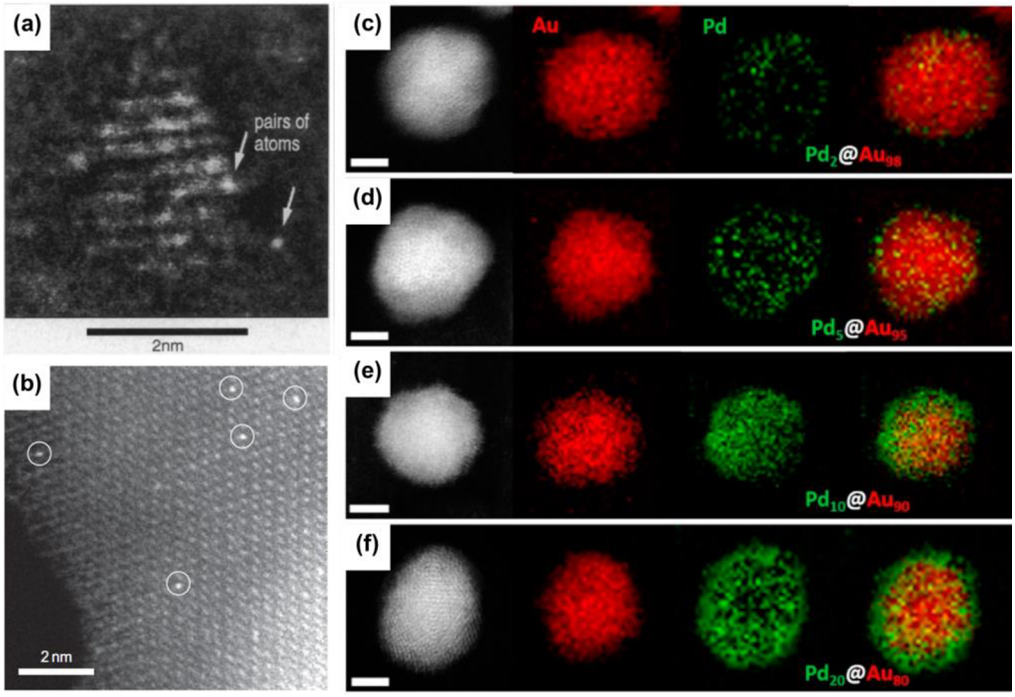

Figure 9. (a) Band-pass-filtered Z-contrast STEM image of ultradispersed Rh supported on γ-Al_2O_3. Some individual Rh atoms and atom-pairs can be resolved. Reproduced with permission from ref 90. Copyright 1996 The American Association for the Advancement of Science. (b) HAADF-STEM image of Pt_1/FeO_x catalyst. The Pt single atoms appear as individual bright dots overlapped on the lattice of iron oxide. Reproduced with permission from ref 4. Copyright 2011 Springer Nature. (c–f) STEM images and EELS-based elemental maps for (c) $Pd_2@Au_{98}$, (d) $Pd_5@Au_{95}$, (e) $Pd_{10}@Au_{90}$, and (f) $Pd_{20}@Au_{80}$, where Au and Pd atoms are represented by red and green pixels, respectively. Scale bar, 2 nm. Reproduced with permission from ref 17. Copyright 2019 American Chemical Society.

https://dx.doi.org/10.1021/acs.chemrev.0c00594
Chem. Rev. 2020, 120, 12217–12314

and co-workers used STEM to visualize dispersed metal centers in $M-N_4-C_4$ (M = Ni, Fe, Co) motifs (Figure 10).[71] The heavy metal atoms could be represented by bright dots throughout the graphene matrix.

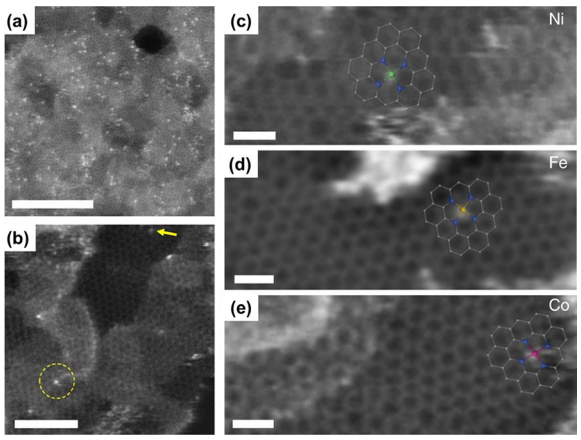

Figure 10. (a,b) Uniform distribution of single metal atoms dispersed in a graphene matrix revealed by low (a) and high (b) magnification TEM images. The circle and arrow indicate some typical individual metal atoms in multilayer and single-layer regions of the graphene support, respectively. Scale bars: (a) 5 nm and (b) 2 nm. (c−e) High-resolution TEM images enable the direct visualization of the atomic metals of (c) Ni, (d) Fe, and (e) Co embedded in the 2D graphene lattice. The overlaid schematics represent the structural models determined from XAFS analysis. Scale bars: 0.5 nm. The bright region at the top part of (d) is attributed to out-of-focus thick graphene layers or nonplanar flakes. Reproduced with permission from ref 71. Copyright 2018 Nature Publishing Group.

The *Z*-contrast strategy, however, may not apply to diluted surface alloys, where the *Z* contrast of the metallic substrate is usually close to the supported single atoms. In a recent report by Wang et al.,[17] electron energy loss spectroscopy (EELS)-based elemental mapping was used to characterize Pd atoms dispersed on Au nanoparticles. *Z*-Contrast STEM imaging was not able to resolve the single atoms in this case, as Au has a higher electron density then Pd. At a low loading of 2 atom %, Pd appears as individual, discrete dots in the map (Figure 9c). As the loading of Pd increases, Pd ensembles of a few atoms start to appear (Figure 9d), and eventually a semicontinuous layer forms at loadings >10 atom % (Figure 9e,f). Hereby, EELS instead of more commonly seen energy-dispersive X-ray spectroscopy (EDS) was used for elemental mapping, owing to the higher signal-to-noise ratio when it is used in the HAADF-STEM mode.

3.1.3. Photoelectron Spectroscopy. As a surface sensitive (from one to a few nanometers, depending on the photon and electron energies) spectroscopy technique, X-ray photoelectron microscopy (XPS) has been widely used for characterizing the compositions and electronic structures of solid-state materials.[91−93] When applied to SAECs, it is able to discern the oxidation state and coordination environment of the single-atom active sites from the measured core-level electron energies and energy shifts. For this reason, it has commonly been used for studying coordinated metal single atoms, and the evolution of peak features associated with variations in metal loading, pretreatment conditions, heteroatomic doping (e.g., N-doped carbon), etc., has been correlated to the electrocatalytic performance to interpret the active sites and catalytic mechanisms. It should be pointed out that XPS by itself is not capable of resolving the atomic dispersion of metal sites and is thus usually combined with other techniques with atomic resolution (e.g., HAADF-STEM and XAS) for the characterization of SAECs.

Peng et al. used XPS to determine the electronic structures of Fe and N in an Fe−N−C type of SAECs for understanding the active sites for ORR.[94] They deconvoluted the N 1s spectrum in the energy range of 396−404 eV into pyridinic N, benzenoid amine, graphitic N, oxidized N, as well as a peak at 399.1 eV assigned to the Fe−N motif (Figure 11a). Meanwhile, the analysis of the Fe 2p spectrum indicated that the Fe species were present in the oxidation states of both +2 and +3 (Figure 11b). On the basis of these observations, they argued the $Fe^{\delta+}$ cations are coordinated to the N dopants on the support. Yang et al. examined a Ni-based SAEC by using XPS and found the Ni metal center is in a low-valence state (1+) (Figure 11c).[95] They performed (quasi-)*operando* XPS measurements under the CO2RR conditions and were able to discern physically adsorbed CO_2 and activated $CO_2^{\delta-}$ adsorbates on the catalyst, accompanied by a decrease of Ni 3d density of state (Figure 11d). On the basis of these observations, they proposed a mechanism of CO_2 activation based on the charge transfer from Ni to the CO_2 adsorbate within the Ni-$CO_2^{\delta-}$ motif, leading to the rise of the Ni oxidation state above +1.

A recent study by Schlögl and co-workers demonstrated that the free-atom-like *d* states could be observed in dilute Cu single atom in AgCu alloy by valence photoemission spectroscopy (VPS).[96] VPS measurements ($h\nu$ = 150 eV) showed that the Cu 3*d* states in AgCu were one-fifth the width in bulk Cu (Figure 11e). Calculated pDOS shows near degeneracy in Cu 3*d* states in AgCu, which are typically split in octahedron field of bulk Cu crystal (Figure 11f). These electronic structure characteristics derived from the photoemission spectra provides a very strong evidence for the existence of Cu single atom and the change in its electron structure from bulk Cu material. The Cu single atom on Ag was then found to exhibit an activation barrier 0.1 eV lower than bulk Cu in methanol reforming.

3.1.4. X-ray Absorption Spectroscopy. In addition to TEM and XPS, XAS is another commonly used technique to characterize single-atom catalysts, whereby it is plausible to derive the electronic and local atomic structure of matter via analysis of the X-ray absorption near-edge structure (XANES) and the extended X-ray absorption fine structure (EXAFS), respectively.[97,98] Compared to the direct but localized view of atoms under TEM, XAS provides a more global view of the catalysts, usually in terms of XANES for the average oxidation states of active sites but requires a rather sophisticated data fitting process for EXAFS to acquire the structural parameters, such as bond length and coordination number (CN).[82,99] XAS is one of the few techniques that can probe the interaction between metal and support in catalysts, making it advantageous to study the coordination of single atoms with the substrate in SAECs.[100,101] With synchrotron light sources, XAS can also be performed under reaction conditions, probing the catalytically active sites upon interaction with adsorbing intermediates *in situ* (or in *operando*).[4,32,34,100,102]

Zhang et al.[103] used XAS to study Pt single atoms stabilized in N-doped porous carbon matrix (denoted as Pt@PCM in their report). They used wavelet transform (WT) analysis, which resolves overlapping EXAFS paths based on the atomic

https://dx.doi.org/10.1021/acs.chemrev.0c00594
Chem. Rev. 2020, 120, 12217−12314

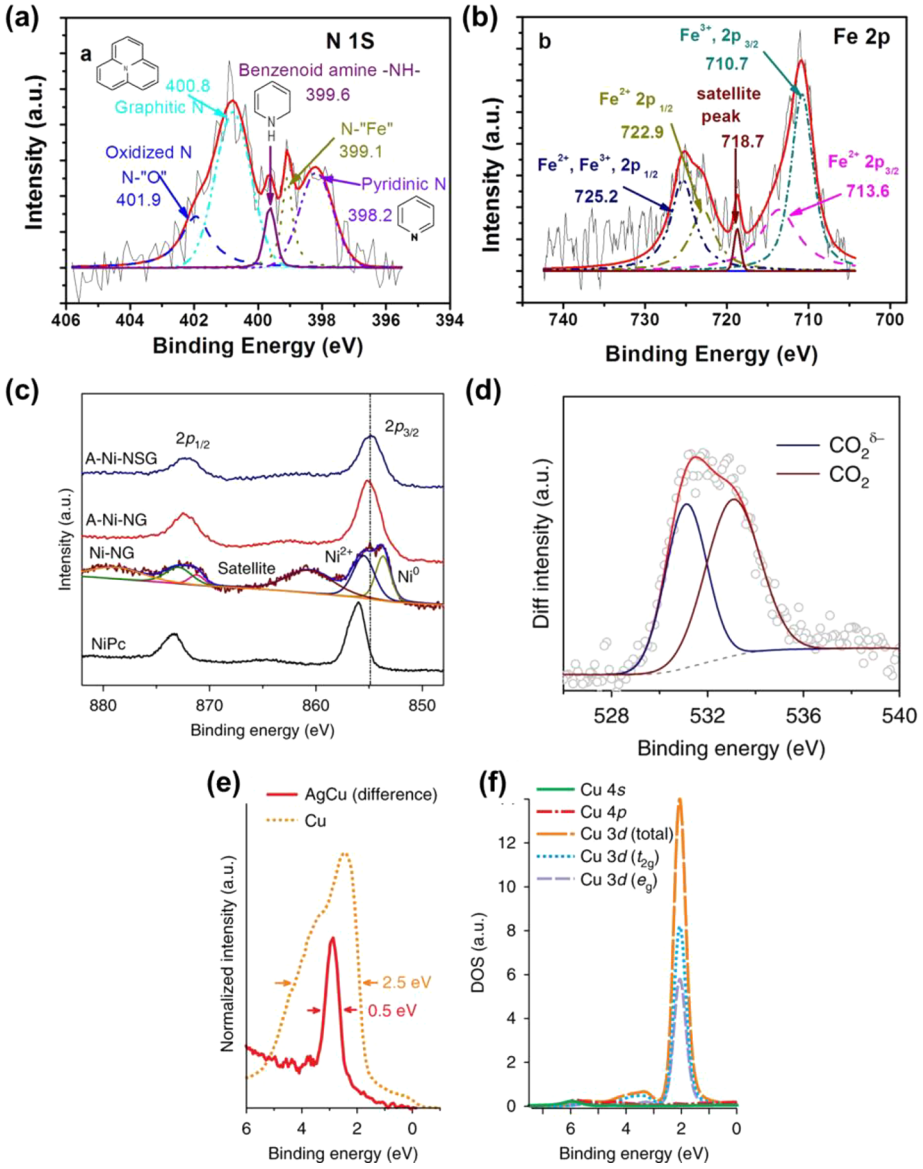

Figure 11. (a,b) High resolution XPS spectra of (a) the N 1s and (b) Fe 2p electrons of Fe-PANI/C-Mela catalyst. Reproduced with permission from ref 94. Copyright 2013 Nature Publishing Group. (c) High-resolution XPS Ni 2p spectra, where Ni in A-Ni-NG and A-Ni-NSG is in a valence state lower than +2 but higher than 0, highlighted by the dashed line. (d) Change in the XPS O 1s intensity induced by CO_2 adsorption for A-Ni-NG. Reproduced with permission from ref 95. Copyright 2018 Nature Publishing Group. (e) Difference spectrum of AgCu and Ag, plotted with a Cu reference spectrum, demonstrate that the Cu 3d states in AgCu are one-fifth the width in bulk Cu. (f) Calculated Cu-based pDOS of $Ag_{31}Cu_1$. The near degeneracy in AgCu indicates a very weak interaction between Cu 3d states and the surrounding Ag matrix. a.u., arbitrary units. Reproduced with permission from ref 96. Copyright 2018 Nature Publishing Group.

numbers of the scattering atoms, to distinguish the Pt−Pt coordination from the bonding between Pt and the light elements (N and C).[104] While the catalyst with Pt nanoparticles (20 wt % Pt/C) shows the Pt−Pt feature at ~8.5 $Å^{-1}$, the Pt@PCM catalyst gives the WT intensity maximum near 5.5 $Å^{-1}$, which was attributed to Pt−N or Pt−C coordination (Figure 12a,b). It was thus confirmed that Pt was isolated as single atoms in Pt@PCM. In another study, Jiao et al.[33] used XAS to characterize Cu atoms deposited on $Pd_{10}Te_3$ alloy nanowires. EXAFS analysis shows that Cu is atomically dispersed and partially oxidized to Cu^{x+} (Figure 12c). By comparing the XANES spectra to the theoretically calculated spectra for Cu clusters of various sizes, they concluded that the Cu species form Cu_4−O motifs in their catalysts (Figure 12d). Further atomistic simulation indicates that one Cu in the Cu_4−O motif binds with the oxygen atom to form Cu^{x+}, which couples with a neighboring Cu^0 atom to form a stable Cu_1^0−Cu_1^{x+} pair (Figure 12e). Shao et al.[105] applied XANES to analyze the oxidation state of Ir single atoms confined in porous organic polymers with aminopyridine functionalities. By comparing the XANES spectra to various references, they found that the Ir single atoms have a lower oxidation state than the Ir precursor (H_2IrCl_6) but higher than bulk Ir metal and Ir-based nanocatalysts (Figure 12f). The unique oxidation state of Ir was ascribed to Ir−O_3−N coordination.

From the above examples, it can be seen that XAS has commonly been used to exclude the presence of metal clusters or nanoparticles in SAECs. It should be noted that XAS only provides average information throughout the entire catalyst. This feature makes it challenging to reliably resolve the valence

https://dx.doi.org/10.1021/acs.chemrev.0c00594
Chem. Rev. 2020, 120, 12217−12314

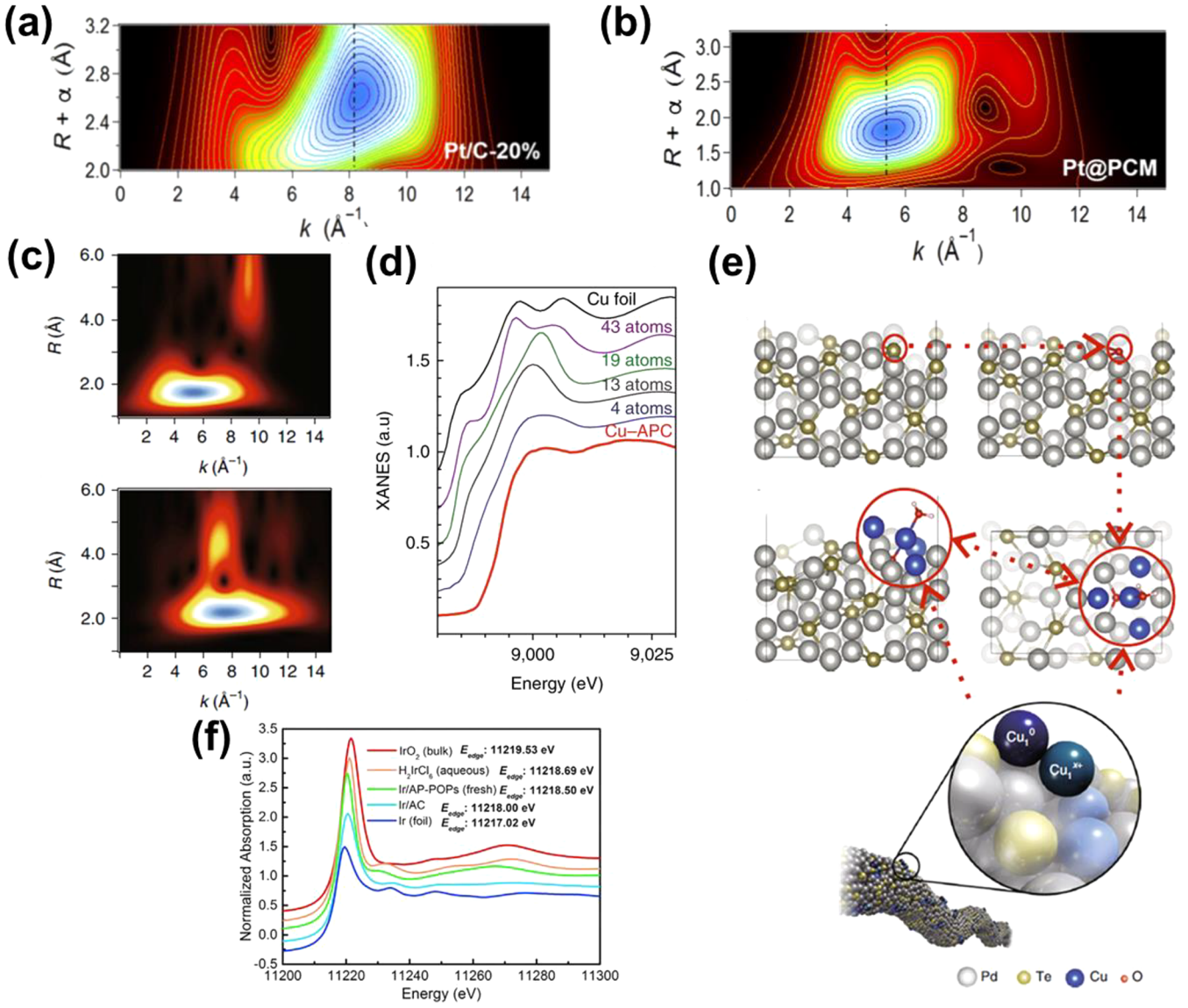

Figure 12. (a,b) EXAFS wavelet transform (WT) for the k^3-weighted EXAFS signals of Pt/C-20% and Pt@PCM. Reproduced with permission from ref 103. Copyright 2018 The American Association for the Advancement of Science. (c) Wavelet transform plots of Cu−APC (0.10% Cu) (top) and Cu foil (down). (d) The XANES spectra of Cu−APC and Cu foil and the corresponding calculation of XANES spectra of varying numbers of Cu atoms. (e) Theoretical calculation with the depicted structures for Cu-doped $Pd_{10}Te_3$ nanowires. Reproduced with permission from ref 33. Copyright 2019 Nature Publishing Group. (f) The normalized XANES spectra at the Ir L_3-edge of different samples. Absorption edge energy values were determined by the first inflection point of each near-edge spectrum. Reproduced with permission from ref 105. Copyright 2019 Cell Press.

or coordination information for nonuniform samples, especially for those minor species that may play a critical role in catalysis. For a comprehensive understanding of the structure−property relationship of SAECs, it is usually important to combine XAS and TEM to acquire the structural information from multiple levels (global vs local) and aspects (indirect vs direct). It is also very rare to derive information on adsorbing reaction intermediates from XAS, even under operando conditions, partially due to the small scattering cross-section of light molecules as compared to the metal atoms.[29] Therefore, other tools such as infrared spectroscopy becomes necessary in order to probe the adsorption properties of atomically dispersed active sites.

3.1.5. Diffuse Reflectance Infrared Fourier Transform Spectroscopy. Diffuse reflectance infrared Fourier transform spectroscopy (DRIFTS) is commonly used to probe molecular adsorbates and active sites related to gas-phase chemical reactions.[9,106,107] Although DRIFTS has rarely been used for characterizing SAECs, we intend to include it here by considering its unique capability of resolving the atomic dispersion of active sites. It typically relies on measurements of the vibrational features associated with a small molecular probe (e.g., CO and NO) to probe the atomic structures and adsorption properties of the active sites. Vibration mode of the small molecular probe is sensitive to the local geometric and electronic structures of the adsorption site, which are reflected as changes in the spectra in terms of bandwidth,[108] frequency,[109] and other characteristics.[110] CO is one of the most commonly used probing molecules, largely because (i) usually one metal atom adsorbs no more than one CO, (ii) CO generally binds strongly to transition metals such as Pt, Pd, and Ni (but relatively weak for Cu, Ag, and Au) that enables

https://dx.doi.org/10.1021/acs.chemrev.0c00594
Chem. Rev. 2020, 120, 12217−12314

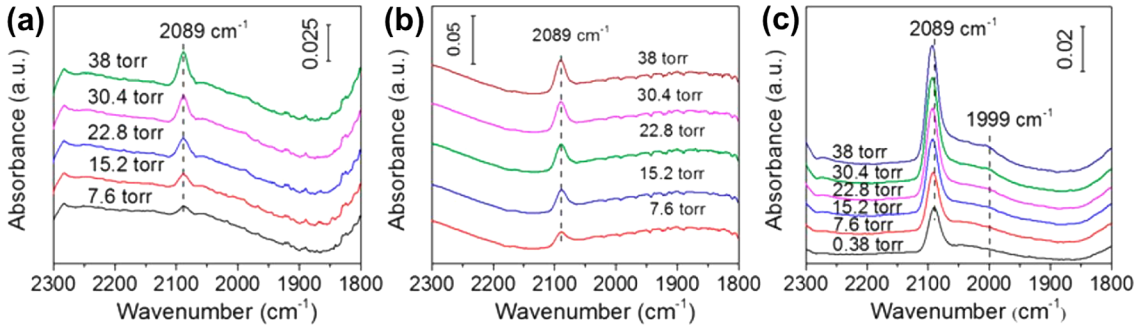

Figure 13. DRIFTS spectra of CO chemisorption at different CO partial pressures on $Pt_1@CeO_2$ with various weight percentages of Pt: (a) 0.25%, (b) 0.5%, and (c) 1.0%. Reproduced with permission from ref 35. Copyright 2018 American Chemical Society.

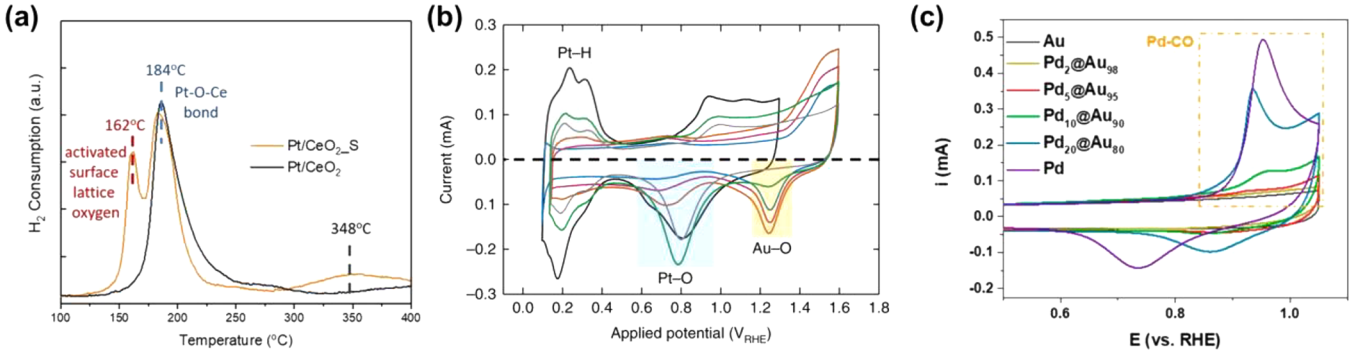

Figure 14. (a) H_2-TPR profiles of Pt/CeO_2 catalysts. Reproduced with permission from ref 117. Copyright 2017 The American Association for the Advancement of Science. (b) Cyclic voltammograms of PtAu nanocatalysts (shown at full amplitude) and commercial Pt nanocatalysts (shown at half amplitude to facilitate the comparison) acquired in 0.1 M $HClO_4$ at a sweep rate of 100 mV/s. Reproduced with permission from ref 12. Copyright 2018 Nature Publishing Group. (c) CO stripping patterns of Pd/Au SAAs recorded on different electrocatalysts (in 0.1 M of $HClO_4$, at a scanning rate of 50 mV/s). Reproduced with permission from ref 17. Copyright 2019 American Chemical Society.

measurements at room temperature, and (iii) polarization of the C≡O bond is sensitive to the electronic structure (e.g., *d* band of transition metals) and coordination of the adsorbing metal site, as well as adjacent adsorbates with dipole−dipole coupling.[82,111] Other probe molecules such as NO can also be used, but it involves much more complex chemistries due to the potential involvement of multiple oxidation states of nitrogen and various types of nitrogenous species, making it more sophisticated to resolve the structural information of the catalysts.[82]

The primary purpose of using DRIFTS to characterize single-atom catalysts is still to distinguish them from metal clusters or nanoparticles. Adsorption of CO on transition metals has been extensively studied, with the stretching frequency of CO_{ad} in linear and bridge configuration well established to be at 2030−2100 and 1750−1950 cm^{-1}, respectively.[82,111,112] Because the bridging adsorption of CO requires two adjacent metal atoms, appearance of this vibrational mode in DRIFTS spectrum is indicative of the presence of metal clusters or nanoparticles in the catalyst and vice versa. In addition, when the metal sites are in a cationic state, it is manifested spectroscopically in a blue-shift of the band position of CO_{ad}, as compared to the case with metallic sites, with reported stretching frequencies in the range of 2080−2170 cm^{-1} for linearly adsorbed CO.[82,111,112] Qiao et al. compared CO adsorption on Pt single atoms and Pt clusters supported by FeO_x.[4] For CO adsorption on Pt single atoms, only a weak band appeared at 2080 cm^{-1}, which was ascribed to linear adsorption of CO on Pt, while bands of both bridge and linear bonded CO were observed on Pt clusters. Xie et al.[35] used CO-based DRIFTS to characterize single-atom Pt supported on CeO_2. Only one peak was observed at 2089 cm^{-1} at 0.25 and 0.5 wt % of Pt loading, which was assigned to the linearly bonded CO adsorbed on $Pt^{\delta+}$ (Figure 13a,b). Another peak at 1991 cm^{-1} appeared at higher Pt loading (Figure 13c), which was ascribed to the bridge bonded CO and corresponds to the formation of Pt ensembles.

From the literature we note that most of the DRIFTS studies for single-atom catalysts are for thermocatalytic reactions. The reason for the rather limited application of DRIFTS to SAECs is probably 2-fold: (i) carbon substrates are typically involved in electrocatalysts and have strong absorption in the infrared wavelength region, which hinders the collection of vibrational signals for the adsorbates on the embedded metal sites; and (ii) typical molecular probes, such as CO, binds relatively weakly to non-noble metal single atoms in M−N−C type SAECs and do not give sufficient coverage for DRIFTS measurements at room temperature. We also note that, although CO is widely used as a molecular probe, its high binding strength can also induce surface reconstruction and cause aggregation of metal single atoms.[113,114]

3.1.6. Other Structural Characterization Techniques. In addition to the above characterization techniques, H_2-TPR, CO-TPR and H_2−O_2 titration have also been used to analyze adsorption properties and bonding information on single-atom catalysts, owing to their distinct dispersion and adsorption/redox properties, as compared to their nanoparticulate counterparts.[6,115,116] Similar to DRIFTS, these methods employ small-molecule probes and are commonly used for characterizing catalysts in thermochemical reactions, but they

https://dx.doi.org/10.1021/acs.chemrev.0c00594
Chem. Rev. 2020, 120, 12217−12314

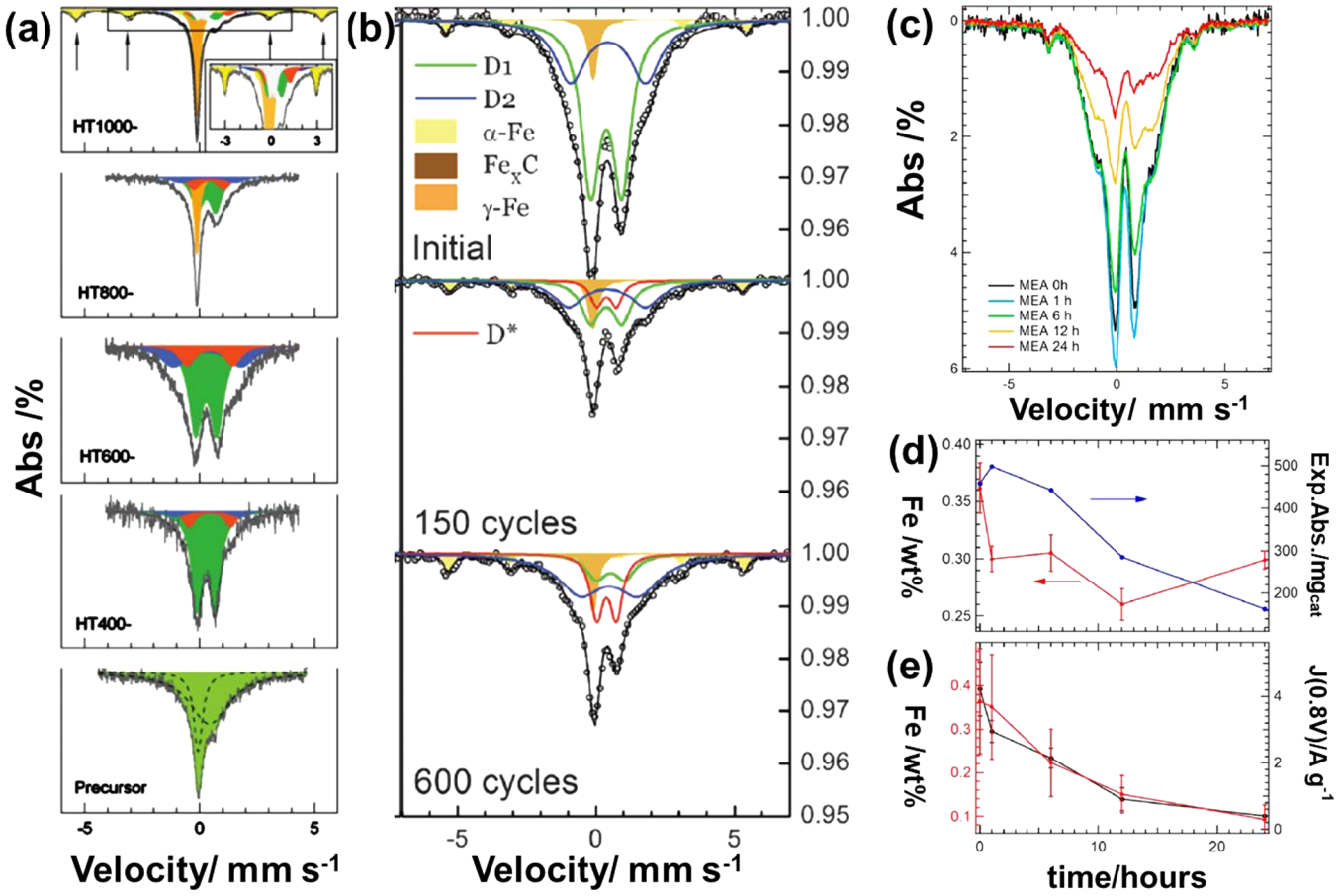

Figure 15. (a) Mössbauer spectra of catalysts prepared by pyrolysis at different temperatures. In the top curve, the inner part of the 1000 °C spectra are enlarged (dark yellow, singlet; green, D1; cyan, D2; orange, D3; gray, D4; and light yellow, sextet). Reproduced with permission from ref 124. Copyright 2011 The Electrochemical Society. (b) Mössbauer spectra of PEMFC cathodes after a number of cycles from 0.9 to 1.4 V. Reproduced with permission from ref 127. Copyright 2014 The Royal Society of Chemistry. (c) Mössbauer spectra of MEA subjected to an oxidizing treatment of increasing length between 1 h and 24 h. (d) Changes in the iron concentration and (e) mass activity measured electrochemically at 0.8 V in the membrane electrode assembly (MEA). Reproduced with permission from ref 128. Copyright 2014 American Chemical Society.

are not subjected to the optical restraints of spectroscopic measurements and are potentially applicable to a broad range of SAECs with carbon as the conductive support. For example, Nie et al. used H_2-TPR to characterize single-atom Pt supported on CeO_2 and assigned the H_2 consumption peaks at 184 °C to a unique feature of the Pt single atoms coordinated via O to the ceria substrate (Figure 14a).[117] By contrast, Pt nanoparticulates exhibit an additional peak at 162 °C that is associated with oxygen adsorbed on the ordered facets. The lower hydrogen reactivity of oxygen associated with Pt single atoms is likely a result of their stronger Pt−O binding than on continual metal surfaces.

The principle of using small molecules to probe the surface structures and adsorption properties of catalysts is also applicable to electrocatalysts, but it has mostly been performed via electrochemical measurements. Duchesne et al. acquired cyclic voltammograms (CVs) on a series of Pt/Au alloy electrocatalysts of different compositions (Figure 14b).[12] They found that the peak heights associated with the reduction of Pt−O and Au−O adlayers exhibit composition-dependent variations, and the Pt−O peak potential has a negative shift at reduced Pt contents, which can be ascribed to the higher oxophilicity of Pt on the more diluted surface alloys. Wang et al. used CO stripping to characterize the diluted surface alloys of Pd@Au, where the charge associated with the oxidation of preadsorbed CO is indicative of the coverage of Pd (Figure 14c).[17] By normalizing the CO stripping charge with the amount Pd sites in the catalyst, one was able to evaluate the dependence of Pd dispersion on the bulk composition of the alloy catalysts, in consideration of the different configurations of CO_{ad} on the Pd ensembles of different sizes. Lin et al. measured the surface concentration of active sites on a cobalt-based SAEC by integrating the charge associated with the Co(II)/Co(I) redox peak.[19] The estimated number of electrochemically active sites was then used to determine the turnover frequency of CO_2 reduction reaction. Noticeably, the validity of such arguments is based on the assumption that the transition metal sites undergoing the redox reaction are the same as those active in the electrocatalytic process.

3.2. Operando Spectroscopic Studies on Single-Atom Electrocatalysts

In situ/ex situ spectroscopies are powerful tools in studying the true active sites, catalysts structure evolution, and reaction mechanisms on single-atom electrocatalysts. In this section, the recent applications and new insights obtained by some selected spectroscopic techniques, including Mössbauer, X-ray absorption, infrared, and Raman spectroscopies are briefly reviewed.

3.2.1. Mössbauer Spectroscopy. Mössbauer spectroscopy has been implemented to probe the local structure and electronic properties of various materials since the discovery of

https://dx.doi.org/10.1021/acs.chemrev.0c00594
Chem. Rev. 2020, 120, 12217−12314

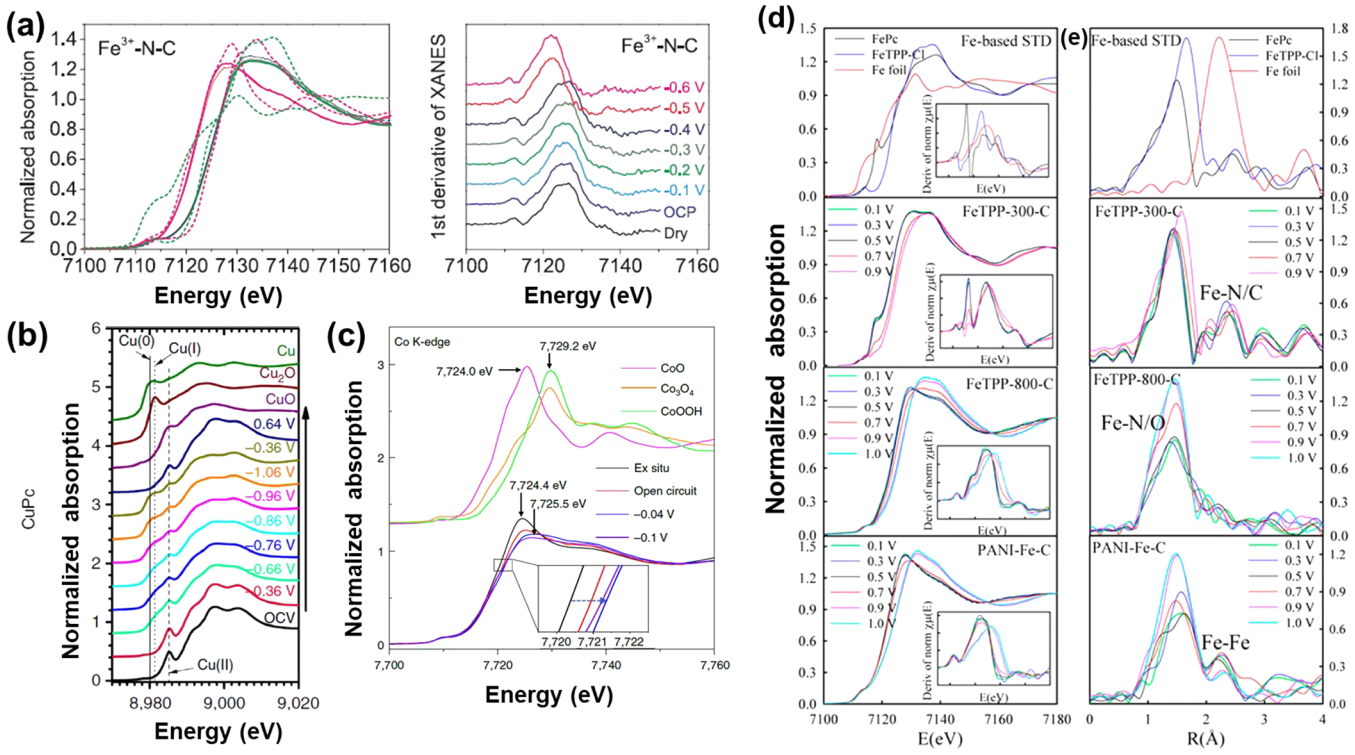

Figure 16. (a) Fe K-edge XANES spectra (left) and the first derivative of the spectra (right) of Fe^{3+}−N−C catalysts at OCP (blue), −0.1 V (light blue), −0.2 V (green), −0.3 V (dark green), −0.4 V (dark blue), −0.5 V (red), and −0.6 V (pink), with the spectra of Fe_2O_3 (blue dashed), Fe^{3+}TPPCl (green dashed), FeO (pink dashed), and Fe foil (orange dashed) as references. Reproduced with permission from ref 131. Copyright 2019 The American Association for the Advancement of Science. (b) Cu K-edge XANES spectra for Cu complex catalysts under electrocatalytic reaction conditions. The slight off-alignment stands for the peak position of Cu(II) and Cu(0). Reproduced with permission from ref 133. Copyright 2018 Nature Publishing Group. (c) Co K-edge of Co_1/PCN at different applied voltages from OCP condition to −0.1 V during HER with the inset of magnified pre-edge XANES region. Reproduced with permission from ref 134. Copyright 2019 Nature Publishing Group. (d) Fe K-edge with insets of first derivatives and (e) corresponding FT-EXAFS of FeTPP-300-C, FeTPP-800-C, and PANI−Fe-C as a function of applied potentials. Reproduced with permission from ref 135. Copyright 2015 American Chemical Society.

^{191}Ir by Rudolf Mössbauer.[118] This technique can directly gain information about the motion of the nucleus along the synchrotron radiation beam.[119] Generally, the Mössbauer spectrum could be deconvoluted into doublets, sextet, and singlet components. Three doublets including low (D1), intermediate (D2), and high (D3) spin state are assigned to M-N_x like sites, which are evidence for the formation of single-atom sites. The Dodelet group[120,121] controlled the pyrolysis atmosphere (Ar or NH_3) to alter the coordination structures of Fe−N−C single-atom catalysts. By combining ex-situ Mössbauer spectroscopic analysis and corresponding fuel cell performance, they proposed that only D1(FeN_4/C) and D3 (N-FeN_{2+2}/C) structures were ORR-active. However, Xiao et al.[122] argued that D1 and D2 both promoted ORR activities. The other doublets are related to surface-oxidized or nitrogen-rich nanoparticles.[121] The existence of sextet and singlet in the deconvolution spectrum indicated the existence of zero-valent crystalline phases.[123] Thus, the fitting quality of the original spectra is critical to determine the presence of any impurity phase (non-single-atom sites). Furthermore, Mössbauer spectroscopy has also been applied to analyze the efficacy of pre- and postsynthesis treatment in optimizing the catalyst structure and activity. Kramm et al.[124] analyzed the Mössbauer spectra of carbon-supported FeTMPPCl under a series of heating temperatures (Figure 15a). They found that higher pyrolysis temperatures (up to 800 °C) increased the electron density of the Fe−N_4 centers through coordination between N and Fe and the ORR activity. Bouwkamp-Wijnoltz et al.[125] demonstrated that pyrolyzing FeTPP-Cl/Vulcan at high temperatures (<700 °C) could promote site heterogeneity in terms of electronic structure and maintain a large number of Fe−N_4 moieties. However, a magnetic iron oxide phase appeared above 800 °C. Sulfuric acid washing could efficiently remove superparamagnetic metallic iron and Θ-Fe_3C but not iron oxides, while after H_2O_2 treatment, similar to the situation after long-term ORR durability test, a significant loss of single Fe active site was observed in the Mössbauer spectrum.[126] Mössbauer spectroscopy can also be applied to study the durability of single-atom catalysts. As shown in Figure 15b, Goellner et al.[127] recorded Mössbauer spectra of Fe−N−C catalysts after repeated cycling between 0.9 and 1.4 V. The noticeable decrease of the D1 and D2 absolute amplitudes after 150 and 600 cycles might be ascribed to the removal of solvated Fe^{2+} or Fe^{3+} by water. Kramm et al.[128] put forward a time-dependent relationship of fuel cell performance and content of iron sites for Fe−N−C catalysts at the oxidizing environment from 0.8 to 1.2 V (Figure 15c−e), where the significantly decreased electrocatalytic performance was accounted for by the oxidation of the carbon support and consequently the loss of its hosted active sites. It should be noted that Mössbauer spectroscopy is a bulk technique that encompasses all types of metal sites in the material. However, electrochemical reactions only occur on surfaces that are

https://dx.doi.org/10.1021/acs.chemrev.0c00594
Chem. Rev. 2020, 120, 12217−12314

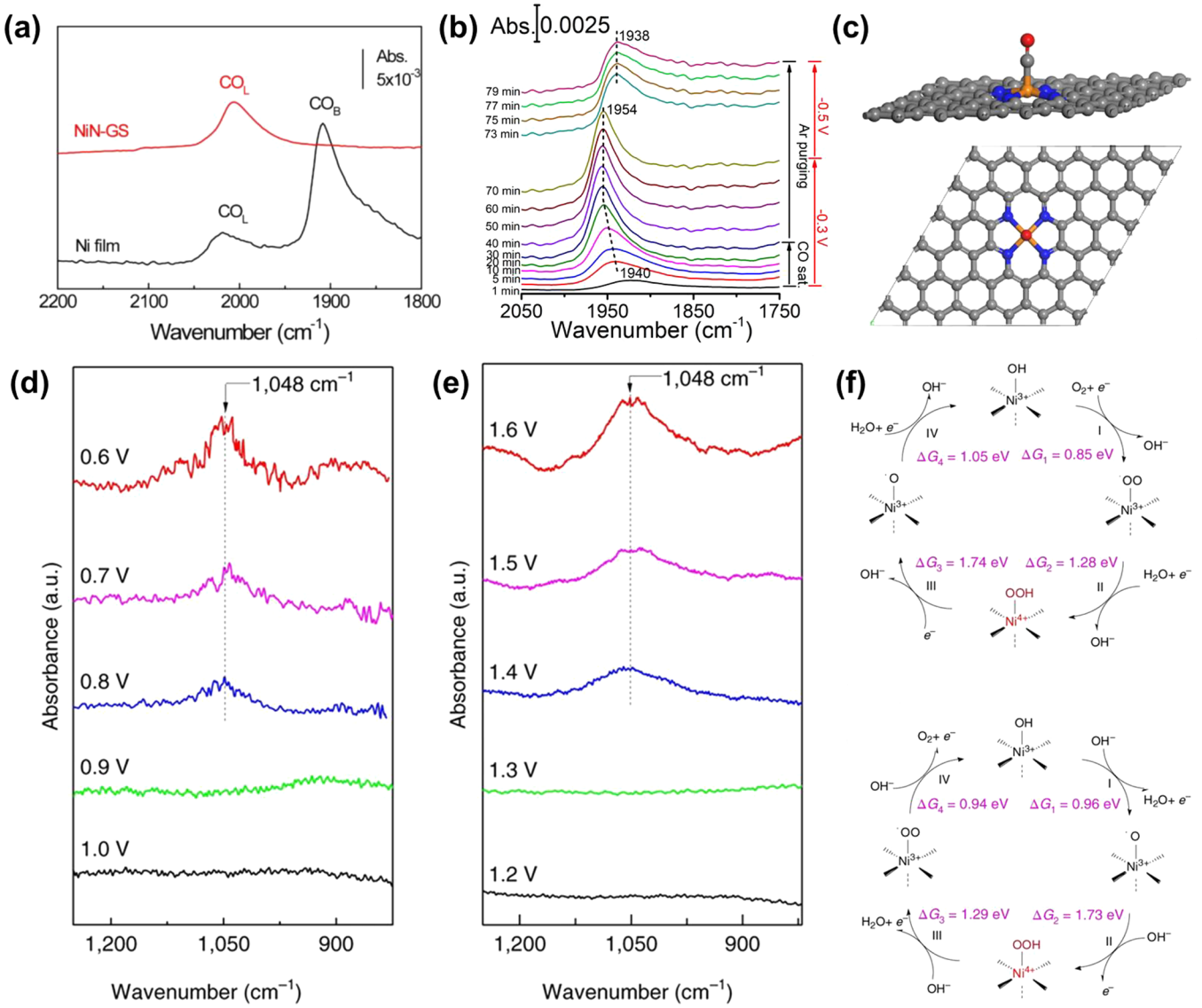

Figure 17. (a) ATR-IR spectra of monolayer CO adsorption on NiN-GS and Ni film electrode. Reproduced with permission from ref 139. Copyright 2017 Cell Press. (b) In situ CO adsorption−desorption spectra recorded on the Fe−N−C catalysts, and (c) the structure of poisoned sites by strongly bonded CO. Reproduced with permission from ref 140. Copyright 2019 American Chemical Society. In situ SR-FTIR spectra recorded at different potentials during (d) ORR and (e) OER, and (f) the proposed reaction mechanisms. Reproduced with permission from ref 141. Copyright 2019 Nature Publishing Group.

accessible by reactants and electrolytes, which may bring discrepancy in explaining the structure−activity correlation.

3.2.2. X-ray Adsorption Spectroscopy. X-ray absorption spectroscopy (XAS) is one of the most frequently used tools in probing the atomic and electronic structures of single-atom catalysts. In situ XAS is also able to monitor the electronic and structural evolutions under reaction conditions. Jiang et al.[129] studied single Ni atom catalysts in CO_2 reduction and found no discernible changes in the in situ XAS spectra acquired at different potentials, indicating high stability of Ni single atoms, due to the efficient confinement effect of graphene vacancies. By using inert Ar instead of CO_2, Liu et al. observed a reduced valence state of Ni centers from +2 to +1 at potentials lower than 0.4 V vs RHE on Ni−N_4 moieties, suggesting that the Ni center was unstable at CO_2 reduction potentials.[130] Surprisingly, the valence state of Ni centers was fixed at +2 when a CO_2 atmosphere was used, consistent with the observation by Jiang et al.[129] It was proposed that the fast donation of a lone pair of electrons from Ni^+ centers to CO_2 molecules would bring its valence back to +2, hence Ni^+ served as the true active sites during the reaction.[130] Similar mechanism was proposed on atomically dispersed nickel on nitrogenated graphene.[95] The evolution of metal center valence is more obvious on some other single-atom catalysts. For instance, Gu et al.[131] observed a constant 3+ valence state in Fe−N−C catalyst at potentials more positive than −0.4 V. However, the reduction of Fe^{3+} to Fe^{2+} (Figure 16a) and a concomitant decrease of CO_2 reduction performance occurred below −0.5 V, suggesting the importance of Fe^{3+} in maintaining the high catalytic activity and stability. Karapinar et al.[132] and Weng et al.[133] (Figure 16b) identified a reversible potential-induced oxidation state change in Cu-based single-atom catalysts during CO_2 reduction. The valence state of Cu centers changed from +2 to zero during a negative potential sweep and returned to +2 when the potential was swept back. The Cu−Cu coordination under CO_2 reduction was also detected, due to

https://dx.doi.org/10.1021/acs.chemrev.0c00594
Chem. Rev. 2020, 120, 12217−12314

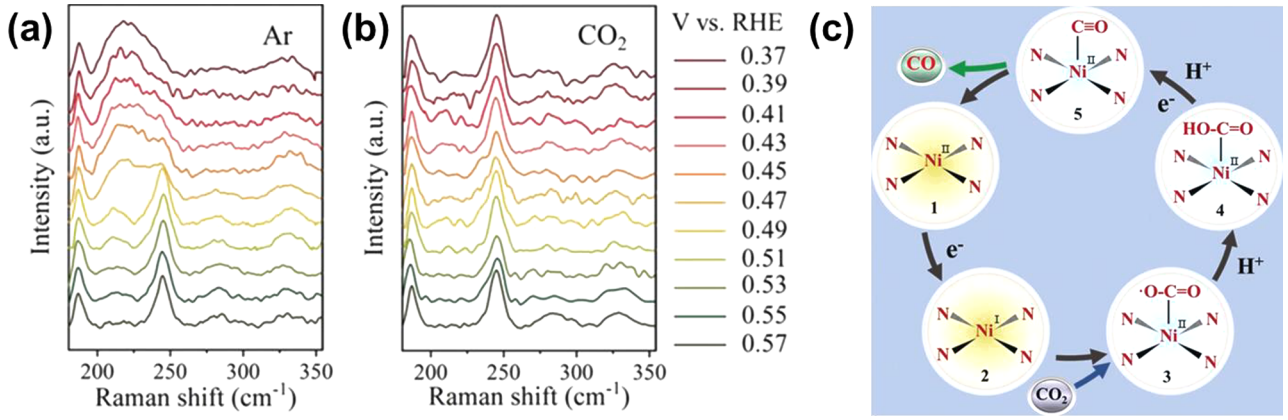

Figure 18. In situ Raman spectra of the Ni-TAPc catalysts during negative sweeping of the electrode potential in (a) Ar- and (b) CO_2-saturated $KHCO_3$ solutions. (c) Proposed reaction mechanisms on Ni-TAPc catalysts. Reproduced with permission from ref 130. Copyright 2020 John Wiley and Sons.

the formation of fine Cu nanoparticles, which rendered the assignment of single Cu as sole active sites questionable.[133] Cobalt single-site catalyst showed excellent hydrogen evolution reaction performance in alkaline electrolytes. In situ XAS measurements[134] (Figure 16c) showed that the atomically dispersed Co site had an increased oxidation state induced by OH^- chemisorption during the reaction. Based on the shift of the Fe K-edge and the change of Fe−N/O scattering peak intensity as a function of applied potentials (Figure 16d,e), the Mukerjee group[135−137] found that the unoccupied Fe−N_4 active sites changed sharply across the Fe^{3+}/Fe^{2+} redox potential, due to the site-blocking effect and Fe moving toward or off rather than remaining static at the N_4-plane during the ORR. According to the above analysis, the structures of single-atom dispersed catalysts may drastically change under reaction conditions.

3.2.3. Infrared Absorption Spectroscopy. Infrared absorption spectroscopy is an important tool for specifically detecting the dipole moment changes of functional groups, which can provide atomic and molecular information on reaction intermediates and pathways and infer the structures of active sites and their dynamic evolution under reaction conditions. To alleviate the interference of water, the attenuated total reflection (ATR) configuration is commonly adopted, especially for reactions that generate a large volume of gas products.[138] Jiang et al.[139] combined CO probe and ATR-IR spectroscopy to investigate the surface structures of single Ni atoms embedded on graphene layers. As compared to Ni films, the absence of bridge-bonded CO (CO_B, ∼1900 cm^{-1}) indicated the lack of neighboring Ni atoms on the single-atom catalyst (Figure 17a), and the lower wavenumber of the linear-bonded CO (CO_L) by tens of cm^{-1} confirmed the changes of local electronic and geometric structures (i.e., the formation of single Ni atoms coordinated with N and C). The Shao group[140] probed the active sites of single Fe atom catalysts, which is highly selective in CO_2-to-CO conversion at low overpotentials. By using DFT calculations, the anchoring sites of adsorbed CO intermediates detected by ATR-IR spectroscopy can be depicted according to their vibrational wavenumbers. In stark contrast to widely believed mechanisms, the Fe−N_4 moiety embedded in complete graphene-like carbon matrix was ruled out as the true active site, which should be poisoned by strongly adsorbed CO according to in situ CO adsorption−desorption spectroscopic studies (Figure 17b,c). These results highlight the importance of vibrational spectroscopies in studying the reaction mechanisms on heterogeneous single-atom catalysts with mixed surface site structures. While the detection of surface-bonded CO in CO_2 reduction is usually facile due to its large dipole moment, observing intermediates/spectators in other electrochemical reactions is generally challenging. Infrared beams obtained from synchrotron radiation (SR) are more powerful, which can significantly increase the detectability on reaction intermediates. Using SR-FTIR in the external reflection configuration, Liu and co-workers detected superoxide *OOH intermediates located near 1048 cm^{-1} during both the ORR and OER processes on NiFe metal−organic framework catalysts (Figure 17d,e), which are further confirmed by isotopic labeling measurements. By the combination of DFT calculations with in situ XAS studies, Ni^{4+} sites were proposed as the active sites, which undergo a fast and efficient $4e^-$ pathway in both O_2 electrocatalysis reactions (Figure 17f).[141] This powerful IR spectroscopic technique was also successful in detecting two potential-dependent vibration modes near 1048 and 1248 cm^{-1} during OER on hetero-N-coordinated Co single-site catalysts, which was assigned to Co−N and Co−O vibrations, respectively, according to theoretical calculations (1063 and 1259 cm^{-1}).[142] The changes of Co−N at lower overpotentials than Co−O suggested that the potential-induced electron redistribution between Co and N atoms would promote the generation of *O intermediates on single Co atoms and trigger the $4e^-$ pathway OER.

3.2.4. Raman Scattering Spectroscopy. Raman spectroscopy is a vibrational spectroscopic technique complementary to FTIR because it is sensitive to the change of polarizability of molecules. As compared to IR spectroscopy, it has a wider wavenumber window that is not limited by the optical prism, which is critical in the detection of chemical bonds below 1000 cm^{-1} that contain abundant information on the material structure and active site-intermediate binding. By grafting Ni-TAPc molecules on carbon nanotubes, a model Ni−N_4−C single-atom catalyst with uniform active sites was developed by Liu et al.[130] for efficiently reducing CO_2 to CO. The red-shift of the Ni−N vibration at potentials more negative than 0.5 V in an Ar-saturated $KHCO_3$ solution suggested the valence changes of Ni atoms from +2 to +1 prior to CO_2 reduction. The shifts of the Ni−N band were not detected under the CO_2 atmosphere, indicating Ni^+ can

https://dx.doi.org/10.1021/acs.chemrev.0c00594
Chem. Rev. 2020, 120, 12217−12314

efficiently activate CO_2 by donating a lone pair of electrons and simultaneously switch back to Ni^{2+}. Therefore the intrinsic active species is single Ni^+ center (Figure 18). This hypothesis was also consistent with results from in situ XAS characterizations.[95,130] The structural stability of catalysts under reaction conditions can also be assessed by Raman spectroscopy. For a ZIF-67 catalyst in alkaline solutions, in situ Raman spectroscopy detected a rapid evolution of the MOF structure toward $Co(OH)_2$ and CoOOH as the potential was swept positively, which served as the true active sites for OER instead of the metal nodes in the pristine MOFs.[143] Kumar et al.[144] studied the catalytic stability of Fe−N−C single-atom catalyst under PEMFC conditions by using ex situ Raman spectroscopy. A much faster loss of ORR activity was observed in O_2 than in Ar even under a mild potential cycling protocol (e.g., 0.3 to 0.7 V vs RHE), where significant oxidation of the carbon matrix was unlikely to be induced solely by potentials. The narrowed D_1 (1350 cm^{-1}) and G bands (1580 cm^{-1}), along with the emergence of second-order Raman spectra between 2500 and 3500 cm^{-1} after cycling in O_2 indicated the occurrence of O_2-induced carbon corrosion and consequently the loss of single Fe active centers. The reactive oxygen species generated due to H_2O_2−Fe Fenton reactions was likely responsible for the severe structure degradation.

3.3. Perspectives about the Characterization of Single-Atom Electrocatalysts

The advancement of characterization tools is enabling more comprehensive studies and understanding of novel electrocatalytic materials with single-atom active sites. The modeling of EXAFS spectra depicts the local coordination structures of SAECs active centers, which has been heavily relied on in the community. However, incorrect use of this surface-insensitive technique might give rise to misleading conclusions. A recent report by Zhong and co-workers pointed out the limitation of EXAFS that it cannot efficiently differentiate small oxide clusters (2.8 nm) from single atoms.[145] Therefore, a combination of microscopic, spectroscopic, and (electro)-chemical techniques, as discussed above, can explicitly resolve the atomic structures and absorption properties of SAECs, allowing for correlations to their electrocatalytic performance and distinguishing it from their nanoparticulate counterparts.

Despite the promising progress, it is noticed that many tools established in the thermocatalysis community have rarely been applied to the study of electrocatalysts, which represents an open area to further explore. The interaction between support and metal active centers still needs to be elucidated. Many studies have shown dramatic enhancement in catalytic activity by changing the properties of the substrates in SAECs. However, it remains unclear if such enhancement originates from the synergies between the metal sites and the substrates.[51,105,146,147] Systematic comparison of the electronic structures and adsorption properties of SAECs to the bulk or nanoparticulate metals are yet to be developed.[96] More connections are also to be drawn between the characterized structures and properties to the computational models of SAECs, which are pivotal to establish and understand the structure−property relationships in electrochemical reactions.

In summary, spectroscopic techniques are indispensable for in-depth understandings of the catalytic processes on single-atom catalysts. The information obtained from spectroscopic measurements can be generally divided into two categories: the geometric and electronic structures of catalyst surfaces and reaction intermediates/pathways. The adoption of in situ spectroscopies is essential because structural changes of single-atom catalysts have been frequently reported under reaction conditions, which may lead to distinctly different results, as compared to those based on ex situ characterizations. Another issue in single-atom catalysts is the presence of different surface moieties, which is particularly common in doped carbon-based ones prepared by pyrolysis. The diversity of surface sites makes the assignment of true active sites challenging. Combining vibrational spectroscopies with theoretical simulations represents a viable strategy to mitigate this issue. The vibrational wavenumbers of intermediates can be fitted by simulations to better understand their binding strength and corresponding structures of adsorption sites and to establish the relationship of specific interactions between catalyst surface and reaction intermediates. Nevertheless, challenges remain in determining the population distribution of different surface sites and quantifying the coverage of various surface species, which are important parameters in understanding the reaction kinetics.

4. SINGLE-ATOM ELECTROCATALYSTS FOR HYDROGEN EVOLUTION REACTION

4.1. Introduction

Increasing global consumption of fossil fuels and the associated environmental issues are motivating researchers to explore alternative energy resources that are sustainable and environmentally friendly.[148,149] Hydrogen gas (H_2) is proposed as a promising candidate for future energy storage, to be used in fuel cells, due to its highest gravimetric energy density among all fuels and with water as the only byproduct (no greenhouse gas emission) in energy conversion processes.[150,151] In addition, H_2 is also a basic feedstock in industries, which is widely used for hydrogenation of hydrocarbons to make important chemical products, for the synthesis of ammonia, as a reducing agent for the production of metals, etc. More than 95% of H_2 produced today is derived from steam reforming of methane or gasification of coal. Such a production route not only consumes nonrenewable fossil fuels but also causes significant emission of CO_2 and other greenhouse gases.[152] Development of alternative technologies toward green hydrogen thus becomes imperative for addressing the challenges in energy, environment, and sustainability.

Water splitting ($H_2O(l) \rightarrow H_2(g) + {}^1/_2O_2(g)$, $\Delta G_0 = +237.2$ kJ mol^{-1}, $\Delta E_0 = 1.23$ V vs normal hydrogen electrode (NHE)) is considered as the most promising and sustainable approach toward H_2 production. Compared to the reforming of fossil fuels, this approach is advantageous in many aspects: (i) the raw material is water, which is an abundant and renewable resource on earth, (ii) the energy source can be renewable solar or wind electricity, (iii) it does not emit greenhouse or pollutive gases, and (iv) it can produce pure H_2 (H_2 and O_2 are separate in electrochemical cells).[153] Water splitting through electrolysis involves two half-cell reactions, namely the hydrogen evolution reaction (HER) on the cathode and the oxygen evolution reaction (OER) on the anode. Therefore, efficient water electrolysis requires electrocatalysts with high activities for both HER ($2H^+ + 2e^- \rightarrow H_2$) and OER ($2H_2O \rightarrow O_2 + 4H^+ + 4e^-$).

Normally, HER is a multistep electrochemical process, which may follow two different pathways depending on the electrolyte pH.[154] The first step is electrochemical hydrogen adsorption (Volmer reaction):

https://dx.doi.org/10.1021/acs.chemrev.0c00594
Chem. Rev. 2020, 120, 12217−12314

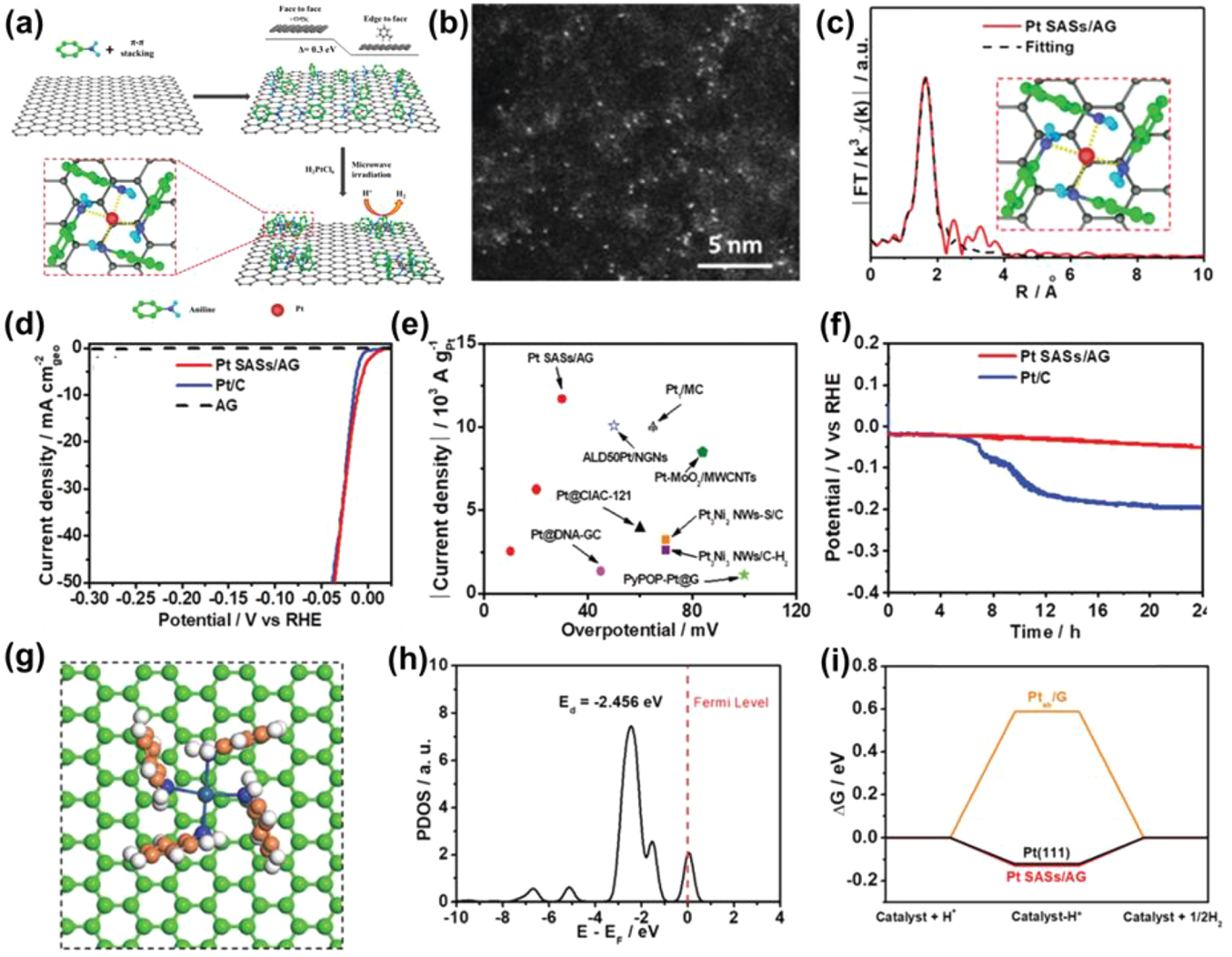

Figure 19. (a) Synthetic scheme of Pt SASs/AG. (b) AC HAADF-STEM image of Pt SASs/AG. (c) Corresponding EXAFS spectrum and fitting curve of the Pt SASs/AG R-space (inset: model of Pt SASs/AG). (d) LSV curves of Pt SASs/AG and Pt/C with current density normalized to the geometry area. (e) Mass activities of Pt SASs/AG, Pt/C, and other state-of-the-art Pt-based catalysts in 0.5 M H_2SO_4. (f) Chronopotentiometric curves of Pt SASs/AG and Pt/C at 10 mA cm^{-2} in 0.5 M H_2SO_4 solution. (g) DFT calculation models (top views) of Pt SASs/AG. (h) PDOSs of the 5*d* orbitals of Pt SASs/AG. (i) Calculated free energy diagrams of HER for Pt(111), Pt_{ab}/G, and Pt SASs/AG. Reproduced with permission from ref 171. Copyright 2019 The Royal Society of Chemistry.

in acid solution: $H^+ + * + e^- \rightarrow H^*$ (3)

in alkaline solution: $H_2O + * + e^- \rightarrow H^* + OH^-$ (4)

The following step has two different pathways to generate the final product of H_2. When the H* coverage is low, the adsorbed hydrogen atom prefers to couple with a new electron and another proton in the electrolyte to evolve H_2. This is the so-called Heyrovsky reaction,

in acid solution: $H^+ + e^- + H^* \rightarrow H_2 + *$ (5)

in alkaline solution: $H_2O + e^- + H^* \rightarrow * + OH^- + H_2$ (6)

However, at a relatively high H* coverage, the combination between the adjacent adsorbed hydrogen atoms becomes favorable, and H_2 is generated via chemical desorption (Tafel reaction),

in both acid and alkaline solution: $2H^* \rightarrow H_2 + *$ (7)

where H* designates a hydrogen atom chemically adsorbed on an active site (*) of the electrode surface. These pathways are strongly dependent on the inherent chemical and electronic properties of the electrode surface; and the rate-determining step of HER can be identified from the Tafel slope of the corresponding HER polarization curves,[155]

$$\eta = a + b\log(j) \quad (8)$$

where η is the overpotential, j is the current density, and b is the Tafel slope.

Currently, platinum (Pt) and its derivatives, typically in the form of nanoparticles supported on carbon black, are the electrocatalysts of choice for HER, which display a high exchange current density (j_0) and a small Tafel slope. However, Pt-based electrocatalysts suffer from high cost and natural scarcity that limits its massive application in water electrolyzers for large-scale production of H_2.[156−158] Therefore, cost-effective alternatives to precious Pt are demanded. Recently, tremendous efforts have been devoted to the exploration of new HER electrocatalysts based on a variety

https://dx.doi.org/10.1021/acs.chemrev.0c00594
Chem. Rev. 2020, 120, 12217−12314

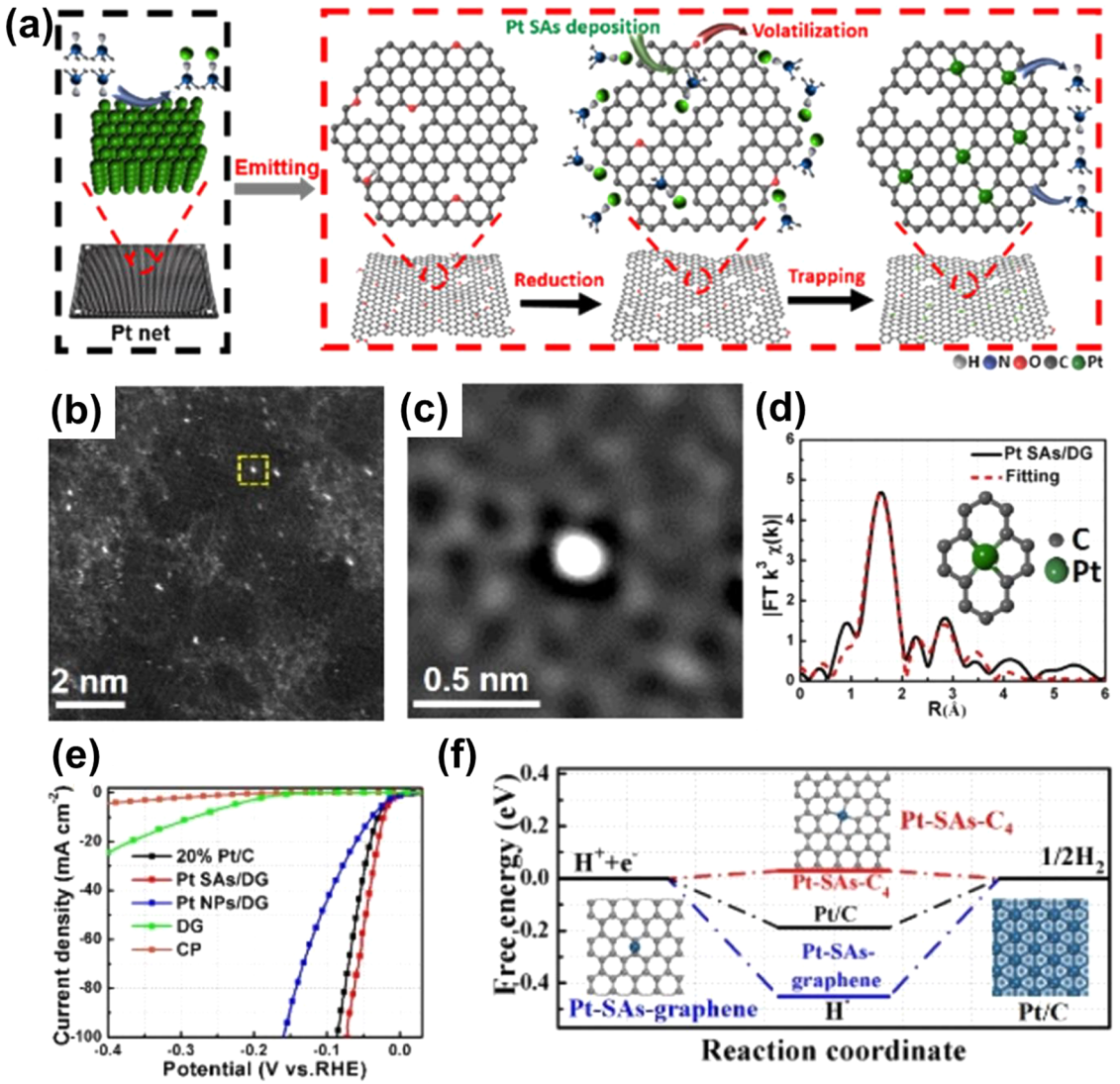

Figure 20. (a) Proposed reaction mechanism for the preparation of Pt SAs/DG. (b) High-resolution HADDF-STEM image of Pt SAs/DG. (c) Zoom-in image of the defective area marked with the yellow dashed frame in panel (b). (d) Corresponding EXAFS spectrum and fitting curve for Pt SAs/DG. Inset: proposed Pt−C coordination environment. (e) HER LSV curves of the catalysts. (f) Calculated Gibbs free energy diagrams of HER on Pt/C, Pt-SAs-graphene, and Pt-SAs-C_4 at the equilibrium potential. Reproduced with permission from ref 170. Copyright 2019 American Chemical Society.

of nonprecious transition metals, such as Co, Ni, Mo, Fe, and their derivatives (i.e., nitrides, carbides, oxides, phosphides, and borides)[159−163] under either acidic or alkaline conditions. In general, the activity of electrocatalysts depends on the density and chemical nature of the active sites, which can be improved via reducing the particle size to expose a larger surface area and tailoring the atomic configuration and electronic structure to alter the adsorption properties, respectively. However, conventional approaches toward down-scaling the size of nanoparticles faces the challenges of instability under electrochemical reaction conditions (vide ante).[164]

SAECs open up a new avenue for the development of advanced electrocatalysts for HER and other energy conversion reactions to achieve maximal atom utilization efficiency (Figure 1) and high catalytic activity.[12,165] In the following discussion, we will summarize recent progress in the development of SAECs for HER that are based on precious metal and nonprecious transition metals (TM). We will wrap up this section with a highlight of remaining challenges and future opportunities for the further development of HER electrocatalysts based on atomically dispersed active sites.

4.2. Precious Metal-based Single-Atom Electrocatalysts

4.2.1. Pt-based Single-Atom Electrocatalysts. Pt is the most active metal for HER, owing to its appropriate binding strength (with the free energy of hydrogen adsorption, ΔG_{H^*}, being close to zero) to atomic hydrogen (*H).[165−167] When Pt is dispersed as single atoms to maximize the atom efficiency, its stability becomes a challenge. Anchoring Pt atoms on a substrate such as metal oxides, carbon, or another crystalline metal, is an intuitive strategy to achieve good stability by impeding migration, agglomeration, and/or dissolution.[71] It is thus important for the design of Pt-based SAECs to find an appropriate conductive support that has strong interaction with Pt single atoms but does not compromise the electrocatalytic activity.[168]

Thus, far, carbon nanomaterials, primarily graphene (G) and carbon nanotube (CNT) have been extensively used as the

https://dx.doi.org/10.1021/acs.chemrev.0c00594
Chem. Rev. 2020, 120, 12217−12314

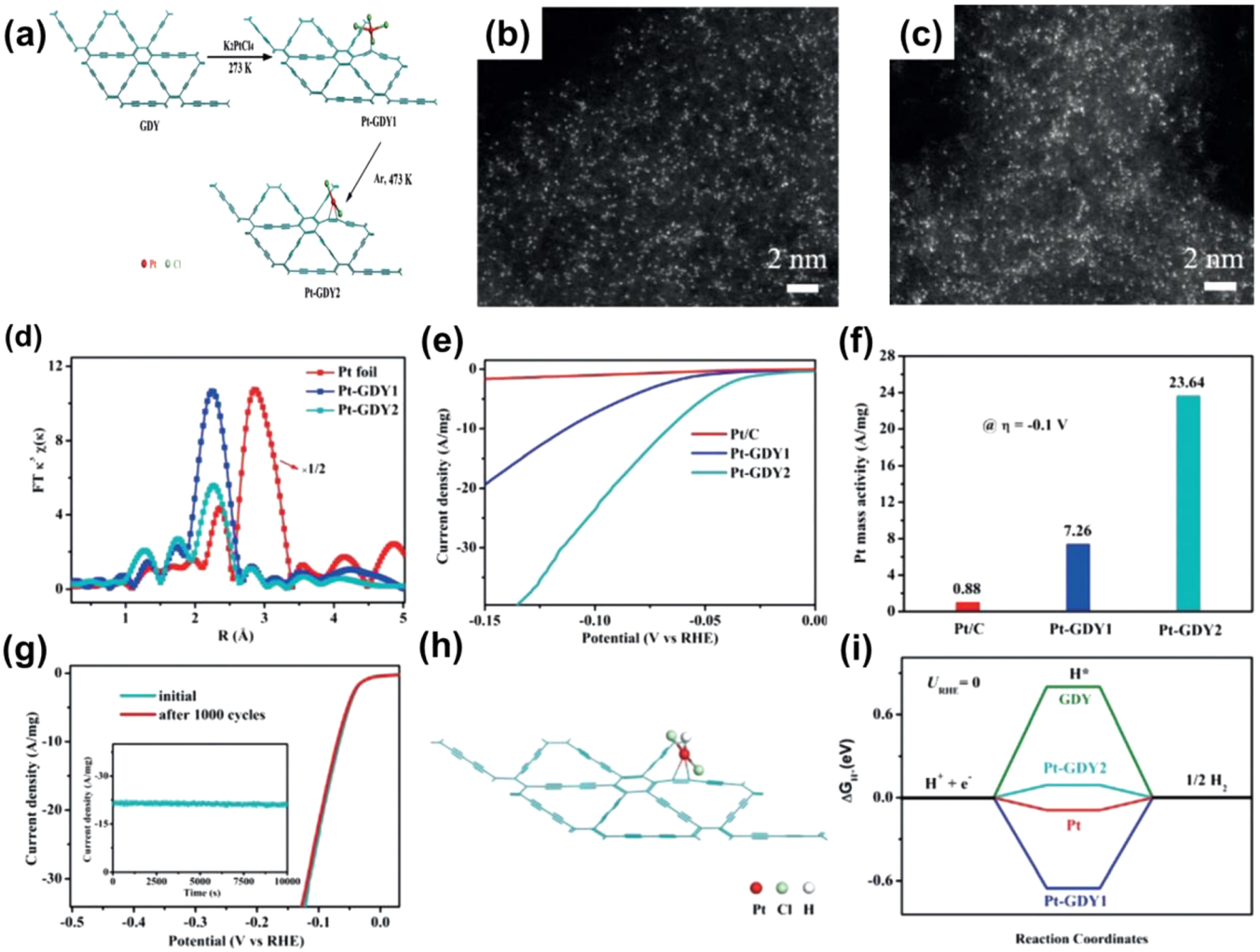

Figure 21. (a) Illustration for the synthesis of Pt-GDY1 and Pt-GDY2. HAADF-STEM images for (b) Pt-GDY1 and (c) Pt-GDY2. (d) Pt L_3-edge k^3-weighted FTEXAFS spectra of Pt-GDY1, Pt-GDY2, and Pt foil (the EXAFS intensity for Pt foil is shown at half value). (e) HER polarization curves for Pt-GDY1, Pt-GDY2, and commercial Pt/C in 0.5 M H_2SO_4 aqueous solution at a scan rate of 5 mV s^{-1}. (f) HER mass activity at 0.1 V for Pt/C, Pt-GDY1, and Pt-GDY2. (g) Polarization curves of Pt-GDY2 in the initial and after 1000 cycles at a scan rate of 5 mV s^{-1} (inset: time-dependent current density curve at −95 mV vs RHE for 10000 s). (h) Configuration of Pt-GDY2 with adsorbed hydrogen. (i) Calculated Gibbs free energy for hydrogen evolution on different catalysts. Reproduced with permission from ref 173. Copyright 2018 John Wiley and Sons.

support for Pt-based SAECs, owing to their low cost, high electrical conductivity, and reasonable corrosion resistance.[169] Moreover, their electronic structures can be readily modulated by chemical doping with select heteroatoms (i.e., N, P, S, etc.).[170] Ye et al. synthesized single Pt atoms anchored on aniline-stacked graphene (denoted as Pt SASs/AG).[171] As shown in Figure 19a, the graphene in these catalysts was functionalized with aniline molecules via $\pi-\pi$ interactions, with the stacked molecules in an edge-to-face configuration. Subsequently, $[PtCl_6]^{2-}$ ions were anchored onto AG by electrostatic interaction between $[PtCl_6]^{2-}$ and $-NH_3^+$. Finally, the anchored $[PtCl_6]^{2-}$ ions were reduced to single Pt atomic sites by using microwave irradiation. HAADF-STEM (Figure 19b) and EXAFS (Figure 19c) characterizations confirmed the formation of atomically dispersed Pt, and the resulting Pt SASs/AG showed a less negative onset potential (Figure 19d) and higher mass activity (Figure 19e) than the other Pt-based electrocatalysts reported in the literature. In addition, chronopotentiometric measurements (Figure 19f) showed that Pt SASs/AG maintained its high catalytic activity during prolonged reaction. DFT calculations based on the structural model shown in Figure 19g suggest that the *d*-band center of Pt SASs/AG is at ca. −2.465 eV (Figure 19h), close to that of Pt (111). The hydrogen adsorption free energy (ΔG_{H^*}) of Pt SASs/AG was estimated to be −0.127 eV (Figure 19i), which is also almost the same as that for Pt (111) (−0.121 eV). Both of these two values are close to the ideal case, 0 eV, for the HER, which is believed to the mechanism for the high HER activity of Pt SASs/AG.

In another study, Li's group synthesized atomically dispersed Pt via a thermal emitting method using bulk Pt metal as the precursor (Figure 20a).[170] Their synthesis derived isolated $Pt^{\delta+}$ ($0 < \delta < 4$) species on defective graphene (DG), as trapped in the divacancy sites (Figure 20b,c). Their EXAFS analysis gives predominantly 4-fold Pt−C coordination for the single-atom sites with a bond length of ∼1.98 Å (Figure 20d). The HER performance of the obtained SAEC (denoted as Pt SAs/DG in their work) was then assessed in a N_2-saturated 0.5 M H_2SO_4 electrolyte. The Pt SAs/DG catalyst displayed an overpotential ($\eta_{10,HER}$) of only 23 mV to reach the geometric current density of 10 mA cm^{-2}, which is even lower than that of Pt/C (−30 mV) and Pt nanoparticles loaded on the same substrate (Pt

https://dx.doi.org/10.1021/acs.chemrev.0c00594
Chem. Rev. 2020, 120, 12217−12314

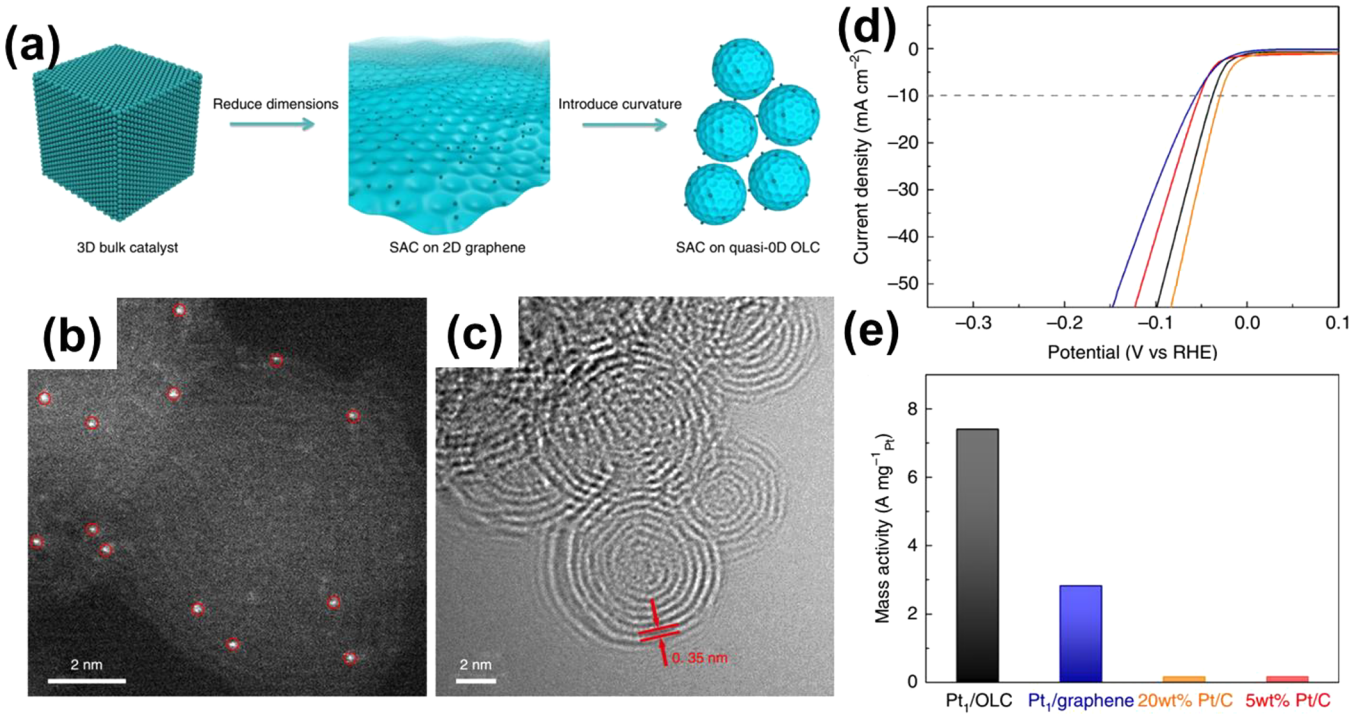

Figure 22. (a) Schematic illustration of the catalytically active particles being reduced in size to a single-atom form on quasi-0D OLCs. (b) HAADF-STEM image of Pt_1/OLC clearly displays Pt single atoms (highlighted by red circles) randomly dispersed on the OLC supports. (c) TEM image of Pt_1/OLC shows a multishell fullerene structure with a layer distance of 0.35 nm. (d) HER polarization curves of Pt_1/OLC (black) in comparison with 5 and 20 wt % commercial Pt/C (red and orange, respectively) and Pt_1/graphene (0.33%) (blue) in a 0.5 M H_2SO_4 electrolyte. The catalyst loading calculated by the total weight is 510 μg cm^{-2} for all the catalysts. (e) Mass activity of Pt_1/OLC is normalized to the Pt loading at η = −38 mV with respect to the reference catalysts. Reproduced with permission from ref 174. Copyright 2019 Nature Publishing Group.

NPs/DG) (−38 mV) (Figure 20e). Moreover, Pt SAs/DG also exhibited a remarkable mass activity of 26.2 A mg_{Pt}^{-1}, which is 31.5 times higher than that of the commercial Pt/C catalyst (0.83 A mg_{Pt}^{-1}). To interpret the high HER activity of Pt SAs/DG, the authors carried out DFT calculations to simulate the three Pt catalysts. As shown in Figure 20f, ΔG_{H^*} for Pt-SAs-C_4 was calculated to be 0.03 eV, which is even closer to zero than that of Pt.[172] It was further argued that compared to Pt single atoms embedded on pristine graphene, the more effective charge transfer between Pt and defective graphene in Pt SAs/DG led to the modification of the electronic structures of Pt, which gave rise to the desirable adsorption properties for HER.

For SAECs, the electronic structure of the single-atom sites strongly depends on their coordination environments, namely bonding and interaction with the substrates, which largely determine the adsorption and catalytic properties of the SACEs. Yet, studies are relatively rare about the influence of metal-substrate coordination on the HER catalytic activity of Pt SAECs, largely due to the challenge in tuning the coordination structure, which has impeded the fundamental understanding of the structure−property relationship of Pt-based SAECs. To address this issue, Yin et al. used graphdiyne (GDY), an allotrope of graphene, to support Pt single atoms and tune their coordination with the substrate.[173] As shown in Figure 21a, Pt-GDY1 was synthesized by directly soaking GDY in a K_2PtCl_4 aqueous solution, while Pt-GDY2 was prepared by thermal annealing of Pt-GDY1. HAADF-STEM imaging found that isolated Pt atoms were abundant on the GDY support (Figure 21b,c). EXAFS analysis showed no Pt−Pt bond in the Pt-GDY catalysts, and the isolated Pt atoms were anchored on the GDY substrate via coordination with one carbon and four chlorine atoms in Pt-GDY1 (C_1-Pt-Cl_4), and two carbon and two chlorine atoms in Pt-GDY2 (C_2-Pt-Cl_2) (Figure 21d). Linear sweep voltammetric (LSVs) measurements showed that Pt-GDY2 was much more active toward HER than Pt-GDY1 and commercial Pt/C (Figure 21e). Mass activities for Pt-GDY2, PtGDY1, and Pt/C at the overpotential of −100 mV were estimated to be 23.64, 7.26, and 0.88 A mg^{-1} (Figure 21f), respectively. That means, Pt-GDY2 was 26.9 and 3.3 times more active than the Pt/C and Pt-GDY1, respectively. Stability test for Pt-GDY2 exhibited no significant attenuation after extensive LSV scans or in prolonged chronoamperometric measurements, signifying the high electrochemical stability of Pt-GDY2 (Figure 21g). On the basis of the configuration shown in Figure 21h, the calculated ΔG_{H^*} for the Pt sites in Pt-GDY2 was estimated to be 0.092 eV, reconciling with its superior activity to Pt/C for HER (Figure 21i).

In conventional nanoparticulate catalysts, the corners, defects, and edges generally show unique catalytic properties owing to their lower coordination numbers than their counterparts on ordered surfaces.[167] Inspired by this general mechanism, Liu et al.[174] used highly curved substrates to support metal single atoms in an attempt to achieve undercoordinated active sites. As shown in Figure 22a, they used surface-oxidized detonation nanodiamonds as the starting material to synthesize atomically dispersed Pt. During their synthesis, the onion-like carbon (OLC) nanospheres was deoxygenated by thermal treatment at various temperatures to precisely tune the type and distribution density of oxygen species.[175] Subsequently, a single-cycle atomic layer deposition (ALD) was conducted to produce isolated Pt atoms over the support. In the HAADF-STEM image of the resulting Pt_1/

https://dx.doi.org/10.1021/acs.chemrev.0c00594
Chem. Rev. 2020, 120, 12217−12314

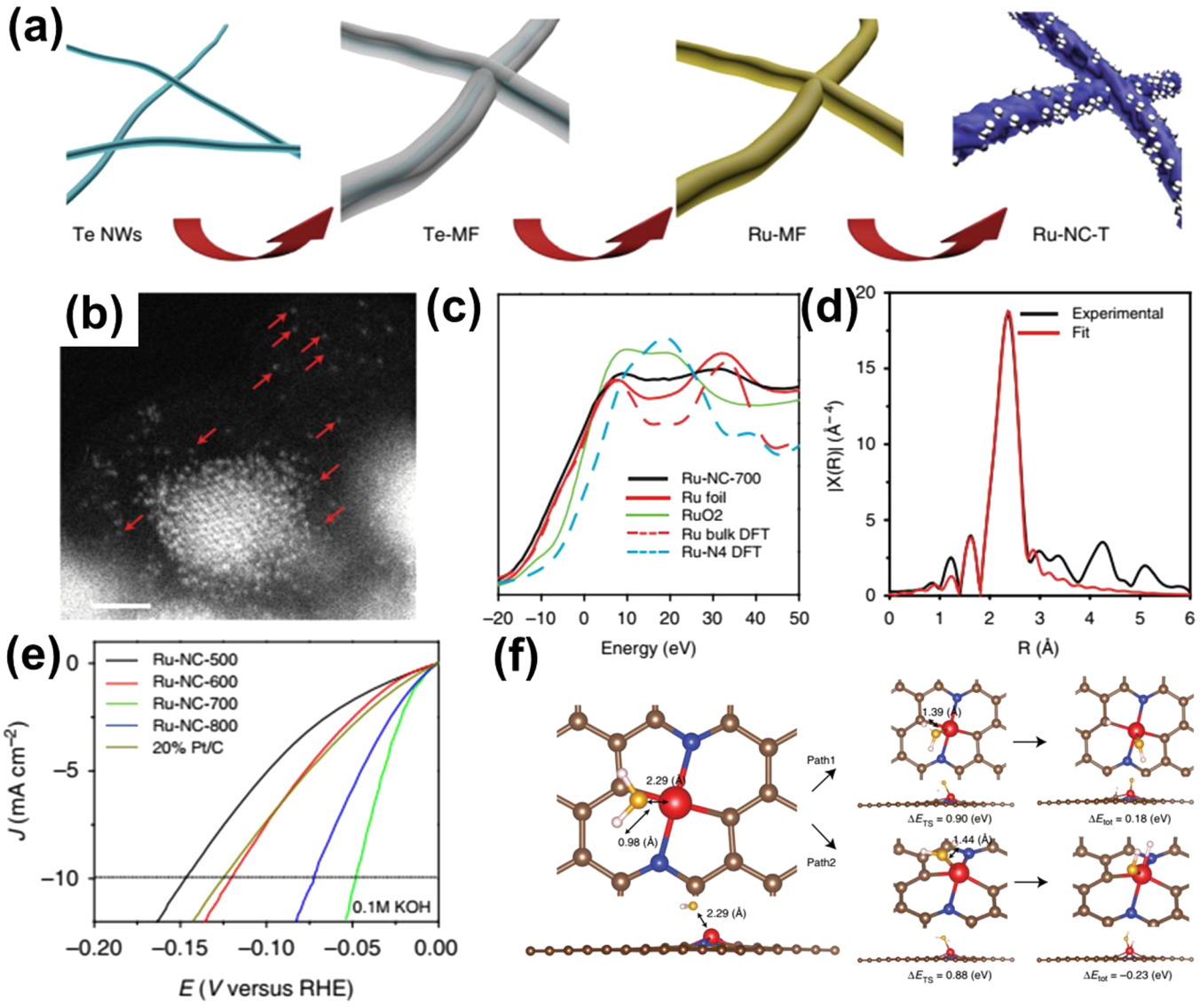

Figure 23. (a) Synthetic procedure of the Ru-NC-T samples. (b) HAADF-TEM image of Ru-NC-800 (scale bar 1 nm). (c) Normalized X-ray absorption near edge structure data for Ru-NC-700, where solid lines are experimental data and dash lines are simulated data by DFT calculations. (d) FT-EXAFS spectrum for Ru-NC-700, where black curve is experimental data and red curve is the best fit. (e) LSV curves of Ru-NC-T and commercial 20 wt % Pt/C in 0.1 M KOH. (f) Reaction barriers and reaction pathways of Volmer's step at RuC_2N_2-1. Reproduced with permission from ref 167. Copyright 2019 Nature Publishing Group.

OLC catalyst (Figure 22b), individual Pt atoms were observed all around the OLC nanospheres but not for Pt nanoparticles or clusters. In addition, clear lattice fringes with a *d*-spacing of 0.35 nm can be seen in the TEM images (Figure 22c), corresponding to the graphite (002) planes, signifying high-level graphitization of the substrate. In electrochemical measurements, despite a low Pt content of only 0.27 wt %, the Pt_1/OLC catalyst displayed a low overpotential ($\eta_{10,HER}$) of −38 mV, comparable to that of commercial 20 wt % Pt/C catalyst and much lower than that of 5 wt % Pt/C (Figure 22d). As depicted in Figure 22e, the Pt_1/OLC catalyst exhibited a mass activity of 7.40 A mg_{Pt}^{-1}, which is ∼2.5 times higher than that of the Pt_1/graphene (2.82 A mg_{Pt}^{-1}) and ∼43 times higher than that of the benchmark commercial Pt/C (0.17 A mg_{Pt}^{-1}). It is interesting that their DFT calculations showed that the adsorption energy of hydrogen (ΔG_{H^*}) is quite negative, namely −0.92 and −0.50 eV for one and two *H per Pt site, respectively. It is suggested that hydrogen bind strongly to the Pt single atoms supported on the curved substrate due to undercoordination between Pt and the carbon support. They argued that the HER catalytic activity is low when the coverage of *H is low on the Pt_1/OLC catalyst, but H_2Pt_1 motifs with two *H adsorbed on one Pt site could form in situ and give rise to high HER activity, as ΔG_{H^*} was reduced to −0.01 eV for the adsorption of the third hydrogen.

In addition to carbon-based substrates, transition metal sulfides, phosphides, and oxides have also been used as supports in Pt-SAECs.[176,177] It is noted that these semiconductor substrates are active for HER only to a certain extent. The introduction of single-atom metal sites is usually aimed to enhance their activities and hopefully gain beneficial synergetic effects, such as electron spillover from the precious metal to the neighboring surface sites on the substrate. Deng et al. reported a hybrid catalyst based on Pt single atoms-doped MoS_2 ($Pt\text{-}MoS_2$), which exhibited significantly enhanced HER

https://dx.doi.org/10.1021/acs.chemrev.0c00594
Chem. Rev. 2020, 120, 12217−12314

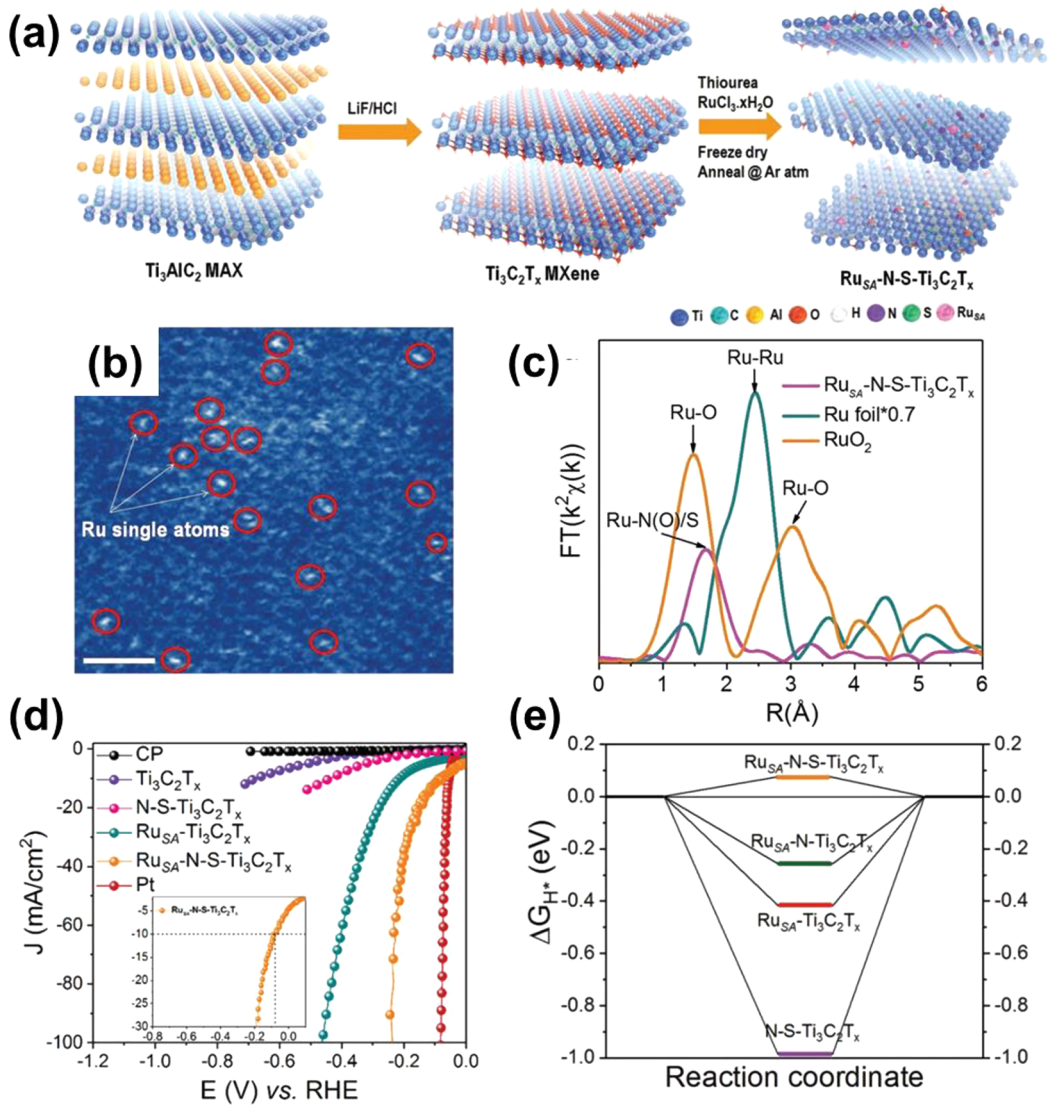

Figure 24. (a) Schematic illustration of the synthesis of the Ru_{SA}−N−S-$Ti_3C_2T_x$ catalyst: $Ti_3C_2T_x$ is synthesized from MAX phase Ti_3AlC_2 using a LiF/HCl mixture and doping of N, S, and Ru_{SA} on the $Ti_3C_2T_x$ is achieved by a freeze-drying process, followed by thermal annealing under Ar atmosphere. (b) Magnified HAADF-STEM image of Ru_{SA}−N−S-$Ti_3C_2T_x$ (bright dots marked with red circles indicate the Ru_{SA} on the $Ti_3C_2T_x$ MXene support). Scale bar: 2 nm. (c) FT-EXAFS spectrum of Ru foil show a main Ru−Ru peak at 2.44 Å (which corresponds to the Ru−Ru shell distance of 2.68 Å, based on fitting), while RuO_2 displays two peaks at 1.47 and 3.0 Å (which correspond to the Ru−O distance of 1.90 and 2.02 Å, respectively) and Ru_{SA}−N−S-$Ti_3C_2T_x$ shows a Ru−N(O)/S peak at 1.67 Å (which corresponds to the Ru−N/O and Ru−S distance of 2.09 and 2.37 Å, respectively). (d) HER polarization curves of bare carbon paper (CP), $Ti_3C_2T_x$, N−S−$Ti_3C_2T_x$, Ru_{SA}-$Ti_3C_2T_x$, Pt, and Ru_{SA}−N−S-$Ti_3C_2T_x$ catalysts recorded in 0.5 M H_2SO_4 (inset: magnified view of the HER polarization curve of Ru_{SA}−N−S-$Ti_3C_2T_x$). (e) Calculated Gibbs hydrogen adsorption free energy (ΔG_{H^*}) diagram of the N−S−$Ti_3C_2T_x$, Ru_{SA}-$Ti_3C_2T_x$, Ru_{SA}−N-$Ti_3C_2T_x$, and Ru_{SA}−N−S-$Ti_3C_2T_x$ catalysts. Reproduced with permission from ref 153. Copyright 2019 John Wiley and Sons.

catalytic activities, as compared to pristine MoS_2. They argued that the Pt single atoms modulated H adsorption on the adjacent S sites via electron spillover, making the latter highly active for HER.[168] Park et al. found that Pt single atoms supported on WO_{3-x} (Pt SA/WO_{3-x}) had enhanced electron spillover, as compared to the interface between Pt nanoparticles and WO_{3-x}, leading to a higher HER activity than the latter.[178] Jiang et al. reported the utilization of Pt single atoms to decorate nanoporous $Co_{0.85}Se$ (Pt/np-$Co_{0.85}Se$) and observed a high HER activity with a low Tafel slope of 35 mV dec^{-1} and a high turnover frequency of 3.93 s^{-1} at −100 mV in a neutral electrolyte, outperforming commercial Pt/C catalysts and many transition metal chalcogenide electrocatalysts reported in the literature. On the basis of operando XAS studies and DFT calculations, it was argued that the cooperation of the interface between Pt and $Co_{0.85}Se$ in this SAEC significantly reduced the energy barrier for water dissociation and improved the adsorption/desorption of hydrogen.[179,180] In addition, Zhang et al.[180] reported Pt single-atom-decorated CoP nanotubes by using an electrochemical potential cycling method. When used as an HER electrocatalyst in a phosphate buffer solution (PBS, pH 7.2), this SAEC exhibited a mass activity four times better than that of Pt/C, along with high stability.

4.2.2. Ru-based Single-Atom Electrocatalysts. Recent studies have shown that Ru-based nanostructures are promising for HER electrocatalysis over a wide pH range, including porous carbon supported Ru nanoparticles (e.g.,

https://dx.doi.org/10.1021/acs.chemrev.0c00594
Chem. Rev. 2020, 120, 12217−12314

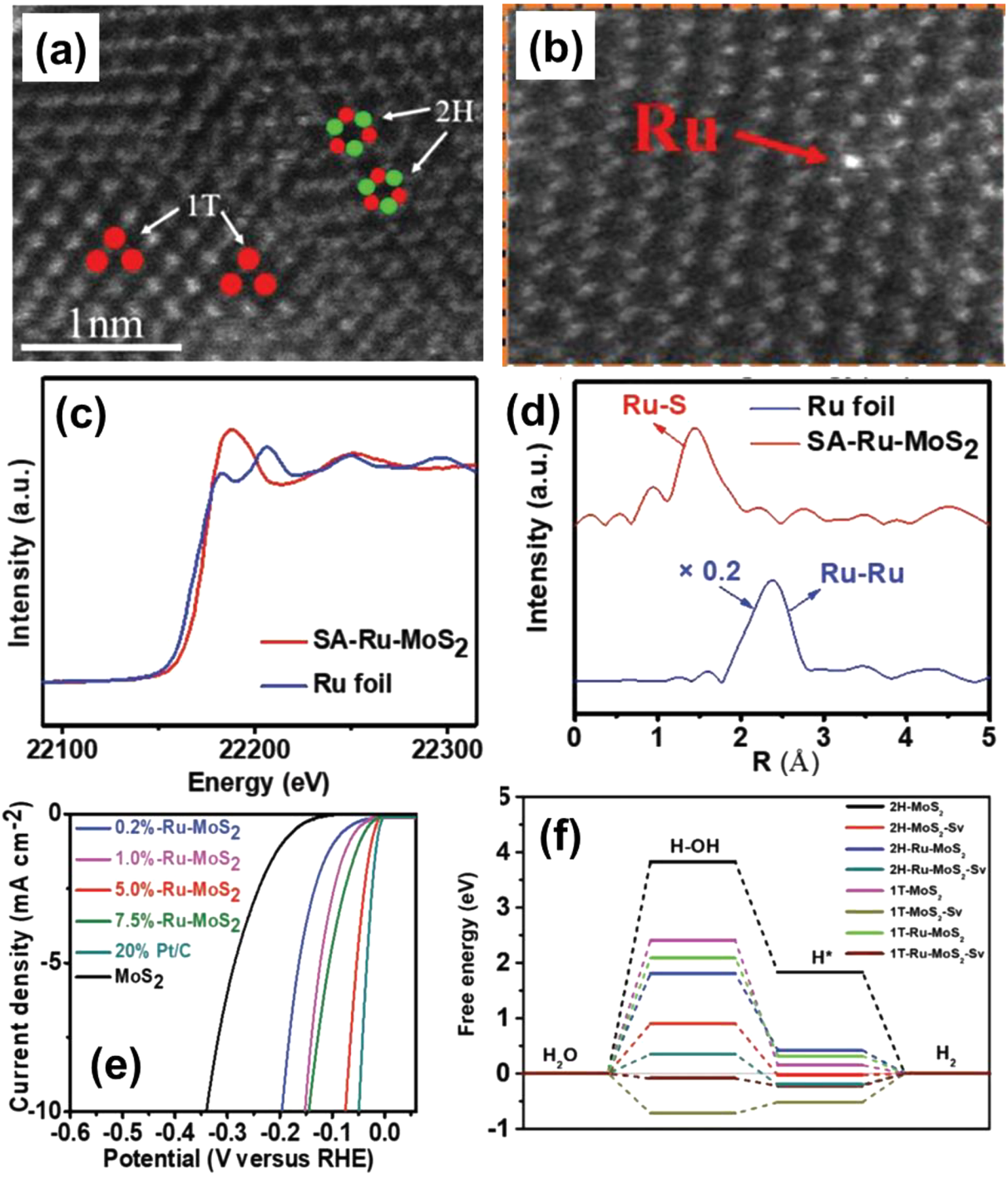

Figure 25. (a) Dark-field STEM image of SA-Ru-MoS_2, where the red and green balls indicate Mo and S atoms, respectively. Scale bar: 1 nm. (b) HAADF-STEM image of SA-Ru-MoS_2. (c) Normalized Ru K-edge XANES spectra of SA-Ru-MoS_2 and Ru foil. (d) k_2-weighted EXAFS spectra of SA-Ru-MoS_2 and Ru foil (e) LSV of pure MoS_2 and the samples with different Ru contents in 1 M KOH at the scan rate of 2 mV s^{-1}. (f) Free energy diagrams of the different MoS2 model catalysts in alkaline media. Reproduced with permission from ref 189. Copyright 2019 John Wiley and Sons.

Ru@NG, Ru/NC, etc.), Ru alloys (e.g., CoRu@NC, NiRu, etc.), and Ru phosphides, sulfides, and borides.[181−183] The Ru−H bond energy (ca. 65 kcal mol^{-1}) is comparable to that of Pt−H. However, the price of Ru is only ∼5% of Pt,[184] which makes Ru-based catalysts a promising alternative to the Pt-based counterparts. Further enhancement of the HER performance of Ru has also been achieved with SAECs.

Chen's group[165−167] reported ruthenium and nitrogen codoped carbon nanocomposites as HER electrocatalysts. As shown in Figure 23a, Ru, N-codoped carbon nanowires (NWs) were synthesized by using Te NWs as sacrificial templates.[167] Isolated Ru single atoms were identified within this Ru-NC composite catalyst by using HAADF-STEM measurement (Figure 23b). The XANES spectra (Figure 23c) show that the absorption edge of Ru-NC was close to that of Ru foil but

https://dx.doi.org/10.1021/acs.chemrev.0c00594
Chem. Rev. 2020, 120, 12217−12314

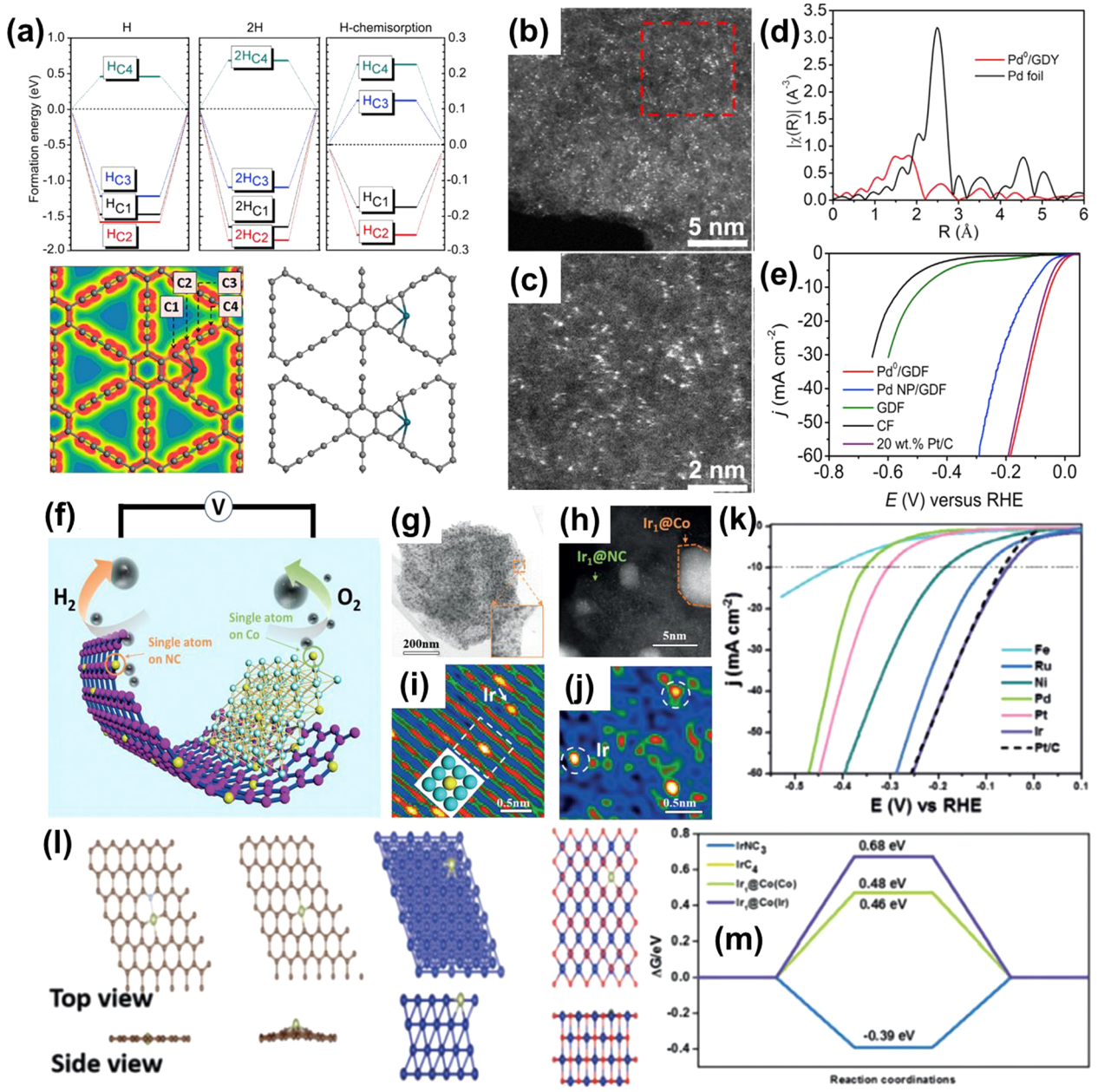

Figure 26. (a) Adsorption formation energies of H and 2H on four different C atom sites (C1, C2, C3, and C4) close to the anchoring Pd atom. The free chemisorption energies are also given, along with the 2D valence charge density maps for the four different C atom sites (C1, C2, C3, and C4), and the structural configuration for H atom adsorption on the C1 and C2 atom sites. (b,c) STEM-HAADF images of the Pd_0/GDY nanosheet. (d) EXAFS spectra of Pd^0/GDY and Pd foil at the Pd K-edge. (e) HER polarization curves of Pd^0/GDY, Pd NP/GDY, GDY, CF, and Pt/C. Reproduced with permission from ref 193. Copyright 2019 Elsevier. (f) Schematic illustration of the working mechanism of the prepared electrodes. (g) Annular bright field (ABF)-STEM images of Ir_1@Co/NC at low magnification. (h) HAADF-STEM image of Ir_1@Co/NC at high magnification. (i) HAADF-STEM image of Ir_1@Co region, (j) FFTI-HAADF image of Ir_1@NC area. (k) Polarization curves of the HER of Ir_1@Co/NC. (l) Top views and side views of $IrNC_3$, IrC_4, Ir@Co, and Ir@CoO, respectively, gray, white, yellow, blue, and red balls represent C, N, Ir, Co, and O atoms. (m) Free energy diagrams for HER at pH = 14 on $IrNC_3$, IrC_4, Ir_1@Co (Co), and Ir_1@Co. Reproduced with permission from ref 194. Copyright 2019 John Wiley and Sons.

quite different from RuO_2. The EXAFS spectrum of Ru-NC shows two main peaks at about 2.68 and 2.03 Å (Figure 23d), which were attributed to Ru−Ru and Ru−N (or Ru−C) bonds, respectively.[185,186] These results clearly signify the formation of both ruthenium nanoparticles and single atoms bonded to N and/or C in the nanowire support. Notably, the Ru-NC catalyst exhibited high HER activity in alkaline media (Figure 23e), featuring an overpotential ($\eta_{10,HER}$) of −47 mV, much lower than that of commercial Pt/C (−125 mV). To understand the catalytic enhancement mechanisms, Lu et al.[167] calculated the hydrogen binding energy for a range of RuC_xN_y structures ($x + y \leq 4$) with 2−4 fold metal-C(N) coordination. Among them, RuC_2N_2 was identified as the most active motif for HER, in which both the Ru site and its adjacent C site have desirable binding strength to hydrogen ($|\Delta G_{H^*}| < 0.2$ eV). Because the water dissociation process (i.e., Volmer reaction, eq 2) is usually the rate-determining step for the HER in alkaline electrolyte, the authors have further calculated the free

https://dx.doi.org/10.1021/acs.chemrev.0c00594
Chem. Rev. 2020, 120, 12217−12314

energy barrier and transition state of water dissociation on this catalyst. As depicted in Figure 23f, two possible pathways were identified for the Volmer step, via hydrogen binding to either the Ru site or the C atom adjacent to Ru. It was found that these two pathways have comparable reaction barriers and hence likely both active for the HER. The dual active site mechanism in this type of SAECs has also been seen elsewhere.[147]

MXenes, a new class of 2D transition metal carbides/nitrides, have high electrical conductivity, a large number of exposed active sites on the basal planes and hydrophilic surface functionalities (such as −O, −OH, and −F groups).[187] These properties make MXenes unique candidates for various electrochemical applications, including supercapacitors, Li-ion and Li-sulfur batteries, and electrocatalysts for the HER.[188] For example, Ramalingam et al. successfully dispersed Ru single atoms (RuSA) on nitrogen and sulfur codoped 2D titanium carbide ($Ti_3C_2T_x$, where T_x denotes the surface functional groups) MXene by taking advantage of the strong coordination between Ru and the doped N and S heteroatoms on the basal plane (Figure 24a).[153] HAADF-STEM studies (Figure 24b) showed a uniform distribution of atomically dispersed Ru atoms on the N−S−$Ti_3C_2T_x$ support. EXAFS studies showed a primary peak at 1.67 Å, which is distinct from Ru−Ru or Ru−O bonding and was attributed to a combination of Ru−N(O) and Ru−S scattering pairs (Figure 24c). The absence of Ru−Ru and Ru−O scattering pairs in RuSA−N−S-$Ti_3C_2T_x$ signifies the formation of atomically dispersed Ru atoms on the MXene support. From Figure 24d, one can see that RuSA−N−S-$Ti_3C_2T_x$ exhibited a small $\eta_{10,HER}$ (−53 mV) in an acid electrolyte. The authors ascribed the HER activity to the electronic interactions between the Ru single atoms and the N and S codopants (Figure 24e).

2D MoS_2 have also been used as a support for SAECs, with the metal single atoms dispersed via coordination with the S sites.[190] Zhang et al. reported the synthesis of a Ru single-atom catalyst on MoS_2 (SA-Ru-MoS_2) by impregnation. In Figure 25a, one can see that the phase of MoS_2 changes from 2H to 1T when Ru was doped into the MoS_2 matrix, with isolated Ru sites visualized by using HAADF-STEM (Figure 25b).[189] XANES measurements show that the Ru single atoms are in a cationic form (Figure 25c). EXAFS analysis shows a first-shell scattering peak at about 1.44 Å, which is much smaller than that for Ru−Ru (2.37 Å) (Figure 25d). These results consistently point to the formation of Ru single atoms embedded inside the MoS_2 lattice, likely through substitution of Mo and stabilization via Ru−S coordination (instead of sitting on top of the MoS_2 slab as adatoms). Figure 25e shows the HER LSV curves of the different catalysts, where SA-Ru-MoS_2 exhibited the best performance among the series of samples, featuring a low $\eta_{10,HER}$ of −76 mV, slightly lower than that of commercial 20 wt % Pt/C catalyst (−51 mV). Taking the experimental and DFT (Figure 25f) results into account, one can conclude that the high HER activity is mainly attributed to the synergy of Ru single-atom doping, S vacancies and the local phase transition in MoS_2, which efficiently tailors the electronic structure of SA-Ru-MoS_2, dramatically reduces the energy barrier of the Volmer step and facilitates the adsorption/desorption of H* throughout the reaction.

4.2.3. Other Precious Metal-based Single-Atom Electrocatalysts. Besides Pt and Ru, SAECs comprising other Pt group metals (PGMs), such as Rh, Pd, and Ir, have also been reported for the HER.[191,192] For example, Yu et al. reported the utilization of ultrathin GDY nanosheets to support zero-valence palladium atoms as a 3D flexible cathode for HER.[193] It was argued that the various C sites (C1−C4 as labeled in Figure 26a) located in the proximity to the Pd single atoms have distinct adsorption properties, due to the different levels of electronic coupling between the carbon *p* orbital and palladium *d* orbital. The adsorption of hydrogen is much stronger on C1 and C2 than on C3 and C4, with C3 being identified as the most active site for the HER. HAADF-STEM study (Figure 26b,c) confirmed the formation of atomically dispersed Pd on GDY. The EXAFS spectrum of Pd-GDY displayed a major peak near 1.5 Å (Figure 26d), but no feature for Pd−Pd coordination, suggesting that the Pd single atoms were bound to C on the GDY substrate. The Pd-GDY catalyst exhibited an $\eta_{10,HER}$ of −55 mV, lower than the commercial Pt/C benchmark (Figure 26e).

In another study, Feng et al. reported a general strategy of utilizing π electrons to anchor single atoms of metals (M), such as Ir, Pt, Ru, Pd, Fe, Ni, etc., on a Co-nanocarbon (Co/NC) composite substrate (Figure 26f).[195] In these M_1@Co/NC catalysts, both Co and NC can serve as substrates to stabilize single atoms, generating two different types of active sites, i.e., diluted surface alloys M_1@Co and coordinated single-atoms M_1@NC.[194] HAADF-STEM studies show that the Co nanoparticles exhibit a roughly dodecahedral shape (Figure 26h), with dense Ir single atoms uniformly dispersed on both the Co nanoparticles and in the C matrix, with the different atoms well resolved by *Z*-contrast mapping (Figure 26i,j). Among the various SAECs prepared, Ir_1@Co/NC stood out to be the most active one, exhibiting an $\eta_{10,HER}$ of −60 mV (Figure 26k). They further performed DFT calculations to understand the catalytic properties of the different possible single-atom sites involved in this catalyst. On the basis of EXAFS and XPS analyses, they considered four structural models: $IrNC_3$, IrC_4, Ir_1@Co(Co), and Ir_1@Co(Ir) (Figure 26l). It turned out that the $IrNC_3$ site gave a relatively low free energy barrier of 0.39 eV for the HER, compared to 0.5−0.6 eV for the other three types of 4-fold coordination Ir sites.

4.3. Nonprecious Metal-based Single-Atom Electrocatalysts

From the above discussion, one can see that Pt and Ru-based SAECs are among the most active HER electrocatalysts, due to their maximized atomic utilization efficiency and also desirable adsorption properties (nearly zero ΔG_{H^*}). Nevertheless, these electrocatalysts are based on precious metals, and for further reduction of cost, SAECs based on nonprecious metals such as Fe,[196,197] Co,[16,134,147,198−202] and Ni[203−207] have attracted increasing interest. These SAECs typically involve transition metal atoms coordinated on substrates such as N-doped carbon (M−N−C motifs) and metal chalcogenides. For nonprecious metals, their metallic forms are unstable under electrochemical reaction conditions, tending to oxidize, dissolve, or leach depending on the electrolyte. How to stabilize the metal single atoms becomes a challenging task for the development of precious metal-free SAECs.

4.3.1. Fe-based Single-Atom Electrocatalysts. Using iron in electrocatalysis is potentially advantageous due to its low toxicity, high abundance, and low cost. Fe SAECs have been extensively studied for ORR, the cathode reaction in fuel cells and Zn−air batteries (see the discussion below in section 6). In the last few decades, many studies have also shown that the OER activity of nickel oxide or hydroxide can be drastically

https://dx.doi.org/10.1021/acs.chemrev.0c00594
Chem. Rev. 2020, 120, 12217−12314

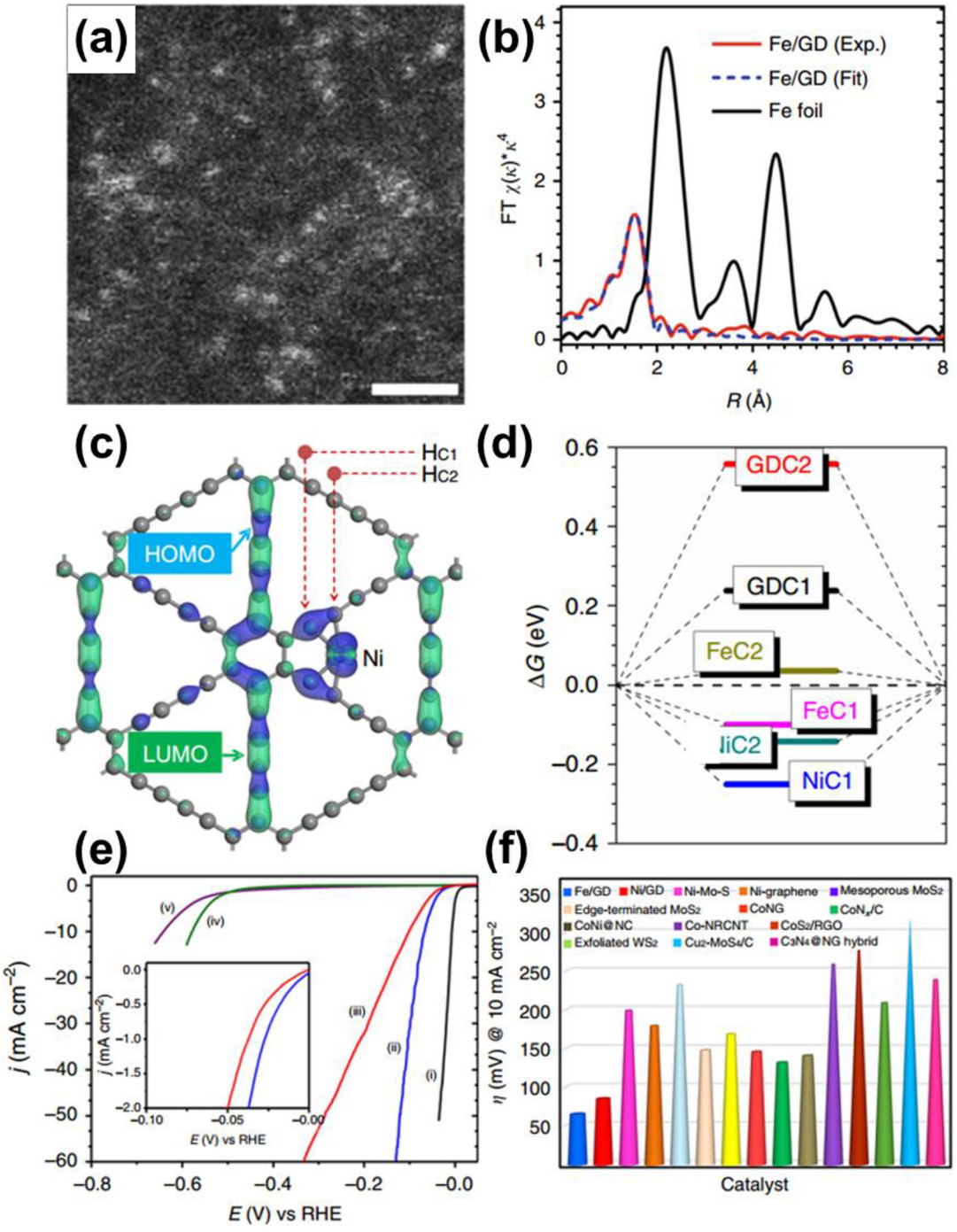

Figure 27. (a) HAADF-STEM image of Fe/GD. Scale bar: 2 nm. (b) Ex situ EXAFS spectra of Fe/GD and Fe foil at the Fe K-edge. (c) Real-space HOMO and LUMO profile plots on Ni-on-GD. The HC1 and HC2 represent the active H adsorption site on different C sites named C1 and C2, respectively. (d) ΔG_H diagram of the Ni/FeC1, Ni/FeC2, GDC1, and GDC2. (Ni/FeC_1 and Ni/FeC_2 mean the HC1 and HC2 of Ni/Fe-on-GD system, respectively; GDC1 and GDC2 denote the H adsorption on pristine GD). (e) HER polarization curves of (i, black line) Pt/C, (ii, blue line) Fe/GD, (iii, red line) Ni/GD, (iv, green line) GDF, and (v, purple line) CC (inset: enlarged view of the LSV curves for Fe/GD and Ni/GD near the onset region) in 0.5 M H_2SO_4 (Fe loading, 0.278 wt % for Fe/GD; Ni loading, 0.68 wt % for Ni/GD). (f) Comparison of the overpotentials at 10 mA cm^{-2} of Ni/GD and Fe/GD (red square) along with other nonprecious single-atom HER catalysts (green circle) and bulk catalysts (olivine triangle). Reproduced with permission from ref 197. Copyright 2018 Nature Publishing Group.

improved by doping with metallic iron (see the discussion below in section 5). Nevertheless, studies of Fe SAECs for HER have been relatively rare.

In a recent study, Xue et al.[197] developed a two-step strategy to disperse single Fe atoms on graphdiyne (GD) (Fe/GD) via first Glaser−Hay cross-coupling to load iron ions and then electrochemical reduction of the iron species. HAADF-STEM (Figure 27a) and XAFS studies (Figure 27b) confirmed the isolation of atomic Fe species on the GD substrate. The Fe/GD catalyst exhibited an $\eta_{10,HER}$ of −66 mV for HER and high stability with a negligible loss after 60 h operation (Figure 27c). Their comparison showed that the Fe-SAEC out-

https://dx.doi.org/10.1021/acs.chemrev.0c00594
Chem. Rev. 2020, 120, 12217−12314

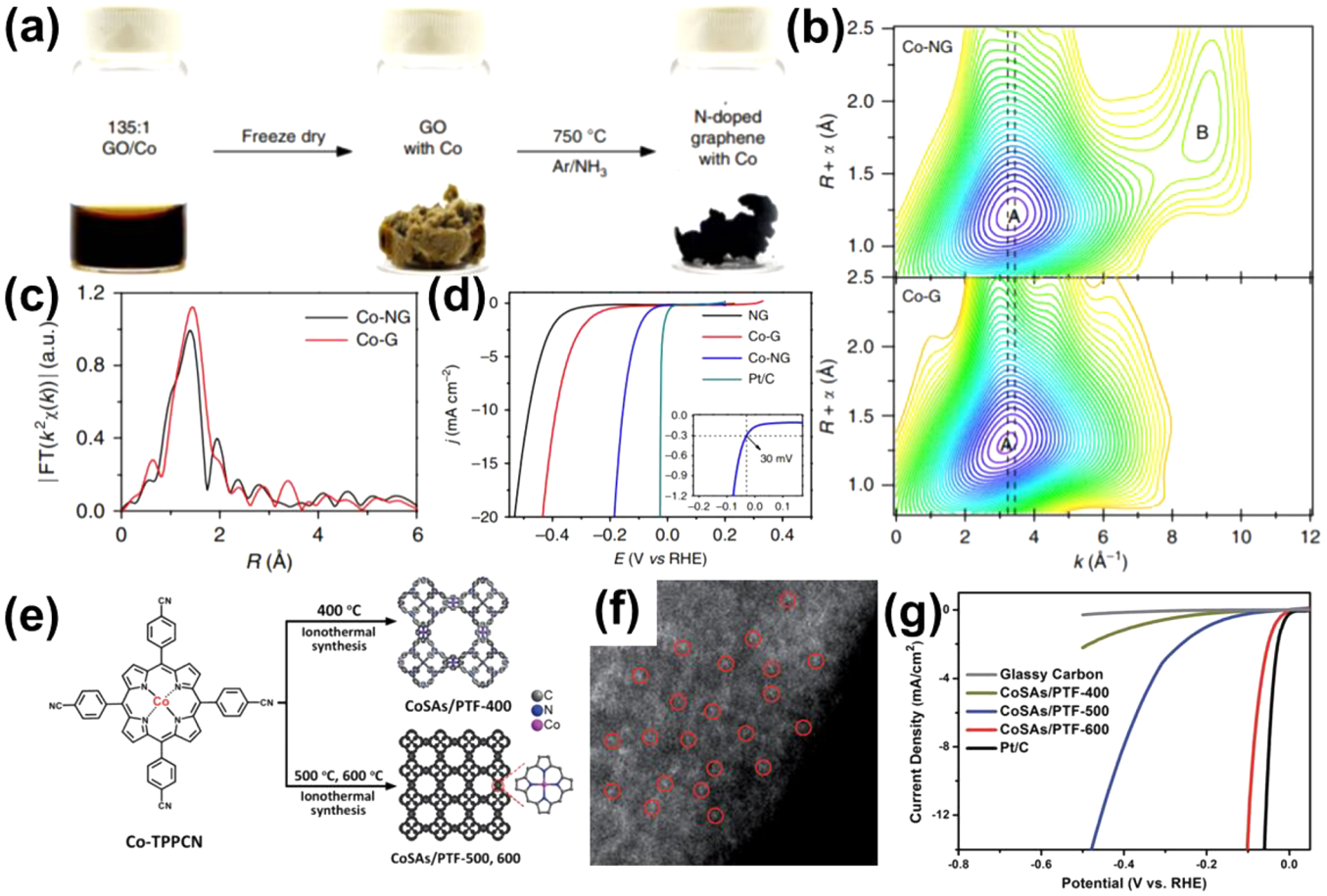

Figure 28. (a) Schematic diagram of the synthesis process for Co−NG. (b) Wavelet-transformed k_2-weighted EXAFS spectra for the Co−NG and Co−G samples. (c) Fourier-transformed k_2-weighted EXAFS spectra in R space of the Co−NG and Co−G samples. (d) LSVs of Co−NG and other catalysts in 0.5 M H_2SO_4 at the potential scan rate of 2 mV s^{-1} (inset: zoom-in LSVs for Co-NG near the onset region). (e) Schematic diagram of the synthesis process for CoSAs/PTF. (f) HAADF-STEM image of CoSAs/PTF-600. (g) HER polarization curves of PTF-600, (Co) PTF-600, CoNPs/PTF-600, and CoSAs/PTF-600 in 0.5 M H_2SO_4 electrolyte. Reproduced with permission from ref 16. Copyright 2015 Nature Publishing Group.

performed other precious metal-free electrocatalysts (Figure 27d). In another study, Fe−N−C SAECs with 4-fold iron−nitrogen coordination were prepared by using Fe and Zn phthalocyanine (Pc) as the precursor for pyrolysis.[196] The Zn species was anchored on the ring center of Pc and partially displaced the Fe sites, which was believed to be the key to suppress the formation of Fe nanoparticles during the pyrolysis process. This catalyst (denoted as Fe−N_4/NPC) showed an $\eta_{10,HER}$ of −202 mV with a Tafel slope of 123 mV dec^{-1} in 1.0 M KOH. DFT calculations indicated that the Fe−N_4 moiety had the lowest ΔG_{H^*} value among Fe−N_4, Fe−C_4, and Fe_6 moieties, meaning that single Fe−N_x sites were ideal for H* adsorption and hence optimal HER performance.

4.3.2. Co-based Single-Atom Electrocatalysts. Among the transition metals, both Co and Ni have two 4*s* electrons in the outermost layer orbital and similar electrocatalytic performance for HER as SAECs. Similar to Fe-SAECs, these nonprecious transition metals are usually stabilized as single-atom sites via coordination with substrates, typically in the form of M−N−C motifs. For instance, Fei et al.[16] prepared single Co atoms dispersed on nitrogen-doped graphene (Co−NG) through heat treatment of a Co salt and graphene oxide in an Ar/NH_3 atmosphere (Figure 28a). Fourier-transformed EXAFS spectrum (Figure 28b) exhibited one strong peak around 1.5 Å for both Co−NG and Co−G (the control without N doping), and wavelet-transformed EXAFS spectrum (Figure 28b) further confirmed direct Co−N rather than Co−C bonding as the predominant coordination for the single atoms, and hence the formation of isolated Co sites in the structure of Co−N−C (Figure 28c). For HER electrocatalysis in 0.5 M H_2SO_4, Co−NG achieved an $\eta_{10,HER}$ of −146 mV, superior to NG and Co−G (Figure 28d). Yi et al. synthesized Co SAECs based on porphyrinic triazine-derived frameworks (PTF) (denoted as CoSAs/PTFs) by incorporating cobalt porphyrin-like units into the covalent triazine frameworks (CTFs), followed by in situ thermalization and acid leaching treatment (Figure 28e).[208] The highly dispersed Co atoms can be clearly visualized in the HAADF-STEM image (Figure 28f). Among the catalysts derived from pyrolysis at different temperatures, CoSAs/PTF-600 showed the highest HER activity with an $\eta_{10,HER}$ of −94 mV in acid (Figure 28g). The HER activity was ascribed to the formation of Co−N_4 active sites anchored on the carbon substrate. Other types of Co−N−C SAECs have also been reported for the HER in acid[162,195,201,207,209,210]

For the more challenging HER in alkaline media, the cleavage of O−H bonds in water and adsorption of *OH need to be considered for the design of SAECs in addition to *H.

https://dx.doi.org/10.1021/acs.chemrev.0c00594
Chem. Rev. 2020, 120, 12217−12314

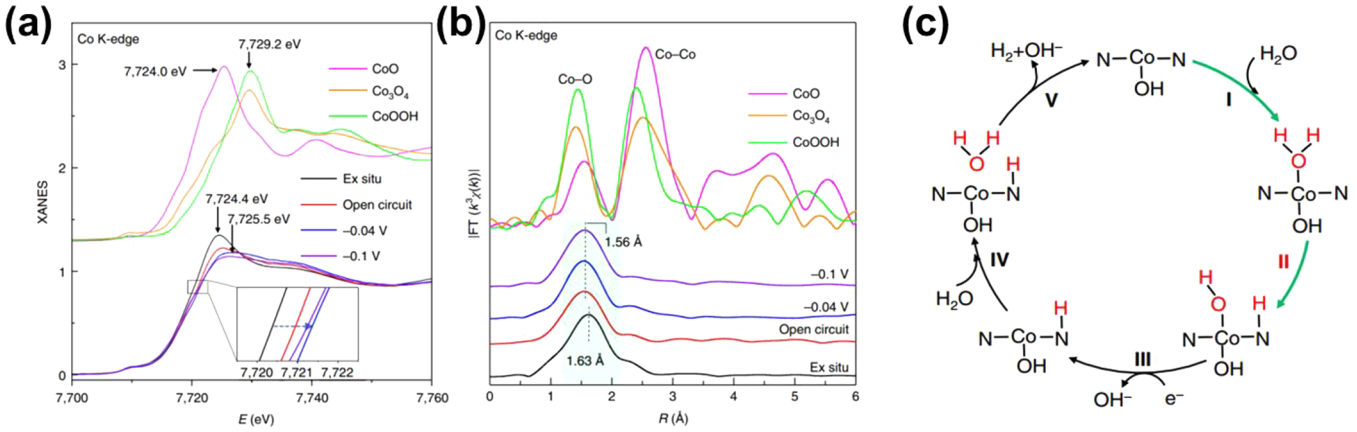

Figure 29. (a) Operando XANES spectra recorded at the Co K-edge. (b) k_3-weighted FTs spectra. (c) Alkaline HER mechanism on HO-Co1/PCN. Reproduced with permission from ref 134. Copyright 2019 Nature Publishing Group.

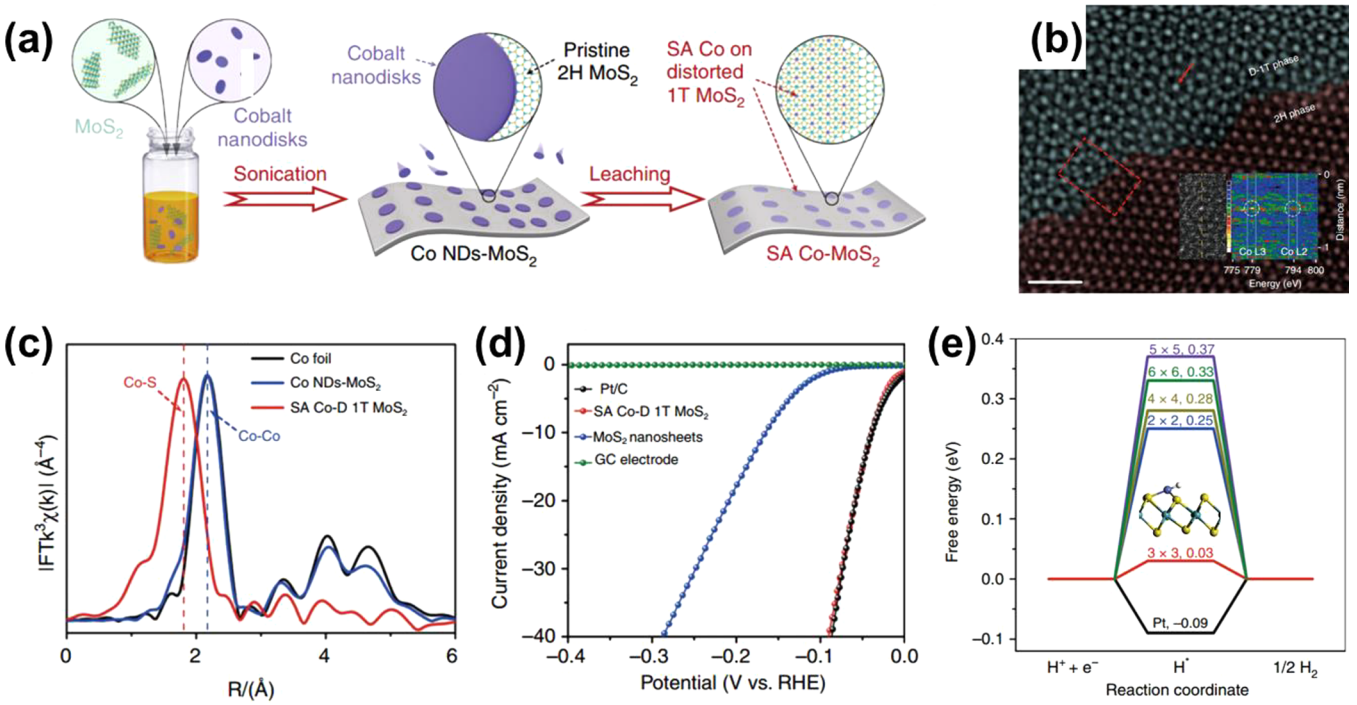

Figure 30. (a) Schematic diagram of the fabrication process of SA Co−D 1T MoS_2. (b) Aberration-corrected HAADF-STEM image of SA Co−D 1T MoS_2, showing the obvious junction between SA Co−D 1T MoS_2 (dark cyan) and pristine 2H MoS_2 (wine) (inset: HRTEM and EELS spectrum of SA Co-D 1T MoS_2). Scale bar: 1 nm. (c) FT-EXAFS spectra of SA Co−D 1T MoS_2 and bulk cobalt foil at the Co K-edge. (d) HER polarization curves of different catalysts tested in Ar-saturated 0.5 M H_2SO_4. (e) Calculated free-energy diagram for HER at a potential of $U = 0$ relative to the standard hydrogen electrode at pH = 0 for different atomic Co loading amounts. Reproduced with permission from ref 147. Copyright 2019 Nature Publishing Group.

Wei et al.[134] reported the in situ XAS characterization of Co single atoms supported on phosphorized C_3N_4 (Co_1/PCN, with ∼0.3 wt % of Co content). They found that Co was primarily present as Co_1-N_4 motif in the as-synthesized catalyst, while the implanted P did not substantially alter the C_3N_4 framework (Figure 29). Under open-circuit condition in an alkaline electrolyte, the Co motif was transformed into $HO-Co_1-N_2$, which was accompanied by a rise of the Co oxidation state (Figure 29a). Under reaction conditions (−0.04 V vs RHE), this motif could accommodate the adsorption of one *OH and one water molecule to form H_2O-($OH-Co_1-N_2$) (Figure 29b). DFT calculations showed that the overall reaction mechanism followed the Volmer−Heyrovsky pathway, and notably, the N site might also participate in the reaction by accommodating the adsorption of *H (Figure 29c). It was believed that the synergy between the Co and N sites was the key to enable the water reduction reaction in alkaline media.

Transition metal sulfides have also been used to support Co single atoms for HER. For instance, Qi et al.[147] prepared a Co-MoS_2 SAEC by using electrochemical deposition. The Co single atoms were covalently bound onto distorted 1T MoS_2 nanosheets via Co−S bonding interactions (denoted as SA Co-D 1T MoS_2, Figure 30a,b). In the R-space EXAFS spectrum, the first-shell scattering was found at 1.79 Å, which was distinctly different from the Co−Co coordination in metallic Co and ascribed to Co−S bonding (Figure 30c). This SAEC achieved a Pt-like activity for HER at similar catalyst loadings

https://dx.doi.org/10.1021/acs.chemrev.0c00594
Chem. Rev. 2020, 120, 12217−12314

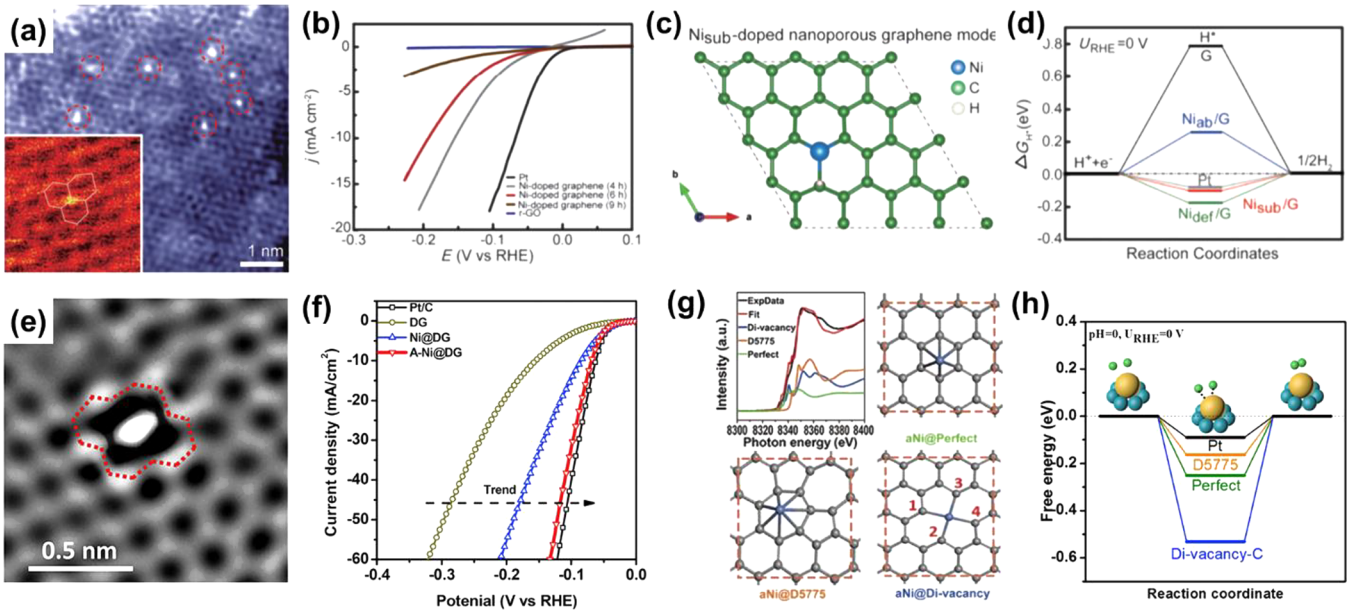

Figure 31. (a) HAADF-STEM image of Ni-doped graphene (inset: enlarged HAADF-STEM image (red circle) shows a substitutional Ni atom (bright-orange spot) occupying a carbon site of graphene lattice (white lines)). (b) HER polarization curves of Pt, Ni-doped graphene with different Ni dissolution time (Ni loading of the 6 h sample: 4−8 at %) and reduced graphene oxide (r-GO) in 0.5 M H_2SO_4. (c) Configuration of the Ni sub-doped nanoporous graphene model. (d) ΔG_H diagram for HER over graphene and Ni doped in graphene at different situation, where Ni_{ab}/G, Ni_{sub}/G, and Ni_{def}/G represent the interstitial Ni atoms in the hollow centers of the carbon rings, Ni atoms replacing C sites in the graphene lattice and anchoring Ni atoms on the defect sites, respectively. Reproduced with permission from ref 211. Copyright 2015 John Wiley and Sons. (e) Zoom-in image of the defective area. (f) HER polarization curves of DG, Ni@DG, A-Ni@DG (Ni loading: 1.24 wt %), and Pt/C performed in 0.5 M H_2SO_4. (g) LCF analysis of XANES theoretical modeling and illustrations of three different types of catalytic active sites. (h) Energy profiles of the three configurations for HER. Reproduced with permission from ref 59. Copyright 2018 Elsevier.

(Figure 30d) and demonstrated long-term stability without performance degradation. Experiments together with DFT calculations (Figure 30e) revealed that the superior catalytic performance was associated with the electrostatic attraction between proton and negatively charged S adjacent to Co. A tilted hydrogen adsorption configuration on Co, as a result, could stabilize this adsorbed H intermediate for HER.

4.3.3. Ni-based Single-Atom Electrocatalysts. Nickel is the fourth most abundant metal (after Fe, Ti, and Zr) and has been widely utilized for the fabrication of Ni-based SAECs.[210] In fact, Ni-based SAECs are among the most active HER catalysts that are free of precious metals, which are particularly promising as alternatives to Pt-based electrocatalysts. The structure−property relationship of Ni-SACEs has thus received great attention.

Chen et al.[211] prepared nickel single-atoms-doped nanoporous graphene (Ni-doped np-G) by acid etching of a Ni foam covered with graphene (Figure 31a). The obtained catalyst showed a low $\eta_{10,HER}$ of −50 mV (Figure 31b). It was proposed based on DFT calculations that the Ni single atoms were embedded in the graphene lattices in three possible configurations: interstitial Ni in the center of the phenyl rings (Ni_{ab}), substitutional doping at the vacancy of the graphene lattice (Ni_{sub}), or anchoring on the defect sites (Ni_{def}) (Figure 31c). The C atoms coordinating with the Ni centers were believed to be the active sites for hydrogen adsorption, exhibiting a $|\Delta G_{H^*}|$ of C−Ni_{ab} > C−Ni_{sub} > C−Ni_{def} all lower than that of pristine graphene (Figure 31d). Notably, $|\Delta G_{H^*}|$ of the carbon adjacent to Ni_{sub} was found to be only 0.10 eV, very close to that of Pt (0.09 eV), indicating that charge transfer between the metal single atom and the substrate (coordinating C here) could lead to the formation of HER-active sites at the "interface".

Zhang et al.[59] further exploited the type of defects on graphene accommodating Ni single atoms. HAADF-STEM imaging showed Ni atoms anchored in the divacancy site on the defective graphene (Figure 31e). Structural analysis by fitting the EXAFS spectra identified three types of Ni−C coordination patterns, with a CN of 4, 2 and 5, respectively. The linear combination fitting (LCF) of XANES revealed that Ni atoms were anchored on divacancy defects (four-coordinate), D5775 defect (two- or five-coordinate), and perfect hexagons structure (four-coordinate, Figure 31g). The activity of A-Ni@DG was found to originate from the unique configurations of atomic Ni in the defects. The electronic structure of the trapped atomic Ni minimizes the energy barrier for HER (Figure 31h). This work enlightens a synthetic strategy to utilize the interaction between non-noble metal SAs and carbon defects. This Ni-SAEC (denoted as A-Ni@DG) exhibited an $\eta_{10,HER}$ of −70 mV (Figure 31f) and a TOF of 5.7 s^{-1} at −100 mV. In the above work the Ni atoms were directly anchored on graphene via Ni−C coordination and the formed SACE was stable under the HER condition in acid. This situation is quite different from other nonprecious metal SAECs that are typically based on M−N−C coordination to stabilize the transition metal sites.

In another study, Zhang et al.[207] employed MoS_2 as a support to disperse Ni atoms to form HER electrocatalysts. They developed a wet impregnation method to decorate Ni single atoms on hierarchical MoS_2 nanosheets grown on multichannel carbon nanofibers (MCM@MoS_2−Ni). EXAFS analysis conformed the absence of Ni−Ni bonds and the formation of Ni−S coordination in MCM@MoS_2−Ni (Figure

https://dx.doi.org/10.1021/acs.chemrev.0c00594
Chem. Rev. 2020, 120, 12217−12314

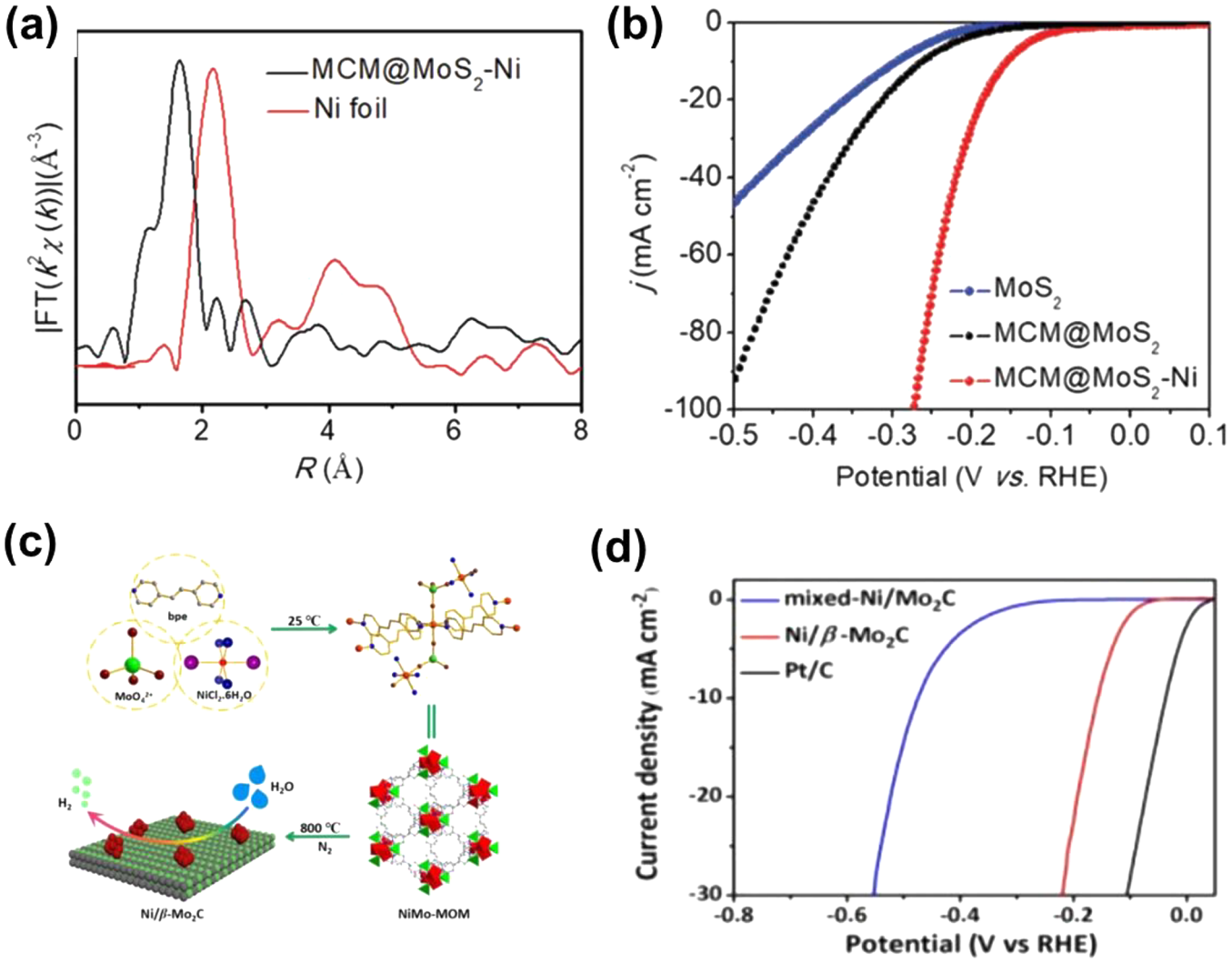

Figure 32. (a) Ni K-edge EXAFS spectra of MCM@MoS_2−Ni and Ni foil. (b) HER polarization curves for different catalysts in 0.5 m H_2SO_4. Reproduced with permission from ref 207. Copyright 2018 John Wiley and Sons. (f) Schematic illustration of the synthesis of Ni/β-Mo2C. (g) HER polarization curves measured in 1.0 M KOH, respectively. Reproduced with permission from ref 205. Copyright 2018 Royal Society of Chemistry.

32a). This Ni-SAEC exhibited an $\eta_{10,HER}$ of −161 mV, in comparison to −297 mV for MoS_2 and −263 mV for MCM@MoS_2 (Figure 32b). Ouyang et al.[205] used porous β-Mo_2C to support Ni single atoms (Ni/β-Mo_2C) (Figure 32c), where the coordination for Ni in Ni/β-Mo_2C was proposed to involve both Ni−Mo and Ni−N_4. This SAEC exhibited an $\eta_{10,HER}$ of −157 mV, and a Tafel slope of 61 mV dec^{-1} in 1.0 M KOH (Figure 32d).

4.3.4. Other Nonprecious Metal-based Single-Atom Electrocatalysts. SAECs of 4*d* and 5*d* nonprecious metals have also been reported for the HER. For example, Wang et al.[190] prepared Co_9S_8 supported Mo (0.99 wt %) by utilizing the surface oxygen species to form an M−O bond and stabilize the Mo single atoms (decorated as Mo−Co_9S_8@C, Figure 33a). The atomically dispersed Mo sites appeared as bright spots uniformly distributed on the support in HAADF-STEM imaging (Figure 33b). The stabilization of Mo single atoms via Mo−O bonds were confirmed by EXAFS analysis, as evidenced by the primary first-shell scattering peak at ca. 1.75 Å and the absence of Mo−Mo and Mo−O−Mo features (Figure 33c). The Mo−Co_9S_8@C displayed an $\eta_{10,HER}$ of −98 mV for HER in acid (Figure 33d), lower than that of bare Co_9S_8 (−310 mV), Co_9S_8@C (−230 mV), and Mo−Co_9S_8 (−140 mV). DFT calculations revealed a hydrogen adsorption energy (ΔG_{H^*}) of −0.17 eV on the Mo site, resembling that of Pt for HER (Figure 33e). In another study, Li et al.[212] supported Mo single atoms on N-doped carbon, 3-fold coordinated by one N atom and two C atoms (denoted as $Mo_1N_1C_2$, Figure 33f). The FT-EXAFS spectrum displayed a first-shell scattering peak at 1.3 Å, due to the Mo−N or Mo−C coordination (Figure 33g). Their wavelet transformed EXAFS spectra on the Mo edge exhibited an intensity maximum at 7.2 $Å^{-1}$, which is distinct from Mo metal and resemble those of Mo−C and Mo−N (Figure 33h). The $Mo_1N_1C_2$ catalyst was found to be more active than Mo_2C or MoN_1, and exhibited an $\eta_{10,HER}$ of −132 mV for HER (Figure 33i). This activity difference was interpreted in terms of different hydrogen adsorption energy (ΔG_{H^*}), as revealed by DFT calculations (Figure 33j). Tungsten SAECs have also been reported with a W−N_4−C active sites by pyrolysis of MOFs-based precursors, and exhibited a low $\eta_{10,HER}$ of −85 mV.[213]

In a computational study, He et al.[214] systematically investigated a series of SACEs with various metal single atoms anchored on 558 grain boundary (GB) site of graphene.

https://dx.doi.org/10.1021/acs.chemrev.0c00594
Chem. Rev. 2020, 120, 12217−12314

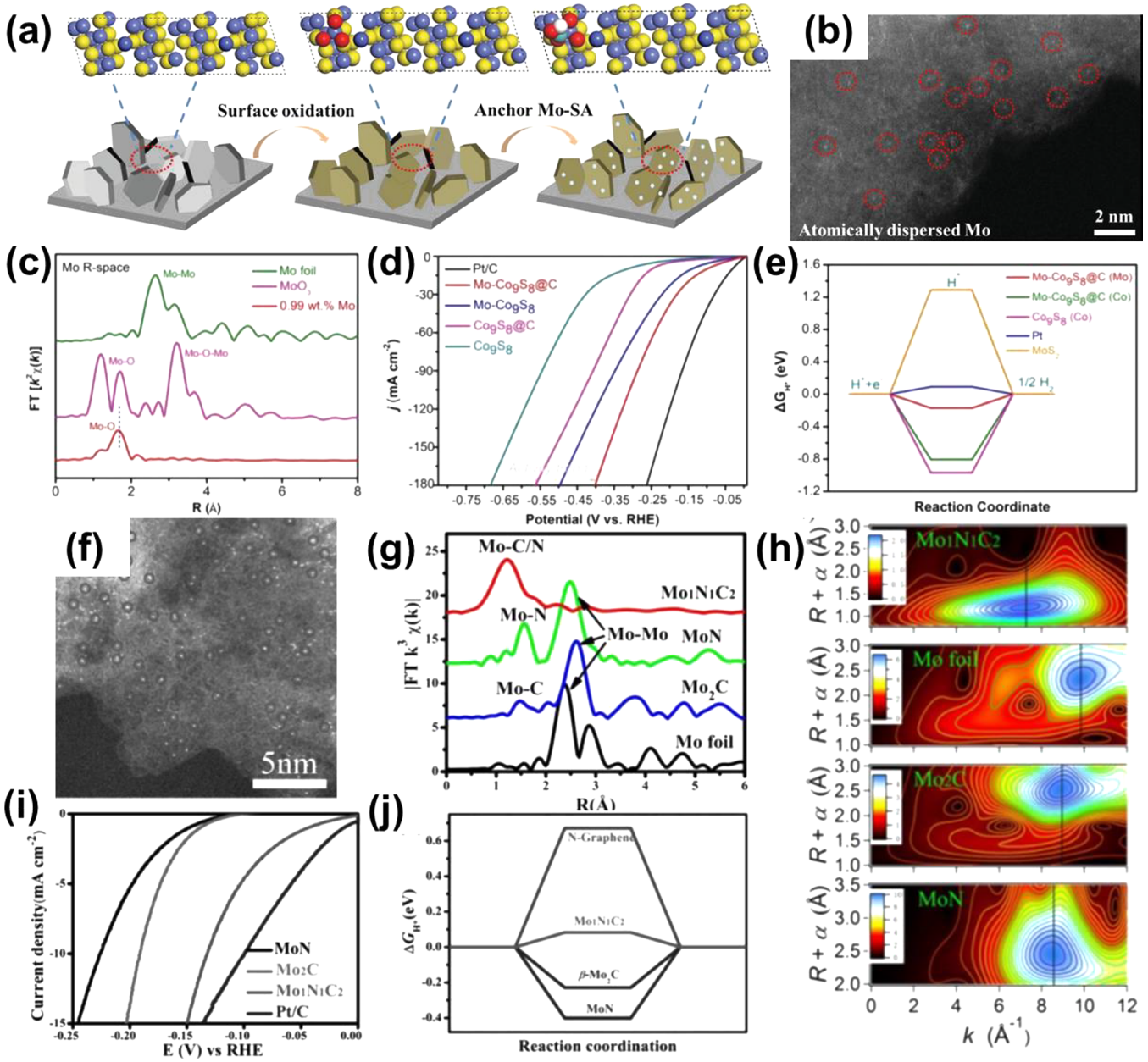

Figure 33. (a) Schematic illustration of the synthetic process for Mo−Co_9S_8@C. (b) Atomic-resolution HAADF-STEM image in which some of the Mo SAs are highlighted by red circle. (c) Fourier transform of the Mo K-edge EXAFS spectra of Mo foil, MoO_3, and Mo−Co_9S_8@C. (d) HER polarization curves of the prepared samples in 0.5 M H_2SO_4. (e) Free-energy diagram for hydrogen evolution at standard conditions. Reproduced with permission from ref 190. Copyright 2019 John Wiley and Sons. (f) AC-STEM image of $Mo_1N_1C_2$. (g) FT-EXAFS curves of the $Mo_1N_1C_2$ at Mo K-edge, (h) WT-EXAFS of $Mo_1N_1C_2$, Mo foil, Mo_2C, and MoN. (i) Electrocatalytic HER performance of the $Mo_1N_1C_2$ in alkaline condition (0.1 M KOH). (j) Gibbs free energy for H* adsorption on $Mo_1N_1C_2$, Mo_2C, and MoN. Reproduced with permission from ref 212. Copyright 2017 John Wiley and Sons.

They built up a volcano plot of the trend of HER activity for these SAECs, and found vanadium (V-GB) being the closest to the peak (Figure 34). It is noted that the ΔG_{H^*} for the V-GB site is ca. −0.01 eV, a value that is even more favorable for the HER than for the Pt metal surface, and both V- and Ni-GB were predicted to be more active than Pt metal. This work suggests that the SAECs may possess similar volcano behaviors in the trend of electrocatalytic activities, similar to what has been established with transition metal surfaces, albeit probably with different metals at the peak position. The latter difference is characteristic of the unique structure and property of single-atom active sites and indicative of the great potential of SAECs for achieving high electrocatalytic activities without relying on precious metals.

4.4. Perspectives about Single-Atom Electrocatalysts for Hydrogen Evolution Reaction

In summary, SAECs represent an emerging class of low-cost, highly efficient electrocatalysts for the HER. Atomic dispersion of metals in these SAECs is usually realized by anchoring the metal atoms onto substrates via coordination to heteroatomic dopants or defect sites. SAECs based on both precious and nonprecious metals have shown remarkable activity toward HER in a wide range of pH. Electronic structures of the metal centers are usually dependent on the element of the metal, its

https://dx.doi.org/10.1021/acs.chemrev.0c00594
Chem. Rev. 2020, 120, 12217−12314

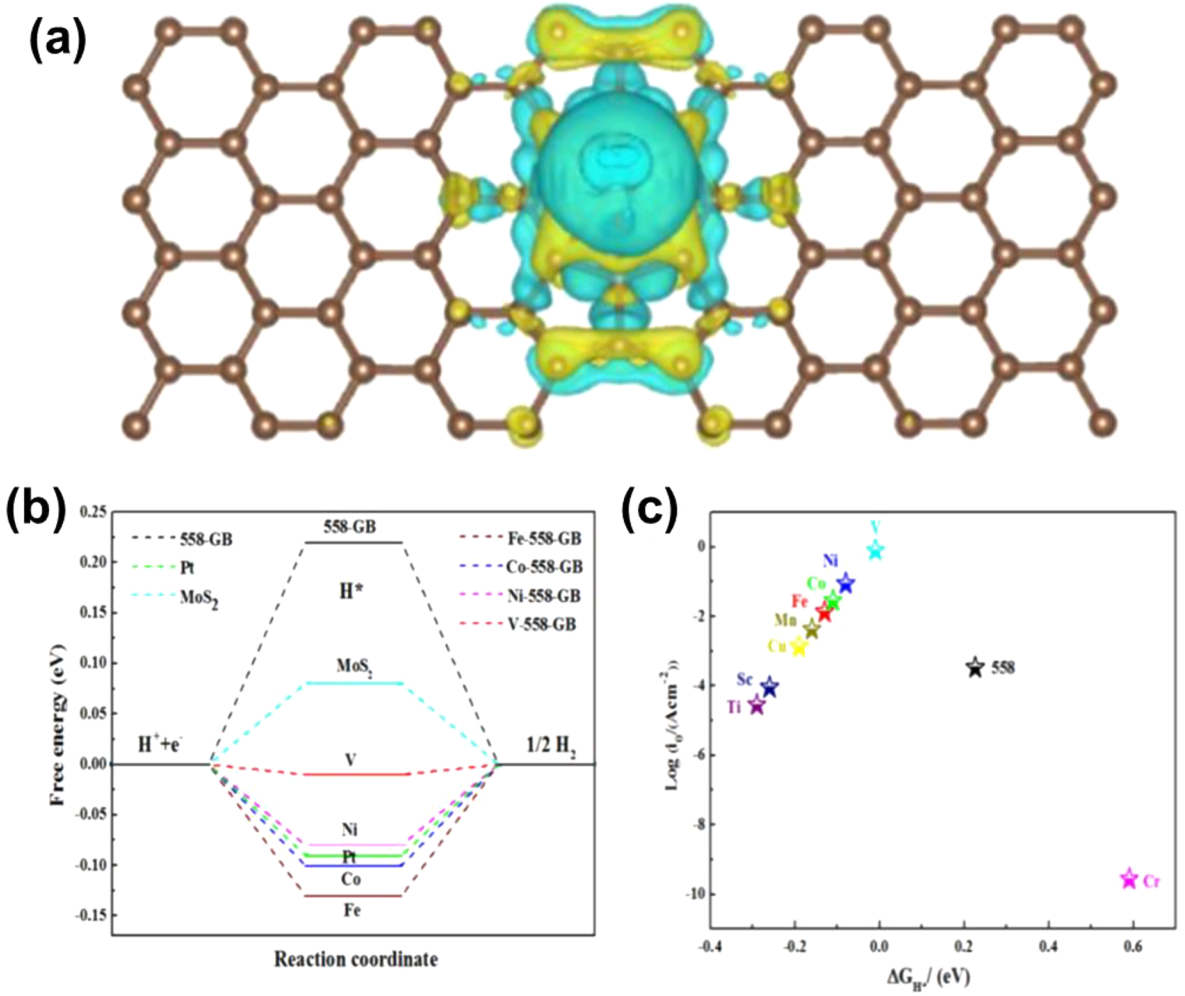

Figure 34. (a) Charge density difference plot for a single V atom anchored on octagon carbon ring. Yellow and cyan isosurface represents electron accumulation and electron depletion. (b) ΔG_H diagram of HER at the equilibrium potential for V supported on 558 grain boundaries, including Fe, Co, Ni, Pt, and MoS_2. (c) Volcano curve of exchange current density as a function of the Gibbs free energy of hydrogen adsorption for various metals atoms supported on the 558 grain boundary. Reproduced with permission from ref 214. Copyright 2018 Elsevier.

coordination environment and the substrate, which further determines the binding strength of *H and thereby the catalytic performance for HER.

As seen from the above discussion, whereas it is rather facile to tune the metal−substrate coordination to achieve desirable adsorption properties (i.e., minimizing $|\Delta G_{H^*}|$) for proton reduction, it has been challenging to optimize the single-atom active sites to facilitate both water dissociation and hydrogen recombination, namely the water reduction and HER in alkaline environment. The latter usually requires synergy between two types of active sites, as manifested in the case of Co_1/PCN (Figure 29). Inspired by this understanding, introduction of another or more atomically dispersed metals to the surroundings of the metal sites, forming bimetallic, dual-site SAECs, is anticipated to be an effective approach for fine-tuning the SAECs for water reduction. More mechanistic studies focusing on synergistic effects of adjacent active sites, and between the metal center and the substrate, can offer more insights into SAECs for enhanced HER activity in alkaline media.

As mentioned above in the discussion of catalyst preparation (section 2), the loading of metals remains quite low (ca. 1 wt % or less in most cases) in SAECs, which has limited the number density of active sites in electrocatalysts. Because catalyst stability is less a concern for the HER, as compared to ORR/OER, it is plausible to develop SAECs with high metal loadings for HER (Table 1). Such an increase of single-atom site density is crucial for improving the volume-specific activity of SAECs, a critical hurdle in the practical implementation of such cost-effective electrocatalysts to replace nanoparticulate Pt in water electrolyzers.

5. SINGLE-ATOM ELECTROCATALYSTS FOR OXYGEN EVOLUTION REACTION

Oxygen evolution reaction (OER), or water oxidation, is the counter reaction to the HER in water electrolyzers.[148,215−220] Because of the rather fast rate of HER, the overall system performance (power and energy efficiency) of water electrolyzers is mostly limited by the sluggish kinetics of the four-electron OER process.[221−224] The instability of OER electrocatalysts under the high-overpotential (typically >1.6 V vs RHE) in acidic or alkaline condition represents an even more severe issue of the durability of water electrolyzers, with only Ir-based low-surface area electrodes (e.g., dimensionally stable anode, DSA) implemented in commercial devices.

https://dx.doi.org/10.1021/acs.chemrev.0c00594
Chem. Rev. 2020, 120, 12217−12314

Table 1. Catalytic Performance of SAECs towards HER

catalysts	electrolyte	$-\eta_{10,HER}$ (mV)	TOF (s^{-1} at a specific overpotential)	mass activity (A g_{metal}^{-1} at a specific overpotential)	ref
Pt SASs/AG	0.5 M H_2SO_4	12		22400@0.05 V	171
Pt SAs/DG	0.5 M H_2SO_4	23		26200@0.05 V	170
Pt-GDY1	0.5 M H_2SO_4	>50		7260@0.1 V	173
Pt-GDY2	0.5 M H_2SO_4	>100		23640@0.1 V	173
Pt_1/OLC	0.5 M H_2SO_4	38	40.78@0.1 V	7400@0.038 V	174
Pt_1/graphene	0.5 M H_2SO_4	>50	17.67@0.1 V	2820@0.038 V	174
Pt-MoS_2	0.1 M H_2SO_4	~145			168
Co-MoS_2	0.1 M H_2SO_4	~185			168
Pt SA/m-WO_{3-x}	0.5 M H_2SO_4	~50	35@0.1 V	12800@0.05 V	178
Pt SA/C	0.5 M H_2SO_4	~90	14.58@0.1 V	6090@0.05 V	178
Pt/np-$Co_{0.85}Se$	0.5 M H_2SO_4	58		13570@0.1 V	179
Pt/np-$Co_{0.85}Se$	1.0 M KOH	58		1280@0.1 V	179
Pt/np-$Co_{0.85}Se$	1.0 M PBS	55	3.93@0.1 V	1320@0.1 V	179
PtSA-NT-NF	1.0 M PBS	24		70@0.05 V	180
Ru-NC	1 M KOH	12			167
Ru-NC	0.1 M KOH	47			167
Ru_{SA}–N–S-$Ti_3C_2T_x$	0.5 M H_2SO_4	76	0.52@0.1 V		153
SA-Ru-MoS_2	1.0 M KOH	76	12.83@0.3 V		189
Pd^0 /GDY	0.5 M H_2SO_4	55	16.7@0.1 V	61500@0.2 V	193
Ir_1@Co/NC	1.0 M KOH	60			194
Fe/GD	0.5 M H_2SO_4	66	4.15@0.1 V	80000@0.2 V	197
Ni/GD	0.5 M H_2SO_4	88	1.59@0.1 V	16600@0.2 V	197
Fe–N_4 SAs/NPC	1.0 M KOH	202			196
Co_1/PCN	1.0 M KOH	89	5.98@0.1 V		134
Co_1/PCN	0.5 M H_2SO_4	151			134
Co_1/CN	1.0 M KOH	138			134
Co_1/CN	0.5 M H_2SO_4	278			134
Co-NG	0.5 M H_2SO_4	>150	1.189@0.2 V		16
Co-NG	1.0 M NaOH	>250			16
SA Co-D 1T MoS_2	0.5 M H_2SO_4	42	7.82@0.1 V		147
CoSAs/PTF-600	0.5 M H_2SO_4	94		2717@0.1 V	208
Ni-doped np-G	0.5 M H_2SO_4	50	0.8@0.3 V		206
A-Ni@DG	0.5 M H_2SO_4	70	5.7@0.1 V		59
MCM@MoS_2–Ni	0.5 M H_2SO_4	161			207
Ni/β-Mo_2C	1.0 M KOH	157			205
Mo–Co_9S_8@C	0.5 M H_2SO_4	98			190
$Mo_1N_1C_2$	0.1 M KOH	132	1.46@0.15 V		212
$Mo_1N_1C_2$	0.5 M H_2SO_4	154	2.59@0.2 V		212
$W_1N_1C_3$	0.1 M KOH	85	6.35@0.12 V		213
$W_1N_1C_3$	0.5 M H_2SO_4	105	~4@0.12 V		213

Generally, the OER process involves the sequential formation of OH*, O*, and OOH* intermediates. In alkaline media, the process follows these steps:

$$4OH^- \rightarrow OH^* + 3OH^- + e^- \quad (9)$$

$$OH^* + 3OH^- + e^- \rightarrow O^* + H_2O + 2OH^- + 2e^- \quad (10)$$

$$O^* + H_2O + 2OH^- + 2e^- \rightarrow OOH^* + H_2O + OH^- + 3e^- \quad (11)$$

$$OOH^* + H_2O + OH^- + 3e^- \rightarrow O_2 + 2H_2O + 4e^- \quad (12)$$

where * denotes an adsorption site on the electrocatalyst surface. In acid, a similar process occurs:

$$2H_2O \rightarrow OH^* + H_2O + H^+ + e^- \quad (13)$$

$$OH^* + H_2O + H^+ + e^- \rightarrow O^* + H_2O + 2H^+ + 2e^- \quad (14)$$

$$O^* + H_2O + 2H^+ + 2e^- \rightarrow OOH^* + 3H^+ + 3e^- \quad (15)$$

$$OOH^* + 3H^+ + 3e^- \rightarrow O_2 + 4H^+ + 4e^- \quad (16)$$

According to the Sabatier's principle, the adsorbates should bind to the catalyst surface neither too strongly nor too weakly to achieve high activity. Because of the difficulties in directly measuring the binding strength of the intermediates, adsorption energies of oxygenated species have commonly been computed as descriptors to understand and predict the activity trend of OER electrocatalysts.[223,224] Ideally, to reach a minimum overpotential, all of the four steps should have an equivalent free energy change of 1.23 V at the equilibrium potential (Figure 35a). However, because both OH* and OOH* species adsorb on the catalyst surface through a single oxygen bond, the binding energies of OH* and OOH* are linearly correlated (Figure 35b). As a result, the difference in adsorption energy between OH* and OOH* is a constant value of 3.2 eV. This so-called scaling relationship indicates

https://dx.doi.org/10.1021/acs.chemrev.0c00594
Chem. Rev. 2020, 120, 12217−12314

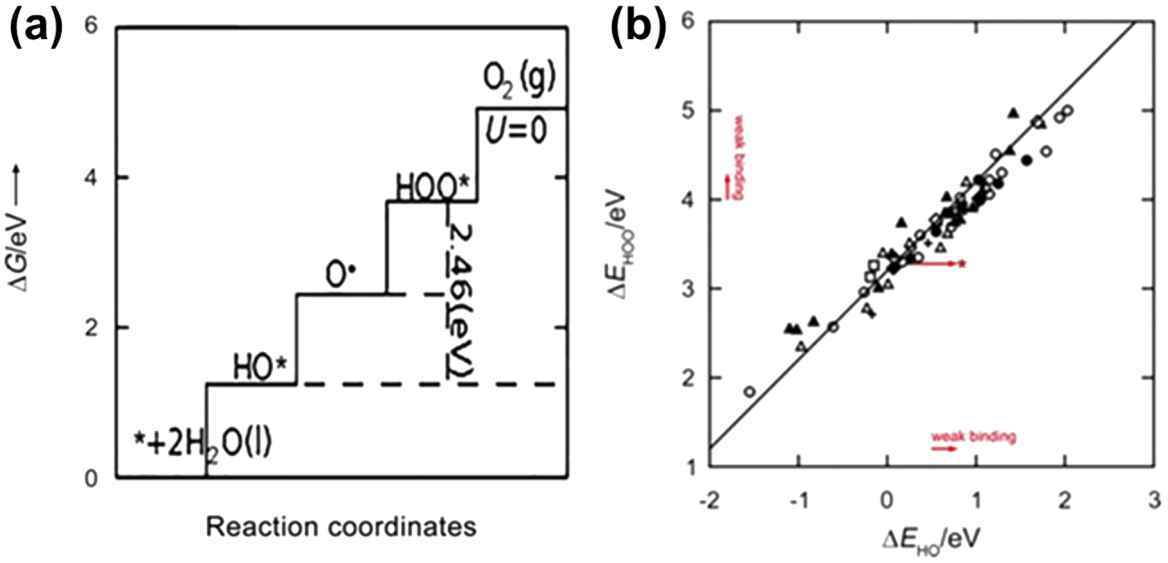

Figure 35. (a) Standard free energies at $U = 0$ for the ideal catalyst. (b) Adsorption energy of HOO* plotted against the adsorption energy of HO* on perovskites, rutiles, anatase, Mn_xO_y, Co_3O_4, and NiO oxides. Hollow symbols represent the adsorption energy on the clean surfaces: perovskites (○), rutiles (△), Mn_xO_y (□), anatase (◇), and Co_3O_4 (+), NiO. Solid symbols represent the adsorption energies on high coverage surfaces, with oxygen atoms representing the nearest neighbors. Reproduced with permission from ref 224. Copyright 2011 John Wiley and Sons.

that there is only one free parameter that can determine the free energy diagram of OER pathway, giving rise to a universal volcano trend for the OER activity as a function of $\Delta G_{O^*} - \Delta G_{OH^*}$. At the apex, a theoretical minimum overpotential of (3.2−2.46 eV)/2 = 0.37 eV is needed to drive the reaction. On the left side of the volcano, the formation of OOH* species limits the reaction kinetics because the surface binds oxygen too strongly. On the other side, the formation of OH* is the rate-determining step due to weak binding of oxygen. To maximize the OER activity, electrocatalysts with intermediate binding strengths and $\Delta G_{O^*} - \Delta G_{OH^*} = 1.6$ eV are desired. In addition to the binding strength of oxygenated intermediates, e_g electron number has also been used as the descriptor for perovskite-based OER electrocatalysts, considering the direct involvement of the e_g orbital in forming σ-bonding with the surface adsorbates.[225] It is suggested that perovskites with an e_g value of ∼1.2 are the most active for OER. With a larger e_g value, the formation of OOH* is rate-limiting, because the binding of reaction intermediates is too strong. On the contrary, catalysts with a smaller e_g value binds oxygenated species too weakly, leading to a large energy barrier for OH* formation. Experimental results have successfully validated the prediction on various perovskites, where $Ba_{0.5}Sr_{0.5}Co_{0.8}Fe_{0.2}O_{3-\delta}$ with $e_g = 1.3$ showed the highest OER activity. However, it was reported later on that a series of $LaBO_3$ (B = Mn, Co, Ni, or $Ni_{0.75}Fe_{0.25}$) perovskites with a similar e_g of −1.0 have quite differential OER activities.[226,227]

More recently, it has been shown that the OER performance of transitional metal oxides is dependent on the covalency of the metal−oxygen bonds.[228−233] As the overlap between metal 3*d* and oxygen 2*p* orbitals increases, ligand holes emerge at the Fermi level, leading to the release of oxygen to form oxygen vacancies (Figure 36).[228,229,234] With the participation of lattice oxygen, a new reaction pathway can be triggered via the so-called lattice oxygen-mediated mechanism (LOM). For the first three steps, both LOM and the traditional adsorbate evolution mechanism (AEM) underwent analogous processes. Unlike AEM, lattice oxygen evolves in the formation of O−O

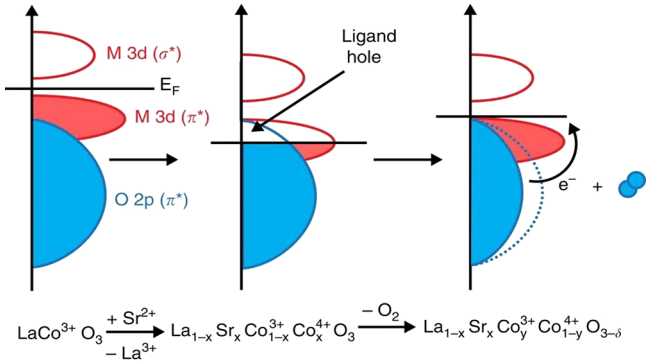

Figure 36. Relationship between oxygen vacancy concentration and Co−O bond covalency. Reproduced with permission from ref 229. Copyright 2016 Nature Publishing Group.

bond in the LOM (Figure 37). This reaction pathway was later on validated by ^{18}O isotopically labeled measurements.[229] The oxides that follow the LOM mechanism exhibit pH-dependent OER activities.[229]

Over the years, numerous OER catalysts have been reported, including metal oxides,[174,176,235,236] (oxy)hydroxides,[179,237,238] sulfides,[239,240] senides,[240,241] perovskites,[225,228,231,233,242,243] and molecular complexes.[244−246] SAECs are promising alternatives with well-defined structures and unique electronic properties. The metal−support interaction could effectively govern the binding energies of intermediates to the metal center for an optimal activity. To compare their catalytic performance, the overpotential for a specific current density (usually 10 mA cm^{-2}) is the most commonly used standard ($\eta_{10,\ OER}$). It should be pointed out that, for practical applications, much higher current densities (e.g., 100−500 mA cm^{-2}) are desired, requiring that the electrocatalysts not only have a low $\eta_{10,\ OER}$ but also exhibit a small Tafel slope.

5.1. Precious Metal-based Single-Atom Electrocatalysts

Generally, Ir and Ru are the most active OER catalysts. Because of their scarcity and high costs, downsizing the noble

https://dx.doi.org/10.1021/acs.chemrev.0c00594
Chem. Rev. 2020, 120, 12217−12314

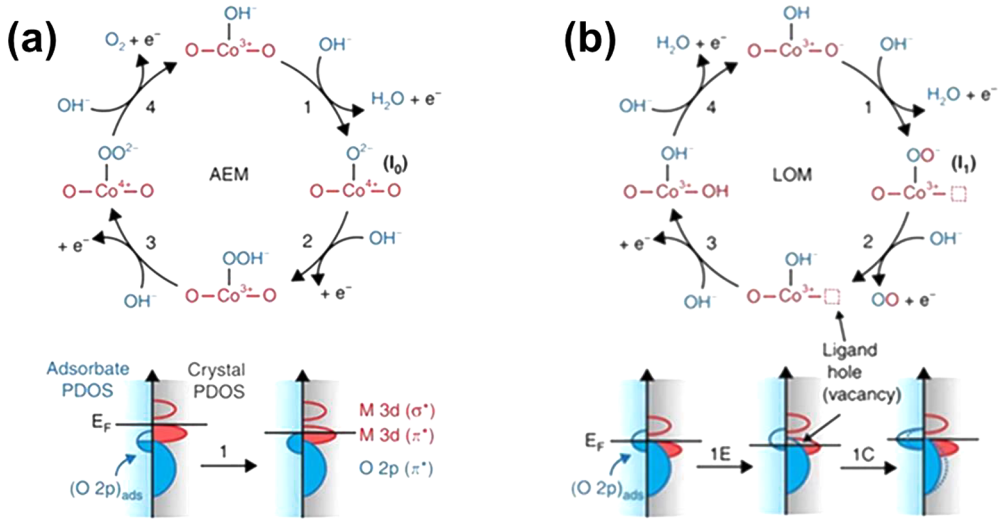

Figure 37. (a) AEM. In the AEM, the transition metal 3*d* bands are significantly higher in energy than the O 2p band in the lattice, as shown qualitatively in the PDOS diagram below the mechanism. Because of this, all intermediates during the reaction originate from the electrolyte and Co in the active site undergoes the catalytic redox reactions. This allows Co to access a higher oxidation state of Co^{4+} in step 1 (b) LOM. As the covalency of the material increases, the transition metal 3*d* bands are lowered into the O 2p band in the lattice, where the Fermi energy is pinned at the top of the O 2p band through generation of oxygen vacancies. For both (a,b), lattice species are shown in red and electrolyte species are shown in blue. In the PDOS diagrams, the electrolyte species are shown to the left of the energy axis and the crystal PDOS are shown to the right. Reproduced with permission from ref 229. Copyright 2016 Nature Publishing Group.

metal nanoparticles into single atoms is a possible strategy for reducing their content in OER electrocatalysts. Because the stability also reduces as the particle size decreases, it is more common to use Ir- and Ru-based SAECs for the OER in alkaline media, where the electrochemical condition is less harsh than that in acid electrolytes.

Zhang et al. incorporated atomic Ir into defect-rich cobalt hydroxides to improve the OER activity.[247] The atomically dispersed Ir species provided abundant active sites for the formation of Co−Ir species. By tuning the concentration of Ir species, CoIr-0.2 exhibited a higher OER activity than other CoIr-*x* (x = 0, 0.5, and 1) samples and IrO_2 in both 1.0 M phosphatic buffer solution and 1.0 M KOH. Characterizations after the OER test revealed that Ir species were oxidized to higher valence state, and atomic dispersion was maintained during the electrochemical oxidation process. Besides, the oxidation process drove the transformation of α-$Co(OH)_2$ substrate to unsaturated CoOOH (Figure 38). The high-valence Ir and unsaturated Co sites cooperatively facilitated the adsorption of reaction intermediates and accelerated the OER process.

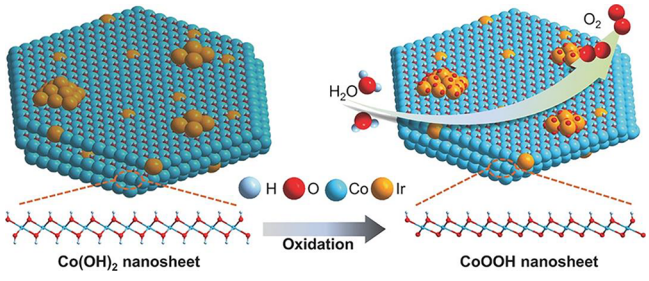

Figure 38. Mechanism diagram of OER on the CoIr-0.2 sample surface and the transformation of α-$Co(OH)_2$ to β-CoOOH phase. Reproduced with permission from ref 247. Copyright 2018 John Wiley and Sons.

Wang et al. introduced atomic Ir and Ru species into self-supported NiV layered double hydroxide (LDH) to accelerate OER kinetics.[248] A one-pot hydrothermal method was used to selectively incorporate Ir and Ru into V sites. Synergistic interactions were also found among Ni, V, and Ir (or Ru) cations. An isomorphic substitution of V by Ir (or Ru) caused possible lattice distortion and V vacancies, modulating the local coordination environments of Ni and V cations. As Ir doping accelerates the M−OH and M−O process, while Ru doping is beneficial to the M−OOH process, the OER activities of both NiVIr-LDH and NiVRu-LDH were improved, relative to NiV-LDH (Figure 39). For NiVIr-LDH with an Ir loading of 0.62 at %, only an overpotential ($\eta_{10,OER}$) of 180 mV was required to reach 10 mA cm^{-2}. After 2000 CV scans, NiVIr-LDH sustained its performance and showed long-term stability for 600 h at 50 mA cm^{-2} and 400 h at 200 mA cm^{-2}.

Li et al. further investigated the interplay between atomic Ru and binary LDHs.[249] The coupling between atomic Ru and LDHs not only improves OER but also reduces the dissolution of Ru. Ru atoms attract d-electrons from M (M = Fe, Co, Ni) via the Ru−O−M bonds, leading to a lower valence state of Ru and coupling effect between Ru and LDHs. Transitional metal LDHs with smaller electronegativity, such as CoFe, provide stronger electronic coupling than NiFe and NiCo with Ru, while main group metal ions without d-electrons, such as Mg^{2+} and Al^{3+}, hardly have coupling effect. In addition, the electron transfer from Co and Fe to Ru also narrowed down the bandgap between the valence and conduction bands of Ru/CoFe-LDHs than that of CoFe-LDHs, improving the conductivity. As a result, Ru/CoFe-LDHs showed better OER activity than atomic Ru on other binary LDHs with an ultralow $\eta_{10,OER}$ of 198 mV (Figure 40a). DFT + *U* calculations demonstrated that the monatomic Ru sites lowered the energy barrier of the rate-determining step for the formation of *OOH from O* by optimizing OOH* adsorption with the assistance of LDH substrate, thus facilitating the OER kinetics

https://dx.doi.org/10.1021/acs.chemrev.0c00594
Chem. Rev. 2020, 120, 12217−12314

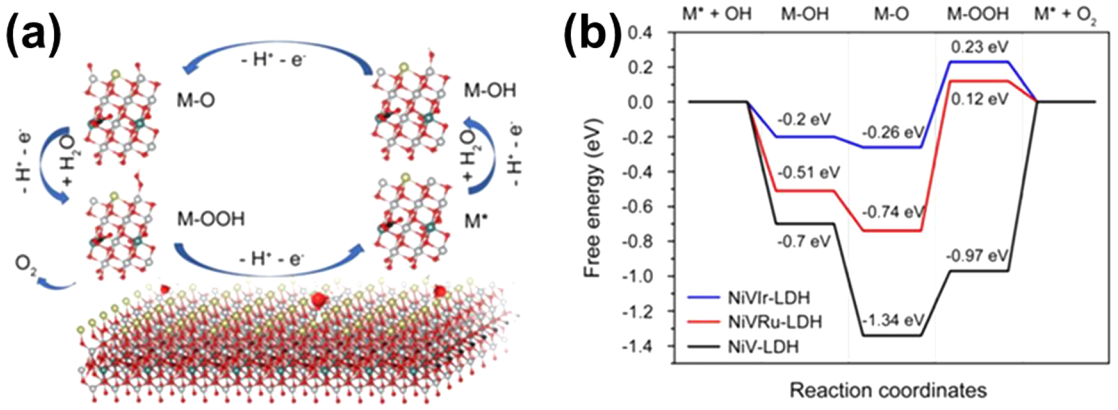

Figure 39. (a) Atomic model of NiVIr-LDH and proposed OER pathway. (b) Free energy diagram of OER on the NiV-LDH, NiVRu-LDH, and NiVIr-LDH catalysts. Reproduced with permission from ref 248. Copyright 2019 Nature Publishing Group.

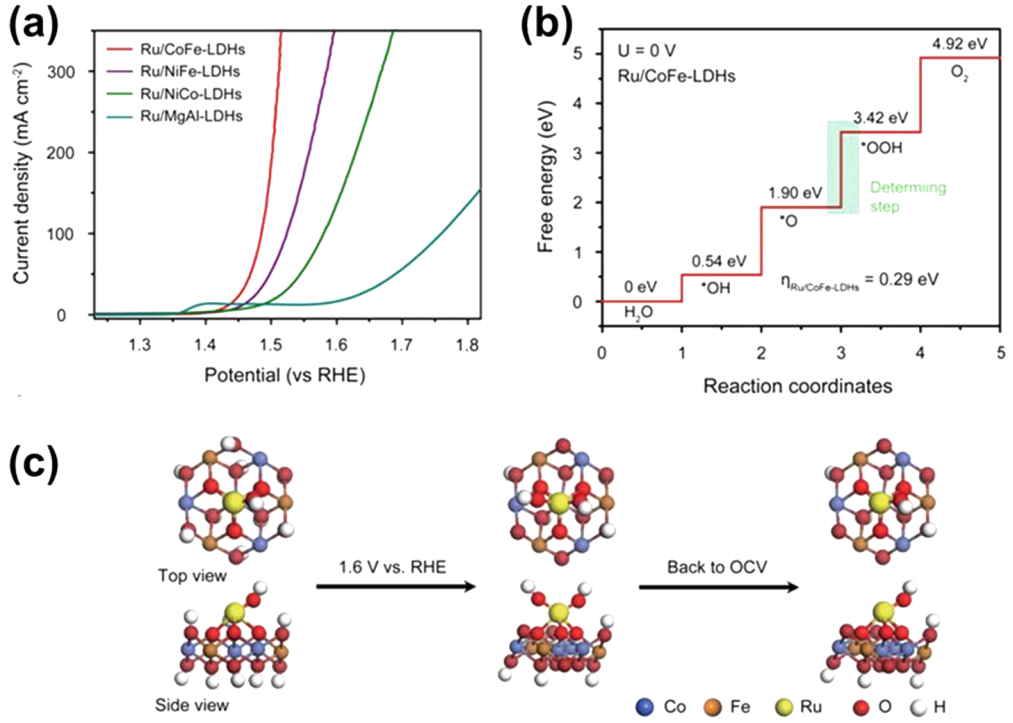

Figure 40. (a) iR-compensated polarization curves of Ru/CoFe-LDHs, Ru/NiFe-LDHs, Ru/NiCo-LDHs, and Ru/MgAl-LDHs. (b) Gibbs free-energy diagram for the four steps of OER on Ru/CoFe-LDHs. The green box step is the rate-determining step, and η stands for overpotential. (c) Schematic illustration of Ru/CoFe-LDHs catalyst during OER. OCV represents open-circuit voltage. Reproduced with permission from ref 249. Copyright 2019 Nature Publishing Group.

(Figure 40b). Operando XAS and in situ EXAFS measurements probed the reversibility of Ru and irreversibility of Fe and Co in valent state and local structure, identifying Ru as the active site. The bond lengths of Co−O, Co−O−Fe, Co−O−Co, Co−O−Ru, Fe−O, Fe−O−Co, and Fe−O−Ru irreversibly shrinks at the potential of 1.6 V, consequently fixing Ru and preventing it from dissolution (Figure 40c).

Except for the highly active Ir and Ru SAECs, single Pt atoms can remarkably improve the OER activity of $CoSe_{2-x}$, despite the fact that Pt is generally inactive toward OER.[250] Single Pt atoms were trapped by selenium vacancies on the $CoSe_{2-x}$ substrate to form atomically coordinated Pt−Co−Se moieties. The Pt loading amount can be as high as 2.25 wt % via a plasma photochemical method. Electrons redistributed from Co and Pt to selenium vacancies and intermediates, due to the difference in electronegativity. Because of the higher electronegativity of Pt (2.28) than that of Ru (2.20) and Ni (1.91), Pt induces a higher degree of electron distribution asymmetry, leading to an appropriate adsorption energy of OH* and OOH*. Therefore, $CoSe_{2-x}$−Pt processes the lowest $\eta_{10,OER}$ of 255 mV, much lower than those of $CoSe_{2-x}$, $CoSe_{2-x}$−Ru, and $CoSe_{2-x}$−Ni.

Au single atoms were also found to activate the OER performance of NiFe LDH (^{s}Au/NiFe LDH).[198] Although the activity was mainly attributed to the Fe sites on LDH, atomic Au induced the charge redistribution of active Fe sites by electron transfer (Figure 41). DFT calculations demonstrated that the energy barrier of the rate-limiting step from *O to *OOH was lowered with Au decoration, in accordance with

https://dx.doi.org/10.1021/acs.chemrev.0c00594
Chem. Rev. 2020, 120, 12217−12314

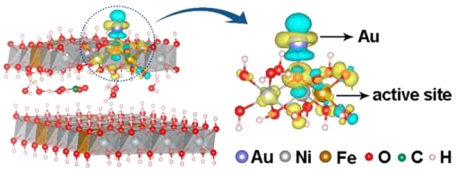

Figure 41. Differential charge densities of NiFe LDH with and without Au atom when one O atom is adsorbed on the Fe site. Isosurface value is 0.004 eÅ^{-3}. Yellow and blue contours represent electron accumulation and depletion, respectively. Reproduced with permission from ref 198. Copyright 2018 American Chemical Society.

the decreased $\eta_{10,OER}$ from 263 mV for NiFe LDH to 237 mV for ^{s}Au/NiFe LDH.

From the above discussion, we can see that precious metal single atoms to modify the transition metal (hydro)oxide electrocatalysts have been used extensively to improve the OER activity in alkaline media. For the OER in acid, coordinated metal single atoms usually do not have sufficient stability, although Ru−N−C SAEC has been reported for the OER with single-atom Ru sites believed to be stabilized by the strong Ru−N bonding.[251] More attention has been paid to diluted surface alloys for the OER in acid. Yao et al. suppressed the dissolution of Ru by embedding atomic Ru on a series of $PtCu_x/Pt_{skin}$ core−shell nanostructures and achieved enhanced OER kinetics via compressive strain in acidic media.[252] Among Ru_1−$PtCu_3$, Ru_1−PtCu, and Ru_1−Pt_3Cu, Ru_1−Pt_3Cu required the lowest $\eta_{10,OER}$ of 220 mV and exhibited enhanced durability, as compared to RuO_2 in 0.1 M $HClO_4$. The enhanced stability of the SAECs was ascribed to the island-like alloy surface that offers defect sites to anchor dispersed Ru atoms. It was argued that the Ru single atoms embedded in the Pt lattice were stabilized via charge compensation from the Pt−Cu core.

5.2. Non-noble Metal-based Single-Atom Electrocatalysts

Besides precious metal SAECs, PGM-free electrocatalysts with single transition metal (Fe, Co, Ni, etc.) atoms coordinated on carbon-based substrates have also been reported for the OER. Modulation of the coordination environment via defect engineering or heteroatomic doping of the substrate has been commonly adopted to modify the adsorption properties of the single-atom active sites, in order to improve their activity.

Zhang et al. anchored atomic Ni (denoted as aNi in their report) with square-planar coordination onto highly defective graphene, achieving a high loading of stabilized single atoms.[59] They investigated three types of Ni-carbon coodination on Divacancy, D5575, and ordered hexagons. aNi@Divacancy showed the lowest density of state (DOSs) near the Fermi level, endowing a desirable adsorption energy of reaction intermediates and giving rise to high OER activity. Zhang et al. compared the OER performance of isolated Ni atoms on hollow carbon matrix with square-planar Ni−C_4 (HCM@Ni) and Ni−N_4 (HCM@Ni−N) coordination.[253] In both alkaline and acidic electrolytes, HCM@Ni−N showed the highest activity with an $\eta_{10,OER}$ of 304 mV. The doping of Ni atom gave rise to charge redistribution of HCM@Ni−N, increasing the covalency between Ni−N bonds. DFT calculations revealed that the Ni−N_4 bonding lowered the electron density near the Fermi level relative to Ni−C_4, reducing the adsorption energy of intermediates (Figure 42a). For pristine HCM, HCM@N and HCM@Ni, the energy barrier of the rate-determining step from OOH* to O_2* was 4.14, 3.6, and 2.36 eV, respectively, while that of HCM@Ni−N was as low as 1.83 eV from OH* to O*(Figure 42b). They further utilized the shielding effect of SCN^- ions to block the activity of Ni sites. The derived HCM@Ni−N showed an overpotential 44 mV lower than HCM@N without Ni at 20 mA cm^{-2}, indicating the vital contribution from Ni−N coordination to the OER activity in acid electrolyte.

Su et al. constructed an atomic cobalt with pyridinic- and amino-N coordination (HNC-Co).[142] Operando synchrotron radiation Fourier transform infrared spectroscopy (SR-FTIR) detected the presence of H_2N-(*O−Co)-N_4, indicating the generation of O* intermediates during OER and verifying the four-step OER process (Figure 43a). The hetero−N−Co bonding strengthened the $2p$−$3d$ hybridization between surface oxo-species and Co active centers, as indicated by the higher density of states near the Fermi level (Figure 43b). As a result, the adsorption energy of H_2O for HNC−Co decreased by ∼0.5 eV, compared to pure carbon paper, thus lowering the energy barrier for the rate-determining formation of *O to 0.36 eV (Figure 43c).

The square-planar M−N_4 (M = metal) configuration have also been reported to be a highly active center toward OER for other $3d$ metals, such as Fe and Mn. Whereas iron-based (oxy)hydroxides are intrinsically less active than Ni- and Co-

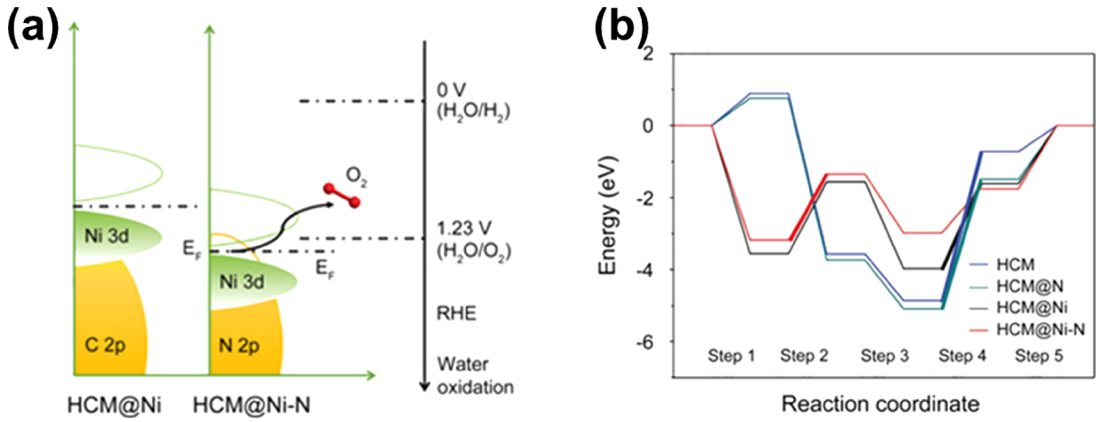

Figure 42. (a) Schematic band diagrams of HCM@Ni and HCM@Ni−N. (b) Free energy diagram at 0 V for OER over HCM, HCM@N, HCM@Ni, and HCM@Ni−N. Reproduced with permission from ref 253. Copyright 2019 John Wiley and Sons.

https://dx.doi.org/10.1021/acs.chemrev.0c00594
Chem. Rev. 2020, 120, 12217−12314

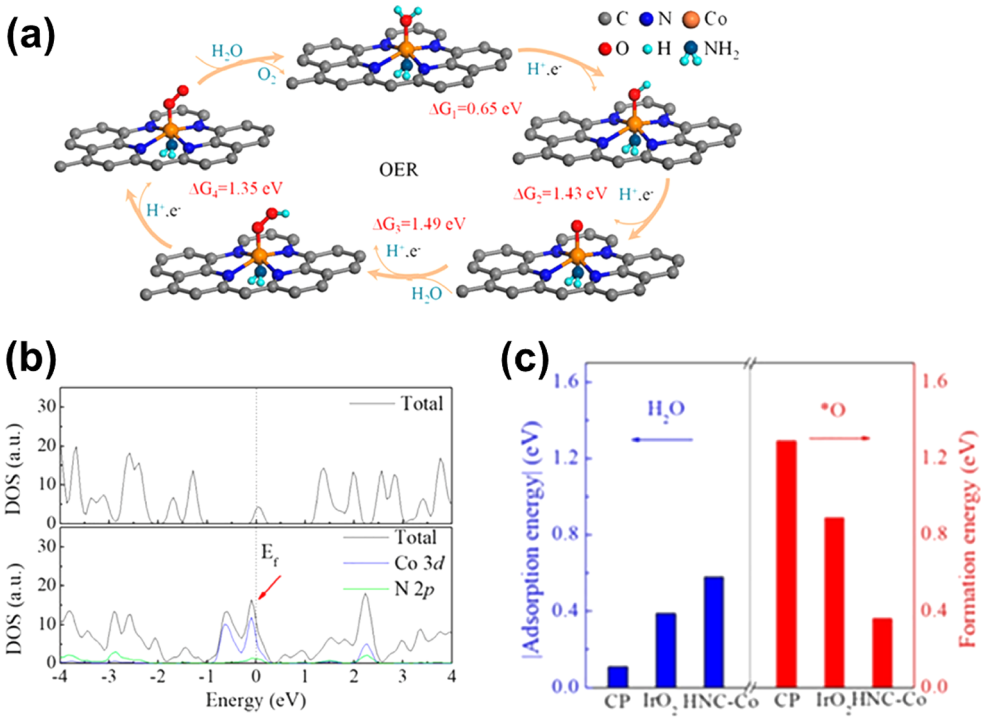

Figure 43. (a) Diagram of $4e^-$ oxygen evolution mechanism for HNC−Co in acidic solution. (b) Calculated density of states (DOS). (c) adsorption energy of H_2O and formation energy of *O intermediates for CP, IrO_2 and HNC−Co. Reproduced with permission from ref 142. Copyright 2019 American Chemical Society.

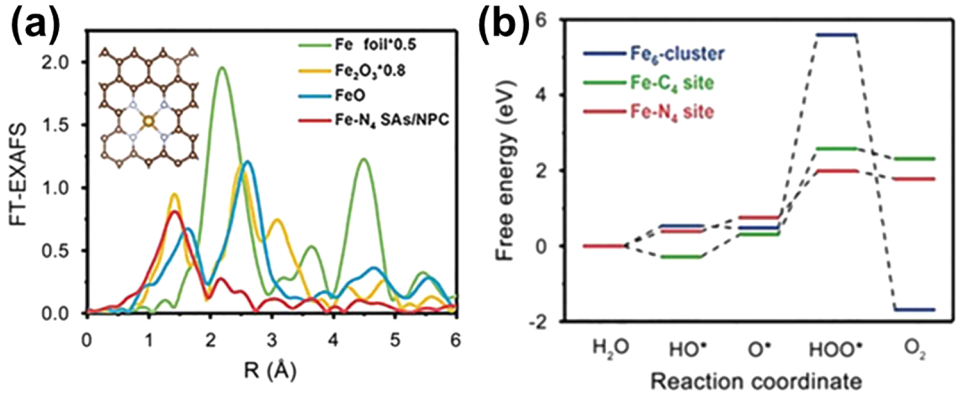

Figure 44. (a) FT EXAFS spectra at R space (inset: Fe atomic structure model, C (golden), N (silvery), and Fe (orange)). (b) Free energy diagrams for OER. Reproduced with permission from ref 196. Copyright 2018 John Wiley and Sons.

based counterparts for the OER, due to their poor conductivity, atomically dispersed iron, together with its coordination environment, has been demonstrated to be highly active for the OER. Pan et al. synthesized Fe−N_4 motifs on N-doped porous carbon (FeN_4 SAs/NPC) (Figure 44a).[196] Compared to Fe−C_4 and Fe_6−cluster, the Fe−N_4 configuration had the lowest $\eta_{10,OER}$ of 0.43 V, owing to the low free energy barrier for the rate-determining step from O* to OOH* (Figure 44b). Lei et al. embedded a mononuclear Fe−N_4 on carbon nanofiber supported on electrochemically exfoliated graphene (FeN_4/NF/EG).[254] Fe−N_4 was identified as the active site via a KSCN poisoning method. They further explored the role that the type and coordination number of nitrogen played in determining the OER activity. The type of coordinated N could greatly affect the OER performance, because graphitic N and pyridinic N are responsible for conductivity and activity, respectively. As the pyrolysis temperature increases, the proportion of graphitic N increases, while that of pyrrolic and pyridinic N decreases. FeN_4/NF/EG pyrolyzed at 900 °C showed the lowest $\eta_{10,OER}$ of 294 mV in 0.5 M H_2SO_4 with an optimum ratio of graphitic N to pyridinic N. Fe−N, Fe−N_2, Fe−N_3, and Fe−N_4 models were also built to calculate their structural stability and OER overpotentials (Figure 45). The charge transfer from Fe to neighboring N was the most suitable on Fe−N_4 for a minimum overpotential of 1.03 V.

Manganese was not expected to be active for OER, due to the sluggish kinetics of hexa-coordinated Mn in OER pathways. Inspired by the oxygen-evolving complex $CaMn_4O_5$ in natural photosystem II, Guan et al. introduced a tetra-coordinated Mn catalytic site on nitrogen-doped graphene (Mn-NG).[255] Mn-NG showed a TOF as high as 214 s^{-1} and an $\eta_{10,OER}$ as low as 337 mV toward water oxidation. According to CV experiments, the Mn−N_4

https://dx.doi.org/10.1021/acs.chemrev.0c00594
Chem. Rev. 2020, 120, 12217−12314

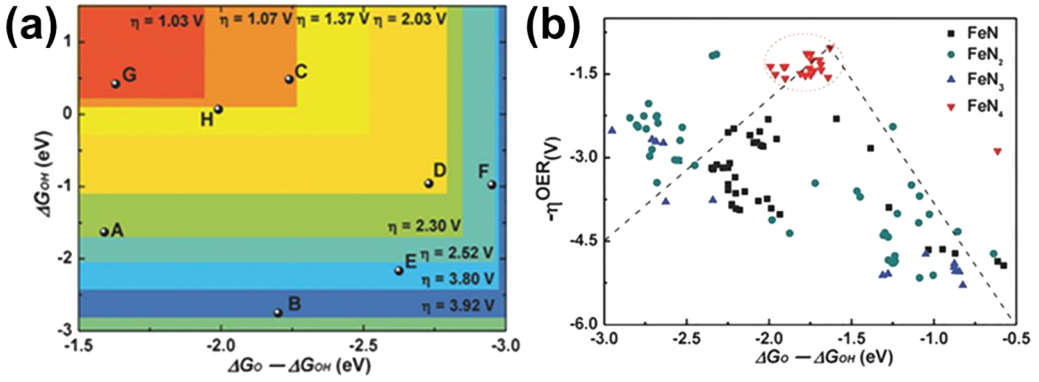

Figure 45. (a) Schematic OER volcano plot of overpotential η versus difference between the adsorption free energy of O* and OH* for Fe−N, Fe−N_2, Fe−N_3, and Fe−N_4 models. A, B, C, D, E, F, G, and H represent Fe−N codoped armchaired nanoribbon, Fe−N codoped zigzag nanoribbon, Fe−N_2-doped armchaired nanoribbon, Fe−N_2-doped zigzag nanoribbon, Fe−N_3-doped armchaired nanoribbon, Fe−N_3-doped zigzag nanoribbon, Fe−N_4-doped armchaired nanoribbon, and Fe−N_4-doped zigzag nanoribbon, respectively. (b) Schematic free energy profile of OH* versus difference between the adsorption free energy of O* and OH* for Fe−N_4 in acid. Reproduced with permission from ref 254. Copyright 2018 John Wiley and Sons.

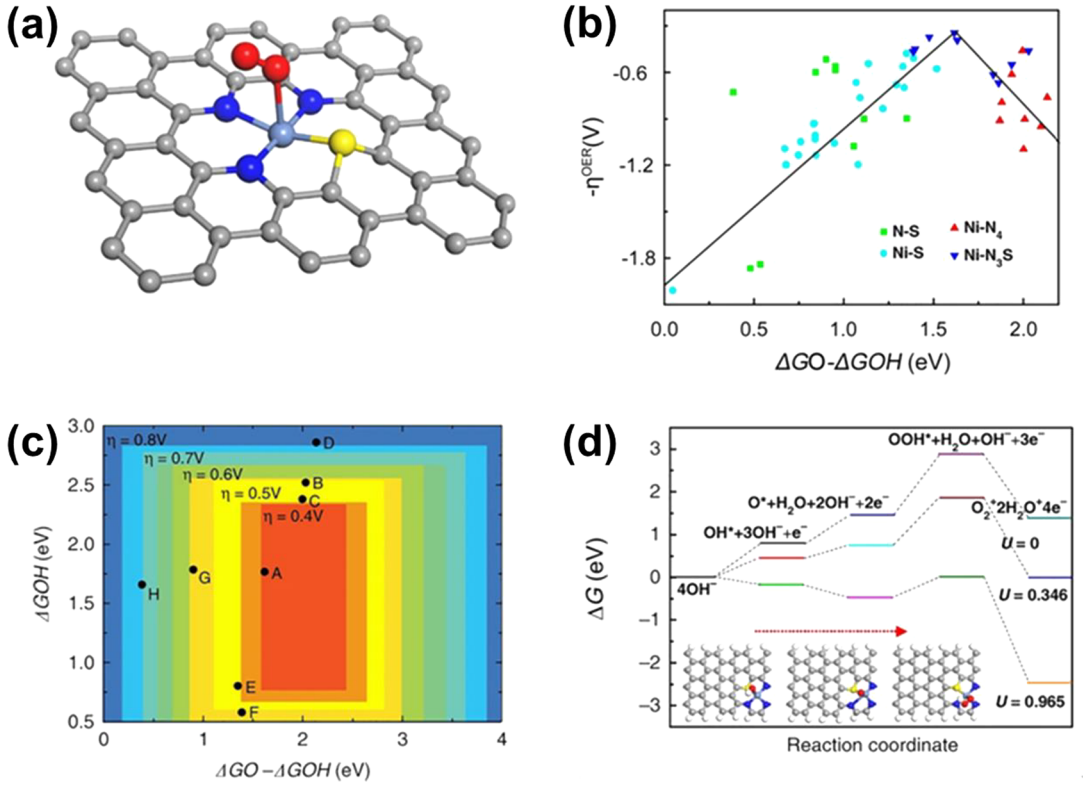

Figure 46. (a) Schematic structural model for S|NiN_x-PC. The steel blue, blue, yellow, gray, and red spheres represent Ni, N, S, C, and O atoms, respectively. (b) OER volcano plot of the overpotential η vs the difference between the adsorption free energy of O* and OH* for the N−S, Ni−S, Ni−N_4, and Ni−N_3S models. (c) Adsorption free energy of OH* vs the difference between the adsorption free energy of O* and OH* for the N−S, Ni−S, Ni−N_4, and Ni−N_3S models. (d) Schematic free-energy profile for the OER pathway on the Ni−N_3S model in alkaline media.. Reproduced with permission from ref 70. Copyright 2019 Nature Publishing Group.

coordination is favorable for the formation of high-valence Mn sites at lower potentials, relative to Mn-G. The energy barrier from Mn^{iv}-oxo to Mn^{iii}-OOH was markedly decreased, thus facilitating the OER process.

Apart from nitrogen doping, the electronic structure of the metal can be further tuned by codoping. Hou et al. isolated atomic Ni onto N and S codoped porous carbon (PC) nanosheets (S|NiN_x-PC) (Figure 46a).[70] The S|NiN_x species were determined to be the active sites by cyanide poisoning experiments. The substitution of one N with one S atom distorted the square planar D_{4h} symmetry of Ni−N_4, shortening the Ni−N bond length. In theoretical calculations, Ni−N_4-, Ni−N_3S-, Ni−N_2S_2-, and Ni-NS_3-doped graphene structures were constructed, among which Ni−N_4 and Ni−N_3S were most thermally stable. Moreover, the S atom and some C atoms in the Ni−N_3S model acted as the active sites and showed a higher energy barrier during the OER pathway than Ni sites, confirming Ni as the favorable OER site. In comparison with Ni−N_4, the S atom in Ni−N_3S acted as an electron donor and reduced the electron transfer from Ni to

https://dx.doi.org/10.1021/acs.chemrev.0c00594
Chem. Rev. 2020, 120, 12217−12314

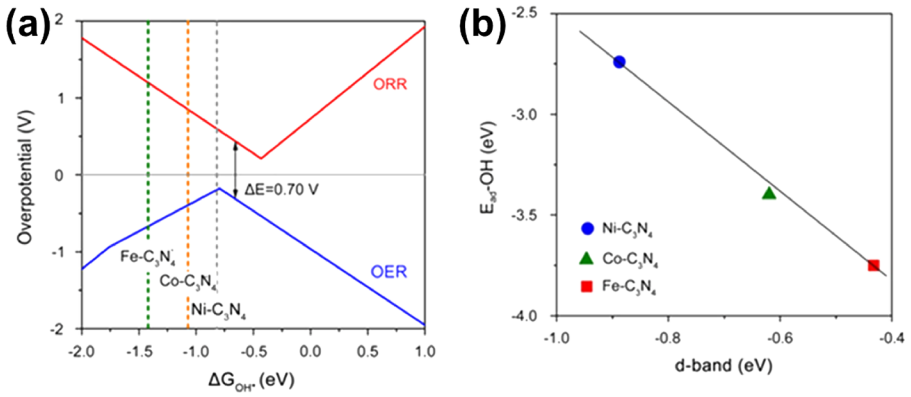

Figure 47. (a) Volcano plot for OER on M-C_3N_4 models. (b) Dependence of E_{ad}-OH* with the *d*-band position on M−C_3N_4 models. Reproduced with permission from ref 257. Copyright 2017 American Chemical Society.

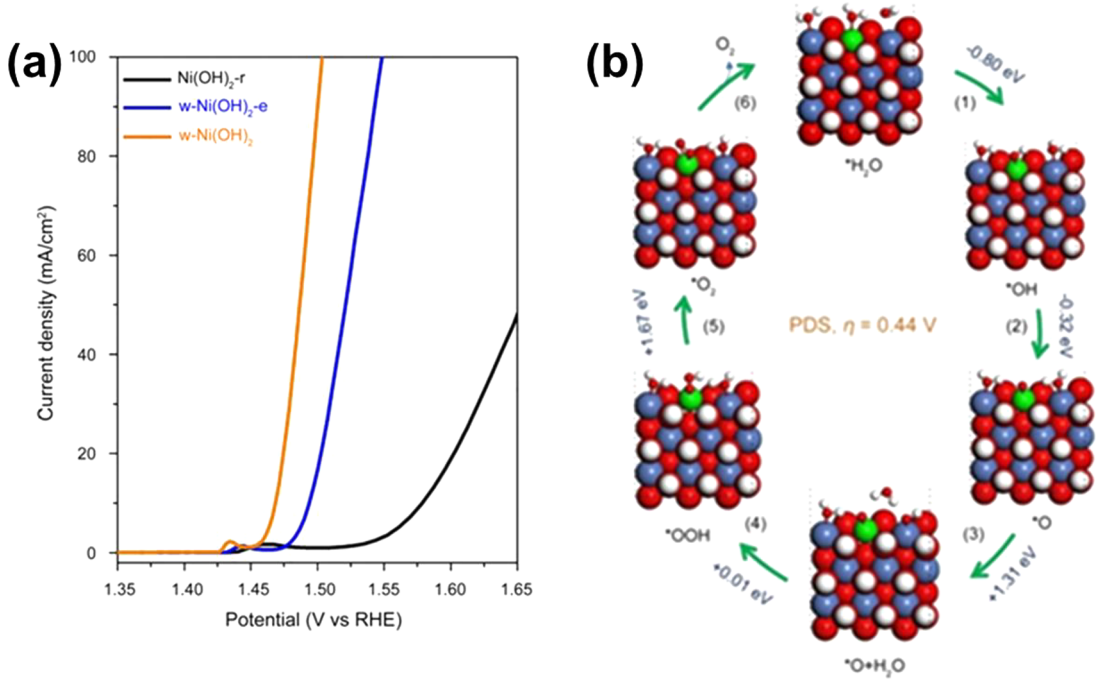

Figure 48. (a) 95% iR-corrected polarization curves of reference $Ni(OH)_2$-r, w-$Ni(OH)_2$-e, and w-$Ni(OH)_2$ samples. (b) Mechanism of OER on W-doped $Ni(OH)_2$, in which red, white, green, and blue atoms represent the oxygen, hydrogen, nickel, and tungsten atoms, respectively. Note that the symbols of "+" and "−" represent endothermic and exothermic free energy. For the step from state (6) to state (1), 1.0 eV endothermic free energy value was required for the sample, where the free energy change is not shown above. Reproduced with permission from ref 259. Copyright 2020 John Wiley and Sons.

neighboring N. Thus, the hybridization between Ni and coordinated N atoms was tuned, resulting in an optimized distribution of density-of-states for Ni−N_3S. The calculated overpotential showed a volcano trend on different structures, where Ni−N_3S displayed the lowest theoretical OER overpotential of 0.346 V (Figure 46b,c). The free energy diagram demonstrated that the limiting barrier for OER process on Ni−N_3S was the conversion from O* to OOH* (Figure 46d).

Similarly, Chen et al. fabricated N and S codecorated carbon layers for anchoring atomic Fe species (S,N−Fe/N/C−CNT).[256] N and S codoping increased the surface area and pore volume of the material, which promoted acid leaching of the Fe-based particles and resulted in exposure of more active sites. In the meantime, charge transfer between N, S, and Fe sites enhanced the adsorption of oxygen species and overall conductivity. This assembly of optimized features accelerated the OER kinetics.

Except for modulating the coordination environment of the metal center, varying the element of metal center can also tailor the OER performance of SAECs. In a previous study, a series of 3*d* metals (Ni, Co, and Fe) were atomically dispersed in nitrogen-doped graphene frameworks (M−NHGFs, M = Ni, Co, and Fe).[71] The as-obtained M−NHGFs exhibited a local coordination structure of MN_4C_4 with one adsorbed O atom on the M site. Because both the M and the C atom close to the doped-N were the potential adsorption sites for oxygenated intermediates, the OER process might proceed through two different reaction mechanisms. By comparing the absorption energy between the two sites, the number of *d* electrons (N_d) of the metal in MN_4C_4 was found to determine the participation of the C sites. For Co (N_d = 7) and Fe (N_d =

https://dx.doi.org/10.1021/acs.chemrev.0c00594
Chem. Rev. 2020, 120, 12217−12314

Table 2. Catalytic Performance of SAECs towards OER

catalyst	electrolyte	$\eta_{10,OER}$ (mV)	TOF (s^{-1} at a specific overpotential)	mass activity (A g_{metal}^{-1} at a specific overpotential)	ref
CoIr-0.2	1.0 M PBS	373			247
CoIr-0.2	1 M KOH	235			247
NiVIr-LDH	1 M KOH	180			248
NiVRu-LDH	1 M KOH	190			248
Ru/CoFe-LDHs	1 M KOH	198			249
Ru_1-Pt_3Cu	0.1 M $HClO_4$	220		6615@0.28 V (normalized by Ru)	252
Ru−N−C	0.5 M H_2SO_4	267	3.72@0.3 V	14283@0.3 V	251
$CoSe_{2-x}$-Pt	0.1 M KOH	255		392.2@0.3 V	250
^{s}Au/NiFe LDH	1 M KOH	237		64.9@0.28 V	198
Ni-NHGF	1 M KOH	331	0.72@0.3 V		71
Co-NHGF	1 M KOH	402	0.0024@0.3 V		71
Fe-NHGF	1 M KOH	488			71
atomic-Ni@DG	1 M KOH	270	~14@0.3 V		59
HCM@Ni−N	1 M KOH	304			253
HCM@Ni−N	0.5 M H_2SO_4	403			253
S|NiN_x-PC/EG	1 M KOH	280	10.9@0.35 V	941.8@0.35 V	70
Co−C_3N_4/CNT	0.1 M KOH	380			257
HNC-Co	0.5 M H_2SO_4	265	2.8@0.265 V	7.6@0.265 V	142
FeN_xNF/EG	0.5 M H_2SO_4	294			254
$Fe-N_4$ SAs/NPC	1 M KOH	430			196
S,N−Fe/N/C−CNT	1 M KOH	370			256
Fe-TiO_2	1 M KOH	270			258
Mn-NG	1 M KOH	337	214		255
w-$Ni(OH)_2$	1 M KOH	237	0.74@0.25 V		259
1% La/$LiCoO_2$	1 M KOH	330			208

6), all the intermediates tended to bind onto the M site rather than the C site, following a single-site mechanism. In the case of Ni (N_d = 8), OH* and O* bound more strongly to C site, while OOH* preferred the M site. Thus, Ni−NHGFs proceeded through a dual-site mechanism. Because of the different adsorption energies of reaction intermediates on these M−NHGFs, Fe−NHGFs showed the highest limiting barrier of 0.97 eV for the conversion of O* to OOH*, while the rate-determining step of Co−NHGFs was O* formation. Ni−NHGFs via the dual-site mechanism showed the lowest energy barrier of the rate-determining step for OOH* formation, hence representing the most active OER catalyst. The experimental results verified that the trend of OER activity was Ni > Co > Fe with an $\eta_{10,OER}$ of 331, 402, and 488 mV, respectively. SAECs with $M-N_2$ coordination were also evaluated in dependence of the transition metal. Zheng et al. successfully synthesized graphitic carbon nitride (g-C_3N_4) coordinated transition metals (M−C_3N_4).[257] The atomic metal center is connected to adjacent pyridinic-N atoms from two separate triazine units. Because of the scaling relationship between oxygenated species, a volcano plot is observed for the OER overpotential against OH* adsorption (Figure 47a). With lower *d*-band position, Ni−C_3N_4 adsorbs OH* more weakly than Co−C_3N_4 and Fe−C_3N_4, leading to the minimum energy barrier of the rate-determining step for O* formation (Figure 47b).

When anchoring atomic metal species onto oxides, the oxygen-coordination brings about unique features other than nitrogen coordination. Shen et al. regulated the spin state of Fe^{3+} by atomic dispersion on ultrathin TiO_2 nanobelts (Fe−UTN), achieving the most active Fe-based OER catalyst with an ultralow $\eta_{10,OER}$ of 270 mV.[258] The strong interaction between Fe and TiO_2 shifted the *d*-band center of Fe 3*d* to a higher energy, while Fe^{3+} was transformed to a low spin state with an ideal e_g filling of 1.08. Therefore, Fe−UTN created a strong σ-bonding with oxygenated intermediates. Moreover, the hybridization between Fe 3*d* and Ti 3*d* orbitals narrowed the bandgap and generated electron delocalization, enhancing the electrical conductibility of the substrate.

Similar to the precious metal SAECs, single-atom doping has also been utilized to modify and improve the performance of OER electrocatalysts. Along this line, $Ni(OH)_2$ nanosheets decorated with OER-inert tungsten (W^{6+}) atoms (denoted as w-$Ni(OH)_2$ in their report) were found to exhibit enhanced OER activity (Figure 48a).[259] A low $\eta_{10,OER}$ of 237 mV was observed for w-$Ni(OH)_2$. Besides, w-$Ni(OH)_2$ showed the lowest overpotential at 50 and 80 mA cm^{-2} among the $Ni(OH)_2$-based OER catalysts reported in the literature. With W doping, the oxidation peaks for Ni^{2+} to $Ni^{3/4+}$ conversion was slightly shifted to a higher potential, suggesting that W doping impeded the oxidation of $Ni(OH)_2$ (Figure 48a). DFT calculations of the reaction pathway suggest that the W^{6+} sites embedded on the $Ni(OH)_2$ surface has a low spin-state d^0 characteristic, which is beneficial for stabilization of the O radicals and assists the spontaneous formation of O−O bond, thereby lowering the kinetic barrier for this rate-limiting step (Figure 48b).[259]

Instead of being the active sites, single atoms can also be introduced as dopants to indirectly improve the performance of OER electrocatalysts. In a previous study with La-doped $LiCoO_2$, the atomic substitution of lattice Co with La was found to boost the OER activity by ~8.3 times.[208] Although atomic La was not the active site, La doping broke the O_h symmetry of the CoO_6 octahedron in $LiCoO_2$. The distorted CoO_6 octahedron strengthened the Co−O hybridization and improved the conductivity of the material, thus improving the electrocatalytic activity.

https://dx.doi.org/10.1021/acs.chemrev.0c00594
Chem. Rev. 2020, 120, 12217−12314

5.3. Perspectives about the Single-Atom Electrocatalysts for Oxygen Evolution Reaction

In summary, various SAECs have been studied for the OER, with the metal centers being Ir, Ru, Pt, Au, Fe, Co, Ni, Mn, etc. The activity of the SAECs is also dependent on the coordination environment and the substrate. While most of the studies focus on the activity enhancement, stability remains a major hurdle for the development of SAECs for the OER. In this aspect, diluted surface alloys represents a more promising system than coordinated metal atoms. Notably, alloy surfaces may turn into oxides under the OER conditions, and thereby this group of SAECs can resemble oxide-supported single atoms in practice. The potential of SAECs in the latter category has been seen in the superior OER performance of oxides doped with active or inert metal atoms (Table 2). Another challenge for the development of OER electrocatalysts lies in how to break the linear scaling relationship of adsorption energies for the oxygenated intermediates and the corresponding activity constraints. With one type of active sites, the theoretical minimum overpotential is 0.37 V. Whether it is plausible to break this limit by taking advantage of the synergistic effects between single-atom metal sites and the substrate, or another active site, has become an interesting question for the development of advanced OER electrocatalysts.

6. SINGLE-ATOM ELECTROCATALYSTS FOR OXYGEN REDUCTION REACTION

Fuel cells convert the chemical energy of fuels, such as H_2, methanol, ethanol, or ammonia, and oxidants (mostly O_2 in practice) into electrical energy. Compared to batteries, fuel cells do not need recharge if the fuel is continuously supplied. Most explored fuel cell technologies include proton-exchange membrane fuel cells (PEMFCs), anion exchange membrane (AEM) fuel cells, and metal (Li, Zn, Al)−air batteries. These technologies offer many advantages over conventional heat engines based on fuel combustion, including improved energy efficiency, no or reduced emissions, and compatibility with renewable fuel sources.[260,261] While the commercialization of fuel cell vehicles (FCVs) is at its early stage, it has shown great potential to reduce our dependence on fossil fuels.[262,263] However, one of the major challenges in fuel cell technology is the sluggish kinetics of ORR on the cathode.[264] ORR in acidic media proceeds via the following steps[214]

$$O_2 + H^+ + e^- \rightarrow *OOH \quad (17)$$

$$*OOH + H^+ + e^- \rightarrow *O + H_2O \quad (18)$$

$$*O + H^+ + e^- \rightarrow *OH \quad (19)$$

$$*OH + H^+ + e^- \rightarrow H_2O \quad (20)$$

whereas in alkaline media, it takes place via

$$O_2 + H_2O + e^- \rightarrow *OOH + OH^- \quad (21)$$

$$*OOH + e^- \rightarrow *O + OH^- \quad (22)$$

$$*O + H_2O + e^- \rightarrow *OH + OH^- \quad (23)$$

$$*OH + e^- \rightarrow OH^- \quad (24)$$

In certain conditions, these four-electron processes toward H_2O production have to compete with the two-electron reduction toward peroxide,

$$*OOH + H^+ + e^- \rightarrow H_2O_2 \quad (25)$$

in acid, and

$$*OOH + e^- \rightarrow HO_2^- \quad (26)$$

in alkaline media. Thermodynamically, four-electron ORR

$$O_2 + 4H^+ + 4e^- \rightarrow 2H_2O \text{ (in acid; } E^0 = 1.23 \text{ V vs SHE)} \quad (27)$$

$$O_2 + 2H_2O + 4e^- \rightarrow 4OH^- \text{ (in alkaline; } E^0 = 0.40 \text{ V vs SHE)} \quad (28)$$

is more favorable than the peroxide production

$$O_2 + 2H^+ + 2e^- \rightarrow H_2O_2 \text{ (in acid; } E^0 = 0.70 \text{ V vs SHE)} \quad (29)$$

$$O_2 + H_2O + 2e^- \rightarrow HO_2^- + OH^- \text{ (in alkaline; } E^0 = 0.065 \text{ V vs SHE)} \quad (30)$$

as evidenced by their higher (more positive) equilibrium potentials, but the two-electron pathway can become kinetically competitive in certain circumstances, e.g., on weakly binding electrocatalysts, such as Au and Ag.

Platinum group metals (PGMs) represent state-of-the-art electrocatalysts with promising activity and durability, especially in acidic electrolytes. Among the precious metal-based materials, Pt, Ir, Pd, etc. have been extensively studied for the ORR.[214,265−269] Owing to their scarcity and high costs, reducing the content of PGMs, especially Pt, while maintaining the desirable fuel cell performance, is highly desirable to meet the cost requirements for fuel cell commercialization.[270] Strategies toward this goal include[271,272] (i) alloying PGMs with a nonprecious transition metal,[273,274] (ii) constructing core−shell nanostructures with PGMs preferentially exposed on the surface,[275,276] and (iii) controlling the shape or multidimensional architecture of nanostructures.[277,278] However, these fine nanostructures have a high tendency to agglomerate or deform during electrochemical processes, leading to unfavorable deactivation and poor stability during long-term operation.[279] Moreover, some of the sophisticated synthetic procedures may not be scalable for industrial production. Alternatively, development of non-noble metal electrocatalysts represents an attractive approach to reduce the cost of ORR electrocatalysts.[10,27,225,280−284] Among the PGM-free catalysts, SAECs have demonstrated promising activity for the four-electron reduction of O_2 with modest stability.[285,286]

SAECs for ORR usually have active metal centers (M = Mn, Fe, Co, etc.) that are coordinated to nitrogen on a conductive support (mostly carbon). In this section, we will focus on the newly discovered M−N−C SAECs for ORR. While the literature has mostly focused on the use of nonprecious 3*d* metal as the active center, we are also aware of the efforts on developing atomically dispersed PGM electrocatalysts, which can also reduce the cost of ORR electrocatalysts by maximizing the utilization efficiency of the precious elements (Figure 1). Typical SAECs are prepared by pyrolysis of templates with predefined metal−nitrogen coordination, such as MOFs, hydrogel, and metal complexes.[286−289] If the atomic centers in the SAECs are the active sites, increasing metal site doping can improve the activity. Strengthening bonds between M, N, and C can improve stability. Some model catalysts in this family exhibit homogeneous structures and morphologies ideal for fundamental studies of PGM-free catalysis.[15,290] In previous

https://dx.doi.org/10.1021/acs.chemrev.0c00594
Chem. Rev. 2020, 120, 12217−12314

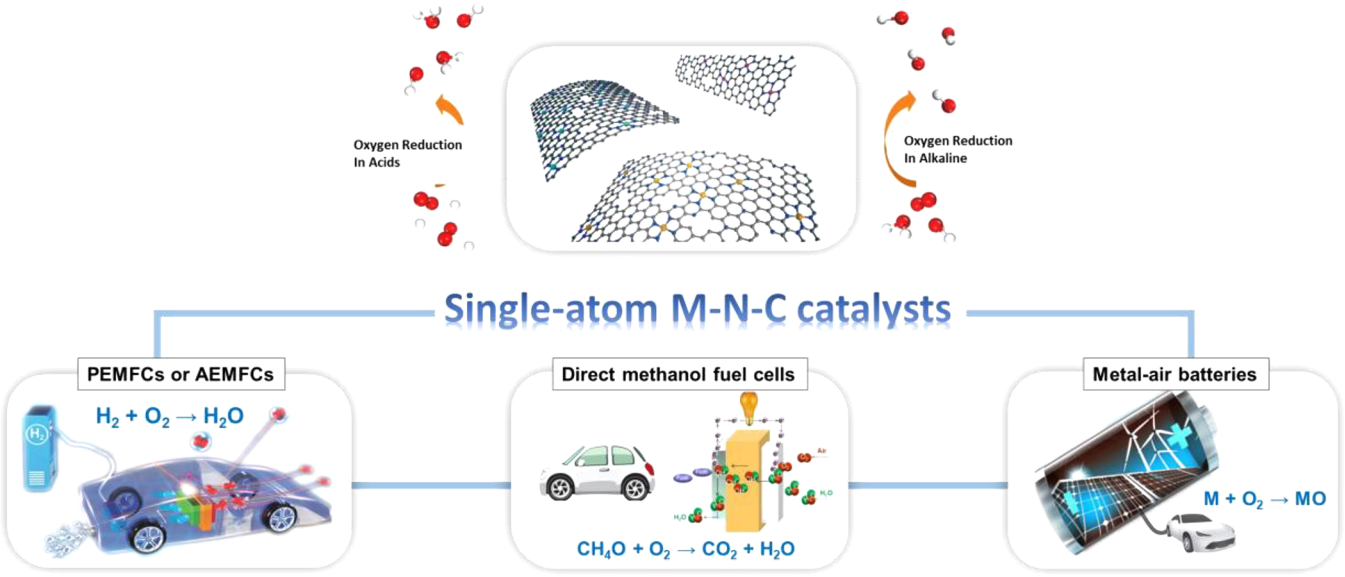

Figure 49. Oxygen electrocatalysis plays a vital role in promoting clean and sustainable electrochemical energy conversion and storage. Reproduced with permission from ref 293. Copyright 2018 IOP.

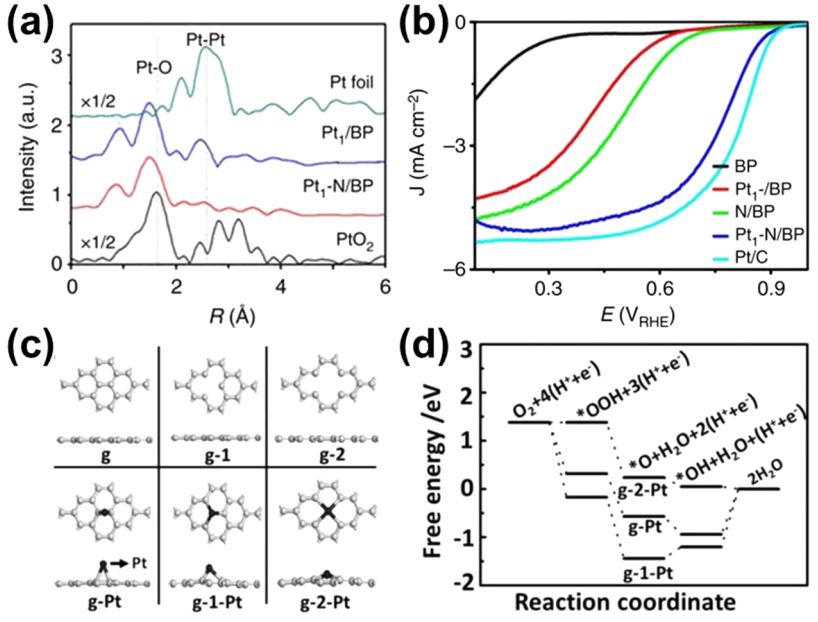

Figure 50. (a) Pt L3-edge XANES for all the samples, Pt foil, N-doped carbon (Pt_1−N/BP), and carbon-supported (Pt_1−BP) Pt SAC. (b) RRDE polarization curves of carbon black (BP), N-doped carbon black (N/BP), Pt_1−BP, Pt_1−N/BP, and commercial Pt/C in O_2-saturated 0.1 M $HClO_4$ with a scan rate of 5 mV·s^{-1} and rotation speed of 1600 rpm. Reproduced with permission from ref 51. Copyright 2017 Nature Publishing Group. (c) Optimized structures of different substrates: pristine graphene (g), monovacancy graphene (g-1), divacancy graphene (g-2), single Pt atom supported on pristine graphene (g-Pt), single Pt atom supported on monovacancy graphene (g-1-Pt, Pt−C3), and single Pt atom supported on divacancy graphene (g-2-Pt, Pt−C4). The gray and black spheres denote carbon and platinum atoms, respectively. (d) Free energy diagram for complete O_2 reduction on g-Pt, g-1-Pt, and g-2-Pt substrates in acidic media at 0.83 V, respectively. Reproduced with permission from ref 295. Copyright 2019 John Wiley and Sons.

perspectives and reviews,[285,286,291,292] the following interrelated objectives have been identified to advance single-atom M−N−C catalysts, aiming to address their catalytic activity and stability issues eventually (Figure 49). They are (i) designing structure-defined 3D MOFs precursors with $M-N_4$ coordination, (ii) determining the promoting ORR mechanism of metals (e.g., Fe, Co, Ni, or Mn), (iii) elucidating the role of carbon in the catalysts, and (iv) identifying catalyst degradation mechanisms.

6.1. Precious Metal-based Single-Atom Electrocatalysts

6.1.1. Pt-based Single-Atom Electrocatalysts. In principle, reducing Pt nanoparticles to Pt single atoms is one of the most effective ways to improve the Pt utilization efficiency and reduce the cost of ORR electrocatalysts. For example, Liu et al. reported that Pt single atoms deposited on N-doped carbon black (Figure 50a) exhibited a high ORR activity in both acid (Figure 50b, with a half-wave potential $E_{1/2}$ of ~0.76 V_{RHE}) and alkaline electrolytes ($E_{1/2}$ of 0.87

https://dx.doi.org/10.1021/acs.chemrev.0c00594
Chem. Rev. 2020, 120, 12217−12314

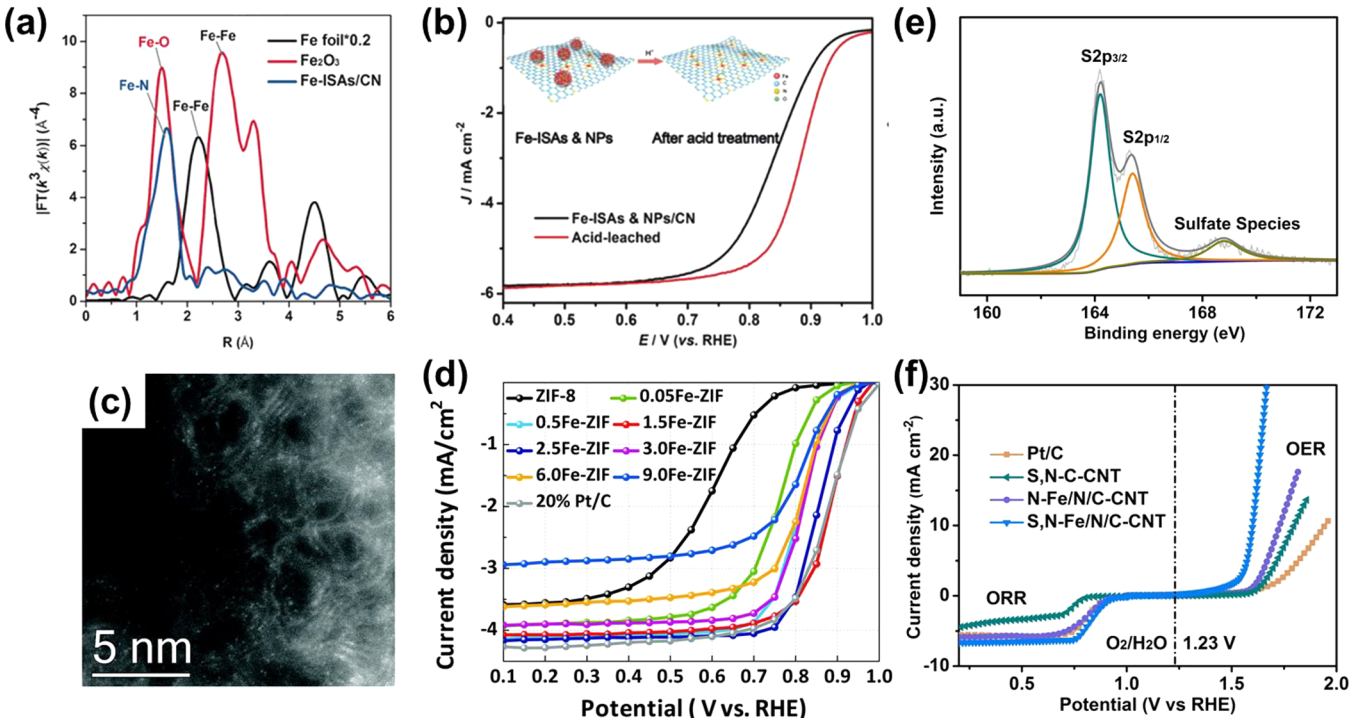

Figure 51. (a) Fourier transform (FT) of the Fe K-edge and wavelet transform (WT) of Fe-ISAs/CN. (b) ORR polarization curves in O_2-saturated 0.1 M KOH. Reproduced with permission from ref 36. Copyright 2017 John Wiley and Sons. (c) HAADF-STEM image of the same depicting the single Fe sites (bright dots) dispersed throughout the carbon phase in the 1.5Fe−ZIF catalyst. (d) RRDE ORR polarization plots in O_2-saturated 0.5 M H_2SO_4. Reproduced with permission from ref 290. Copyright 2019 The Royal Society of Chemistry. (e) XPS spectra of S 2p for S,N−Fe/N/C−CNT. (f) The overall polarization curves of all samples in the whole ORR and OER region in a 0.1 M KOH solution. Oxygen electrode activities (ΔE) were evaluated by the potential for OER at a current density of 10 mA cm^{-2} and half-wave potential at a current density of −3 mA cm^{-2}. Reproduced with permission from ref 256. Copyright 2017 John Wiley and Sons.

V_{RHE}).[51] According to DFT calculations, Pt single atoms anchored on pyridine nitrogen (Pt−N motifs) acted as the main active site. It was argued that Pt−N centers can improve the distribution of Pt single atoms and enhance O_2 adsorption on Pt. However, it has also been reported that Pt single atoms may not be ideal for ORR because the cleavage of the O−O bond usually occurs on the ensembled Pt sites, hindering the $4e^-$ pathway on Pt SAECs.[292,294] Liu et al. engineered defects on carbon support to improve the ORR activity of Pt SAECs.[295] A four-electron ORR process was concluded from the activity similar to that of commercial Pt/C. Structural characterizations and DFT calculations showed that the single Pt atoms were anchored to four carbon atoms in the double-vacancy graphene (denoted as g-2-Pt in their report), which were believed to be the active sites. The presence of double vacancies places the Pt atoms in almost the same plane as the graphene skeleton, thereby promoting the adsorption of O_2 in the end-on form (Figure 50c). On the basis of the calculated free energy diagrams of ORR on different substrates, a "downhill" pathway can be accommodated on g-2-Pt, giving rise to enhanced ORR activity (Figure 50d). It is suggested that rational design of Pt-based SACEs could still yield efficient and durable ORR electrocatalysts.

6.1.2. Ir-based Single-Atom Electrocatalysts. Among the various specimens, the adsorption free energy of OH* (ΔG_{OH*}) of the atomic Ir−N−C configuration is the closest to the peak of the classic volcano plot, implying its high catalytic activity for ORR.[296] This theoretical prediction is consistent with the fact that iridium porphyrin has the highest ORR activity among the metal porphyrins in acidic electrolytes.[297] Motivated by this prediction, Chen's group used ZIF-8 as a host for Ir precursors to derive Ir−N−C SAECs for the ORR.[298] STEM and XAS analysis confirmed that the active site was individual Ir atoms coordinated with four N atoms. As expected, the obtained Ir−SAEC exhibited a remarkable catalytic performance for the ORR in acid, with a high $E_{1/2}$ of 0.864 V_{RHE}. DFT calculations illustrated that the moderate ΔG_{OH*} accounts for the enhanced catalytic activity. The finding provides an essential guidance for the future development of high-performance Ir-based SAECs.

6.1.3. Pd-based Single-Atom Electrocatalysts. The ORR on Pd single atoms supported on graphitic carbon nitride (Pd/g-C_3N_4) has been studied computationally at different Pd coverages.[299] It was found that the ORR activity depends on the coverage of Pd, and the SAEC with a 25% coverage showed the lowest energy barrier of 0.39 eV for ORR among the series, which was even lower than that (0.80 eV) of Pt. Validation of this prediction has not been demonstrated in experiments yet, which might be challenging due to the relatively low conductivity of the C_3N_4 substrate.

6.2. Nonprecious Metal-based Single-Atom Electrocatalysts

Macrocyclic compounds (e.g., porphyrins and phthalocyanines) containing $M-N_4$ (M = Fe and Co) moieties were first discovered as active sites for the ORR in the early 1970s.[300−302] The dependence of ORR activity on the metal center for such molecular catalysts can be explained using the molecular orbital (MO) theory and shows the trend of Fe > Co > Ni > Cu ≅ Mn.[303] This early finding is insightful for understanding the catalytic mechanisms of M−N−C SAECs

https://dx.doi.org/10.1021/acs.chemrev.0c00594
Chem. Rev. 2020, 120, 12217−12314

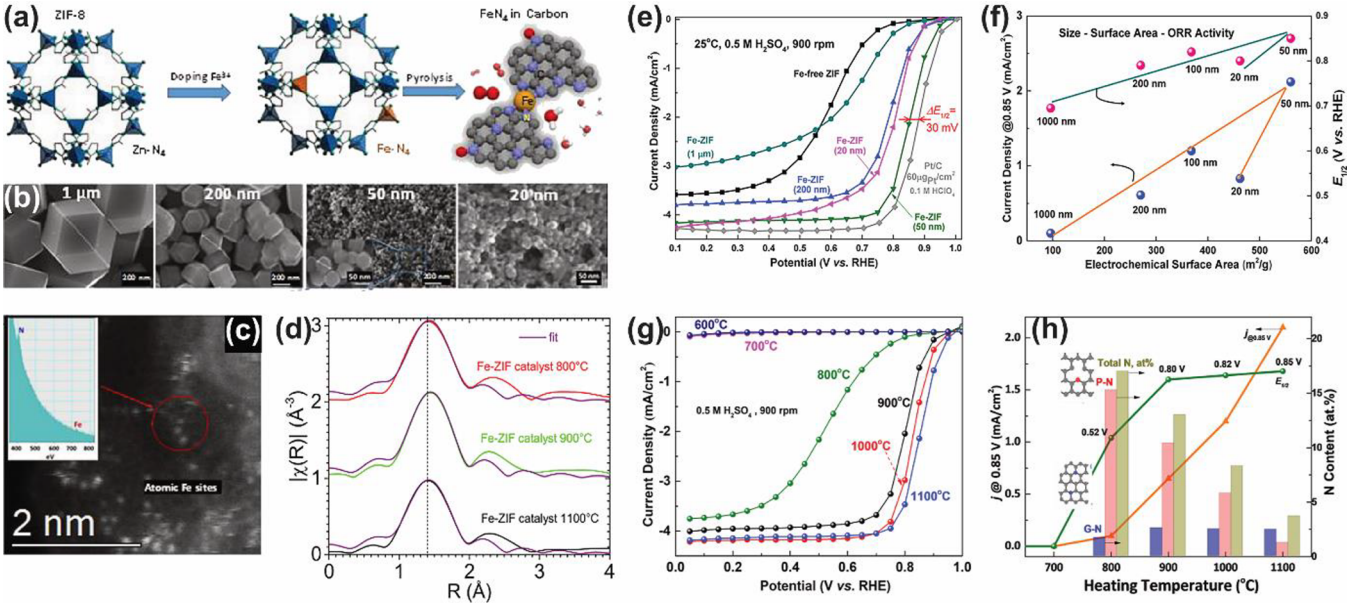

Figure 52. (a) Synthesis of Fe-doped ZIF-derived catalysts. (b) Accurately controlled sizes of the Fe-ZIF catalysts. (c) HAADF-STEM image of the Fe-doped ZIF catalyst and EELS analysis (inset to panel (c)). (d) EXAFS spectra and fittings of the catalysts prepared at different temperatures. (e) ORR polarization plots for Fe-ZIF-derived catalysts of different particle sizes in 0.5 M H_2SO_4. (f) Correlation between ORR activity and particle size. (g) ORR activity of Fe-ZIF catalysts prepared at various temperatures. (h) Correlation between ORR activity and new bond formation associated with heating temperature. Reproduced with permission from ref 15. Copyright 2017 American Chemical Society.

that have received great attention over recent years in the development of PGM-free electrocatalysts for the ORR.

6.2.1. Fe-based Single-Atom Electrocatalysts. It is suggested by DFT calculations that Fe and N codoped graphene can accommodate FeN_4 motifs that are as active as Pt metal for the ORR.[304−306] In principle, a high-performance Fe-based SAEC can be achieved by arranging N and Fe atoms to form the single-metal-atom FeN_4 sites that are uniformly dispersed on porous carbon. Relative to other precursors, ZIF-8 has attracted extensive attention as a sacrificial template to synthesize Fe−N−C SAECs, as their unique microporous structures are advantageous for the accommodation of Fe and N to give high-density FeN_4 sites after facile high-temperature pyrolysis.[287,307−310] Although there is an emergence of pyrolysis-free strategies,[311] thermal pyrolysis of composite precursors containing Fe, N, and C remains the primary methodology for the synthesis of Fe−N−C SAECs.

Lai et al. demonstrated a host−guest strategy to construct Fe-mIm nanoclusters (guests) @ ZIF-8 (host) precursors to obtain Fe−N−C SAECs.[312] The uniform dispersion of Fe species in the ZIF-8 precursor led to an even distribution of Fe single sites in the derived electrocatalysts. The obtained Fe−N/C catalyst with abundant $Fe-N_4$ motifs delivered a current density of 5.12 mA/cm^2 at 0.4 V_{RHE}. Chen et al. designed a synthesis route to derive isolated Fe atoms anchored on N-doped porous carbon starting from an Fe doped ZIF-8 precursor (Fe-ISAs/CN, Figure 51a).[36] After removal of Fe nanoparticles, a side product from thermal treatment, the $Fe-N_4$-based catalysts showed an ORR activity comparable to that of commercial Pt catalyst in 0.1 M KOH (Figure 51b). Wu and co-workers constructed an Fe SAEC rich in $Fe-N_4$ motifs by exchanging the Zn cations in the ZIF-8 precursor with Fe prior to the thermal activation (Figure 51c).[290] The Fe SAEC obtained from 1.5 at% Fe doped ZIF-8 precursor (1.5Fe-ZIF) was found to the most active for the ORR, with an $E_{1/2}$ of 0.85 V_{RHE} in O_2-saturated 0.5 M H_2SO_4 (Figure 51d). They argued that the key is the high yield of single Fe sites in this case, as a reduced loading of Fe in the precursor yielded a low site-density of $Fe-N_4$ and higher loadings led to the formation of inactive clusters or nanoparticles. Apart from the pyrolysis of seemingly pricy imidazolate frameworks, researchers have also been searching for synthesis methods that utilize less or cheaper ligands.[71,313,314] Chen et al. reported the pyrolysis of Fe^{3+} and SCN^- decorated CNTs.[256] After acid leaching, uniform $Fe-N_4$ moieties were formed on N, S modified CNTs (S, N−Fe/N/C−CNT). Two main peaks were identified in the XPS spectra of the S 2p electrons at 164.0 and 165.1 eV, which were ascribed to the sulfur dopants (−C−S−C−) (Figure 51e). The introduction of N and S dopants induced an uneven charge distribution in the carbon framework, producing positively charged carbon atoms, which were believed to enhance the adsorption of oxygen species on the $Fe-N_x$ sites (Figure 51f). Polymer hydrogels have also been used as 3D carbon/nitrogen precursors to derive Fe SAECs.[315]

Zhang et al. systematically studied the impact of precursor particle size and thermal activation conditions on the ORR performance of Fe−N−C SAECs.[15] Fe-doped ZIF was synthesized with control over the particle size (Figure 52a,b)). STEM and EXAFS studies revealed that Fe was atomically dispersed via coordination with N and C in the carbon matrix (Figure 52c,d)). As presented in Figure 52e, the best SAEC was derived from Fe-ZIF of 50 nm in particle size, achieving an $E_{1/2}$ of 0.85 V vs RHE in 0.5 M H_2SO_4, only 30 mV lower than that of Pt/C. The ORR activity was found to decrease with increasing particle size of the Fe-ZIF precursor (Figure 52f). The effect of pyrolysis temperature was further studied on the Fe−N−C electrocatalyst, derived from 50 nm precursor nanoparticles. It was found that 800 °C was the lowest temperature to activate the formation of Fe−N−C sites to give ORR activities (Figure 52g). The ORR activity increased with the pyrolysis temperature up to 1100 °C (Figure 52h). This was ascribed to the loss of pyridinic N and

https://dx.doi.org/10.1021/acs.chemrev.0c00594
Chem. Rev. 2020, 120, 12217−12314

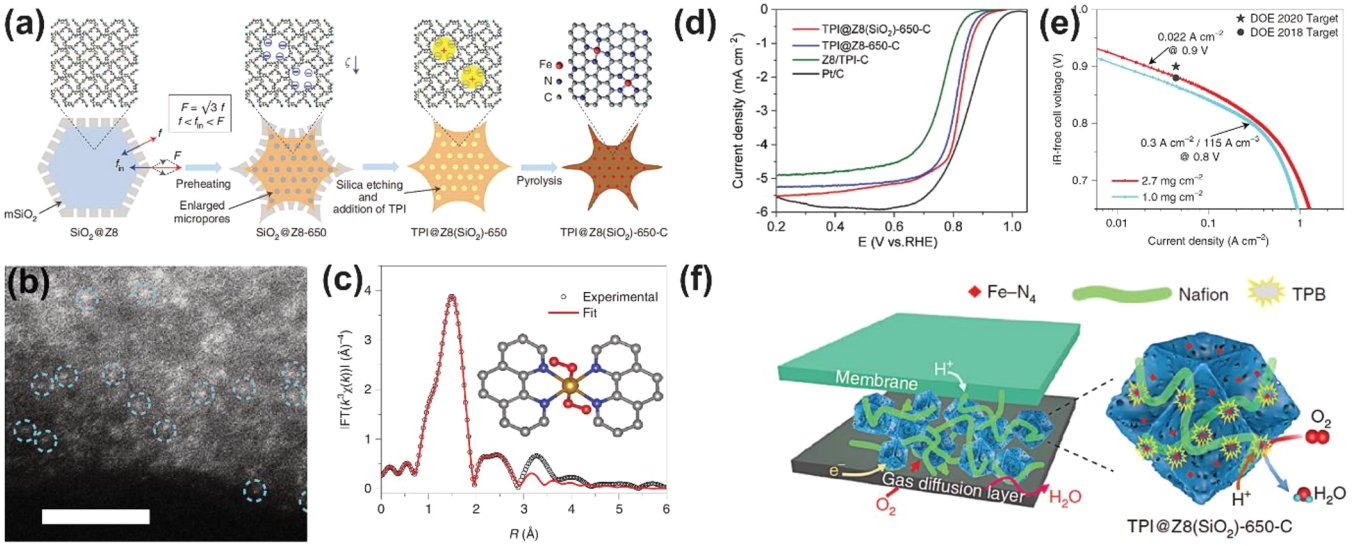

Figure 53. (a) Schematic synthesis process of TPI@Z8(SiO_2)-650-C. (b) HADDF-STEM image. Scale bar: 2 nm. (c) FT-EXAFS profile (inset: predicted structure of the FeN_4C_8 moiety with two O_2 molecules adsorbed in the end-on mode). The brown, blue, gray, and red spheres represent iron, nitrogen, carbon, and oxygen atoms, respectively. (d) ORR performances in O_2-saturated 0.5 M H_2SO_4 (0.1 M $HClO_4$ for Pt/C). (e) Tafel plot for the determination of TPI@Z8(SiO_2)-650-C activity at 0.9 $V_{iR\text{-free}}$ and volumetric activity at 0.8 $V_{iR\text{-free}}$ measured under 1 bar H_2–O_2. (f) Schematic illustration of the three-phase boundary (TPB) active sites in three representative Fe–N–C catalyst-based electrodes. Reproduced with permission from ref 47. Copyright 2019 Nature Publishing Group.

5-fold bonded pyrrolic N and the increase of graphitic N at higher temperatures. Pyridinic N provides coordination sites to atomic Fe in the form of FeN_x, whereas graphitic N affects the geometric and electronic structures of the carbon substrate. More recently, Wu et al.[316] investigated FeN_4 site formation mechanisms by anchoring Fe cations onto a nitrogen-doped carbon followed by a controlled thermal activation. In contrast to previous understanding, thermal activation at only relatively low temperatures (400 °C) was required to form active FeN_4 sites, although 700 °C gave the optimal ORR performance. Further increase of pyrolysis temperature often led to a loss of N dopants, causing a decline in activity.

Coating ZIFs with polymers or inorganic thin films are found to introduce mesopores to the derived SAECs,[317] increasing the atomic utilization efficiency and also improving the mass transport.[47,146,318] Besides, defects induced from pore formation can afford more edges to host the active sites.[71,305,313,319] Zhang et al. constructed concave-shaped Fe–N–C SAECs with mesopores and extended surface area through a mesoporous SiO_2 ($mSiO_2$) coating strategy (Figure 53a).[47] An uneven shrinkage of ZIF-8 during thermal treatment was induced by $mSiO_2$ thin film, leading to a concaved external surfaces and abundant mesopores within the nanoparticles. As revealed in HAADF-STEM measurements, highly dense atomically dispersed Fe atoms existed in the mesoporous carbon polyhedra (Figure 53b)). A possible structure of the FeN_4C_8 moiety with two O_2 molecules adsorbed in the end-on mode was proposed for the active site (Figure 53c). Figure 53d shows that the $E_{1/2}$ gap was only 12 mV for TPI@Z8(SiO_2)-650-C and TPI@Z8–650-C; nevertheless, the kinetic activity difference would be significantly magnified in fuel cell, due to the high catalyst loading in the membrane electrode assembly (MEA). Under the DOE testing protocol, the TPI@Z8(SiO_2)-650-C achieved current densities of 0.022 A cm^{-2} (@ 0.9 $V_{iR\text{-free}}$) and 0.047 A cm^{-2} (@0.88 $V_{iR\text{-free}}$), which surpassed the DOE 2018 target (Figure 53e)). As illustrated in Figure 53f, TPI@Z8(SiO_2)-650-C possessed a high density of FeN_4 moieties and a large surface area, which affords a large number of active sites at the three-phase boundary (TPB) in a fuel cell. The efficient mass transport in the catalyst layer is expected to promote most of these TPB active sites, allowing them to participate in the ORR even in the high current region.

6.2.2. Co-based Single-Atom Electrocatalysts. Although significant progress has been achieved in the promotion of activity for Fe SAECs, its durability issue is yet to be addressed. Typically, free radical species produced from Fenton reaction catalyzed by Fe will lead to an activity loss in PGM-free catalysts.[313] To mitigate the Fenton reactions caused by Fe, which generate radical species to attack catalysts and ionomers, there is an urgent need to develop PGM-free and Fe-free catalysts for low-cost and durable PEMFCs.[320] Yin et al. developed a stable Co SAECs by pyrolysis of a predesigned Zn/Co bimetallic MOFs.[321] The introduction of Zn can efficiently space Co atoms from agglomerating and generate micropores during pyrolysis. The obtained Co-N_x single sites exhibited a remarkable ORR performance ($E_{1/2}$ = 0.881 V) and durability in alkaline electrolyte. Recently, a catalyst with atomically dispersed CoN_4 sites has been synthesized through a simple one-step thermal activation of Co-doped ZIF precursors.[49] The best Co SAECs, obtained by the most optimal thermal activation condition, possessed an excellent ORR activity ($E_{1/2}$ = 0.80 V) and good stability in acid media. However, severe aggregation occurred at high Co loadings, which limited the maximum ORR activity for this type of catalyst.

Later on, an innovative surfactant-assisted MOFs method was reported to construct a core–shell Co SAEC@F127 with a significantly increased density of single-atom Co-active sites, which was inspired by the strong interaction between surfactant F127 block copolymer layer and ZIF precursor particles (Figure 54a).[322] The carbon shell derived from the F127 layer effectively retained dominant micropores and high content of N in the carbon matrix during the pyrolysis,

https://dx.doi.org/10.1021/acs.chemrev.0c00594
Chem. Rev. 2020, 120, 12217–12314

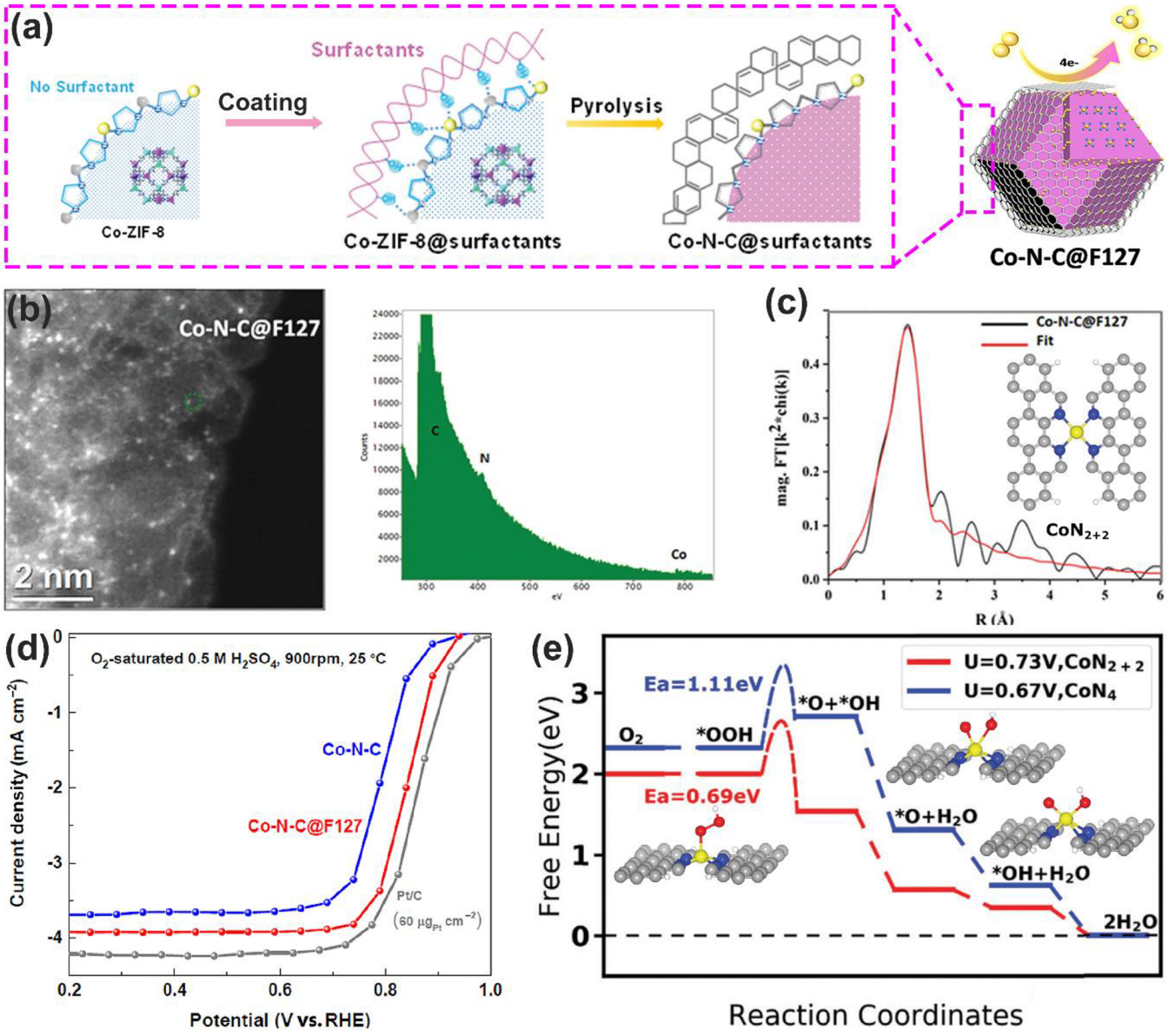

Figure 54. (a) In situ confinement pyrolysis strategy to synthesize core−shell Co−N−C@F127. (b) AC-HAADF-STEM image with accompanying EELS point spectrum of Co−N−C@F127. (c) Co K-edge FT-EXAFS profile and fitting curve for the Co−N−C@F127 catalyst (inset: CoN_{2+2} structure). Gray, blue, yellow, and white balls represent C, N, Co, and H atoms, respectively. (d) ORR polarization plots in 0.5 M H_2SO_4. (e) Calculated free energy evolution diagram for $4e^-$ ORR pathway on the CoN_{2+2} site and CoN_4 site under a limiting electrode potential. Atomistic structures of the initial state (left), transition state (middle), and final state (right) for OOH dissociation reaction on the CoN_{2+2} site. Reproduced with permission from ref 322. Copyright 2019 The Royal Society of Chemistry.

realizing the formation of highly dense atomically dispersed Co-active sites (Figure 54b). A CoN_{2+2} active site configuration was proposed by fitting the Fourier transform of the k_2-weighted EXAFS data (Figure 54c). In acidic electrolytes, the Co SAEC@F127 catalyst had a significantly enhanced ORR activity with an $E_{1/2}$ of 0.84 V_{RHE}, which was comparable to the most advanced Fe SAEC catalyst (Figure 54d). Figure 54e depicts the transition state and predicts the activation energies for the *OOH dissociation on CoN_{2+2} and CoN_4 structure. The Co SAEC@F127 catalyst yielded a large amount of CoN_{2+2} active sites that could effectively catalyze the ORR through the $4e^-$ pathway.

6.2.3. Mn-based Single-Atom Electrocatalysts. Despite the extensive efforts dedicated to Fe−N−C and Co−N−C electrocatalysts, they still suffer from insufficient durability for the ORR, especially at the desirable high-potential reaction conditions (e.g., >0.6 V vs RHE), which has limited their practical applications in PEMFCs. Preliminary DFT calculations indicate that Mn-based SAECs containing MnN_4 moieties embedded in carbon could have comparable activity but enhanced stability, relative to the Fe-based SAECs.[323] Mn-based SAECs have thus received increasing attention for the development of PGM-free electrocatalysts for the ORR.

Xiong et al. reported the deposition of atomically dispersed manganese−nitrogen−carbon thin films (2.5 ± 0.2 nm thick) on an oxygen pretreated CNT substrate (denoted as f-MnNC/CNT in their report) (Figure 55a)).[324] HAADF-STEM and EDS elemental mapping confirmed a uniform dispersion of Mn atoms throughout the Mn−NC film (Figure 55b−d). Mn−N_4 coordination was revealed from the K-edge EXAFS analysis

https://dx.doi.org/10.1021/acs.chemrev.0c00594
Chem. Rev. 2020, 120, 12217−12314

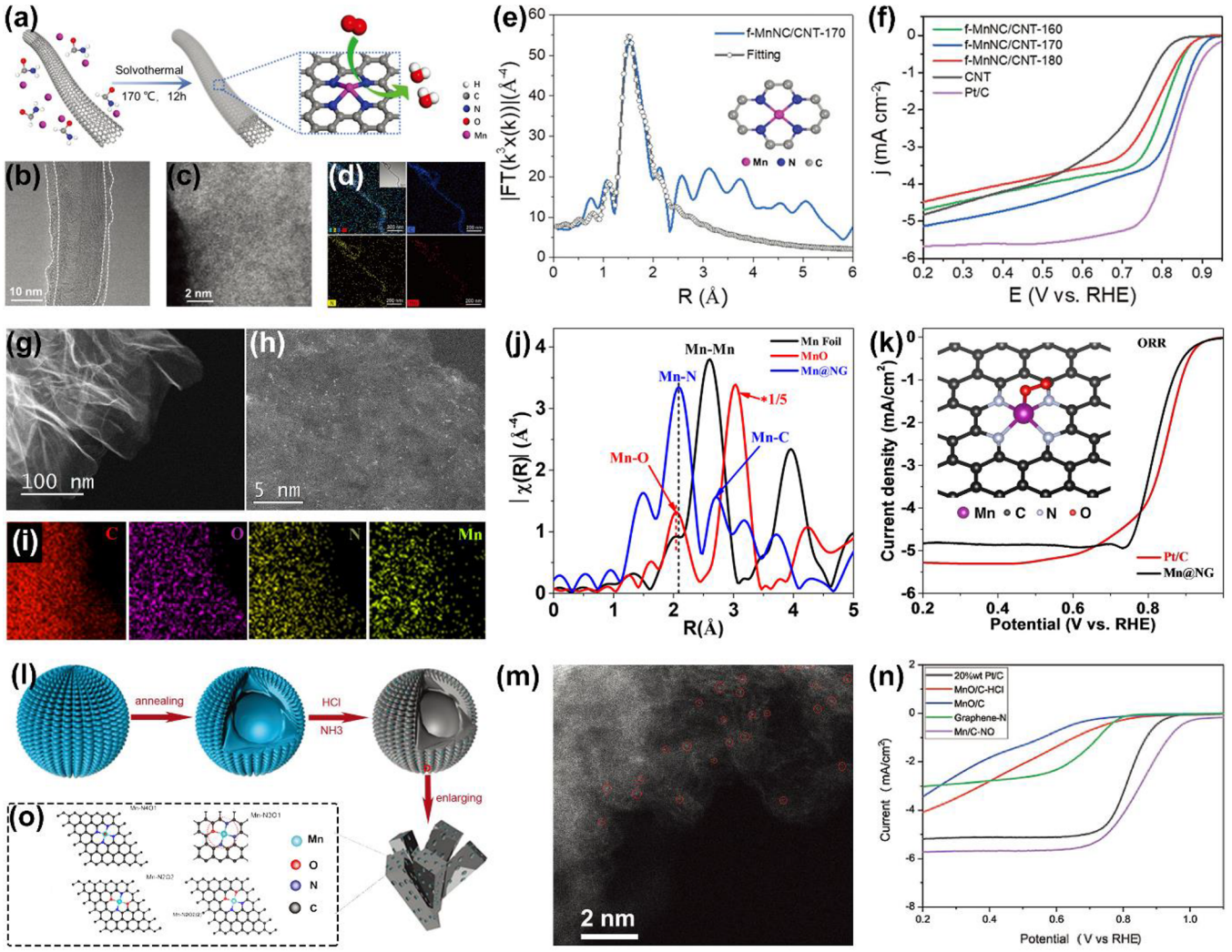

Figure 55. (a) Synthesis scheme of f-MnNC/CNT, and the corresponding (b) HRTEM, (c) HAADF-STEM, and (d) element mapping images. (e) Mn K-edge FT-EXAFS profile with the proposed structure shown in the inset. (f) RDE polarization curves in O_2-saturated 0.1 M KOH. Reproduced with permission from ref 324. Copyright 2019, The Royal Society of Chemistry. (g,h) HAADF-STEM images of Mn@NG at different magnifications. (i) Corresponding EDS elemental maps of C, O, N, and Mn. (j) Mn K-edge FT-EXAFS spectra. (k) Polarization curves of Pt/C and Mn@NG in O_2-saturated 0.1 M KOH. Reproduced with permission from ref 325. Copyright 2019 Elsevier. (l) Schematic illustration of the synthetic process of Mn/C-NO. (m) AC- HAADF-STEM image of Mn/C-NO. (n) RDE polarization curves in O_2-saturated 0.1 M KOH at a sweep rate of 10 mV s^{-1} and 1600 rpm. (o) Possible ORR active sites in Mn/C-NO. Reproduced with permission from refs 198,326. Copyright 2018 John Wiley and Sons.

(Figure 55e). As shown in Figure 55f, the $E_{1/2}$ of f-MnNC/CNT-170 was 0.83 V (vs RHE), which was close to that of commercial Pt/C (0.85 V). Bai et al. codoped graphene with Mn and N to derive a Mn@NG SAEC by high-temperature pyrolysis and subsequent acid-leaching.[325] Only atomically dispersed manganese was observed in Mn@NG (Figure 55g,h). EXAFS studies of Mn@NG showed that the primary scattering was ascribed to the Mn−N_4−C motif. This catalyst exhibited an $E_{1/2}$ of 0.82 V (Figure 55k). Yang et al. introduced atomic Mn into nitrogen and oxygen modified 3D graphene frameworks (Figure 55l).[326] As illustrated in Figure 55m, a large amount of Mn was atomically dispersed in the carbon matrix. This Mn/C−NO SAEC exhibited an $E_{1/2}$ of 0.86 V, which was even higher than that of Pt/C employed as a control in this study (Figure 55n). Theoretical calculations revealed that the intrinsic catalytic activity of atomic Mn was significantly improved via the changing local geometry of its coordination to O and N atoms. The computational results showed that Mn−N_1O_3, Mn−N_2O_2, and Mn−N_3O_1 were possible ORR active sites (Figure 55o).

Compared to Fe- and Co-based SAECs, it is even more challenging to increase the density of Mn−N_4 active sites in Mn−N−C electrocatalysts, because Mn is more prone to the formation of unstable and inactive metal oxides or carbides during the pyrolysis.[326,327] Conventional one-step chemical doping only introduces low-density atomic Mn sites.[328] To effectively increase the density of Mn−N_4 active sites in the catalyst, a two-step synthesis strategy involving doping and adsorption processes was reported to obtain the Mn SAECs rich in single-atom Mn sites (Figure 56a)).[39] In the first step of the synthesis, Mn-doped ZIF-8 precursors were prepared through the conventional chemical doping method. After carbonization and acid leaching, the derived porous carbon was employed as a host to adsorb additional Mn and N sources, followed by thermal activation. This atomically dispersed Mn SAEC achieved promising activity with an $E_{1/2}$ of 0.80 V_{RHE}

https://dx.doi.org/10.1021/acs.chemrev.0c00594
Chem. Rev. 2020, 120, 12217−12314

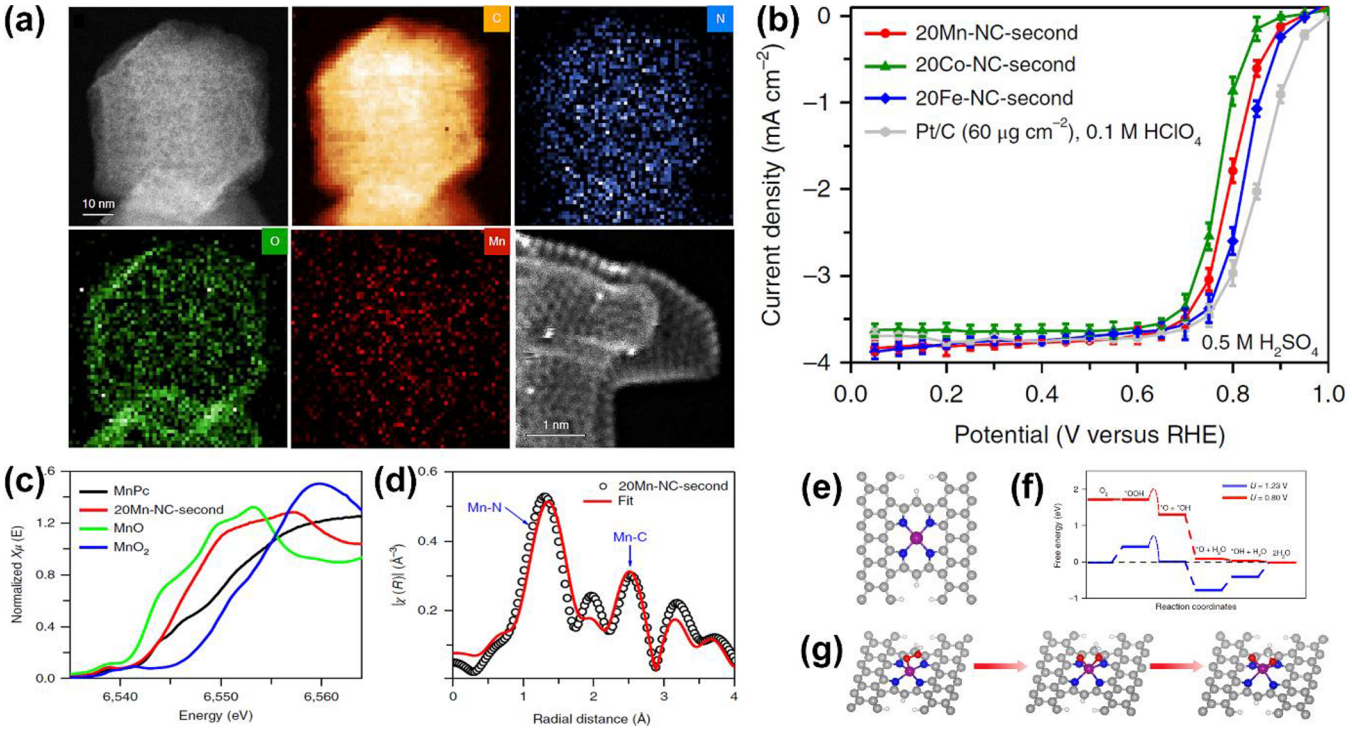

Figure 56. (a) EELS elemental maps of C, N, O, and Mn in a selected area. (b) Comparison of the catalytic activity of Fe−, Co−, and Mn−N−C catalysts prepared from identical procedures. (c) K-edge XANES spectra of 20Mn-NC-second catalyst and reference samples. (d) Mn K-edge FT-EXAFS profiles of the 20Mn-NC-second catalyst. (e) Atomistic structure of MnN_4C_{12} active site in the 20Mn-NC-second catalyst. (f) Calculated free-energy evolution diagram for ORR through a $4e^-$ associative pathway on the MnN_4C_{12} active site under electrode potential of $U = 1.23$ V and $U = 0.80$ V. (g) Atomistic structure of the initial state (left panel, that is, state *OOH in (b), transition state (middle panel), and final state (right panel, that is, state *O + *OH in (b) for OOH dissociation reaction on MnN_4C_{12} active site. Reproduced with permission from ref 39. Copyright 2018 Nature Publishing Group.

and excellent stability in acids (Figure 56b)). By fitting the Fourier transformed EXAFS profile in Figure 56c, an MnN_4C_{12} site was proposed as the active site. In Figure 56f, DFT calculations further confirmed that the MnN_4C_{12} site displayed an appropriate binding strength with the ORR species and could be the active sites for the $4e^-$ pathway. Therefore, the reported Mn SAEC demonstrated an alternative concept to develop a robust and highly active PGM-free catalyst to replace the Fe counterparts in future PEMFC technology.

6.3. Current Challenges in the Development of Single-Atom Electrocatalysts for the ORR

As a critical half-cell reaction for fuel cells and metal−air batteries, the ORR requires highly active, stable, and low-cost electrocatalysts to drive the sluggish kinetics for practical implementations. Although PGM-based catalysts have reached the application level of catalytic performance, their scarcity and high cost limits the commercial competitiveness of these technologies. In this regard, PGM-free (or low-PGM content) SAECs represent a promising solution. As the most active moieties in this series, Fe−N−C, however, still suffers from poor durability, as the macrocycle decomposes in H_2O_2, a byproduct produced in ORR.[39,329] Various strategies have been proposed to enhance the stability of M−N−C SAECs.[280,330] While the $M-N_4$ moieties are conventionally embedded into carbon substrate through annealing of macrocyclic precursors,[126,331] nonmacrocyclic N/C/Fe composites have been studied recently.[27,28,332−357] Despite the progress,[27,264,281,346,350,358−360] at least two prominent challenges remain for the practical implementation of PGM-free electrocatalysts..

6.3.1. Heterogeneity of Single-Atom Metal Sites Derived from Pyrolysis. Overall, probing active sites in the M−N−C electrocatalysts is more challenging than in traditional Pt-based catalysts (Figure 57a). Typically, M−N−C catalysts are prepared by pyrolyzing a mixture of M/N/C precursors and high-surface-area carbon supports, followed by acidic leaching and subsequent heating treatment.[361] After pyrolysis, the original structure of precursor is often lost[362] and thus lacks control over the uniformity of active sites (Figure 57b).[27,357,363−365] In typical M−N−C catalysts, C is the dominant component (up to 90 at %). In contrast, graphitic and pyridinic N consists of only ∼7 at % by doping at the edges and planes of the carbon substrate.[332] The rest is transition metal, in forms of $M-N_x$ moieties, metal aggregates, and metal oxides, up to 3 at %. DFT calculations indicate that $M-N_4$ (especially FeN_4) adsorbs O_2 strongly and can enable the dissociative mechanism of ORR,[296,305] which has also been verified by experimental results.[354,366] The bonding mechanism and optimal coordination among N, Fe, and C (e.g., in-plane, edge, subsurface) have yet to be identified conclusively. Moreover, compared to pristine $Fe-N_4$ coordination in macrocycles, the formation mechanism of $Fe-N_x$ sites during thermal treatment is unknown.[349] Therefore, it is of great interest to understand these underlying mechanisms by elucidating atomic structure transformation during the pyrolysis.

6.3.2. Insufficient Catalytic Activity and Catalyst Stability. Even though many promising M−N−C electrocatalysts have been reported over the past decade, the catalytic performance and durability of SAECs for the ORR still fall

https://dx.doi.org/10.1021/acs.chemrev.0c00594
Chem. Rev. 2020, 120, 12217−12314

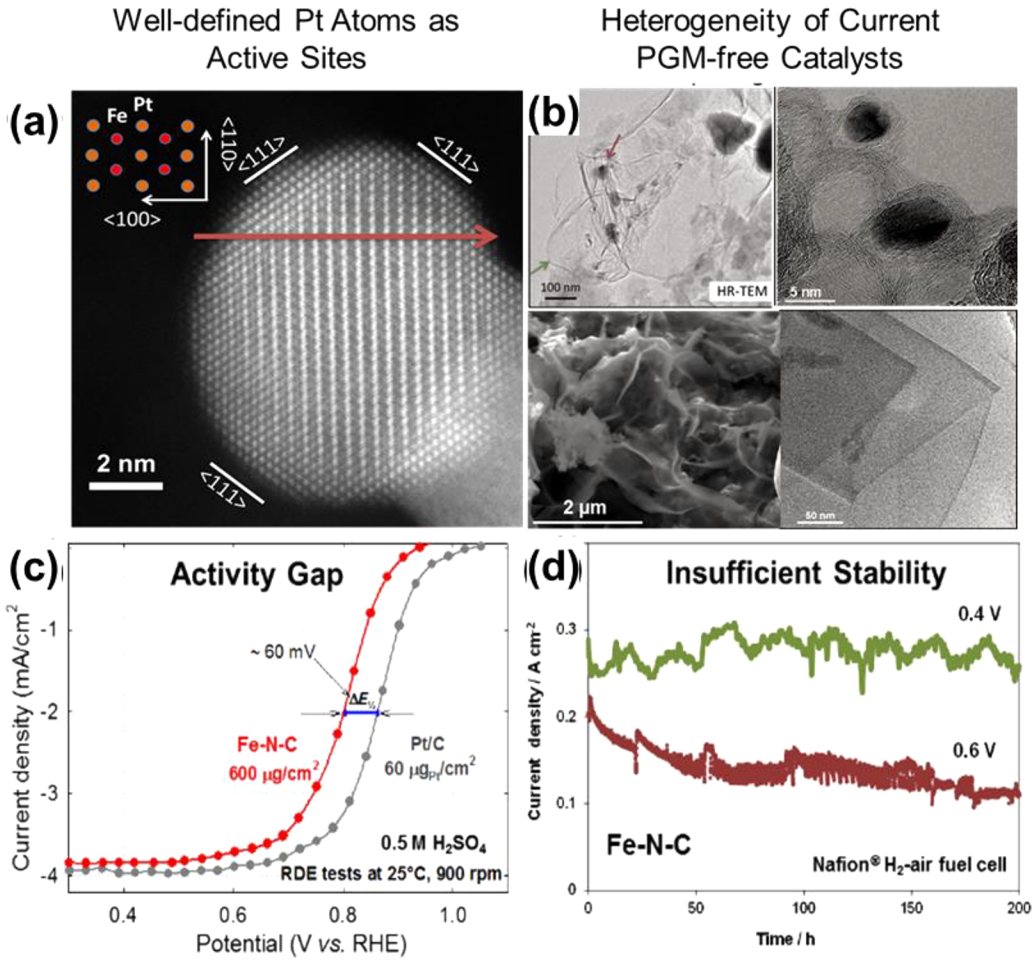

Figure 57. (a) Comparison between Pt catalyst with well-defined Pt atoms as active sites. Reproduced with permission from ref 361. Copyright 2015 American Chemical Society. (b) Highly heterogeneous Fe/Co−N−C catalysts are masking real active species. Reproduced with permission from ref 357. Copyright 2009 The American Association for the Advancement of Science. (c) Performance gap between Fe−N−C and Pt catalysts. Reproduced with permission from ref 27. Copyright 2011 The American Association for the Advancement of Science. (d) Fast performance degradation of Fe−N−C at high voltages. Reproduced with permission from ref 367. Copyright 2009 The Electrochemical Society.

behind those of Pt-based catalysts.[361] It is generally seen that the PGM-free electrocatalysts require an overpotential >60 mV higher than Pt-based catalysts, corresponding to at least 10 times slower turnover on the single-atom active sites (Figure 57c).[27] In principle, increasing the density of active sites can compensate for this gap. However, previous work indicates that merely raising the metal loading in the precursors is ineffective, as it causes aggregation and formation of inactive metal oxide or carbide compounds or nanoparticles.[123,368,369] To increase the catalytic activity, it is essential to uniformly disperse active sites onto the carbon matrix, which remains a challenge in this field. On the other side, although long-term fuel cell stability has been achieved by the recently developed polyaniline-based FeCo−N−C catalysts (up to 700 h of operation),[264,354,367] it was operated at a relatively low cell voltage (0.4 V). Unfortunately, the FeCo−N−C catalyst degraded very fast at the more desirable cell voltage of 0.6 V (Figure 57d).[367] Therefore, the stability issue must be resolved before PGM-free electrocatalysts become viable for future fuel cell technologies.[349,370] To address these challenges, more research efforts are needed for the design, synthesis, characterization and mechanistic understanding of the SAECs.[214,371]

6.4. Theoretical Understanding of Single Metal MN_4 Sites

6.4.1. ORR Pathways on MN_4 Sites. Zelenay group at Los Alamos National Laboratory and Wang group at the University of Pittsburgh have performed comprehensive first-principles DFT calculations to investigate the reaction pathways of ORR on various M−N_4 active sites embedded in graphene.[305,306,372−376] Wang et al. calculated the adsorption energy of ORR species (including O_2, H^+, *O, *OH, *OOH, HOOH, and H_2O) and the energetics (heats of reaction and activation energies) of all the possible ORR elementary reactions (O═O bond dissociation reactions and hydrogenation reactions) on FeN_4.[303] The results indicate that the O_2 molecule was only chemisorbed to the metal centers of Fe−N_4 moieties, suggestive of the pivotal role of Fe−N_4 in the activation of ORR. They compared the activation energy the for rate-determining steps in three possible pathways: O_2 dissociation pathway, *OOH dissociation pathway, and HOOH dissociation pathways. The *OOH dissociation pathway is kinetically favorable on Fe−N_4 moieties, with the lowest activation energy of 0.56 eV for the rate-determining step, the dissociation of *OOH. More importantly, Wang and co-workers explained how the 4e^- ORR pathway (breaking O═O bond) was possible on a single active site. As shown in Figure 58a, in the initial state (IS) of the reaction, the OOH

https://dx.doi.org/10.1021/acs.chemrev.0c00594
Chem. Rev. 2020, 120, 12217−12314

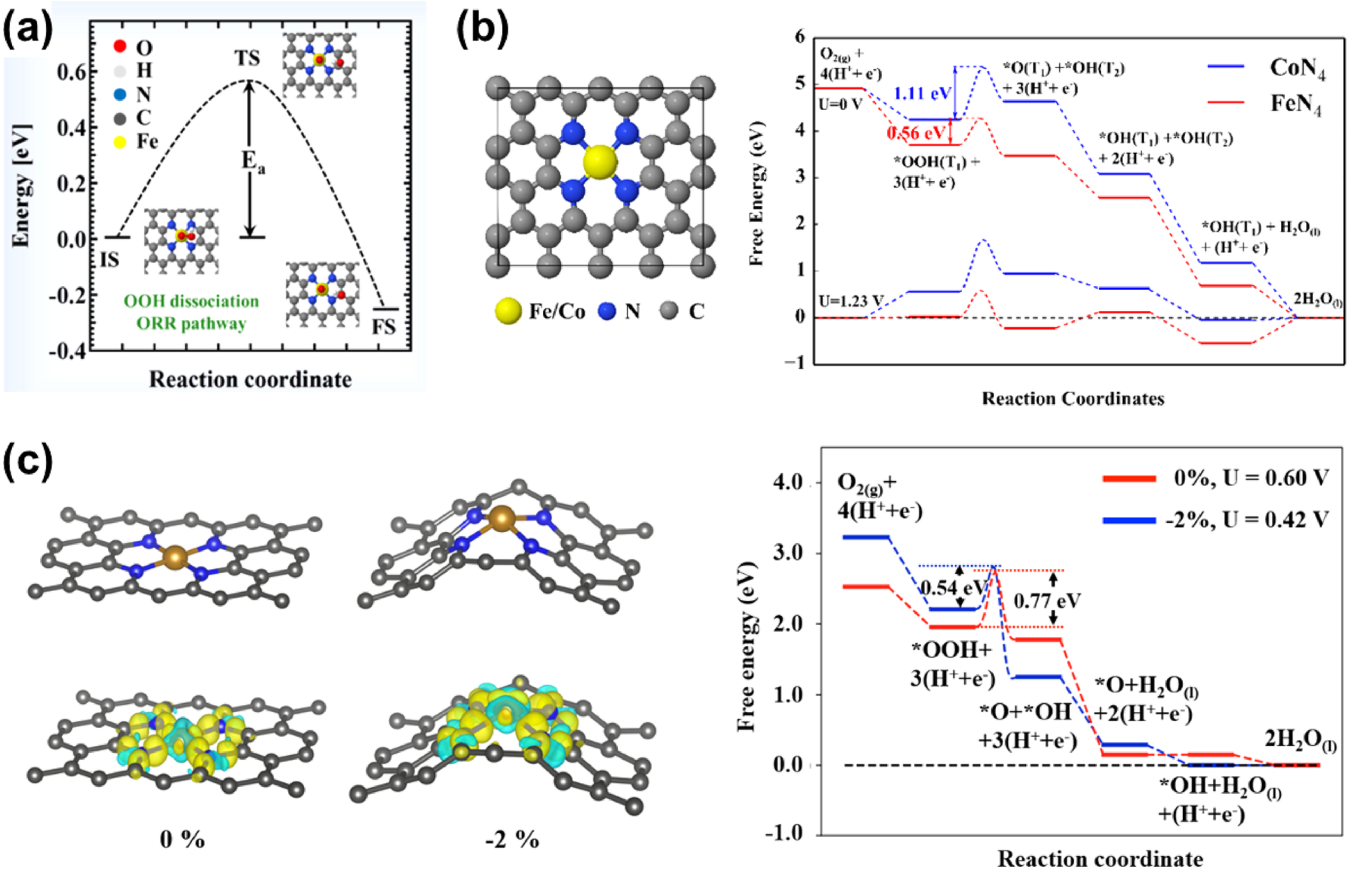

Figure 58. (a) Intermediate OOH dissociation reaction on Fe−N_4 sites embedded in carbon. Reproduced with permission from ref 306. Copyright 2014 American Chemical Society. (b) Calculated free energy evolution diagrams for the O_2 reduction through $4e^-$ associative pathway to produced H_2O on the CoN_4 and FeN_4 active sites in acid medium. Reproduced with permission from ref 375. Copyright 2016 American Chemical Society. (c) Calculated free energy evolution diagrams for the O_2 reduction through $4e^-$ associative pathway to produced H_2O on three FeN_4 active sites with different local carbon structures in acid medium. Reproduced with permission from ref 378. Copyright 2019 John Wiley and Sons.

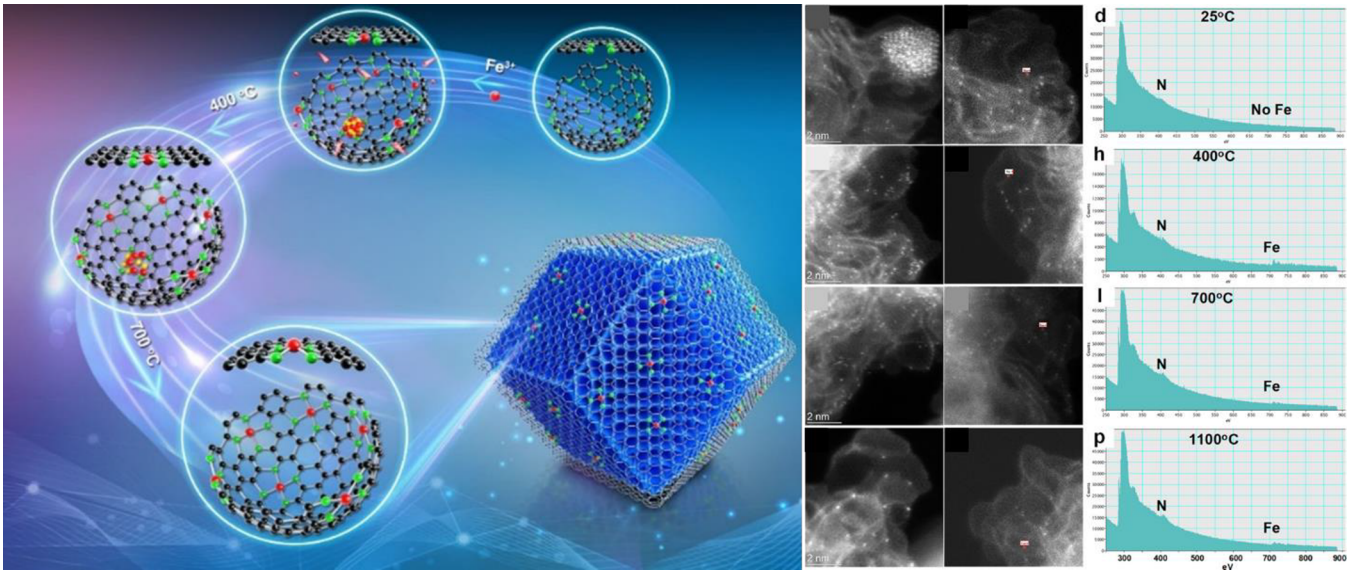

Figure 59. Model systems established by adsorbing Ni into N-doped carbon to elucidate the formation mechanism of FeN_x sites during thermal activation. Reproduced with permission from ref 378. Copyright 2019 John Wiley and Sons.

adsorbs on the metal center of Fe−N_4. Once the breaking of the O═O bond occurs, the dissociated O will be adsorbed on Fe center, while OH is adsorbed on the adjacent carbon atom in the final state (FS).

6.4.2. Role of Metal Center in MN_4 Moieties. The role of transition metal center was further elucidated by Liu et al. in a comparative study of CoN_4 and FeN_4 motifs (Figure 58b).[375] They argued that the O_2 molecule could be favorably adsorbed

https://dx.doi.org/10.1021/acs.chemrev.0c00594
Chem. Rev. 2020, 120, 12217−12314

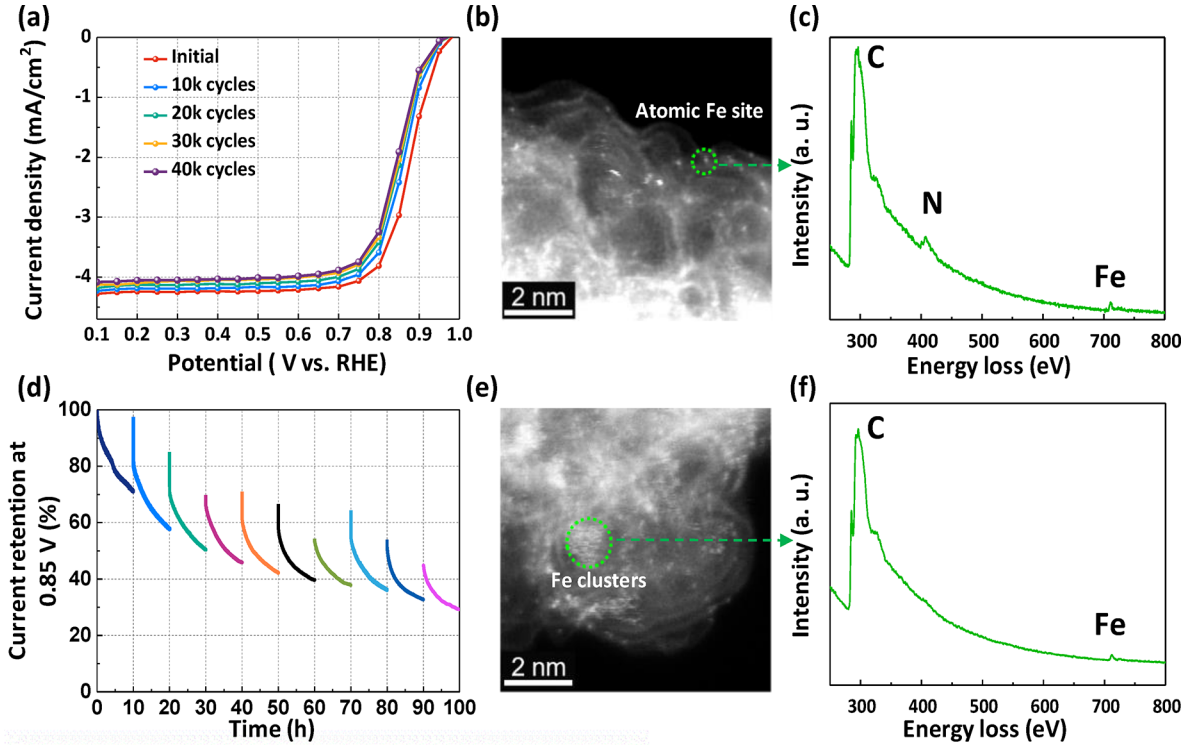

Figure 60. RDE stability tests of the atomic FeN_4 site catalyst in O_2-saturated 0.5 M H_2SO_4 electrolyte using different test protocols. (a–c) Potential cycling between 0.60 and 1.0 V with less significant activity loss, indicating minor carbon corrosion and atomically dispersed Fe sites still coordinated by N. (d–f) Holding at a constant potential of 0.85 V for 100 h led to significant degradation, depicting severe carbon corrosion and the appearance of Fe clusters due to Fe–N bond breaking and Fe–Fe bond formation. Reproduced with permission from ref 290. Copyright 2019 The Royal Society of Chemistry.

on the metal center, while the end product of ORR, H_2O, could be easily removed from FeN_4 and CoN_4 sites. The key to the high ORR activity by FeN_4 was argued to be the modest energy barrier (0.56 eV) for the rate-determining step, dissociation of OOH, as compared to 1.11 eV on CoN_4. This study demonstrated the pivotal role of the active metal center in $M–N_4$ moieties, amid the dramatic difference in ORR activity between different metals in a similar $M–N_4$ structure. The FeN_4 moiety is predicted to promote $4e^-$ ORR to produce H_2O, whereas CoN_4 mainly produces H_2O_2 via a $2e^-$ process, well in-line with experimental observations.[27,377]

6.4.3. Role of Carbon Substrates. The underlying carbon substrate structure is also thought to affect the ORR activity of MN_4-based catalysts. Liu et al. studied the ORR activity on FeN_4 catalysts with different supporting carbon structures.[373,378] They compared FeN_4 sites with three types of adjacent carbon structures, each showing a different state of strain. As shown in Figure 58c, compressive strain in the local carbon structure leads to a shortening of the Fe–N bond and off-plane displacement of central Fe in a FeN_4 site. They argued that the shortening of the Fe–N bonds led to changes in electronic structure, such as the positive shifting of the 3*d*-orbitals of central Fe. DFT calculations predicted the adsorption energies of key intermediates (i.e., O_2, OOH, O, and OH) and the activation energy for OOH dissociation for FeN_4 catalysts with and without 2% compressive strain. The catalyst support with a compressive strain requires an activation energy 0.13 eV lower to dissociate OOH. This study shows that engineering the substrate structure can enhance the intrinsic activity for the ORR.

6.4.4. Formation Mechanisms of Single Metal MN_4 Sites. Although $M–N_4$ moieties are widely recognized as the most efficient PGM-free active sites, their formation mechanisms have remained elusive for decades. The formation of the M–N bond convolutes with uncontrollable carbonization and nitrogen doping during high-temperature treatment. Recently Li et al. developed a model system to study the formation mechanism of MN_4 sites. A well-defined nitrogen-doped carbon derived from ZIF-8 precursors can adsorb target metal ions (e.g., Fe^{3+}) followed by a controlled thermal activation from 200 to 1100 °C (Figure 59).[378] This approach can deconvolute the M–N bond formation from carbonization and nitrogen doping, which allows us to correlate M–N bond properties with activity and stability of MN_x sites as a function of thermal activation temperature. In combination with XAS analysis and STEM measurements, the local coordination environments of FeN_4 sites are associated with the structure of active sites. DFT calculations revealed the reaction mechanism and pathways on these active sites with different coordination. The FeN_x configuration was formed by adsorbing Fe^{3+} into nitrogen-doped carbon hosts at room-temperature. These FeN_x sites are acid-resistant but possess insufficient intrinsic activity for the ORR. However, a thermal activation at a relatively low temperature, such as 400 °C, is sufficient to generate stable and ORR-active FeN_4 sites, which become more active at 700 °C with optimal $Fe–N_4$ coordination environments. The evolution of the catalytic performance of MN_x sites driven by thermal activation was studied in terms of the possible factors: (i) the active site density can be increased through transferring FeO_x particles to atomically dispersed FeN_4 sites and (ii) the enhancement of the intrinsic activity of

https://dx.doi.org/10.1021/acs.chemrev.0c00594
Chem. Rev. 2020, 120, 12217–12314

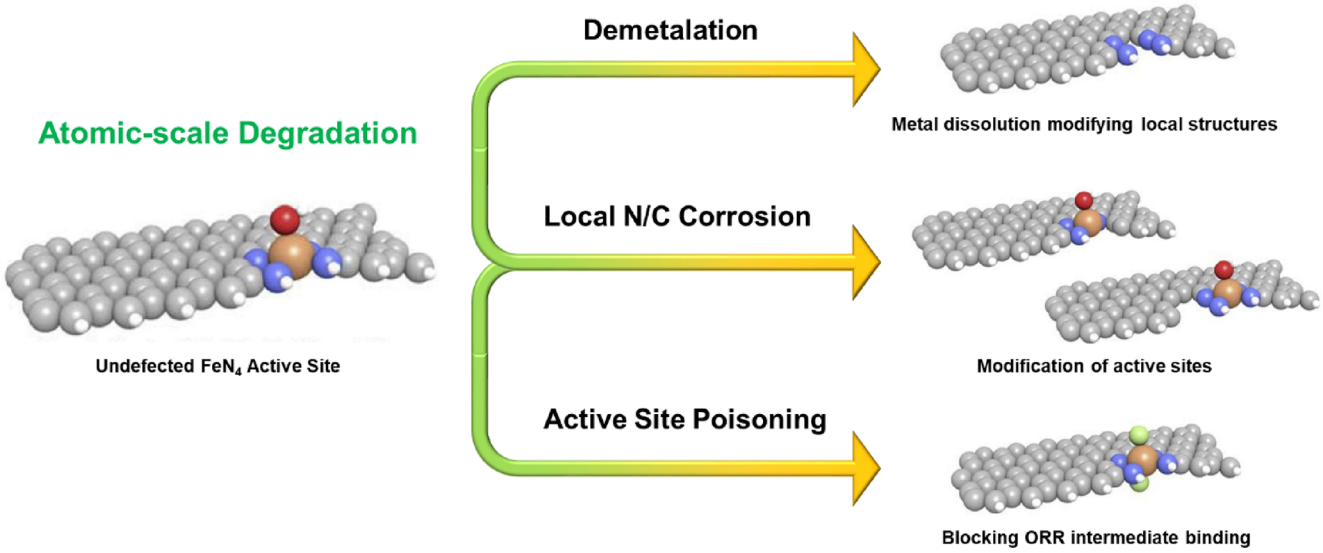

Figure 61. Proposed mechanisms for activity loss of PGM-free active sites. Reproduced with permission from ref 382. Copyright 2018 Elsevier.

FeN_4 sites through strengthening bonding strength and shortening length from room temperature to the optimal 700 °C. Thermal activation at a higher temperature, such as 900 and 1100 °C, may further improve stability but often leads to the loss of doped nitrogen, causing a decline of activity. This adsorption method provides precise control of the density of FeN_4 active sites without changing the carbon structure and morphologies, which is an ideal platform for mechanistic studies. Besides, the adsorption approach has proven useful to synthesize high-performance Fe−N−C catalysts, showing very encouraging ORR activity in both acidic electrolytes and fuel cells.[378]

6.5. Stability Studies and Degradation Mechanisms

According to extensive experimental observation,[290,378,379] the degradation of MN_4 sites during the ORR is generally due to two causes, (1) M−N/C−N bond breaking caused by chemical and electrochemical oxidation or reduction, and (2) carbon matrix corrosion and loss of electrical contact with active sites. As shown in Wu's recent work (Figure 60),[290,380,381] RDE stability tests of the atomic FeN_4 site catalyst were carried out in O_2-saturated 0.5 M H_2SO_4 electrolyte using different test protocols. Potential cycling tests between 0.60 and 1.0 V led to a less significant activity loss, indicating minor carbon corrosion and atomically dispersed Fe sites still coordinated by N. However, holding at a constant potential of 0.85 V for 100 h caused significant degradation, depicting severe carbon corrosion and the appearance of Fe clusters due to Fe−N bond breaking and Fe−Fe bond formation. The general understanding of the degradation mechanism of MN_4 sites suggests that strengthening M−N and C−N bonding in a robust and corrosion-resistant carbon may improve stability. Precursor properties, including $M-N_4$ complex, local hydrocarbon groups, and crystal size, as well as proper carbonization, will be critical factors to enhance catalyst stability. In combination of computation, experimental efforts should focus on (1) metal site dissolution, (2) doped N oxidation, and (3) carbon corrosion to eventually address the stability issue (Figure 61).

6.6. Single-Atom Electrocatalysts for other Electrochemical Devices

The development of efficient, durable, and economical single-atom PGM-free electrocatalysts is of great significance for the commercial applications of electrochemical energy conversion and storage technologies.[12,383−385] In the following sections, we outline the latest advances of single-atom M−N−C catalysts in some key energy conversion and storage applications, which demonstrate their high potentials in achieving efficient electrochemical ORR process.

6.6.1. Proton-Exchange Membrane Fuel Cells (PEMFC). Compared with internal combustion engine vehicles, PEMFCs can be a clean energy technology to provide high efficiency, fast start-up, low operating temperature, and high power for transportation applications.[386] Significant progress has been made in the synthesis of highly active single-atom M−N−C catalysts and their applications in PEMFCs,[47,165,285,387−389] aiming to eliminate two major technical obstacles to their viable and large-scale applications, the insufficient density of active sites and unsatisfactory durability of current PGM-free catalysts. For example, by adjusting the doped iron content in ZIF-8 precursors, Zhang et al. obtained an Fe−N−C catalyst with the highest atomically dispersed FeN_4 active site density, which showed considerable ORR activity in a challenging acidic electrolyte and promising performance in a practical PEMFC.[290] The optimum Fe content was believed to be the critical factor behind the high ORR activity of the Fe−N−C catalyst (Figure 62a−c).[290] Besides, it was found that iron salts would have a great impact on the ORR activity of single-atom Fe−N−C catalysts.[368] Replacing $FeCl_3$ with $Fe(SCN)_3$ can almost double the ORR activity, which may be related to S doping and high surface area. As reported previously,[390,391] the enhancing ORR performance can be explained by the redistribution of spin and charge densities originating from the dual doping of S and N atoms, which results in a large number of active carbon atoms in M−N−C catalysts thus improving the ORR activity. When this S-doped Fe−N−C catalyst was employed as a cathode catalyst in an H_2-O_2 cell, the maximal power density can even exceed 1.0 W cm^{-2}.[368]

https://dx.doi.org/10.1021/acs.chemrev.0c00594
Chem. Rev. 2020, 120, 12217−12314

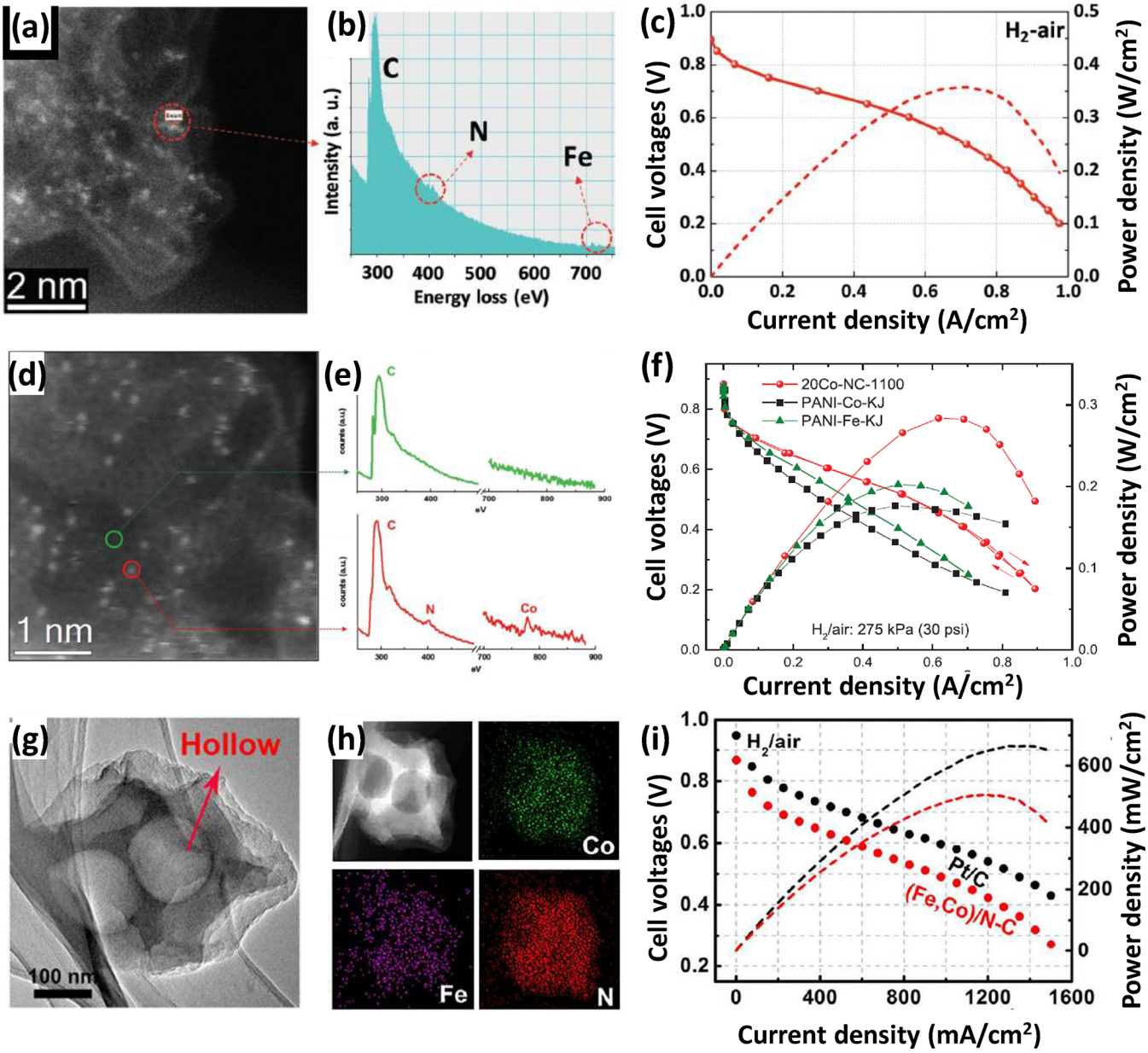

Figure 62. (a,b) Atomic dispersion of Fe sites in Fe-doped ZIF catalysts. (c) Fuel cell performance of the 1.5Fe-ZIF catalyst. Reproduced with permission from ref 290. Copyright 2019 The Royal Society of Chemistry. (d,e) STEM image and element analysis and (f) fuel cell performance for the best performing 20Co-NC-1100 catalysts. Reproduced with permission from ref 392. Copyright 2018 John Wiley and Sons. (g) HRTEM image, (h) corresponding EELS mapping images of Co, Fe and N, and (i) H_2/air fuel cell polarization plots of (Fe, Co)/N−C catalyst. Reproduced with permission from ref 390. Copyright 2017 American Chemical Society.

Furthermore, to avoid possible Fenton reactions caused by iron from severely damaging organic ionomers and membranes, Pt-free and Fe-free cathode catalysts are urgently needed for durable and inexpensive PEMFCs. Herein, Wu's research team synthesized a high-performance single-atom Co−N−C catalyst derived from Co-doped MOFs by one-step thermal activation.[392] By studying the effects of Co doping content and thermal treatment temperature, the optimal single-atom Co−N−C catalyst showed considerable activity and stability in acidic media and promising fuel cell performance (Figure 62).[392] It is expected that increasing the single-atom metal loading will lead to maximum improvement in its overall electrochemical performance. Thus, the same group developed a new type of single-atom Co−N−C catalyst with double-active sites density by a surfactant-assisted MOFs method, which attributed to the confinement effect between the surfactant F127 and MOFs to alleviate agglomeration of the active sites and reduce the damage to the microporous structure during the high-temperature pyrolysis. This catalyst has a very high initial performance with a maximum power density of 0.87 W cm^{-2} and encouraging durability in H_2−O_2 fuel cells, and represents the highest reported PGM-free and Fe-free catalyst performance.[378] According to DFT calculations, a large number of CoN_{2+2} sites in this Co−N−C@F127 catalyst, instead of traditional CoN_4 sites, were considered to be more active and have a thermodynamic advantage for the four-electron ORR pathway. In the meantime, Xiao et al., also designed a new binuclear active

https://dx.doi.org/10.1021/acs.chemrev.0c00594
Chem. Rev. 2020, 120, 12217−12314

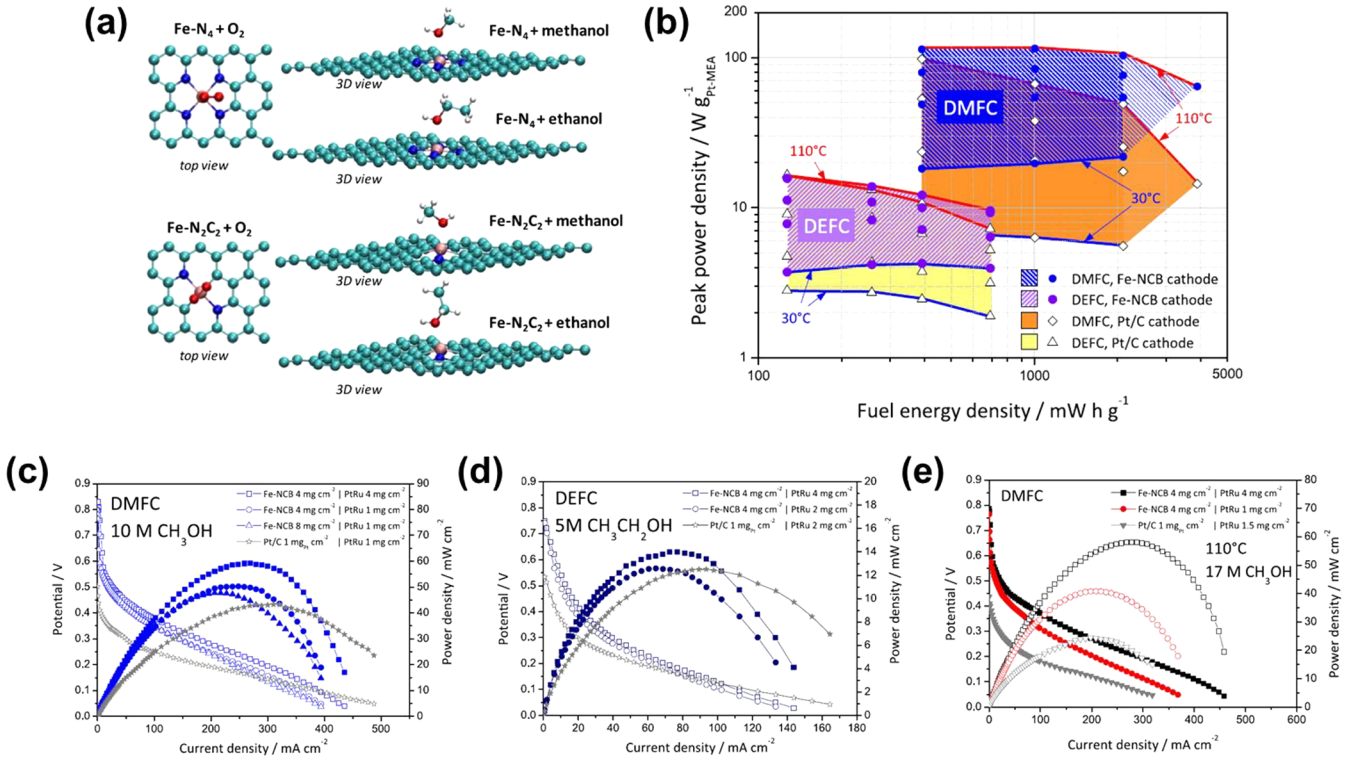

Figure 63. (a) DFT optimized structures of Fe−N_4 and Fe−N_2C_2 sites with adsorbed methanol and ethanol. (b) The ragone-like plot of the DMFC and DEFC experimental results and the fuel energy density according to alcohol concentration. Effect of electrodes composition and loading on the performance of (c) DMFC and (d) DEFC. (e) DMFC polarization and power density curves at high temperature (110 °C) and high methanol concentration (17 M). Reproduced with permission from ref 397. Copyright 2017 Elsevier.

site structure Co_2N_5, whose ORR activity was about 12 times higher than that of the conventional CoN_4 site, according to the theoretical calculation, which suggests that the preadsorbed OH on Co_2N_5 can act as a modified ligand to promote the *OH → H_2O reaction.[392] Even at U = 0.52 V, no thermodynamic barrier was found at the Co_2N_5 (OH) position, and a 0.115 eV barrier occurred on CoN_4, which suppressed the spontaneous ORR process. Despite the unusual catalytic activity of the corresponding catalyst in acidic electrolytes, more efforts should be invested to explore its practical PEMFC performance.

Recently, researchers predict that the performance of single-atom catalysts can be further improved by the rational design of double-metal active site structure, although it is very challenging. A new type of electrocatalyst with Fe−Co dual metal sites embedded on N-doped porous carbon was constructed via a host−guest strategy, demonstrating its superior activity and durability for the ORR in acidic media and in H_2/O_2 and H_2/air conditions (Figure 62g−i).[390] On the basis of DFT calculations, it reveals that the (Fe, Co)/N−C dual-site is favorable for the facial cleavage of the O−O bond to achieve the high activity for ORR and high selectivity to the four-electron reduction pathway. The underlying reason was attributed to the strong binding of O_2 on Fe−Co dual-site as well as the Fe−Co dual sites for the dissociated O atoms. Therefore, the design and fabrication of dual-atom and/or multiatom PGM-free catalysts seems to be a key research goal to achieve improved performance in PEMFCs application.

6.6.2. Direct Methanol Fuel Cells (DMFCs). Compared with other PEMFC technologies, DMFCs are expected to become portable power sources, due to the high energy density of methanol and bypassing the fuel barriers of storing hydrogen as fuel.[393] However, their performance is limited by various factors, especially the crossover of methanol from the anode to the cathode of the cell. Due to the intrinsic high tolerance of methanol by PGM-free catalysts, the development of DMFCs provides new opportunities for single-atom PGM-free catalysts to replace expensive Pt-based cathode catalysts.[394,395] For example, Gu et al. used a single-atom Fe−N−C cathode catalyst in DMFCs, showing an encouraging performance with a maximum power density of 33 mW cm^{-2} in alkaline media and 47 mW cm^{-2} in acidic media.[396] Detailed studies on the composition-structure−property correlation suggest that Fe−N_4 sites, along with graphitic-N and pyridinic-N, were useful for ORR.

Compared with that in alkaline media, the ORR performance of single-atom PGM-free materials in acid is not satisfactory for Pt substitution, due to reduced electron-transfer kinetics.[383] In one study as shown in Figure 63a, DFT calculations proved for the first time that Fe−N_4 and Fe−N_2C_2 active sites preferentially adsorbed O_2 with a much higher energy than methanol and ethanol, while nitrogen−carbon related sites (pyridinic and graphitic nitrogen) are much less selective for ORR.[397] Half-cell electrochemical results verified that the Fe−N−C catalyst is superior to Pt in acidic electrolytes containing methanol or ethanol at concentrations as low as 0.01 M (Figure 63b). At high methanol (up to 17 M) and ethanol (up to 5 M) concentrations (Figure 63c−e), Fe−N−C cathode catalysts have proven beneficial for the DMFCs. Also, Lo Vecchio et al. and Osmieri et al. reviewed the latest research on single-atom PGM-free catalysts to explore their potential applications in DMFCs cathodes.[398,399] The synthesis

https://dx.doi.org/10.1021/acs.chemrev.0c00594
Chem. Rev. 2020, 120, 12217−12314

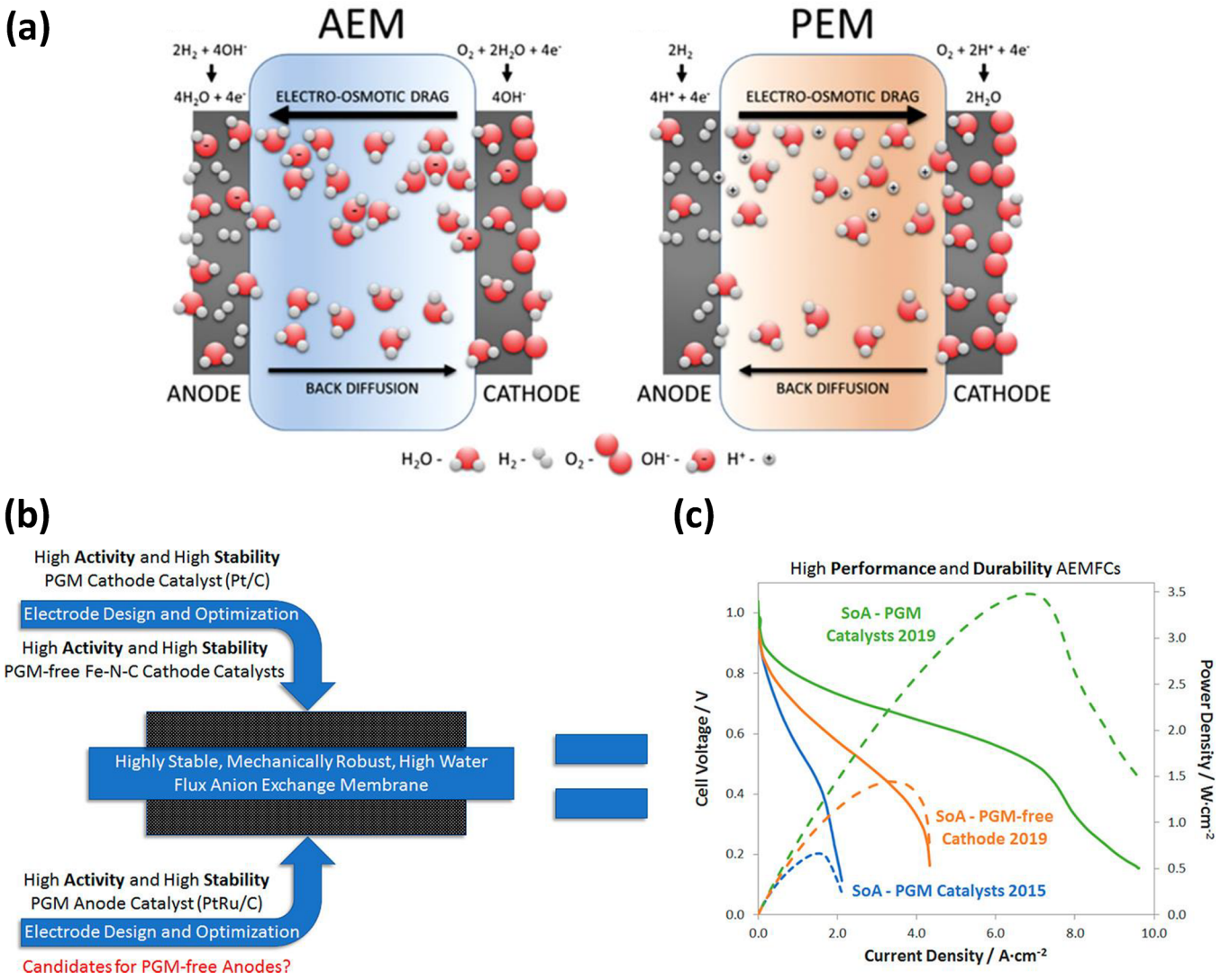

Figure 64. (a) Difference in water production and consumption in AEMFCs and PEMFCs. (b) Schematic of AEMFC, and (c) polarization and power curves for an AEMFC using a Fe−N−C cathode. Reproduced with permission from ref 404. Copyright 2019 American Chemical Society.

involved different metals, nitrogen, and carbon sources, and the structures were correlated with the ORR activity and cathode performance and methanol tolerance in DMFCs. There are some analogies between the data obtained in RDE and DMFCs: (1) iron is the highest performing metal in M−N−C catalysts, compared to cobalt and nickel so far, and (2) the most suitable nitrogen precursors (porphyrins, phthalocyanines, etc.) contain aromatic conjugated double bonds capable of supplying electrons to the positively charged metal.

6.6.3. Alkaline Anion Exchange Membrane Fuel Cells (AEMFCs). Despite the application of low-temperature PEMFCs in automobiles, such as Toyota Mirai, cost and durability remain the biggest challenges for large-scale commercialization.[400] Especially, recent results indicate that although high microporosity of single-atom M−N−C catalysts may have a high initial activity in PEMFC, water flooding of micropores on the cathode will cause a rapid loss of catalytic activity.[401] Encouragingly, the utilization of AEMFCs can easily avoid this issue, because water forms on the anode (Figure 64a). Also, the ORR activity of single-atom M−N−C catalysts is generally higher in alkaline media than in acidic media. Therefore, alkaline fuel cells have attracted much attention, mainly due to the use of PGM-free catalysts exclusively on the cathode side of the MEA.[402,403] For example, Palaniselvam et al. proposed a novel approach to prepare a bimetallic Fe,Co−M−C catalyst for AEMFCs, through establishing the bimetallic M−N coordination assisted by utilizing edge-site in the N-doped porous graphene.[391] The obtained catalyst, when used as a cathode catalyst, was found to help significantly reduce the ORR overpotential in alkaline solution and provide a maximum power density of about 35 mW cm^{-2} in a single cell of an AEMFC. This study predicted that the following four different factors are responsible for the realization of PGM-free SAEC in AEMFC application: (1) carbon with defect sites, (2) metal precursors with Fe or Co or all with Fe, (3) nitrogen-rich precursors, and (4) surface functional groups on the carbon support. However, the exact structural properties and quantification of different entities in these active sites are still unclear. A detailed inspection should be further conducted to clarify these useful parameters. Firouzjaie et al. summarized recent promising approaches to obtain highly efficient and durable PGM-free catalysts for AEMFCs and provided perspectives to advance the AEMFCs catalysts, such as increasing the number of active sites and

https://dx.doi.org/10.1021/acs.chemrev.0c00594
Chem. Rev. 2020, 120, 12217−12314

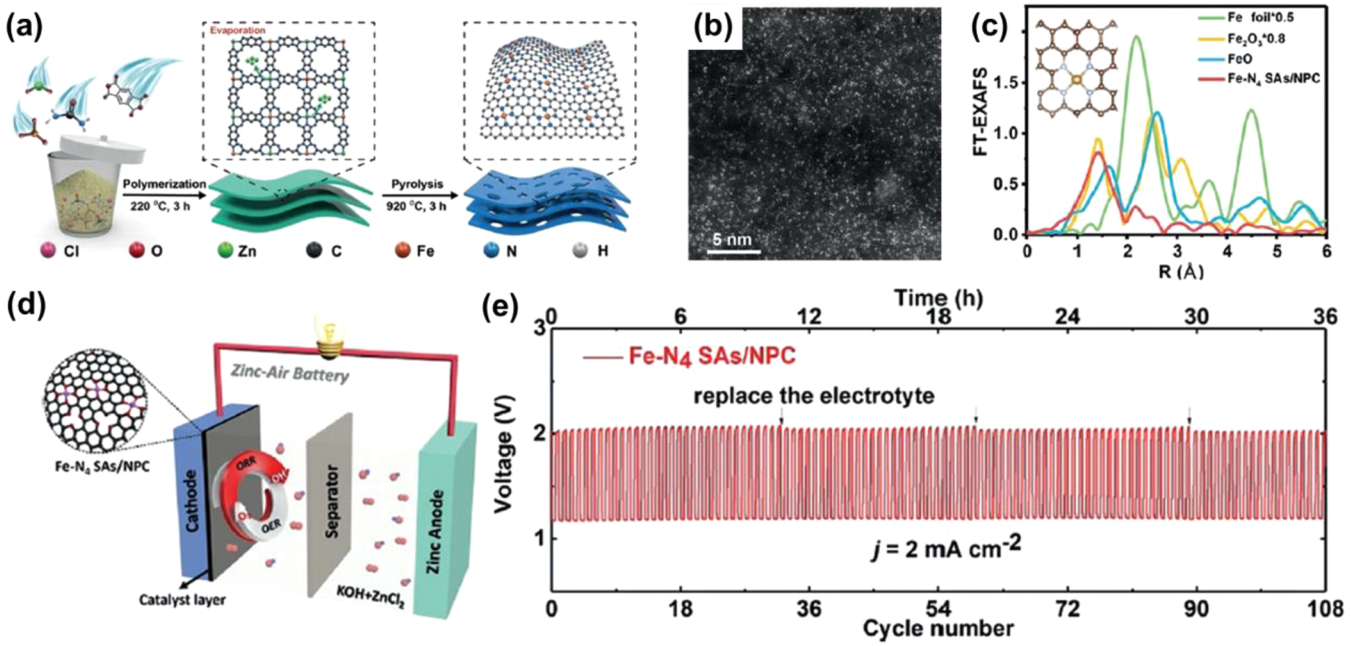

Figure 65. (a) Synthesis, (b) AC HAADF-STEM image, and (c) XANES of FT at R space of the Fe−N_4 SAs/NPC. (d) Representation and (e) charge−discharge cycling performance of Zn−air battery. Reproduced with permission from ref 196. Copyright 2018 John Wiley and Sons.

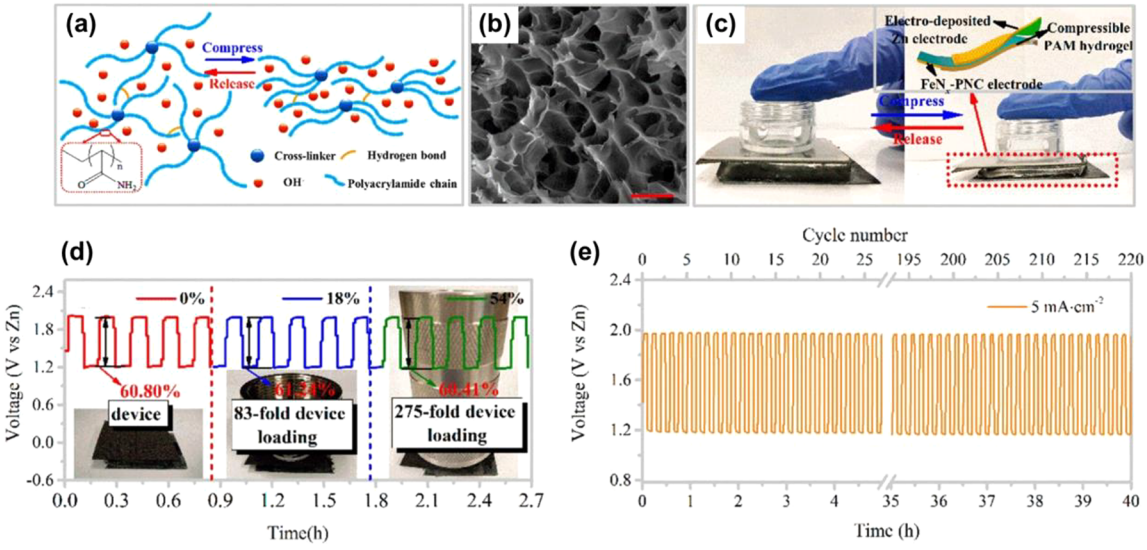

Figure 66. (a) Schematic diagram of the origin of high compressibility for PAM hydrogel electrolyte. (b) SEM image of freeze-dried polyacrylamide (PAM) hydrogel. (c) Compression−release process of the as-assembled compressible zinc−air battery, the inset is the schematic diagram of the construction process for the solid-state zinc−air battery. (d) Galvanostatic discharge−charge cycling curves and (e) cycling measurements for rechargeability at a current density of 5 mA cm^{-2}. Reproduced with permission from ref 414. Copyright 2018 Nature Publishing Group.

optimizing the cathode electrodes structure.[404] Furthermore, they fabricated an AEMFC cathode with highly active state-of-the-art Fe−N−C catalysts to achieve a record peak power density of 1.44 W cm^{-2} through employing their electrode manufacturing technology (Figure 64b,c).[404,405] Their work provides new ideas for the design and optimization of AEMFCs.

6.6.4. Metal−Air Batteries. Because of the high theoretical energy output, metal−air batteries represent a class of promising power devices that can be used for energy storage in next-generation electronic equipment, electrified transportation, and energy storage.[323,352,406−408] Among different types of metal−air batteries, primary Zn−air batteries have been commercialized as hearing-aid batteries; Al−air and Mg−air batteries have also found in military applications.[409−411] Recently, a simple and effective polymerization−pyrolysis−evaporation strategy was proposed to synthesize a single-atom Fe−N−C catalyst derived from predesigned bimetal Zn/Fe polyphthalocyanine (Figure 65a,c).[196] DFT calculations were then conducted to explain the vital role of Fe−N_4 catalytic sites in promoting ORR and OER, in which the Fe−N_4 sites showed a lower free energy during the ORR process as well as a lower theoretical overpotential for the conversion of rate-determining O* into OOH* step during the OER process of

https://dx.doi.org/10.1021/acs.chemrev.0c00594
Chem. Rev. 2020, 120, 12217−12314

Table 3. Catalytic Performance of SAECs toward ORR

catalysts	electrolyte	electron transfer number	half-wave potential (V vs RHE)	onset potential (V vs RHE)	ref
Pt_1−N/BP	0.1 M $HClO_4$	4	0.76	∼0.9	51
Pt_1−N/BP	0.1 M KOH	4	0.87	>0.9	51
Ir-SAC	0.1 M $HClO_4$	4	0.864	0.97	298
Fe-ISAs/CN	0.1 M KOH	4	0.9	0.986	36
5% Fe−N/C	0.5 M H_2SO_4	4	0.735	0.861	312
1.5Fe-ZIF	0.5 M H_2SO_4	4	0.88	0.98	290
S, N−Fe/N/C−CNT	0.1 M KOH	4	0.85	>0.9	50
Fe-ZIF 50 nm	0.5 M H_2SO_4	4	0.85	>0.9	15
TPI@Z8(SiO_2)-650-C	0.5 M H_2SO_4	4	0.823	∼0.9	47
TPI@Z8−650-C	0.5 M H_2SO_4	4	0.811	∼0.9	47
Co SAs/N−C(800)	0.1 M KOH	4	0.881	0.982	321
Co−N−C@F127	0.5 M H_2SO_4	4	0.84	0.93	322
20Co-NC-1100	0.5 M H_2SO_4	4	0.8	0.93	392
f-MnNC/CNT-170	0.1 M KOH	4	0.83	0.91	324
Mn@NG	0.1 M KOH	4	0.82	0.95	325
Mn/C-NO	0.1 M KOH	4	0.86	0.94	326
20Mn-NC-second	0.5 M H_2SO_4	4	0.8	>0.95	39
(Fe,Co)/N−C	0.1 M $HClO_4$	4	0.863	1.06	390
Co−N−C-10	0.1 M $HClO_4$	4	0.79	0.92	392
ZIF/MIL-10-900	0.1 M $HClO_4$	4	0.79	∼1.0	383
Fe−N−C	0.1 M NaOH	4	0.88	1.08	396
Fe−N−C	0.1 M $HClO_4$	4	0.75	0.85	396
Fe/Co-NpGr	0.1 M KOH	4	>0.8	0.93	391
Fe−N_4 SAs/NPC	0.1 M KOH	4	0.885	0.972	196
meso/micro-FeCo-Nx-CN-30	0.1 M KOH	4	0.886	0.954	412
FeNx-PNC	0.1 M KOH	4	0.86	0.997	414

Fe−C_4 and Fe_6 clusters. The results suggest that the Fe−N_4 site can significantly improve the ORR and OER activity. Because of the synergy between Fe−N_4 catalytic sites and porous conductive carbon networks, this catalyst can be used as an efficient trifunctional electrocatalyst for Zn−air batteries (Figure 65d,e). This strategy is universal to obtain single-atom M−N−C catalysts (M = Co, Ni, Mn) by merely changing metal precursors. Besides, the choice of supports and their corresponding properties are essential for the design of single-atom PGM-free catalysts. An example was illustrated to discuss how nanoarchitectures, such as morphology and meso/microporosity of the carbon materials, influence the reversible oxygen catalytic activity and stability, where two types of templates, namely active metal salts and silica nanoparticles, were applied to achieve hierarchical meso/microporous FeCo−N−C catalysts.[412] The obtained catalyst demonstrated high and reversible oxygen electrocatalytic performances for both ORR and OER, further confirming its potential applications in rechargeable Zn-air batteries. The promising electrochemical activity can be attributed to the following factors: (1) carbon sheets can effectively enhance the transport of electrons and oxygen, (2) mesoporous/microporous structure is beneficial to the diffusion of gas and electrolyte during electrochemical reactions, and (3) the combination of Fe, Co, and N doping can adjust the electronic properties and surface polarity, thereby improving the activity of the catalyst.

The rapid rise of modern flexible electronic products has made our daily life move toward high-tech design, multifunctional experience, and user-friendly interface, such as roll-up displays, flexible smartphones, implantable biosensors, wearable devices, etc.[146] While attractive, the development of effective, flexible energy conversion and storage devices is still in its infancy and faces enormous challenges. The devices should meet unique requirements, such as high energy and power density, safe operation, nontoxicity, shape adaptability, and excellent flexibility.[413] Therefore, the compressible flexibility of batteries is a prerequisite for wearable electronic devices and/or portable electronic devices. For example, Ma et al. proposed a strategy to obtain a single-atom Fe−N−C catalyst on a two-dimensional high-graphite porous nitrogen-doped carbon layer as shown in Figure 66a,b, which achieved an excellent catalytic activity toward ORR/OER in alkaline media and good performance in a solid-state compressible and rechargeable Zn−air battery with a low charge−discharge voltage gap and a large power density (118 mW cm^{-2}) (Table 3).[414] It can be compressed to a strain of 54% and bent to 90° without any degradation in charge/discharge performance and output power (Figure 66c−e). The usage of polyacrylamide (PAM) hydrogel-based electrolyte with high compressibility and excellent ion conductivity is the key to develop a compressible solid zinc−air batteries with excellent compressible flexibility and outstanding electrochemical performance. The viable strategies for making highly efficient compressible and rechargeable Zn-air batteries may inspire the design and development of other functional electronic devices.

7. SINGLE-ATOM ELECTROCATALYSTS FOR CO_2 REDUCTION

7.1. Fundamentals of CO_2 Reduction Electrocatalysis

Anthropological accumulation of carbon in the atmosphere due to combustion of fossil fuels has caused a series of environmental and sustainability challenges.[415] As the cost of renewable electricity generated from solar, wind, hydropower, etc., has been decreasing substantially,[416] electrochemical reduction of carbon dioxide (CO_2) to value-added fuels and chemicals becomes a promising approach to closing the carbon

https://dx.doi.org/10.1021/acs.chemrev.0c00594
Chem. Rev. 2020, 120, 12217−12314

Table 4. Standard Reduction Potentials (E^0) for Major Product in CO2RR

product name	reactions	E^0 (V vs RHE)
carbon monoxide	$CO_2 + 2H^+ + 2e^- \rightarrow CO_{(g)} + H_2O$	−0.10
formic acid	$CO_2 + H^+ + 2e^- \rightarrow HCOOH_{(aq)}$	−0.12
methanol	$CO_2 + 6H^+ + 6e^- \rightarrow CH_3OH + H_2O$	0.03
methane	$CO_2 + 8H^+ + 8e^- \rightarrow CH_4 + 2H_2O$	0.17
acetic acid	$2CO_2 + 8H^+ + 8e^- \rightarrow CH_3COOH_{(aq)} + 2H_2O$	0.11
ethanol	$2CO_2 + 12H^+ + 12e^- \rightarrow C_2H_5OH + 3H_2O$	0.08
ethylene	$2CO_2 + 12H^+ + 12e^- \rightarrow C_2H_4 + 4H_2O$	0.07
n-propanol	$3CO_2 + 18H^+ + 18e^- \rightarrow C_3H_7OH + 5H_2O$	0.10

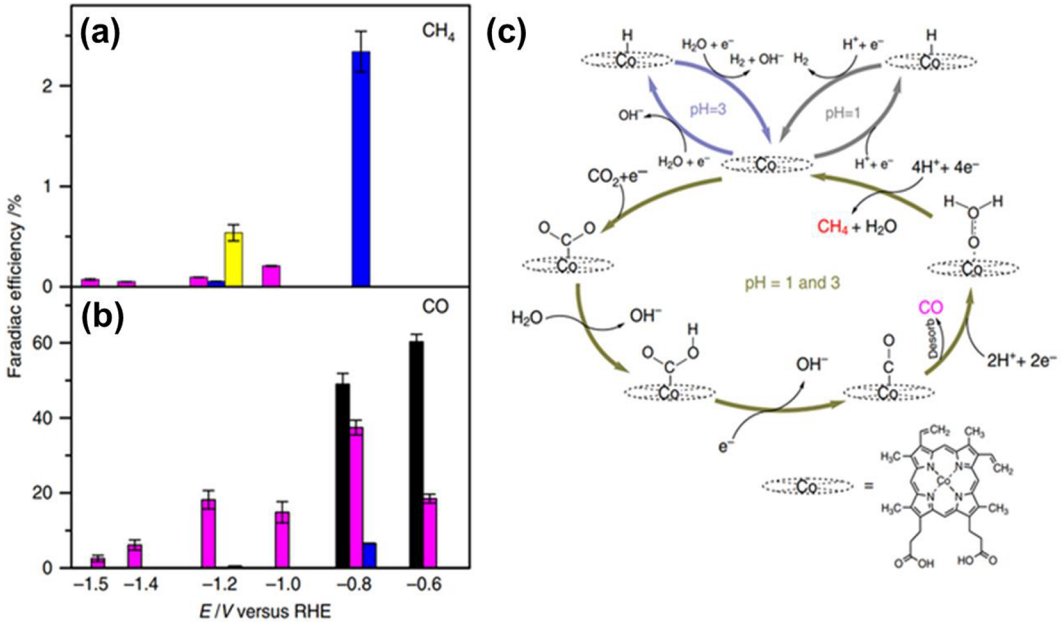

Figure 67. Faradaic efficiencies to CO and CH_4 were determined for yellow bars, pH = 1, P_{CO2} = 1 atm; blue bars, pH = 1, P_{CO2} = 10 atm; magenta bars, pH = 3, P_{CO2} = 1 atm; black bars pH = 3, P_{CO2} = 10 atm. FE for (a) methane and (b) carbon monoxide of CO_2 electroreduction at different potential. (c) Schematic mechanism of CO_2 reduction reaction on cobalt protoporphyrin in acidic environment. Reproduced with permission from ref 447. Copyright 2015 Nature Publishing Group.

cycle and utilization of off-peak, intermittent renewable electricity. Over the past 30 years, a variety of metal electrocatalysts have been studied,[417] and more than 16 products have been identified.[418] Late transition metals, such as Au and Ag, are typically active for the selective reduction of CO_2 to CO. For example, the Faradaic efficiency (FE) of carbon monoxide (CO) production could exceed 90% with Au- and Ag-based electrocatalysts.[17,50,419−423] Copper (Cu) is unique as the only metal known for the production of (oxygenated) hydrocarbons from the electroreduction of CO_2, capable of generating methane,[418,424] ethylene,[425,426] acetate,[427] or ethanol[428] at significant rates. With the increasing attention to carbon emission, escalating efforts have been devoted to understanding the reaction mechanisms and structure−property relationships of electrocatalysts for the CO2RR.

Table 4 lists the typical products obtained from the CO2RR and the corresponding equilibrium potentials. In the reversible hydrogen electrode (RHE) scale, the equilibrium potentials (E^0) of most products are above 0 V, meaning that the reaction is thermodynamically more favorable than the HER. However, the kinetics of CO2RR is usually much more sluggish than that of HER, with the latter becoming a significant or dominant pathway on many electrodes.[429] The activation of CO_2, a chemically inert molecule, is often argued to be the rate-determining step for the overall process of CO2RR electrocatalysis and determine the overpotential (η),[430,431] although different mechanisms have been proposed to interpret the selective production of C_2 hydrocarbons (e.g., ethylene) on Cu-based electrocatalysts.[432,433] The catalytic activity and selectivity of CO2RR electrocatalysts largely governs the energy efficiency of CO_2 reduction (the cathodic half-cell reaction of a CO_2 electrolyzer) as

$$E_{\text{energy}} = \frac{E^0}{E^0 + \eta} \times \text{FE}_{\text{CO2}} \tag{31}$$

although one should notice that the overall cell performance is also dependent on the anodic reaction (typically OER), transport, and ohmic losses, etc.[434]

Compared to metallic electrodes or electrocatalysts, SAECs containing cationic metal centers are advantageous for CO_2 reduction. The SAECs not only have a high utilization of the metal sites but are also able to stabilize carbonaceous reaction intermediates (e.g., $CO_2^{\cdot-}$) and restrict the configurations of adsorbates, giving rise to enhanced catalytic activity and selectivity, respectively.[11] However, the carbon substrate and the heteroatomic dopants are usually active for the HER, reducing the FE of CO_2 reduction at the applied negative

https://dx.doi.org/10.1021/acs.chemrev.0c00594
Chem. Rev. 2020, 120, 12217−12314

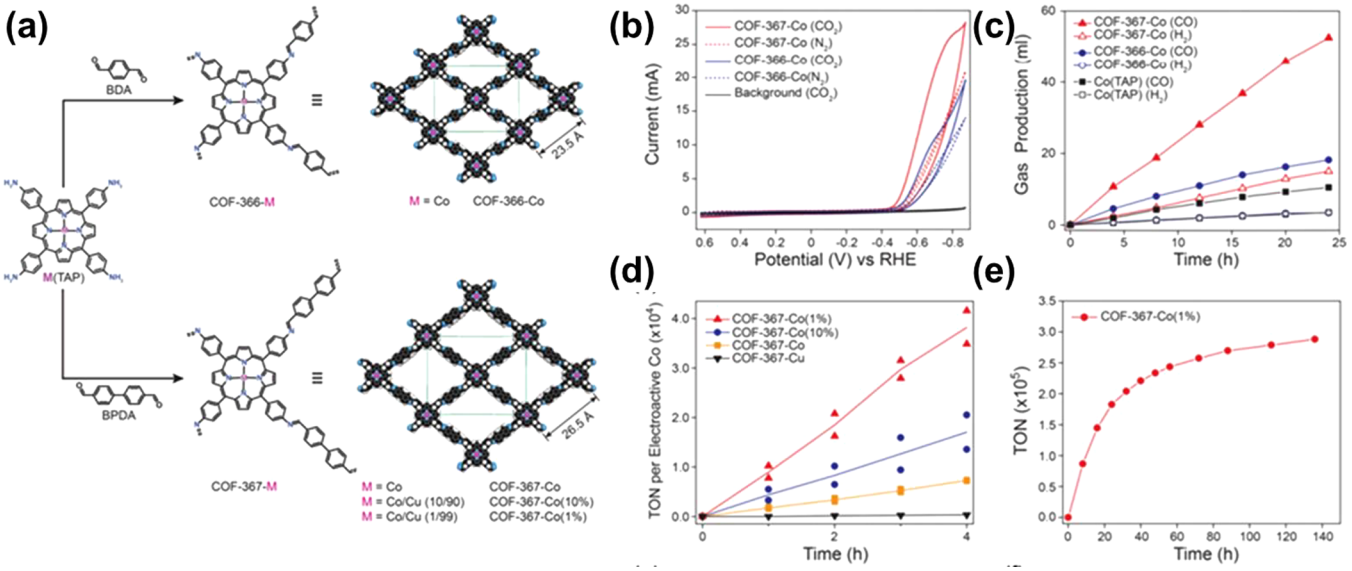

Figure 68. Schematic illustration of COF-366-M and COF-367-M (a). Cyclic voltammetry curve of the electrocatalysts in N_2 and CO_2 environment (b). Gas production performance of the electrocatalysts for CO and hydrogen (c). The turnover frequency per electroactive cobalt atom (d) and the turnover number (e) of the electrocatalysts with different Co loading. Reproduced with permission from ref 19. Copyright 2015 The American Association for the Advancement of Science.

potentials (vs RHE). How to tailor the atomic structures of the single-atom metal centers to balance these factors thus becomes pivotal for the development of SAECs for CO_2 reduction.

7.2. Molecular Electrocatalysts for CO_2 Reduction

Many metal complexes were found to be able to catalyze the CO2RR in the 1980s.[435] These molecular electrocatalysts are distinguished from the M−N−C type of SAECs that have attracted more attention recently by not having direct chemical bonding to a conductive substrate. Among a range of molecular complexes, metal porphyrins and metal phthalocyanines are the most attractive candidates, featuring long-term stability, reproducible performance, and potential for large-scale synthesis.[436−438] The coordination structure and chemical environment of the molecular catalysts are well-defined, which can be readily tuned to tailor the activity and selectivity for the CO2RR. With isolated active sites, supported molecular catalysts bridge the gap between heterogeneous catalysts and homogeneous catalysts, enabling distinct product selectivity from conventional catalysts with continual surfaces of active sites. However, the current density of CO2RR is usually quite low with molecular catalysts, mainly due to the poor conductivity as compared to metallic catalysts. The products derived from molecular catalysts are mostly limited to C_1 species, because C−C coupling typically requires adjacent active sites.[439]

Similar to enzymes present in nature for biochemical carbon conversion, metalloporphyrins do not only have excellent adsorption capacities for small molecules, such as oxygen and carbon dioxide, but also enable the efficient electron transfer from the metal centers to the adsorbates.[440,441] Behind these unique properties lies the great potential for catalyzing the electrochemical CO_2 reduction. After the initial report by Takahashi et al., porphyrin-based molecular catalysts have been studied for over 40 years.[442−446] Shen et al. studied the reaction mechanism of CO2RR on cobalt photoporphyrin through both pH-dependent electrochemical measurements and theoretical calculations.[447] The graphite-immobilized cobalt protoporphyrin can reduce CO_2 to CO and CH_4 in acidic solutions at potentials more negative than −0.5 V, with remarkable stability and high selectivity (FE_{CO} up to ∼60%) (Figure 67a,b). The rate-determining factor of the reaction pathway is determined to be the stabilization of a radical intermediate, $CO_2^{\cdot-}$, where the Co site behaves like a Brønsted base (Figure 67c).

To improve the conductivity of metalloporphyrins, various strategies have been investigated to immobilize the molecular catalyst on conductive substrates. Such immobilization is usually based on physical attachment and does not involve chemical bonding between the active center and the substrate, with the latter usually being the case for M−N−C type of SAECs to be discussed in the following sections. One effective way is to polymerize metalloporphyrin derivatives to obtain conductive polymers. Diercks et al. reported a two-dimensional covalent organic framework (COF) with cobalt porphyrin.[448] The thin-film COF enables efficient charge transfer, achieving a high Faradaic efficiency of over 87% toward carbon monoxide and a current density of 65 $mA{\cdot}cm^{-2}$ at −0.55 V. Lin et al. incorporated cobalt porphyrin into 3-dimensional COFs with different pore sizes (Figure 68a).[19] The 3D-COF with cobalt porphyrin demonstrated a turnover frequency of 290 000 h^{-1}, representing a 26-fold improvement in activity, as compared to molecular cobalt porphyrin complexes (Figure 68b−e). Besides immobilization, efforts have also been dedicated to atomic substitution of the macrocyclic ligand, aiming at tuning the geometric and electronic structures of the active center. Azcarate et al. introduced positively charged trimethylanilinium groups to iron tetraphenylporphyrins.[449] The modified catalyst achieved a high turnover frequency of 10^6 s^{-1} for the CO2RR, associated with a reduced Tafel slope.

One interesting phenomenon observed with metalloporphyrin electrocatalysts is the ability to catalyze CO2RR in the presence of oxygen. Mondal et al. found that CO2RR on iron porphyrin is 500 times faster than ORR, whereas the case is reversed on most metallic catalysts.[450] This finding is of interest for utilization of practical CO_2 sources (present in

https://dx.doi.org/10.1021/acs.chemrev.0c00594
Chem. Rev. 2020, 120, 12217−12314

power plants, cement factories, etc.) in which oxygen is usually present.[451,452]

Different from porphyrin that is a widely existing structure in nature, phthalocyanine is a completely synthetic compound. Discovered in 1907 as an unidentified blue compound, phthalocyanine has been widely used in dyeing.[453] The application of metal phthalocyanine in CO2RR was first reported by Hiratsuka et al. and has been studied to date.[454−457] Metal phthalocyanine, like most molecular catalysts, has the disadvantage of low charge-transfer efficiencies. To overcome this challenge, Han et al. developed a polymerized cobalt phthalocyanine electrocatalyst supported on carbon nanotubes.[458] The polymeric form of cobalt phthalocyanines has higher conductivity and larger electrochemically active surface area. As a result, this catalyst reached a CO Faradaic efficiency of >90% and a turnover rate of 4900 h^{-1} at −0.5 V. It was also demonstrated with long-term durability with no degradation in the activity or selectivity observed in 24 h of reaction. Ren et al. demonstrated a strategy to disperse the cobalt phthalocyanine on activated carbon with a high loading of 50 wt %. They fabricated GDEs with this catalyst and demonstrated over 150 mA·cm^{-2} of current density and 90% Faradaic efficiency toward CO.[20]

While molecular catalysts typically produce CO from the CO2RR, recent studies show that methanol, a desirable liquid product for the purpose of energy storage, can be generated with cobalt phthalocyanine catalysts.[81,459] Wu et al. found that the six-electron process of methanol synthesis can be achieved on carbon nanotube-supported cobalt phthalocyanine (CoPc/CNT), with a Faradaic efficiency of over 40% and a current density of 10 mA·cm^{-2} at −0.94 V (Figure 69).[81] In this process, carbon monoxide was found to be the key reaction intermediate, which was further reduced to methanol. The authors hypothesized that the CNT substrate might have played a synergistic role in catalyzing the CO_2-to-methanol conversion, because CoPc supported on other substrates, such as Vulcan XC72 and Ketjenblack (different types of carbon black), barely produced methanol from this reaction. They also argued the importance of the macrocycle structure in CoPc, as none of the other cobalt macrocycle complexes, such as cobalt chlorin and cobalt porphyrin, has the same methanol production activity.

In addition to metal porphyrins and phthalocyanines, other types of metal macrocylic complexes have also been studied for the CO2RR. For example, Reuillard et al. reported a Mn(bipyridine)-pyrene catalyst for CO_2 electroreduction.[460] This complex was immobilized on multiwalled carbon nanotubes. In situ infrared spectroscopy and electrochemical studies show that CO is the favored product (FE_{CO} = 34%) at high Mn loadings, whereas formate becomes the major product ($FE_{formate}$ = 8%) at low loadings. It can be seen from the above general discussion that the various immobilized molecular electrocatalysts typically involve isolated metal sites that serve as the active centers for the CO2RR. In the following sections, we aim to further discuss the M−N−C type of SAECs for the CO2RR based on the metal being involved as the active site.

7.3. Fe-based Single-Atom Electrocatalysts

As early as 1985, Hori et al. reported the study of metallic Fe electrode for CO_2 electrolysis in aqueous carbonate electrolytes. In this experiment, the Fe electrode was found to produce mainly hydrogen, with FE_{H2} being >95%.[461] Follow-up research by the same group confirmed the inactive nature of

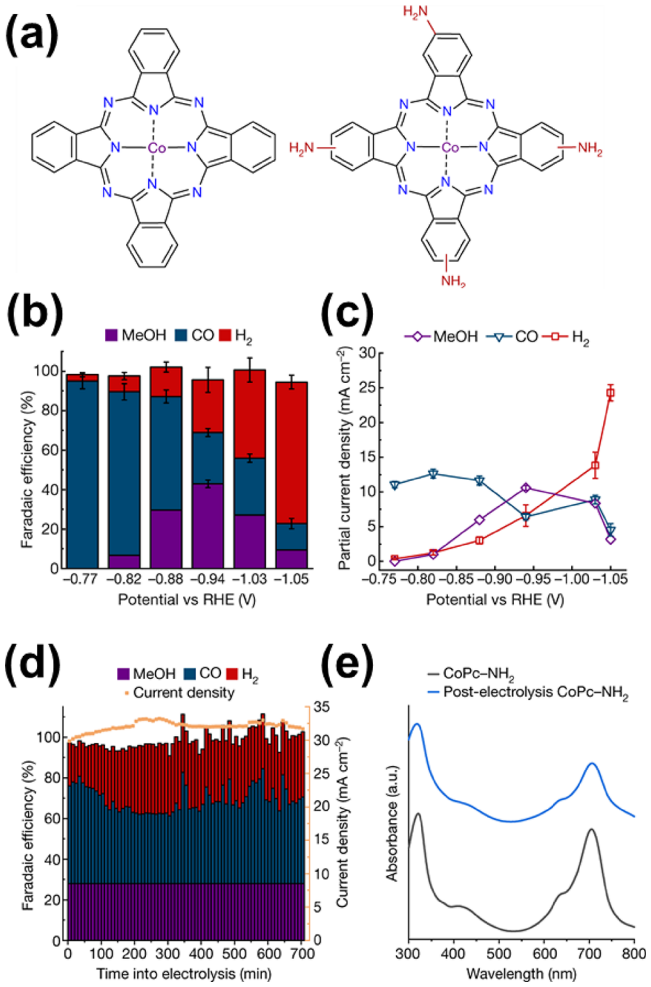

Figure 69. Molecular structure of CoPc and CoPc-NH_2 (a). Faradaic efficiency (b) and partial current density (c) toward MeOH, CO, and H_2 of CoPc/CNT at different potentials. Stability study of CoPc-NH_2 (d) and the inferred spectra of CoPc-NH_2 before and after the stability study (e). Reproduced with permission from ref 81. Copyright 2019 Nature Publishing Group.

metallic Fe in CO_2 reduction.[417,462] Since then, Fe as an electrocatalyst has not attracted much research interest for the CO2RR, until the demonstration of $Fe^{\delta+}-N_x$ centers being active for this reaction by Strasser and co-workers in 2015.[463] They found that single atoms of Fe coordinated on N-doped carbon (Fe−N−C, Figure 70a) could achieve >80% FE_{CO} at a current density of 35 mA cm^{-2}, which is comparable to the CO2RR activity of Au foil, one of the most active metal catalysts for electroreduction of CO_2 to CO. The onset potential was also found to be reduced by 100 mV, as compared to the Au benchmark. They proposed that $M-N_4$ type of moieties account for the formation of CO.

In a later study by Huan et al., $Fe-N_4$ was confirmed to be the active site for CO_2 reduction to CO by comparing Fe nanoparticles and $Fe-N_4$ moieties on N-doped carbon (Figure 70b).[464] The $Fe-N_4$ structure was identified by EXAFS measurements. Catalysts with homogeneous $Fe-N_4$ active sites could achieve a FE_{CO} of 80%, while Fe nanoparticles produced mostly H_2. Ye et al. reported the copyrolysis of ammonium ferric citrate and ZIF-8 to derive Fe−N−C and achieved 89.1% of FE toward CO.[310] Tour and co-workers dispersed Fe single atoms on N-doped graphene at 1.25 wt %

https://dx.doi.org/10.1021/acs.chemrev.0c00594
Chem. Rev. 2020, 120, 12217−12314

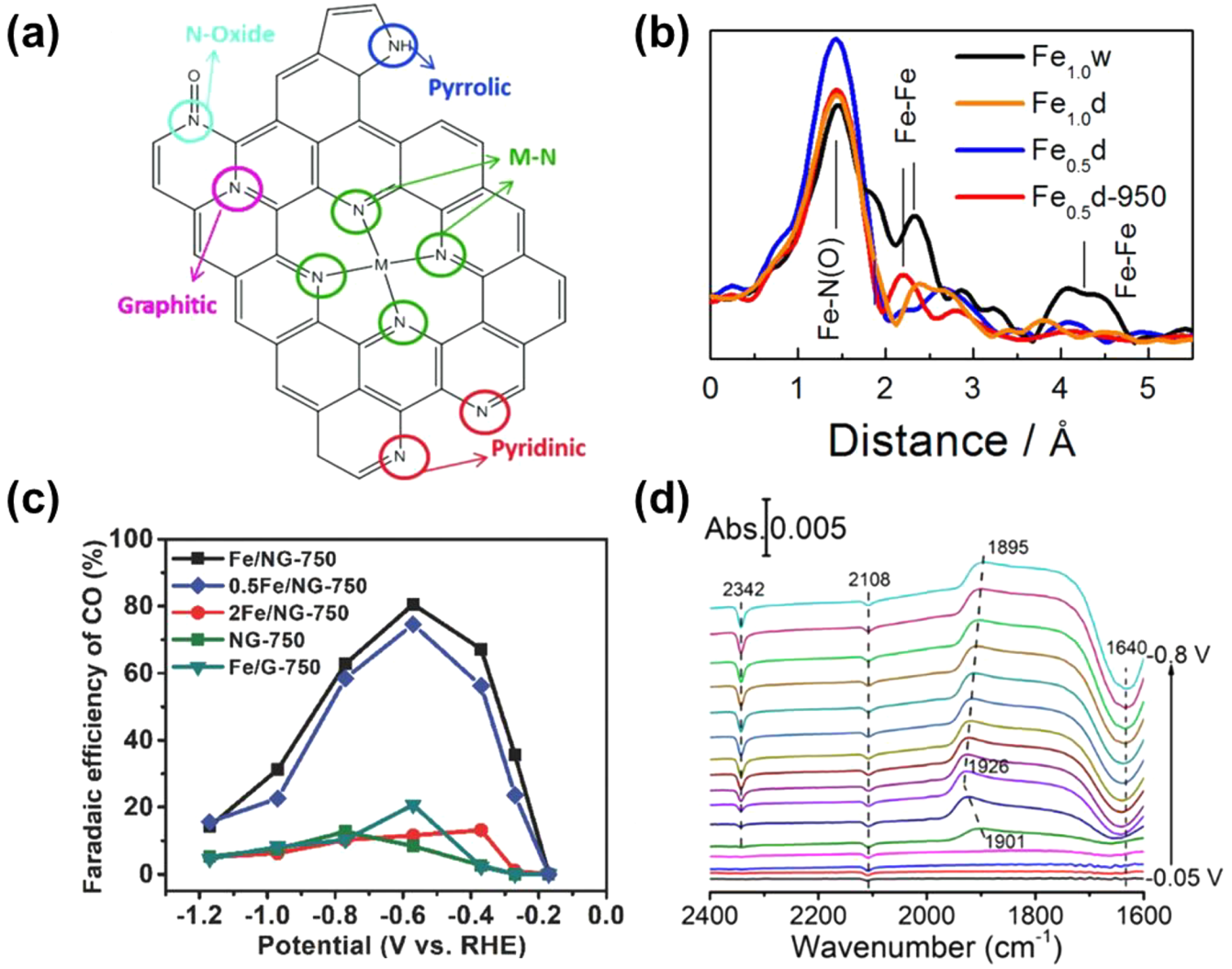

Figure 70. (a) Structural models of nitrogen atoms in various chemical environments in the N−C catalyst. Reproduced with permission from ref 463. Copyright 2015 John Wiley and Sons. (b) k^2-weighted Fourier transforms of the experimental EXAFS spectra. Mössbauer and EXAFS spectra of $Fe_{1.0}$d, $Fe_{0.5}$d, $Fe_{0.5}$d-950, and $Fe_{1.0}$w have been already reported separately. Reproduced with permission from ref 464. Copyright 2017 American Chemical Society. (c) FE of CO for electrochemical CO_2 reduction in case of Fe/NG control samples prepared under different conditions in comparison with Fe/NG-750. Reproduced with permission from ref 69. Copyright 2018 John Wiley and Sons. (d) Real-time ATR-IR spectra recorded while stepping the potential of the Fe−N−C-loaded Au/Si prism in the CO_2-saturated 0.5 M $KHCO_3$. Reproduced with permission from ref 140. Copyright 2019 American Chemical Society.

of Fe loading (Figure 70c).[69] They identified a +2 oxidation state for Fe within the Fe−N_4 motifs, which were believed to be the active sites for the CO2RR. A promotion effect of neighboring nitrogen dopants on the graphene substrate was further claimed to be beneficial for the electrocatalytic process on this catalyst. A recent study by Shao and co-workers used in situ infrared absorption spectroscopy in an attenuated total reflection mode (ATR-IR) to study the adsorption of *CO on Fe SAECs (Figure 70d).[140] The band near 1900 cm^{-1} was attributed to the adsorption of *CO on Fe−N_4 moieties, which was absent from the spectra collected on the control (N−C) without metal doping.

Despite the aforementioned reports, debates remain about the active sites and corresponding mechanisms of CO2RR on Fe SAECs. For example, Fe−N_5 has recently been reported to be more active than Fe−N_4 (Figure 71a).[53] Zhang et al. obtained 97% of FE_{CO} in their study of CO2RR on Fe and N codoped multilayer graphene. On the basis of DFT calculations, they claimed that a fifth N on the underlying layer of graphene coordinates to Fe^{3+} to form Fe−N_5 centers, with the additional pyrrolic N atom depleting the 3*d* electron density of Fe and reduces the π back-donation of Fe−CO binding, which is believed to be beneficial for facilitating CO desorption. Deng and co-workers have reported Fe SAECs confined in carbon foams and also attributed the active sites to Fe−N_4.[465] Interestingly, they have detected the Fe^{3+} species in their Fe SAECs using XPS, corroborating the role of Fe^{3+} in CO_2 electrolysis. Recently, Gu et al. reported a Fe SAEC on N-doped carbon (Fe−N−C) that produces CO at an overpotential as low as 80 mV.[131] In situ XANES measurements confirmed the persistent presence of Fe^{3+} throughout the CO2RR (Figure 71b). They further compared Fe^{2+}−N−C and Fe^{3+}−N−C and concluded with superior activity for CO formation (FE_{CO} > 90%) on the latter catalyst, due to weaker CO absorption on the Fe^{3+} sites.

Although CO has been the primary product from the reported studies, Fe SAECs have the potential to produce hydrocarbons from CO2RR. An early study of Fe−N−C by

https://dx.doi.org/10.1021/acs.chemrev.0c00594
Chem. Rev. 2020, 120, 12217−12314

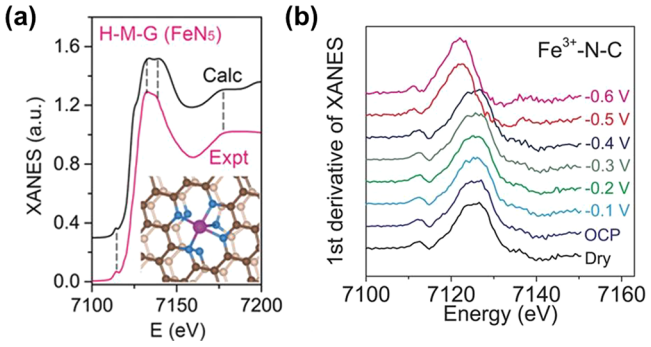

Figure 71. (a) Comparison of the experimental XANES curves with the calculated XANES data of and FeN_5. Reproduced with permission from ref 53. Copyright 2019 John Wiley and Sons. (b) First derivative of the Fe K-edge XANES spectra of Fe^{3+}−N−C as dry powder (black) and loaded on glassy carbon electrodes at open circuit potential (OCP) (blue), −0.1 V (light blue), −0.2 V (green), −0.3 V (dark green), −0.4 V (dark blue), −0.5 V (red), and −0.6 V (pink) versus RHE. Reproduced with permission from ref 131. Copyright 2019 The American Association for the Advancement of Science.

Varela et al. demonstrated 0.4% FE for CH_4 production at −0.9 V.[463,466] In a later in situ XAS study, Leonard et al. revealed the change of oxidation state from Fe^{2+} to Fe^{1+} in Fe−N−C under the reaction condition.[467] This Fe^{2+}/Fe^{1+} redox transition was believed to account for the formation of CH_4, as the transition potential coincided with the onset potential of CH_4 formation. In follow-up mechanistic studies, Strasser and co-workers proposed a reaction pathway on Fe−N−C for CH_4 production via CO intermediate and sequential steps of proton coupled electron transfer (PCET).[467,468]

7.4. Co-based Single-Atom Electrocatalysts

Over the past decades, cobalt-based molecular electrocatalysts have received intensive attention due to their CO2RR activity.[469−472] Although Co-based molecular catalysts, such as cobalt phthalocyanine and cobalt tetraphenylporphyrin, have been reported to be active for CO_2 reduction, early experimental studies have shown that the trend of CO_2-to-CO conversion reactivity in M−N−C type of SAECs follows Ni ≥ Fe ≫ Co in the coordination configuration of $M-N_4$.[473] It is interesting that the Co centers in the molecular electrocatalysts sit at the peak position of the volcano-type dependence of CO_2 reduction activity.[474] Given similar $Co-N_4$ coordination for the metal centers, the substantial difference in both adsorption properties and catalytic activity between the Co molecular catalysts (Co−Pc) and $Co-N_4-C$ suggests great research opportunities in engineering Co-based SAECs in the CO_2 reduction electrocatalysis.[475]

Considering a large effect of coordination number on the electronic structures of metal centers in SAECs, significant

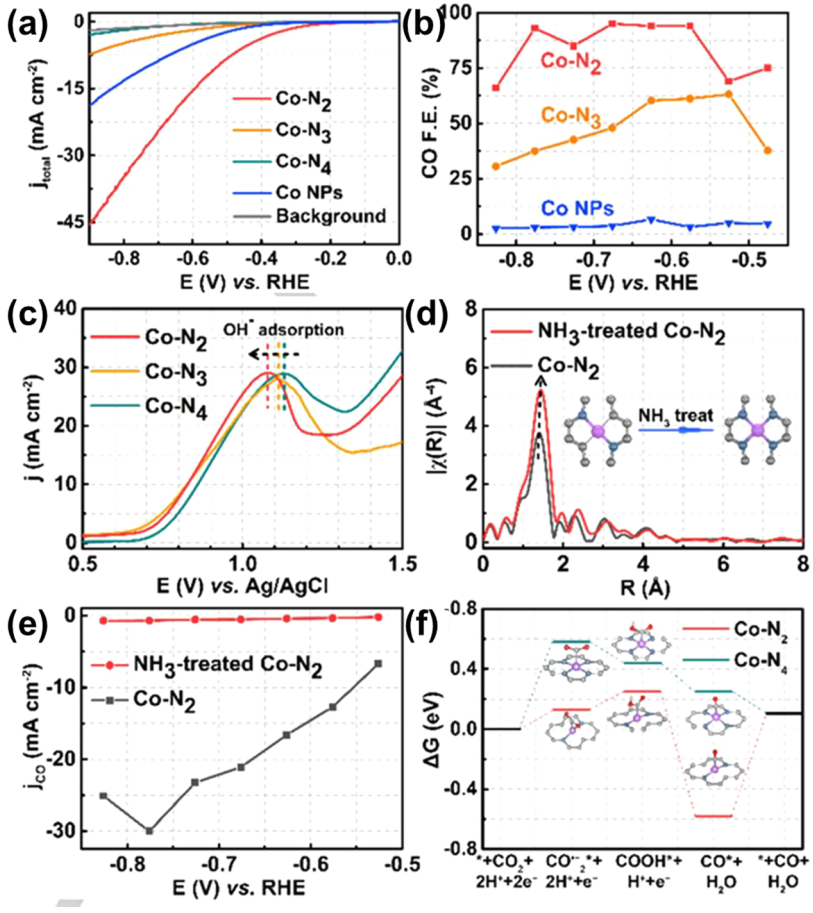

Figure 72. Linear scanning voltammetry curve (a) and OH adsorption activity (c) of Co SAECs with different nitrogen coordination numbers. The EXAFS spectra of the Co SAECs before and after NH_3 treatment (d). Partial current density toward carbon monoxide of Co SAECs before and after NH_3 treatment (e). DFT-calculated energy barriers of the CO_2 reduction reaction on $Co-N_2$ and $Co-N_4$. Reproduced with permission from ref 478. Copyright 2018 John Wiley and Sons.

https://dx.doi.org/10.1021/acs.chemrev.0c00594
Chem. Rev. 2020, 120, 12217−12314

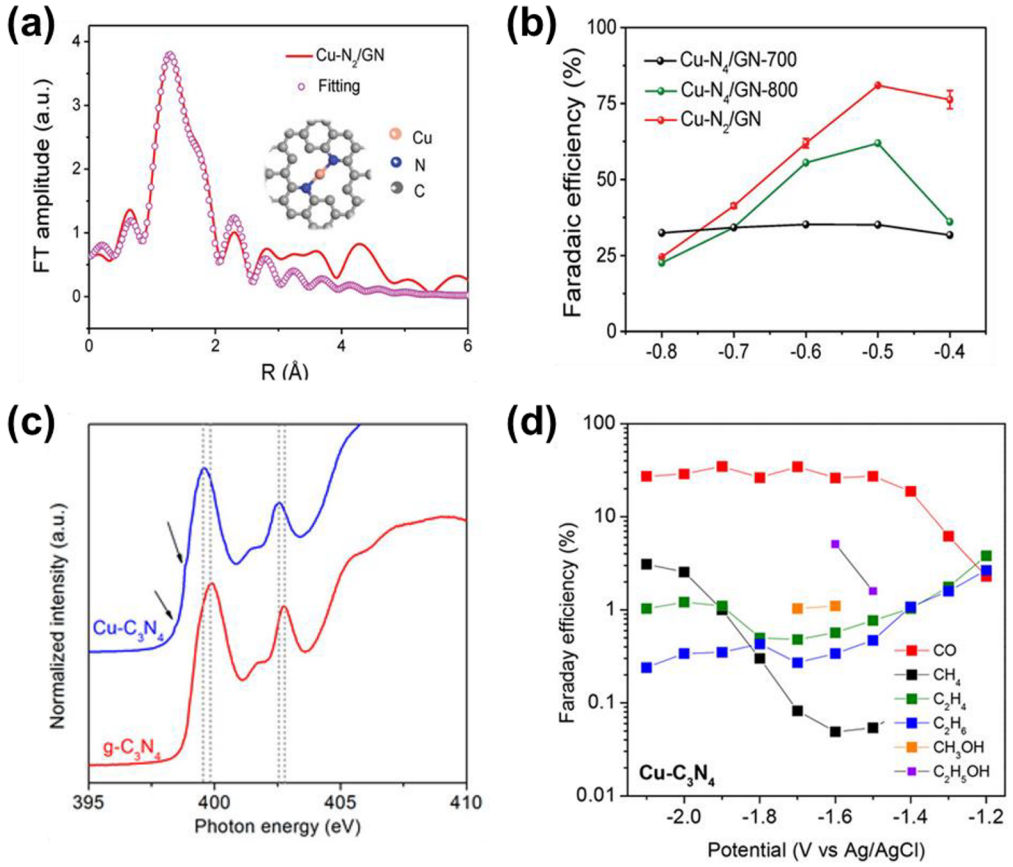

Figure 73. (a) FT-EXAFS fitting results of Cu−N_2/GN, (b) CO FE of Cu−N_4/GN-700, Cu−N_4/GN-800, and Cu−N_2/GN. Reproduced with permission from ref 52. Copyright 2020 John Wiley and Sons. (c) Nitrogen K-edge NEXAFS of Cu−C_3N_4 and pure g-C_3N_4. Arrows show the weak shoulders in the N K-edge assigned to the Cu−N interaction. Dotted lines show the channels of photon energy in the two samples, (d) Measured Faradaic efficiencies of various products on Cu−C_3N_4. Reproduced with permission from ref 486. Copyright 2017 American Chemical Society.

efforts have been devoted to the investigation of Co−N−C SAECs with different atomic structures. Wang et al. synthesized a series of atomically dispersed Co−N−C electrocatalysts with the metal−nitrogen coordination number varying from 2 to 4 by pyrolyzing Co/Zn ZIFs at controlled temperatures (Figure 72).[476,477] The catalytic activity for CO production was found to follow the trend Co−N_2 > Co−N_3 > Co−N_4, with Co−N_2 centers achieving a current density of 18.1 mA cm^{-2} and 94% for FE_{CO} at an overpotential of 520 mV. It was further shown by DFT calculations that, compared to Co−N_4−C, Co−N_2−C has lower energy barriers for activating CO_2 molecules to form $CO_2^{\cdot-}$, which benefits the CO production. In contrast, Pan et al. reported Co−N_5 as a more active center for the electroreduction of CO_2 to CO, achieving an FE_{CO} of >90% in the potential range between −0.57 and −0.88 V.[477] DFT calculations suggested a nearly zero thermodynamic barrier (0.02 eV) for COOH* formation on Co−N_5. Han et al. constructed a well-defined, two-dimensional assembly of metal−porphyrin complex and used it as a platform to perform coordination-dependent study of CO2RR.[478] They reported 96% FE toward CO at an overpotential of 500 mV and argued that the activity of CO_2 electroreduction was improved by a direct nitrogen coordination from the bottom layer, which elevated the d_z energy level of the metal atom. DFT calculations showed that the extra nitrogen bonding significantly reduced the thermodynamic barrier of *COOH formation by 0.76 eV, as compared to Co center without an extra nitrogen coordination. These studies indicate that it is plausible to modify the structures and properties of cobalt coordination to make the CO_2-to-CO conversion favorable on the Co SAECs.

7.5. Ni-based Single-Atom Electrocatalysts

Similar to cobalt and iron, the CO2RR activity of Ni can only be manifested in a single-atom configuration, whereas bulk Ni electrodes favor the evolution of hydrogen.[479] Among the various coordination structures, Ni−N_4−C is also the most widely studied and generally considered to be the active sites for the electroreduction of CO_2 to CO.[480] Li et al. developed controlled synthesis of Ni−N_4−C electrocatalysts using a topochemical transformation method.[481] In this approach, the Ni−N_4 structure was obtained by directly pyrolyzing nickel-doped g-C_3N_4 with a layer of carbon coating, through which the formation of other coordination structures or aggregation of Ni was believed to be avoided with the rationally designed precursor. The Ni−N_4−C electrocatalyst exhibited >90% FE toward CO in a wide range of potential, i.e., from −0.5 V to −0.9 V. DFT calculations indicate that the Ni−N_4−C sites have lower limiting overpotentials for CO_2 reduction, as compared to Ni−C (without N). Jiang et al. investigated a series of Ni SAECs supported on graphene nanosheets that have different substrate structures.[129] An FE_{CO} of 95% was achieved with this Ni SAEC at an overpotential of 0.55 V with excellent stability of over 20 h. In situ XAS measurement and DFT calculations identified different Ni atomic configurations in graphene vacancies, such as single vacancies (Ni@SV), double vacancies (Ni@DV), single vacancies with nitrogen

https://dx.doi.org/10.1021/acs.chemrev.0c00594
Chem. Rev. 2020, 120, 12217−12314

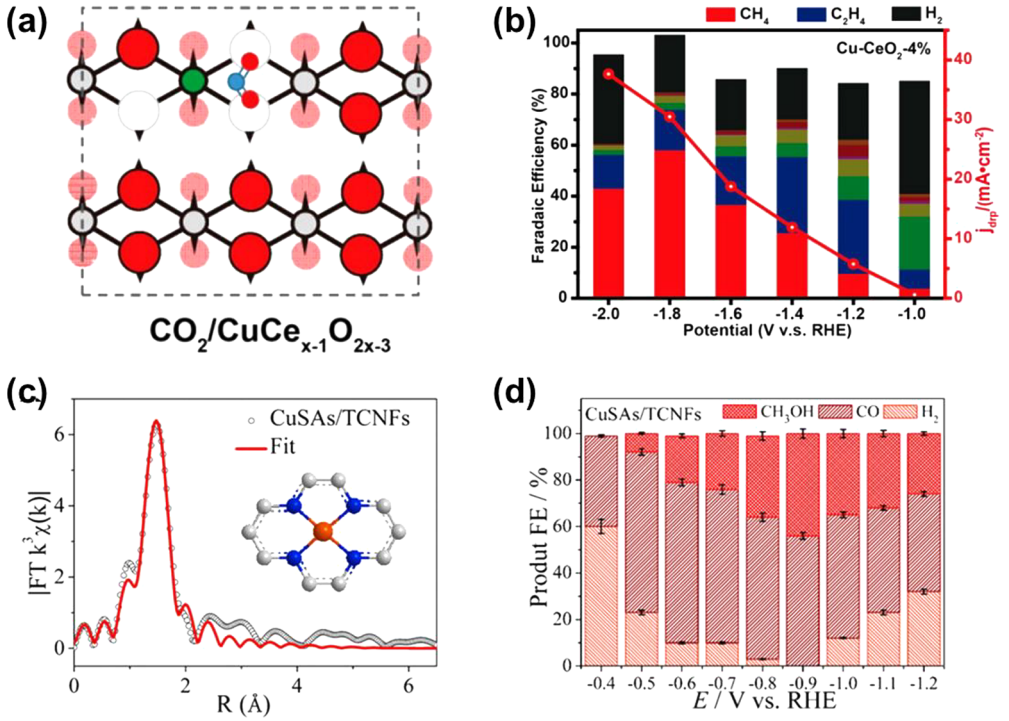

Figure 74. (a) Structure models of these Vo-bound, single-atomic Cu site on CeO_2 for CO_2 adsorption and activation. (b) Faradaic efficiencies (bars, left *y*-axis) and deep reduction products current density (j_{drp}, red curves, right *y*-axis) of Cu-CeO_2-4%. Reproduced with permission from ref 56. Copyright 2018 American Chemical Society. (c) fitting for EXAFS data of CuSAs/TCNFs. (d) Faradaic efficiencies of all products at CuSAs/TCNFs. Reproduced with permission from ref 487. Copyright 2019 American Chemical Society.

dopant (Ni−N@SV), and double vacancies with nitrogen dopant (Ni−N@DV). Among different coordination structures with or without nitrogen bonding, Ni sites with the slightly larger vacancies (DVs) facilitate the CO_2-to-CO conversion by lowering the CO desorption barrier. Yan et al. also prepared Ni SAECs by pyrolyzing Ni−Zn@ZIF-8 and claimed that the close-packed Ni−N_3 exhibited the lowest thermodynamic barrier for CO production among the series of Ni−N_x−C structures (x = 2−4).[482] Su et al. used covalent triazine frameworks (CTFs) to modify Ni SAECs, which exhibited improved CO_2 reduction activity.[483] Their Ni-CTF electrocatalyst achieved an FE_{CO} of 90% at −0.8 V. Besides the coordination structures, the valence of nickel was also investigated in the Ni SAECs for the CO2RR. Yang et al. reported >97% FE_{CO} with a Ni(I) SAEC.[95] The unpaired electron in Ni(I) with an electronic configuration of d^9, as observed by using electron paramagnetic resonance spectroscopy (EPR), was believed to be the key active sites accounting for the CO2RR activity.

The high activity and selectivity of Ni SAECs in CO2RR offer opportunities for scalable applications. For that purpose, it is important to synthesize high-performance Ni SAECs at large scales and low costs. Yang et al. demonstrated 98.9% of FE_{CO} with a kilogram-scale synthesis of Ni SAECs.[319] Zheng et al. obtained gram-scale Ni SAECs by pyrolyzing a mixture of Ni salt, urea, and activated carbon.[319] CO production at nearly 100% FE has been demonstrated for GDEs of ca. 100 cm^2 in size, which achieved a total current of 8 A.[413,484]

7.6. Cu-based Single-Atom Electrocatalysts

Copper (Cu) is the most studied metal for CO_2 reduction, due to its unique capability of catalyzing C−C coupling and producing value-added hydrocarbons, such as ethylene, acetate, ethanol, etc. Despite the reported different mechanisms, it is generally accepted that the C−C coupling pathway requires a high coverage of *CO intermediate on continuous Cu surfaces, which suggests the unlikely formation of C_{2+} hydrocarbons on single-atom Cu sites.[431,456,485] Research interests in Cu SAECs have thus been steered toward enhancing the selectivity toward C_1 hydrocarbons, such as methanol and methane.

In early works, Cu SAECs often appear as control groups in systematic studies of PGM-free electrocatalysts.[319] Recently, Zheng et al. investigated the effect of Cu−N_x coordination number on CO_2 reduction to CO (Figure 73a,b).[52] They found the undercoordinated Cu−N_2 sites are more active than Cu−N_4 by accelerating the first electron transfer to CO_2. Jiao et al. demonstrated the potential of producing C_1 hydrocarbons by using C_3N_4 supported Cu single atoms in spite of relatively low activity and FEs (Figure 73c,d).[486] They proposed that the *d*-orbital of Cu can be efficiently uplifted by coordination with the C_3N_4 framework, strengthening the adsorption of carbonaceous intermediates. Zheng and co-workers reported a Cu SAEC supported on ceria, a substrate known to possess strong metal−support interactions (Figure 74a,b).[56] Cu atoms in CeO_2 nanorods are highly dispersed and have a low coordination number of 5, which was believed to be associated with three oxygen vacancies. The $CuCe_{x-1}O_{x-3}$ structure was highlighted by its high selectivity toward CH_4 (58% FE), being one of the first SAECs that produce hydrocarbon as the major product. Yang et al. decorated isolated Cu on through-hole carbon nanofibers (CuSAs/TCNFs) and demonstrated 44% FE toward methanol at a current density of 93 mA/cm^2 (Figure 74c,d).[487] Synergistic effects between the carbon substrate and the Cu single atoms was claimed to be the key for the reduction of CO_2 to methanol.

https://dx.doi.org/10.1021/acs.chemrev.0c00594
Chem. Rev. 2020, 120, 12217−12314

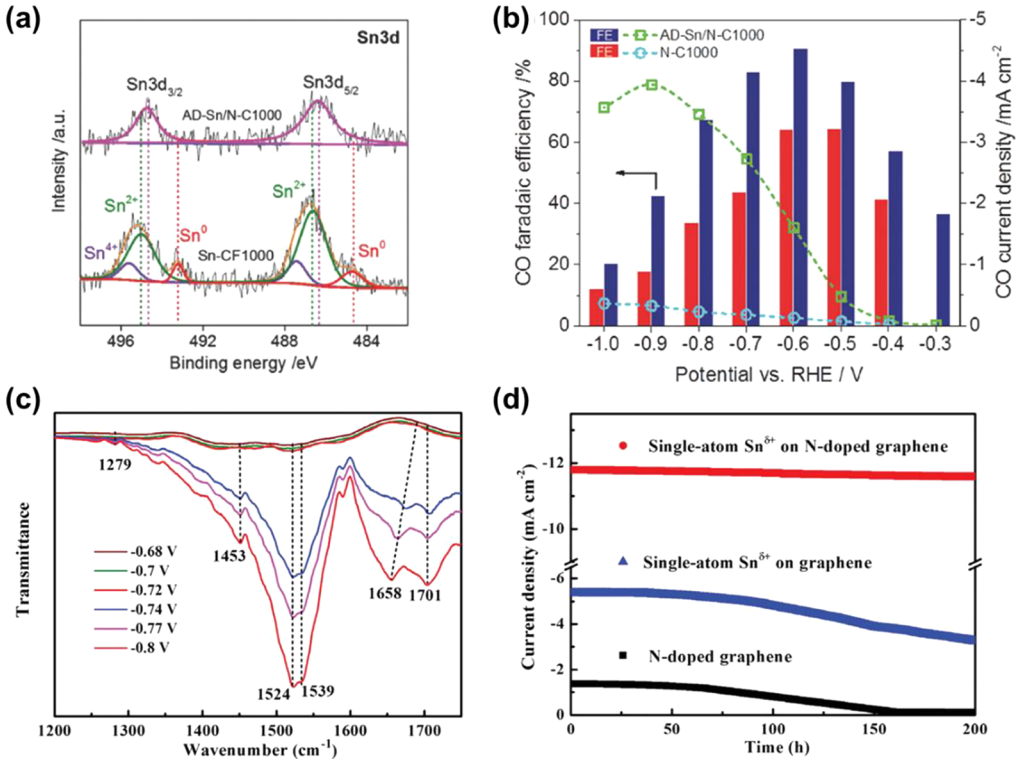

Figure 75. (a) High-resolution Sn 3d XPS spectra for AD−Sn/N−C1000 and Sn−CF1000. (b) CO faradaic efficiency and partial current density for these two catalysts. Reproduced with permission from ref 489. Copyright 2018 John Wiley and Sons. (c) Electrochemical in situ FTIR spectra at different potentials of the single-atom $Sn^{\delta+}$ on N-doped graphene. (d) Chronoamperometry results at the potentials of −1.6 V versus SCE. Reproduced with permission from ref 490. Copyright 2019 John Wiley and Sons.

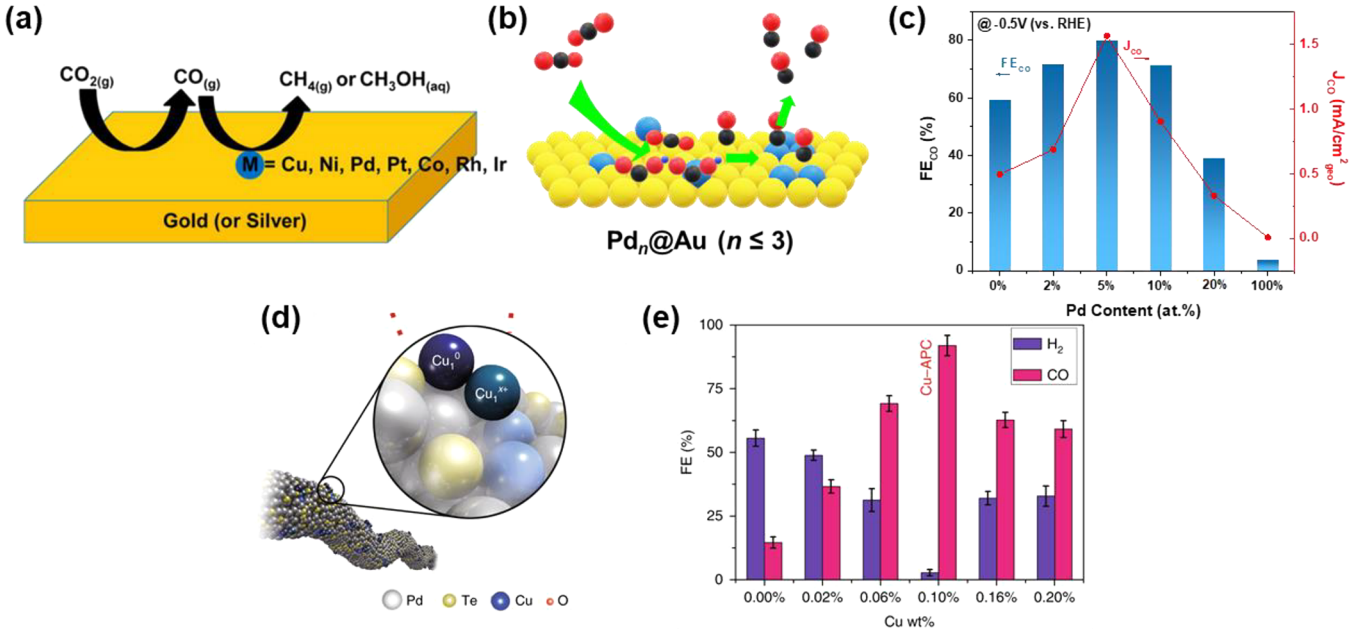

Figure 76. (a) Schematic description of proposed one-pot tandem catalytic reaction. The proposed electrocatalyst is composed primarily of gold or silver (colored gold), alloyed with small amounts of M (M = Cu, Ni, Pd, Pt, Co, Rh, and Ir). The feedstock CO_2 is first reduced to CO by gold or silver and is subsequently captured and further reduced to C_1 products by M. Reproduced with permission from ref 66. Copyright 2016 American Chemical Society. (b) Illustration of the concept using atomically dispersed Pd sites on Au surface to enhance CO_2 reduction (the yellow and blue spheres represent Au and Pd atoms, respectively. For the molecular structures, red, gray, and purple colors represent oxygen, carbon, and hydrogen, respectively). (c) dependences of FE_{CO} and partial current density toward CO (J_{CO}) (at −0.5 V) on the Pd content within the Pd@Au nanoparticles. Reproduced with permission from ref 17. Copyright 2019 American Chemical Society. (d) Cu atom pair anchored on $Pd_{10}Te_3$ nanowires. (e) FE_{CO} and FE_{H2} of different Cu-loaded samples at −0.78 V (versus RHE). Reproduced with permission from ref 33. Copyright 2019 Nature Publishing Group.

https://dx.doi.org/10.1021/acs.chemrev.0c00594
Chem. Rev. 2020, 120, 12217−12314

Table 5. Catalytic Performance of SAECs towards CO2RR

catalyst	electrolyte	product	FE (%)	overpotential (V)	current density (mA cm^{-2})	ref
CoPP-PG	0.1 M $HClO_4$	CO	60	0.5	0.08	447
COF-366-F-Co	0.2 M KH_2PO_4+0.5 M $KHCO_3$	CO	87	0.55		448
Fe-o-TMA	DMF + 0.1 M *n*-Bu_4NPF_6 + 0.1 M H_2O + 3 M PhOH	CO	100	0.22		449
Fe-p-TMA	DMF + 0.1 M *n*-Bu_4NPF_6 + 0.1 M H_2O + 3 M PhOH	CO	93	0.22		449
COF-366- Co	0.2 M KH_2PO_4+0.5 M $KHCO_3$	CO	90	0.55		19
$FeFc_4$ complex	3 M PhOH	CO	92			450
CoPPc/CNT	0.5 M $NaHCO_3$	CO	90	0.45	>10	458
CoPc-MWCNT	0.5 M $KHCO_3$	CH_3OH	0.3	0.91	11.25	459
CoPc/CNT	0.1 M $KHCO_3$	CH_3OH	44	0.97	10.6	81
FeN_5 SAC	0.1 M $KHCO_3$	CO	97	0.35	~5	53
CoPc	0.5 M $KHCO_3$	CO	>95		150	20
CNT|Mn_{pyr}	0.5 M $KHCO_3$	CO	34	0.36	~5	460
Mn−N−C	0.1 M $KHCO_3$	CO	~80	0.45	~3	463
Fe−N−C	0.1 M $KHCO_3$	CO	~80	0.5	~4	463
FeMn−N−C	0.1 M $KHCO_3$	CO	~85	0.4	~2	463
$Fe_{0.5}$d	0.5 M $NaHCO_3$	CO	91	0.4	7.5	464
$Fe_{0.5}$d	0.1 M $NaHCO_3$	CO	91	0.5	4.5	464
Fe/NG-750	0.1 M $KHCO_3$	CO	80	0.47	~2.7	69
Fe−N_4/CF-1000	0.5 M $KHCO_3$	CO	94.9	0.4	~3	465
Fe−N_4/CF-900	0.5 M $KHCO_3$	CO	~85	0.4	~4.5	465
Fe−N_4/CF-800	0.5 M $KHCO_3$	CO	~65	0.4	~5	465
Fe^{3+}−N−C	0.5 M $KHCO_3$	CO	>90	0.34	~104	131
Fe−N−C	0.5 M $KHCO_3$	CO	93.5	0.4	~6	140
C-AFC@ZIF-8	1 M $KHCO_3$	CO	89.1	0.33	~5	310
Co−N_2	0.5 M $KHCO_3$	CO	94	0.52	18.1	477
Co−N_3	0.5 M $KHCO_3$	CO	63	0.43	~2	477
Co−N_5/HNPCSs	0.2 M $NaHCO_3$	CO	>99	0.63	6.2	477
STPyP-Co	0.5 M $KHCO_3$	CO	96	0.5	~6.5	478
NiSA-NGA-900	0.5 M $KHCO_3$	CO	90.2	0.7	~6	480
Ni−N_4−C	0.5 M $KHCO_3$	CO	99	0.71	28.6	481
Ni−NG	0.5 M $KHCO_3$	CO	>95	0.55	>50	129
C−Zn_1Ni_4 ZIF-8	1 M $KHCO_3$	CO	98	0.73	~60	482
Ni-CTF	0.1 M $KHCO_3$	CO	>90	0.7	~2	483
A-Ni-NSG	0.5 M $KHCO_3$	CO	97	0.61	~22.7	95
Ni-NCB	0.5 M $KHCO_3$	CO	99	0.58	100	47
Cu−CeO_2-4%	0.1 M $KHCO_3$	CH_4	58	1.97	70	56
Cu−N_2/GN	0.1 M $KHCO_3$	CO	81	0.4	<5	52
Cu−N_4/GN-700	0.1 M $KHCO_3$	CO	35	0.4	<5	52
Cu−N_4/GN-800	0.1 M $KHCO_3$	CO	62	0.4	<5	52
CuSAs/TCNFs	0.1 M $KHCO_3$	CH_3OH	44	0.93	93	487
CuSAs/TCNFs	0.1 M $KHCO_3$	CO	56	0.8	93	487
AD-Sn/N−C1000	0.5 M $KHCO_3$	CO	91	0.69	1.55	489
$Sn^{\delta+}$ on N-doped graphene	0.25 M $KHCO_3$	$HCOO^-$	74.3	0.88	11.7	490
Mo@NG	4 mol % $EmimBF_4$ aqueous solution	$HCOO^-$	30	1.32	~180	491
Zn−N-G	0.5 M $KHCO_3$	CO	90.8	0.4	~5	492
Bi SAs/NC	0.1 M $NaHCO_3$	CO	97	0.29	>4	494
0.1% Cu-APC	0.2 M $NaHCO_3$	CO	97	0.68	>8.8	33
Pd_5@Au_{95}	0.1 M $KHCO_3$	CO	80	0.4	2	17

7.7. Sn-based Single-Atom Electrocatalysts

Previous studies of metal electrodes have demonstrated SnO_x as the essential active sites for CO_2 reduction catalyzed by Sn.[488] Wallace and co-workers have synthesized atomically dispersed $Sn^{\delta+}$ ($0 < \delta < 2$), anchored on nitrogen-doped carbon nanofibers (Figure 75a,b).[489] The positively charged $Sn^{\delta+}$ was found to be active for CO and $HCOO^-$ formation. The mechanism of CO_2 activation on $Sn^{\delta+}$ was later on revealed by Zu et al. (Figure 75c,d).[490] They compared single-atom $Sn^{\delta+}$ supported on graphene and on N-doped graphene. The $Sn^{\delta+}$−N_4 center was identified to be the most active sites for CO_2 reduction. Further, in situ FTIR studies showed that a mere 60 mV overpotential was needed for $HCOO^-_{ad}$ formation on $Sn^{\delta+}$−N_4, as compared to 280 mV and 420 mV on $Sn^{\delta+}$−graphene and N-doped graphene. Consequently, $Sn^{\delta+}$−N_4 exhibited very low onset potential for formate production.

https://dx.doi.org/10.1021/acs.chemrev.0c00594
Chem. Rev. 2020, 120, 12217−12314

7.8. Other Metal (Bi, Mo, Zn)-based Single-Atom Electrocatalysts

Besides the use of 3*d* transition metals to fabricate SAECs, other types of SAECs have also been reported for CO2RR with the metal centers including Bi, Mo, and Zn. For example, Huang et al. developed a synthetic route for Mo SAECs coordinated on N-doped graphene.[491] $Mo^{\delta+}-N_x$ structures were identified to be the active sites for delivering 30% $FE_{formate}$. Liu and co-workers synthesized Zn SAECs coordinated to N-doped graphene by pyrolyzing a mixture of graphene, melamine, and Zn precursors.[492] The $Zn-N_4$ moieties were identified and found to be selective for CO production, achieving >90% of FE_{CO}. Yang et al.[493] compared $Zn-N_4-C$ and Zn−C on graphene substrates and confirmed the stabilization of *COOH intermediate on the $Zn-N_4$ moieties. Similar $M-N_4-C$ active centers was also reported for Bi coordinated on N-coped carbon.[494] The Bi SAECs was prepared via pyrolysis of Bi-based MOFs and achieved 97% of FE_{CO} at a low overpotential of 0.39 V.

7.9. Diluted Surface Alloys

Bell and co-workers reported the concept of single-atom alloy (SAA) as a one-pot tandem catalyst for the CO2RR.[66] Such SAA catalysts were made by introducing an atomically dispersed metal (e.g., Cu, Ni, Pd, Pt, Co, Rh, or Ir) on a Au or Ag substrate.[12,96] It was proposed that CO_2 would be first reduced to CO on the Au/Ag surface and then further reduced to C_1 hydrocarbons on the single-atom sites of the other metal (Figure 76a). The reactivity and product distribution of such SAA catalysts were believed to be dependent on the synergistic effects between the single atoms and the metal substrate. Wang et al. systematically studied the effect of atomic ensemble size on the CO2RR activity for such SAA catalysts.[17] By decorating Au nanoparticles with controlled doses of Pd, they prepared a series of Pd_n@Au electrocatalysts with the Pd species varied from isolated atoms to continuous domains. They found that an intermediate dose likely gave rise to small Pd ensembles (e.g., $n = 2$), with a fine balance between the strong adsorption of *CO originating from Pd and the facile activation of CO_2 through *COOH on Au (Figure 76b,c). In line with the concept of SAA, Jiao et al. reported a strategy to construct Cu atomic pairs on $Pd_{10}Te_3$ alloy nanowires (Figure 76d,e).[33] The active centers for CO_2 reduction to CO were identified to be $Cu_1^0-Cu_1^{x+}$, where the H_2O molecule adsorbed on Cu_1^{x+} might play a role in stabilization of the CO_2 molecule chemisorbed on the neighboring Cu_1^0 site to promote the activation of CO_2.

7.10. Perspectives of Single-Atom Electrocatalysts for CO_2 Reduction

Many questions remain about the mechanisms of SAECs in catalyzing CO2RR (Table 5). Fundamental understanding about the difference in catalytic mechanisms between supported or unsupported molecular electrocatalysts (such as cobalt phthalocyanine) and $M-N_x-C$ type of SAECs derived from pyrolysis is of urgent need. While the metal centers are generally believed to be the active sites for the adsorption of *CO/*COOH intermediates, it remains unexplicit whether the nitrogen atoms in bonding with the metal site, or the neighboring carbon atoms on the substrate play a role in the catalytic process. Possible interplays between the metal centers and the coordinating substrate causes challenges for the mechanistic studies of CO2RR on SAECs, which also represents an opportunity for further research. The optimal coordination structure of $M-N_x-C$ for CO_2 reduction is still in debate, which is also the case for the oxidation state of the metal center. What should be underlined here is in situ characterizations under reaction-relevant conditions, or ex situ post-electrocatalytic studies, considering the plausible structural alternations of the single-atom metal centers when subjected to electrochemical potentials and adsorption of reactive intermediates.

XAS, including XANES and EXAFS, and XPS have been commonly employed to characterize and understand the structure−property relationships of SAECs in the CO2RR. While X-ray is able to probe the atomic structure of the metal centers and statistical average of the coordination environment, it has limited capability of telling the reaction pathway and adsorbing intermediates on the catalysts. Molecular spectroscopic studies are still limited for SAECs, primarily owing to the significant absorption background of the carbon-based substrates. Besides spectroscopy, there are many useful, but simple techniques/principles that could help one understand the reaction kinetics. For example, if CO_2 activation is a critical step in the proposed reaction pathway, Tafel slope and CO_2 reaction order could help discern the rate-limiting step.[430,431,495] Dependence of the catalytic activity and selectivity on (local) pH is known for CO_2 reduction on metal electrodes, but few work has been done for SACEs.[432,433]

Computation studies, mostly based on DFT calculations, have been extensively reported, but are usually based on hypothesized pathways or adsorbates, owing to the lack of reaction intermediate information. Simulations based on DFT typically only give free energies, along with the reaction coordinate, lacking information on activation barriers for the key rate- and selectivity-determining steps. Kinetic and microkinetic modeling are valuable approaches that could merge this gap, but comprehensive kinetic studies in experiments have not been seen for SAECs.

One concern about the design of control experiments is the potential presence of impurity metal atoms in the substrate. Many studies use Zn-based MOFs to prepare SAECs. Because $Zn-N_4$ are also highly active for CO_2 reduction to CO, even at a trace amount (0.1 wt %),[492,493] it is important to carefully examine the presence and role of residual $Zn-N_x$ moieties in the catalysts derived from pyrolysis.

Methanol is a promising liquid fuel for energy storage in the foreground of artificial carbon recycling. However, it is rarely seen, or only present as a minor product, from the CO2RR on most bulk or nanostructured catalysts, likely due to the slow kinetics of methanol formation[496] and unfavorable competition with the C−C coupling pathway on continuous metal surfaces.[496] SAECs have been shown with the potential to break this limitation, as C−C coupling could be suppressed by confining C_1 reaction intermediates on the single-atom metal centers. In this aspect, Cu- and Co-based SAECs have been shown for being capable of producing methanol, albeit the need for further improvement of the selectivity.[81,459,487] It is interesting to further develop the understanding for the methanol pathways on SAECs and design highly efficient electrocatalysts for selective reduction of CO_2 to methanol.

8. SINGLE-ATOM ELECTROCATALYSTS FOR NITROGEN REDUCTION REACTION

Nitrogen is an indispensable element for all lives on Earth, constituting the basic building block of organisms, such as amino acids, proteins, nucleoside triphosphates, and nucleic

https://dx.doi.org/10.1021/acs.chemrev.0c00594
Chem. Rev. 2020, 120, 12217−12314

acids.[497−499] Besides, many important chemicals in modern industries contain the nitrogen element, such as ammonia, nitric acid, organic nitrates (propellants and explosives), and cyanides.[500−503] It is well established that the most abundant nitrogen source on Earth comes from dinitrogen molecules (N_2) in the atmosphere, which accounts for ∼79% of the air in volume. However, the triple bond in N_2 requires a large dissociation energy (945.41 kJ/mol) to activate, leading to the inert nature of N_2 molecules.[504]

Nitrogen fixation is a process that converts nitrogen in air to ammonia (NH_3) or related nitrogenous compounds in soil. In the nitrogen cycle, N_2 fixation is carried out in soil by diazotrophs, a kind of bacteria including *Azotobacter* and archaea.[505−507] To meet the growing demand from agriculture and industry, many researchers have explored the possibility of artificial nitrogen fixation to manufacture fertilizers in a more controllable way. In the 1900s, Haber and Bosch developed an industrial process to convert N_2 and H_2 to ammonia, under high temperatures (∼500 °C) and pressures (200−300 atm).[508,509] The so-called Haber−Bosch process fundamentally changed the landscape of agriculture and even human society, contributing to the explosive global population growth during the past century. However, the Haber−Bosch process is highly energy-intensive, consuming 1−2% of the global annual energy output. Moreover, the production of H_2, a key reactant, is accompanied by a huge consumption of fossil fuels, responsible for over 400 million metric tons of CO_2 emission annually.[510,511] To meet the ever-increasing demand for ammonia and ease the energy consumption of the Haber−Bosch process, there is an urgent need to develop a highly efficient and sustainable approach to produce ammonia at milder conditions.

8.1. Fundamentals of Nitrogen Reduction Reaction

Electrocatalytic approach has been considered as an energy-saving and environment-friendly alternatives to achieve ammonia synthesis at ambient temperature and pressure.[512−519,520] Fuel cell provides the possibility to achieve nearly 100% energy efficiency by direct conversion of chemical energy to electricity, which is superior to the efficiency of state-to-the-art internal combustion engines, which is theoretically limited by the Carnot cycle.[521,522] Electrocatalysis, in a similar manner, is operated under ambient conditions, which can also reduce the energy consumption and CO_2 emission. Electrochemical NRR in aqueous solution is a proton-coupled electron transfer (PCET) reaction that involves a six-electron process to produce two ammonia molecules from one N_2 molecule or a four-electron side reaction to hydrazine, making the NRR a more complicated process than the four-electron ORR/OER and two-electron HER/hydrogen oxidation reaction (HOR). In the thermodynamic aspect, the onset potential of NRR vs RHE corresponding to the formation of gaseous ammonia is calculated as follows,

$$N_2(g) + 6H^+ + 6e^- \rightleftharpoons 2NH_3(g)\ E^0 = 0.0577\ \text{V vs RHE} \quad (32)$$

The high solubility of ammonia in water is well established. As a moderate Brønsted base, the energy from dissolution−hydration and protonation of ammonia hydrate is not negligible, especially in acid electrolyte,[523,524]

$$NH_3(g) + H_2O(l) \rightleftharpoons NH_3{\cdot}H_2O(aq) \quad \Delta_r G_m^0 = -247.23\ \text{kJ mol}^{-1} \quad (33)$$

$$NH_4^+(aq) + H_2O(l) \rightleftharpoons NH_3{\cdot}H_2O(aq) + H^+ \quad pK_a = 9.25 \quad (34)$$

Considering all these calculations above as well as the standard electrode potentials reported by Bratsch,[525] one can obtain a detailed Pourbaix diagram for the N_2−water system (Figure 77),[526] which renders the phase diagrams under

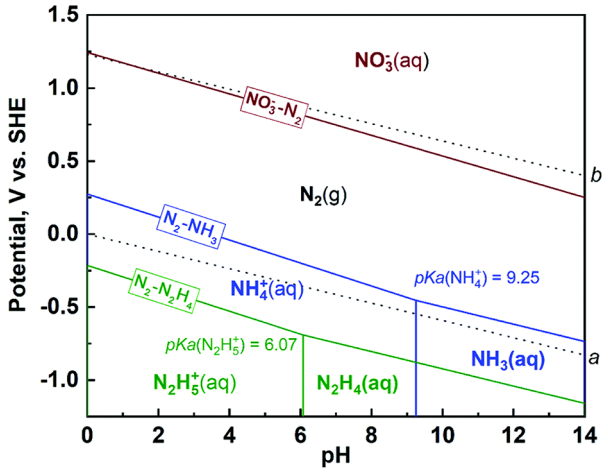

Figure 77. Partial Pourbaix diagram of the N_2−H_2O system including N_2, NH_3, N_2H_4, and NO_3^-. Region between dotted lines a (HOR/HER) and b (OER/ORR) correspond to the condition of water stability. Reproduced with permission from ref 526. Copyright 2019 The Royal Society of Chemistry.

different pH and potentials for nitrogen in aqueous system. The calculated potential for water splitting reactions (HER and OER) are also added for comparison. There is a narrow window for us to explore the electrochemical NRR before HER becomes dominant under all pH. The onset potential for NRR can be calculated as follows,

$$N_2(g) + 8H^+ + 6e^- \rightleftharpoons 2NH_4^+(aq)\ (pH < 9.25)\ E^0 = 0.274\ \text{V vs RHE at pH} = 0 \quad (35)$$

$$N_2(g) + 8H_2O(l) + 6e^- \rightleftharpoons 2NH_3{\cdot}H_2O(aq) + 6OH^-(aq)\ (pH \geq 9.25)\ E^0 = 0.092\ \text{V vs RHE} \quad (36)$$

It should also be noted that like ORR, partial reduction of N_2 follows a four-electron pathway to hydrazine or a two-electron pathway to diazene.

Four-electron pathway:

$$N_2(g) + 5H^+ + 4e^- \rightleftharpoons N_2H_5^+(aq)\ (pH < 6.07)\ E^0 = -0.214\ \text{V vs RHE at pH} = 0 \quad (37)$$

$$N_2(g) + 4H_2O(l) + 4e^- \rightleftharpoons N_2H_4(aq) + 4OH^-\ (pH \geq 6.07)\ E^0 = -0.332\ \text{V vs RHE} \quad (38)$$

Two-electron pathway:

$$N_2(g) + 2H^+ + 2e^- \rightleftharpoons N_2H_2(g)\ E^0 = -1.10\ \text{V vs RHE at pH} = 0 \quad (39)$$

However, up to now, there has been no report about efficient processes for four-electron and two-electron NRR.

https://dx.doi.org/10.1021/acs.chemrev.0c00594
Chem. Rev. 2020, 120, 12217−12314

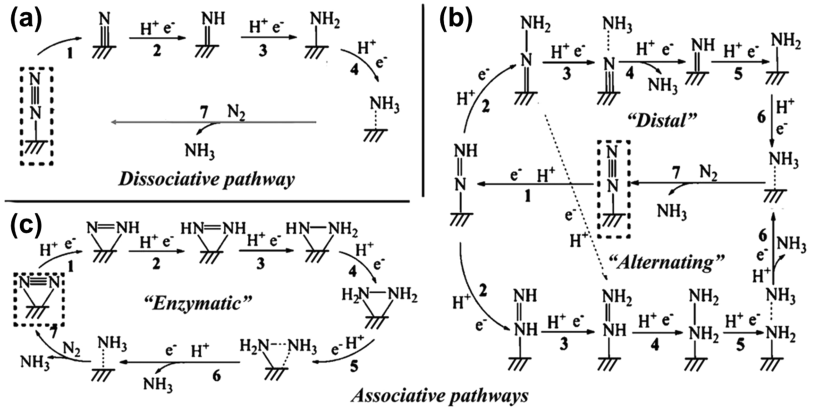

Figure 78. Three possible reaction mechanism for electrochemical NRR to synthesize ammonia, (a) dissociative pathway, (b) associative pathways including distal pathway and alternating pathway, and (c) enzymatic pathway. Reproduced with permission from ref 528. Copyright 2018 John Wiley and Sons.

Generally speaking, the proposed mechanisms for electrochemical NRR to NH_3 can be classified into the dissociative pathway and the associative pathway (Figure 78).[527−529] In the dissociative pathway, one N_2 molecule first dissociates into two N atoms, where the N≡N triple bond is broken before the addition of protons (Figure 78a). In the associative pathway, the N≡N bond is cleaved simultaneously with the release of one NH_3 molecule. The associative pathway includes the distal pathway and the alternating pathway, with different protonation sequences. In the distal pathway, the remote nitrogen atom is hydrogenated first and released as NH_3. For comparison, two N atoms are protonated simultaneously in the alternating pathway (Figure 78b). Notably, the enzymatic pathway (Figure 78c), which resembles associative pathway, exhibits a distinctive feature of its side-on adsorption mode of N atoms, instead of an end-on adsorption mode of N atoms that is proposed on most heterogeneous surfaces.

8.2. Computational Screening of Single-Atom Electrocatalysts for Nitrogen Reduction Reaction

Tremendous efforts have been spent on theoretical calculations on the reaction mechanism, which guides the catalysts design for NRR.[530−534] Different from catalysts with continuous metal surfaces, single-atom catalysts usually exhibit unique properties for N_2 adsorption and activation. The metal center in single-atom catalysts is usually partially charged, due to the coordination with supporting atoms, which substantially strengthens the adsorption of N_2. One of the exciting features of SAECs is its uniform active sites, which could be characterized and modeled precisely on the atomic scale. Theoretical calculations can in turn benefit experimental research on SAECs for NRR, in a way that guides the optimization of SAECs with the best predicted descriptors.

Recently, a series of DFT calculations have been reported to predict the NRR activity of SAECs on various supports, for instance, graphitic carbon nitride, boron nitride, metal chalcogenides, phosphides, etc. In a detailed study, Choi et al. investigated the catalytic activity of NRR on SAECs anchored at the defected graphene sites containing carbon vacancy and nitrogen.[535] Four different types of structures were constructed, including $M@C_3$, $M@C_4$, $M@N_3$, and $M@N_4$. It was found that SAECs exhibited a more positive $\Delta G(*H)$ than most metal surfaces, which suppressed the competitive HER and improved the selectivity of NRR. Consequently, N_2 adsorption would be less hindered by *H on SAECs, compared to bulk metal surfaces with same metal atoms. Besides, the interaction with support gives positive charges to the metal sites, making metal center easier to polarize and bind N_2 more strongly. On the basis of screening, $Ti-N_4$ and $V-N_4$ moieties were proposed as promising candidates for NRR at room temperature (Figure 79a). Zhao et al. reported an investigation about SAECs for NRR by comparing the stability of 18 types of transition metals on nitrogen-doped graphene. They calculated the competitive adsorption of N_2 and H_2 on various metal sites (13 of 18 transition metal elements are included in Figure 79b).[536] Mo_1/N_3-G and Cr_1/N_3-G are theoretically predicted as selective and active catalysts for NRR with a low overpotential and high selectivity (0.34 V and 40% for Mo, 0.59 V and 100% for Cr, respectively).

Chen et al. unraveled the mechanism of NRR by SAECs on defective graphitic carbon nitride by DFT calculations.[537] Ti@ nitrogen vacancies (NVs)-*g*-C_3N_4 were revealed as the most promising candidate featuring the lowest free energy of 0.28 eV with an accessible energy barrier of 0.57 eV in the first PCET step. It should be noted that N_2 chemisorption activity could be enhanced on metal crystals by reducing their coordination number. However, no catalytic activity was found for the metal crystals anchored on NVs-*g*-C_3N_4, even on under-coordination sites. Zhang et al. also conducted DFT calculations of gt-C_3N_4 coordinated transition metal single atoms for NRR in two N_2 adsorption modes.[538] For the standing-on mode, Mo/g-C_3N_4 was found to exhibit the most negative limiting potential for NRR among all the investigated materials, whereas V/g-C_3N_4 is most active in the lying-on mode.

Inspired by the results from theoretical calculations, many researchers have tried to optimize SAECs for NRR following the predicted structures. By combining experiments and theoretical simulations, great progress has indeed been achieved on SAECs for NRR in recent years.

8.3. Precious Metal-based Single-Atom Electrocatalysts

8.3.1. Ru-based Single-Atom Electrocatalysts. Ruthenium has exhibited the best performance for ammonia synthesis via the Haber−Bosch process.[539−541] Therefore, many efforts have been made to achieve electrochemical NRR with Ru-based catalysts. However, Ru usually shows excessive activity for HER that suppresses the FE of NRR, especially at larger current intensity. However, by tuning the adsorption

https://dx.doi.org/10.1021/acs.chemrev.0c00594
Chem. Rev. 2020, 120, 12217−12314

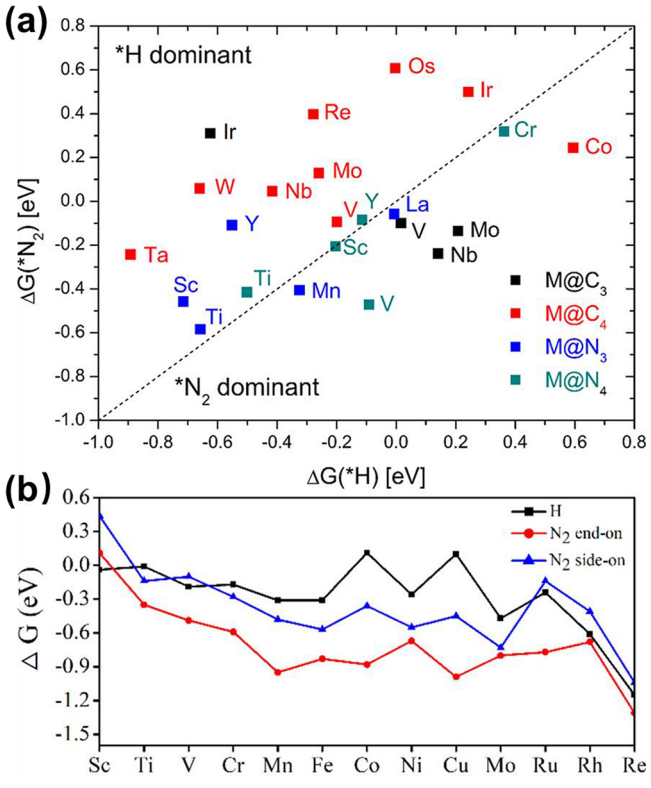

Figure 79. Theoretical calculation to predict the NRR activity of single-atom catalysts on N-doped carbon. (a) Calculated $\Delta G(*H)$ and $\Delta G(*N_2)$ on SAECs that satisfy ΔG_{PDS} 1.0 eV. Dashed line indicates $\Delta G(*H) = \Delta G(*N_2)$. SAECs in the $\Delta G(*H) > \Delta G(*N_2)$ region ($*N_2$ dominant region), under the dashed line, correspond to N_2 adsorption being more favorable than *H formation at 0 V (vs RHE). Reproduced with permission from ref 535. Copyright 2018 American Chemical Society. (b) Adsorption Gibbs free energy of H and N_2 adsorbed on 13 kinds of M_1/N_3-G. Black, red, and blue lines represent the adsorption of atomic hydrogen, end-on mode nitrogen, and the side-on mode nitrogen, respectively. Reproduced with permission from ref 536. Copyright 2019 American Chemical Society.

properties of N_2 and protons on Ru single atoms, optimized NRR selectivity and activity could be achieved.

Geng et al. synthesized well-dispersed Ru single atoms at 0.18 wt % by pyrolysis of $Ru(acac)_3$ loaded on ZIF-8, with Ru stabilized by nitrogen atoms in the frameworks (Figure 80a,b).[542] The coordination number of Ru−N is determined to be 3.4 by XAFS experiment. Ru single atoms on nitrogen-doped carbon (Ru SAs/N−C) exhibits very high activity and selectivity for NRR, with an NH_3 yield rate of 120.9 $\mu g_{NH3} \cdot mg_{ca.}^{-1} h^{-1}$ and an FE of 29.6% at −0.2 V in 0.05 M H_2SO_4. In comparison, 3.5 nm Ru nanoparticles/N−C synthesized in a similar route showed less than half of the activity and selectivity (Figure 80c). The corresponding DFT calculations showed that NRR follows the distal pathway on Ru SAECs. The change of Gibbs free energy from $*N_2$ to *NNH on Ru−N_3 and Ru−N_4 moiety was 0.73 and 0.77 eV, respectively, much lower than that on Ru(101) surface (0.91 eV) (Figure 80d), which was argued to be the key to the enhanced NRR performance.

Tao et al. designed a Ru-based SAEC supported on nitrogen-doped carbon (Ru@NC) from amino-containing metal−organic frameworks (UIO-66-NH_2).[543] The obtained Ru@NC (Figure 81a) showed an NH_3 yield rate of up to 3.665 $mg_{NH3} \cdot h^{-1} mg_{Ru}^{-1}$ at −0.21 V vs RHE in 0.1 M HCl. In contrast, commercial Ru/C and Ru nanoparticles on graphene reduced by $NaBH_4$ possessed almost zero NRR activity but vigorous HER activity. The lackluster performance from Ru particles was mainly attributed to the relative larger Ru particle size (>3 nm) (Figure 81b). This result indicates the suppression of HER could be achieved by reducing the Ru particle size to atomic scale. The doped N atoms stabilized the atomic dispersion of Ru by coordinate bonds, while the presence of ZrO_2 significantly suppressed the HER. The highest FE for NRR (21%) was reached at −0.11 V (Figure 81c). Subsequent DFT calculations indicated that the Ru atoms are anchored on the surface O-vacancies of ZrO_2 that formed in thermal treatment. Ru single-atom sites embedded on either ZrO_2 or N-doped C showed improved NRR activity, as compared to the Ru(0001) surface, with reduced free-energy change at potential-determining steps (PDS) (Figure 81d).

2D graphitic carbon nitride (g-C_3N_4) has also been used to support Ru single atoms, taking advantage of its highly dense anchoring sites provided by pyridine-like nitrogen.[544] The as-synthesized $Ru_1-C_3N_4$ exhibits excellent catalytic activity and selectivity with an NH_3 yield rate of 23.0 $\mu g \cdot mg_{ca.}^{-1} h^{-1}$ and FE of 8.3% at a low overpotential (0.05 V vs RHE), which is far better than its bulk Ru counterparts. According to the DFT calculations, the H adsorption significantly reduces the number of NRR active sites on Ru(0001). This H poisoning effect, however, is much less significant at Ru_1/C_3N_4, leading to the enhanced activity. They further argued that the *d*-band center (average energy of the d-electrons) of $Ru_1-C_3N_4$ was closer to the Fermi level, leading to a stronger binding energy to adsorbates.

8.3.2. Au-based Single-Atom Electrocatalysts. Au-based catalysts have shown great potential as a noble-metal NRR electrocatalyst. Surface-enhanced infrared absorption spectroscopy measurements deliver a direct observation of surface adsorbates on an Au thin film electrode during NRR in 0.1 M KOH electrolyte.[545] At potentials below 0 V (vs RHE), vibrational bands related to adsorbed N_2H_y intermediates were observed, indicating an alternative associative pathway. Motivated by the spectroscopic results, optimization of Au-based catalysts have focused on crystalline facets, crystallinity, electronic structures, and nanomorphology.[546−550]

Downsizing the Au particles, eventually to an atomic dispersion, represents a promising strategy to enhance the NRR performance. Qin et al. reported Au single atoms anchored on hierarchical N-doped porous carbon (NDPC) via a SiO_2 template-assisted method.[551] At 0.2 V vs RHE, the obtained Au_1-NDPC exhibited a stable NH_3 yield of 2.232 $\mu g \cdot h^{-1} cm^{-2}$ and a corresponding FE of 12.3% in 0.1 M HCl, much higher than those of its nanoparticles counterparts. Au SAEC on C_3N_4 (Au_1/C_3N_4) was also reported to exhibit good performance for electrochemical NRR by Wang et. al (Figure 82a,b).[552] The highest FE of Au_1/C_3N_4 was 11.1%, at −0.1 V vs RHE in 5 mM H_2SO_4, whereas Au nanoparticles only achieved 6% under the same condition. The NH_3 yield was as high as 1.305 $mg \cdot h^{-1} mg_{Au}^{-1}$, which was roughly 22.5 times higher than that of supported Au nanoparticles (Figure 82c). The reaction pathways on Au_1/C_3N_4 favor the alternating mechanism, considering the much lower energy barrier for the rate-limiting step (the reduction of N_2 to $*N_2H$) (Figure 82d), which is 0.68 eV lower than that on Au(211) (Figure 82e). It is noteworthy that the coordination bond between Au and N also induces a 0.56e positive charge for each Au atom, which helps

https://dx.doi.org/10.1021/acs.chemrev.0c00594
Chem. Rev. 2020, 120, 12217−12314

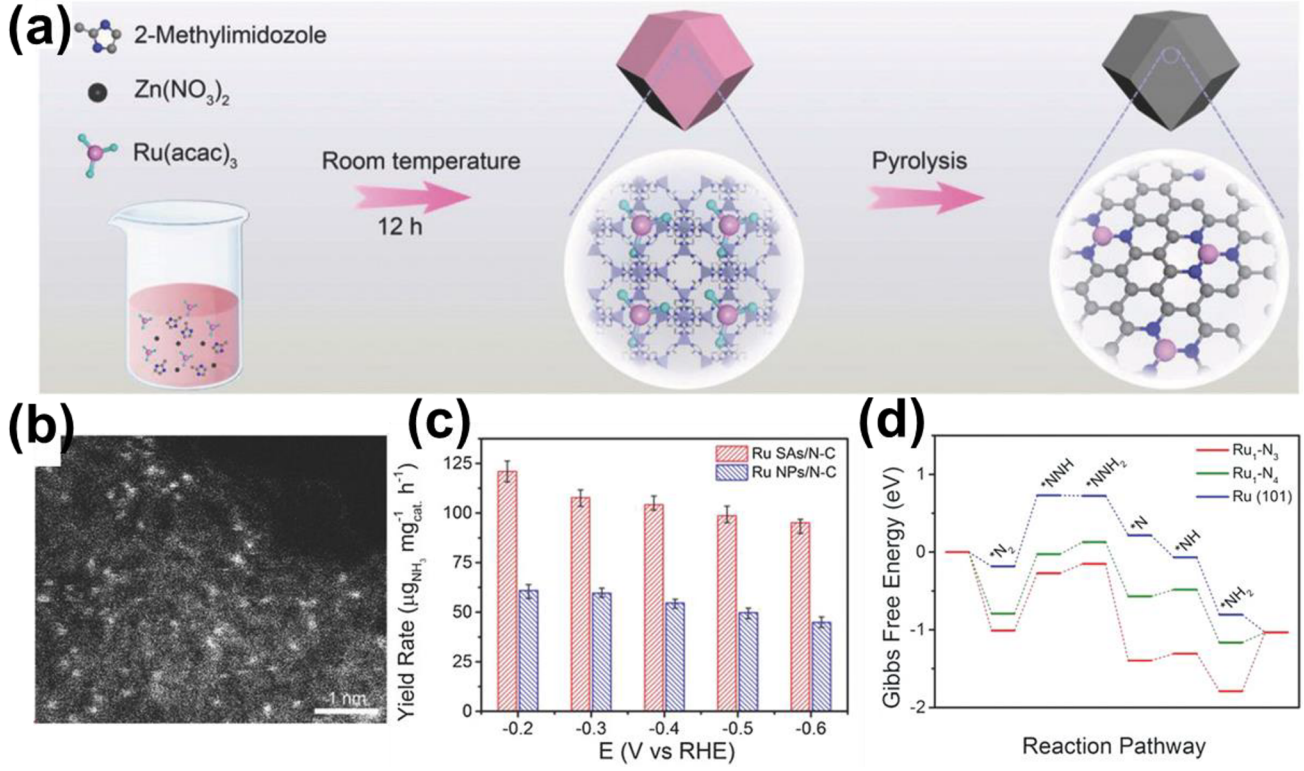

Figure 80. Ru SAs/N−C catalysts for electrochemical NRR. (a) Schematic illustration about the synthesis of Ru SAs/N−C catalysts. (b) Magnified HAADF-STEM image of Ru SAs/N−C catalysts. (c) NH_3 yield rate of Ru SAs/N−C and Ru NPs/N−C catalysts. (d) Free energy diagram of the N_2 electrochemical reduction with a distal pathway on Ru_1-N_3, Ru_1-N_4, and Ru (101). * represents an adsorption site. Reproduced with permission from ref 542. Copyright 2018 John Wiley and Sons.

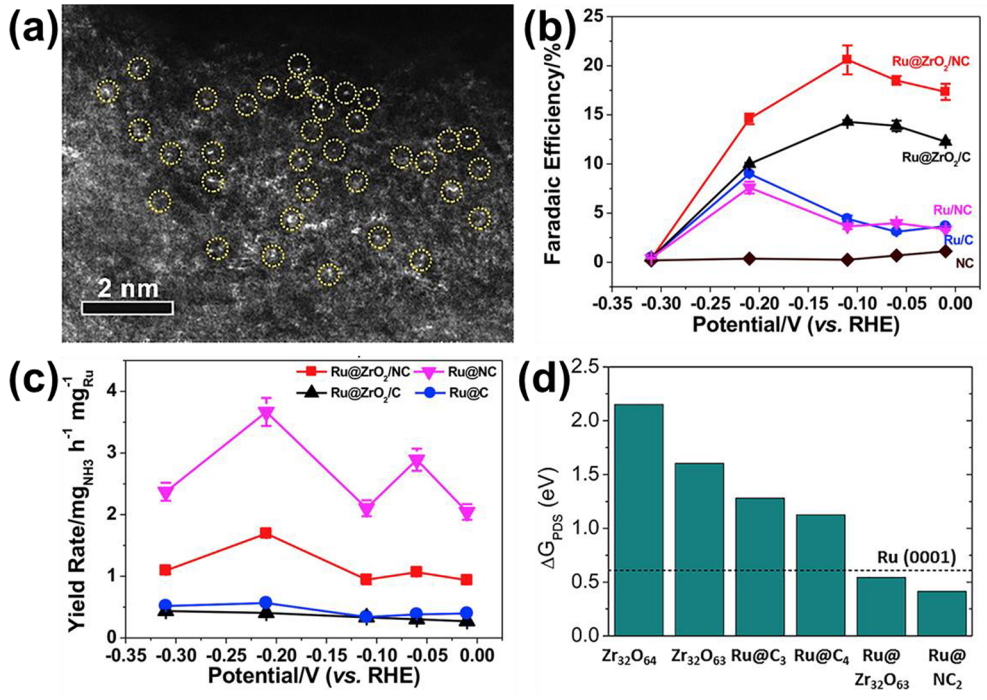

Figure 81. (a) HAADF-STEM image of the synthesized $Ru_1-ZrO_2/N-C$ catalysts. Single Ru sites are annotated with yellow dotted circles in (a). (b) Faraday efficiency and (c) NH_3 yield comparison of various Ru catalysts at applied potentials. (d) Energy barriers of the potential-determining steps for the NRR on various reaction sites, ΔG_{PDS} of Ru (0001) for NRR is also plotted with the dashed line in (d) for comparison. Reproduced with permission from ref 543. Copyright 2018 Elsevier.

stabilize key intermediates. Furthermore, difference in limiting potentials for NRR and HER is smaller for Au_1/C_3N_4 (−0.88 V) than for Au(211) (−1.67 V), indicating that thermodynamically the former is favored for NRR (Figure 82f).

https://dx.doi.org/10.1021/acs.chemrev.0c00594
Chem. Rev. 2020, 120, 12217−12314

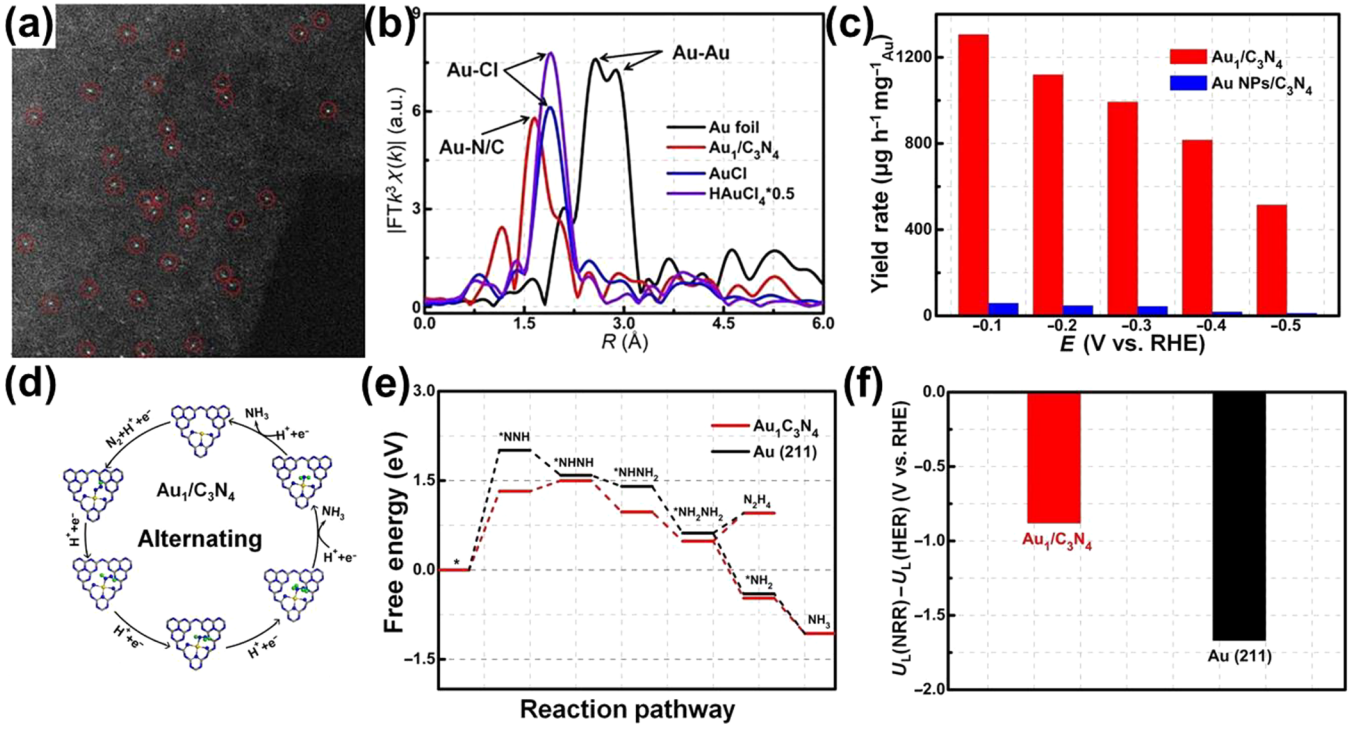

Figure 82. (a) Magnified HAADF-STEM images of Au_1/C_3N_4 directly show the atomic dispersion of Au atoms. (b) EXAFS spectra confirm the atomic dispersion of Au_1/C_3N_4. (c) NH_4^+ yield rates normalized by Au mass. (d) Optimized geometric structures of various states (*NNH, *NHNH, *NHNH, $*NH_2NH_2$, $*NH_2$) of NRR proceeded on Au_1/C_3N_4 following the alternating mechanism. (e) Free energy profile of NRR on Au_1/C_3N_4 and Au(211) at zero potential following the alternating mechanism. (f) Difference in limiting potentials for NRR and HER. Reproduced with permission from ref 552. Copyright 2018 Elsevier.

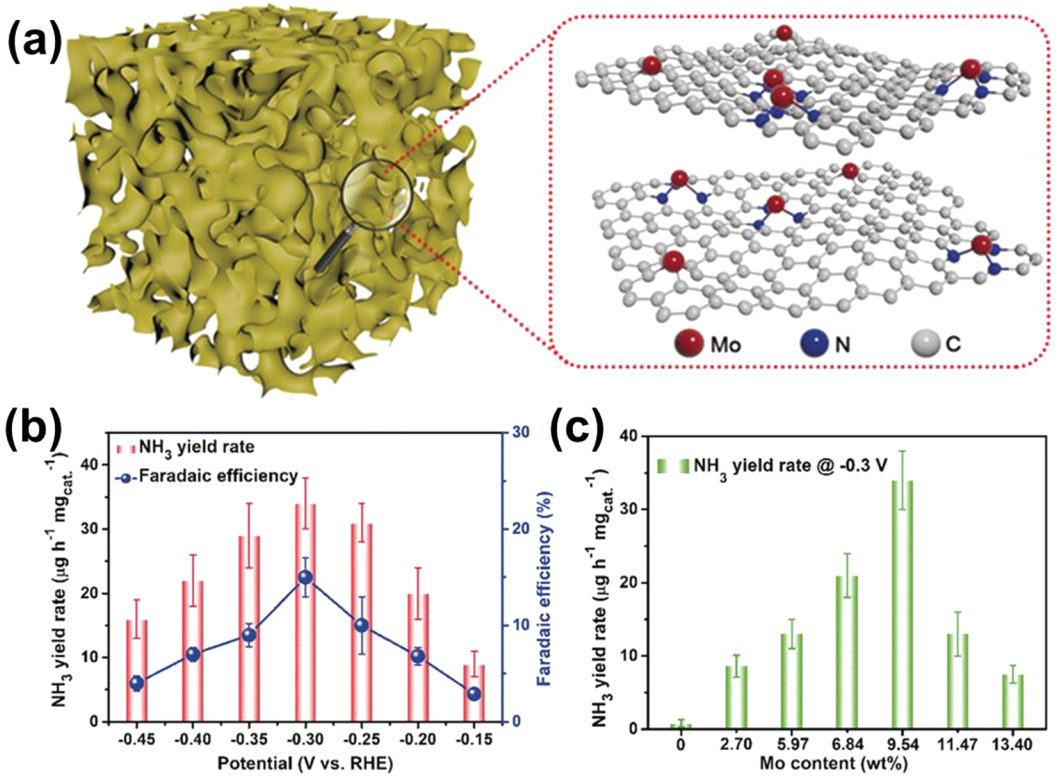

Figure 83. (a) Schematic illustration of Mo_1/NPC and its corresponding atomic structure model, (b) NH_3 yield rate and faradic efficiency for Mo_1/NPC catalysts at applied potentials, and (c) NH_3 yield rates of Mo_1/NPC samples with different Mo loadings. Reproduced with permission from ref 558. Copyright 2018 John Wiley and Sons.

https://dx.doi.org/10.1021/acs.chemrev.0c00594
Chem. Rev. 2020, 120, 12217−12314

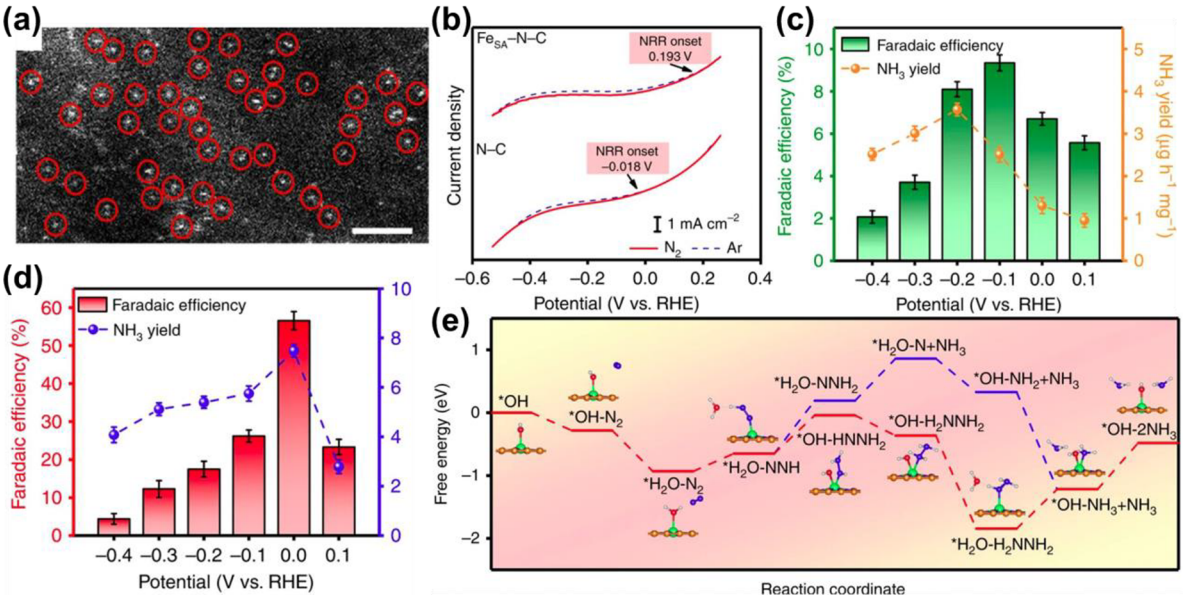

Figure 84. (a) HAADF-STEM image of Fe_{SA}–N–C. Single Fe atoms are highlighted by red circles. Scale bar: 2 nm. (b) Linear sweep voltammograms of Fe_{SA}–N–C and N–C in Ar-saturated (dashed line) or N_2-saturated (solid line) 0.1 M KOH solution with a scan rate of 50 mV s^{-1}. NH_3 Faradaic efficiencies and mass-normalized yield rates at each given potential of Fe_{SA}–N–C (c) and N–C (d). (e) Free energy diagram for the nitrogen reduction reaction (NRR) on the Fe_{SA}–N–C catalyst at U = 0 V. Inset models represent the corresponding adsorbates. The orange, blue, red, green, and gray spheres represent C, N, O, Fe, and H atoms, respectively. Reproduced with permission from ref 561. Copyright 2019 Nature Publishing Group.

8.4. Nonprecious Metal-based Single-Atom Electrocatalysts

8.4.1. Mo-based Single-Atom Electrocatalysts. Mo exists in nearly all nitrogenase enzymes as a metal center in bacteria to achieve N_2 fixation at ambient conditions.[553] On the basis of DFT calculations, Mo SAECs on various supports, such as N- doped graphene, boron nitride, carbon graphitic nitride, metal chalcogenides, and metal phosphors, have been reported to be electrocatalytically active toward NRR.[554−557]

Experimentally, Han et al. recently reported a Mo SAEC anchored on N-doped porous carbon (Mo_1/NPC) as an efficient NRR catalyst (Figure 83a).[558] The best catalyst exhibited a remarkable FE of 14.6 ± 1.6%, with a NH_3 yield rate of 34.0 ± 3.6 $\mu g_{NH3} \cdot h^{-1}$ $mg_{cat.}^{-1}$ at −0.3 V in 0.1 M KOH at room temperature. Most Mo atoms in Mo_1/NPC were bonded with C or N atoms, with a small fraction in the form of clusters. The peak NH_3 production coincided with the maximum loading of Mo single-atom sites, which was argued to be a key factor in determining the NRR activity.

A new class of zerovalent molybdenum graphdiyne-based atom catalysts (Mo^0/GDY) was reported as efficient electrochemical NRR electrocatalysts.[559] The Mo sites led to a redistribution of the charge from C sites to adsorbates, playing an central role in stabilizing intermediates for NRR. DFT calculations reveal that the strong electron-rich local environment preserves Mo^0 by a strong p−d coupling. Fast and reversible Mo−C_1 charge transfer enables a high protonation rate on N and curbs the selectivity and activity toward NRR. The obtained catalyst exhibited a high Mo single atom loading (7.5 wt %) and promising reactivity for NRR in neutral (0.1 M Na_2SO_4) electrolytes, with a yield rate of 145.4 $\mu g \cdot h^{-1}$ $mg_{cat.}^{-1}$ and FE > 21%.

8.4.2. Fe-based Single-Atom Electrocatalysts. Fused-iron catalysts have been utilized worldwide in the industrial Haber−Bosch process for over a century. Besides, iron plays a crucial role in all biological nitrogenases for N_2 fixation. Therefore, Fe is among the earliest transition metals to be examined for electrochemical NRR. Metallic iron was tested as a cathode for NRR in 6 M KOH electrolyte under ambient temperature and pressure by Sclafani et al. They observed a volcano-shaped relation between ammonia yield rates and applied potentials, with the peak yield at 1.06 V vs SCE.[560] Metallic Fe reaches a maximum yield of 2 $mmol \cdot h^{-1}$ m^{-2} and FE of around 1%. However, the sluggish NRR kinetics on Fe surface and the corrosion of Fe in alkaline electrolyte hindered further study on Fe-based catalysts. The emergence of Fe SAECs provides unique opportunities to tune the catalytic activity and durability of Fe-based catalysts via strong coordination with heteroatoms such as N.

In a recent study, Wang et al. constructed Fe_{SA}–N–C catalysts via optimized modulation of the polypyrrole−iron coordination complex. (Figure 84a).[561] The obtained Fe_{SA}–N–C catalysts shifted the ammonia synthesis to a positive onset potential of 0.193 V (Figure 84b), enabling a dramatically enhanced Faradaic efficiency of 56.55% at 0 V in 0.1 M KOH. In comparison, the FE for N–C was less than 7% under the same condition (Figure 84c,d). The FE for NRR on Fe_{SA}–N–C was maintained after 15 cycles of test. Notably, Fe single atoms remained well dispersed after the durability test, suggesting marked stability for Fe-based catalysts in the alkaline electrolyte. DFT calculations reveal that the energy barrier for water dissociation was as high as 2.91 eV, indicating negligible adsorption of *H on Fe_{SA}–N–C, while NRR pathways were favored during the electrolysis (Figure 84e).

In the studies by Lü et al. and Zhang et al., Fe−N_4 structures were constructed by direct pyrolysis of different types of Fe-based MOFs (PCN-222 and Fe-ZIF) (Figure 85).[562,563] Further study by He et al. identified FeN_4 as the active site for NRR in FePc molecule.[564] Fe_1/N–C shows efficient ammonia synthesis with a yield rate of 1.56 × 10^{-11} $mol \cdot cm^{-2}$

https://dx.doi.org/10.1021/acs.chemrev.0c00594
Chem. Rev. 2020, 120, 12217−12314

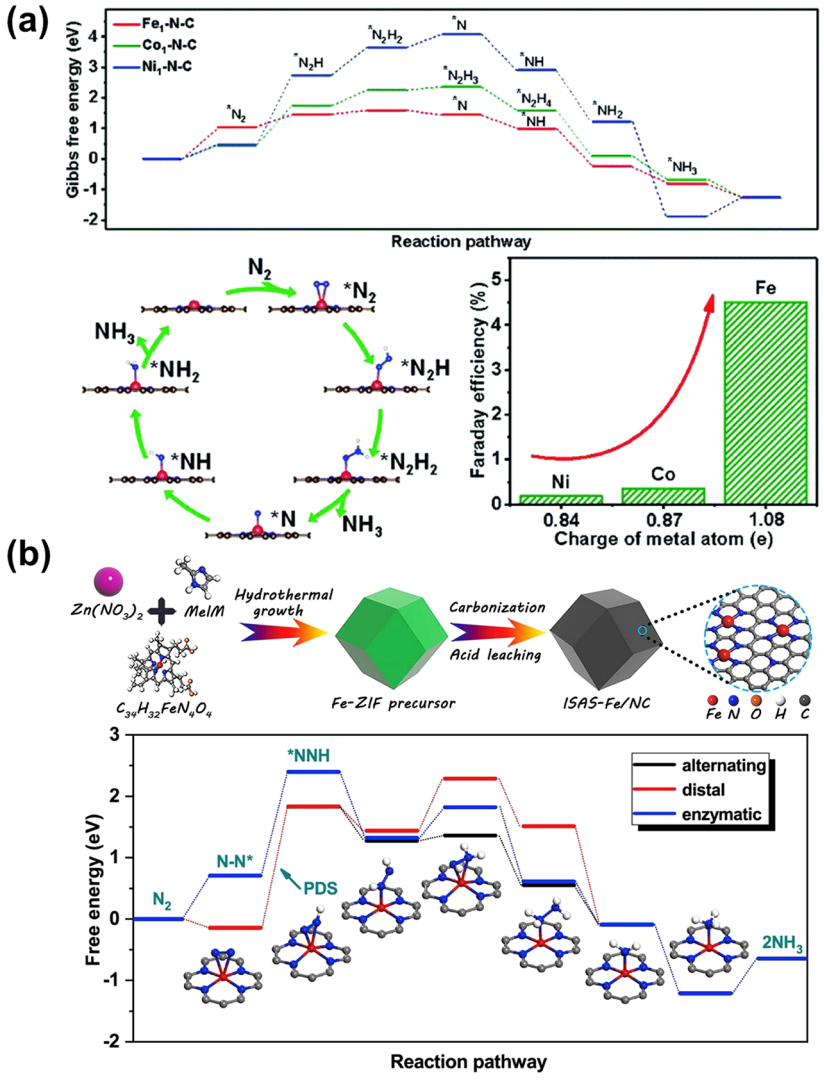

Figure 85. (a) Free energy plot of the NRR on $Fe_1/Co_1/Ni_1$−N−C, the intermediates in the distal path of the NRR on Fe_1−N−C, and the Bader charge analysis of $Fe_1/Co_1/Ni_1$−N−C. Reproduced with permission from ref 562. Copyright 2019 The Royal Society of Chemistry. (b) Schematic illustration describing the synthesis of ISAS-Fe/NC catalysts. (b) Free energy profiles for NRR on ISAS-Fe/NC catalysts for three possible pathways. Reproduced with permission from ref 563. Copyright 2019 Elsevier.

s^{-1} and FE of 4.51% at −0.05 V (vs RHE), outperforming Co_1/N−C and Ni_1/N−C synthesized in a similar procedure (Figure 85a). Notably, as shown in Figure 85b, the obtained isolated Fe atomic sites were anchored to N-doped carbon frameworks (ISAS-Fe/NC) and achieved an FE of 18.6% and an NH_3 yield rate 62.9 $\mu g \cdot h^{-1}$ $mg_{ca.}^{-1}$ at −0.4 V (vs RHE) in 0.1 M PBS. In contrast, the highest FE on Fe foil, Fe nanoparticles/NC, and NC was measured to be 0.08%, 1.3%, and 0.45%, respectively. It should be noted that for the Fe−N_4 structures, the side-on configuration for N_2 adsorption and the enzymatic mechanism are preferred based on DFT calculations.

Recently, Fe−N_3 species was reported to show better performance than Fe−N_4 in a Fe_1−N/C hybrid structure by mixing Fe-ZIF precursor with carbon nanotubes (Figure 86a).[565] The highest average yield of NH_3 was 34.83 $\mu g \cdot h^{-1} \cdot mg^{-1}_{ca.}$ for Fe−N/C−CNTs, representing an improvement factor of 77.4× and 4.52×, as compared to CNTs and NC−CNTs, respectively. The FE for NRR was increased to 9.28% at −0.2 V for Fe−N/C−CNTs (Figure 86b,c). The yield rate of NH_3 was found to correlate with the loading of pyridinic N (Figure 86d). Pyridinic N was argued to provide the anchoring sites for Fe−N_3, a primary NRR active site. The role of Fe−N_3 sites was further confirmed by KSCN poisoning experiment. According to DFT calculation, N_2 could be spontaneously chemisorbed on the Fe−N_3 sites with a free energy of −0.75 eV (Figure 86e). Besides, the Fe−N_3 species exhibited a large spin moment of 3.16 μB, which could promote N_2 adsorption and activate N≡N triple bond.[566,567]

8.5. Other Metal-based Single-Atom Electrocatalysts

The planar Co−N_4 structure obtained from MOFs pyrolysis has shown activity for NRR.[568] Co single-atom/N-doped porous carbon obtained at 750 °C (CSA/NPC-750) shows the highest NH_3 yield rate of 0.86 $mmol \cdot cm^{-2}$ h^{-1} −0.2 V. In comparison with Co nanoparticles (Co/NPC), CSA/NPC-750 exhibited an NH_3 production rate that was 2 times greater, even at a lower loading of 6.8 wt %. Temperature is an important parameter for tuning N loading in this material. CSA/NPC-750 had the highest total N content (20.6 at%), followed by CSA/NPC-850 (15.3 at%) and CSA/NPC-950 (13.0 at%). The improved electrocatalytic activity of CSA/

https://dx.doi.org/10.1021/acs.chemrev.0c00594
Chem. Rev. 2020, 120, 12217−12314

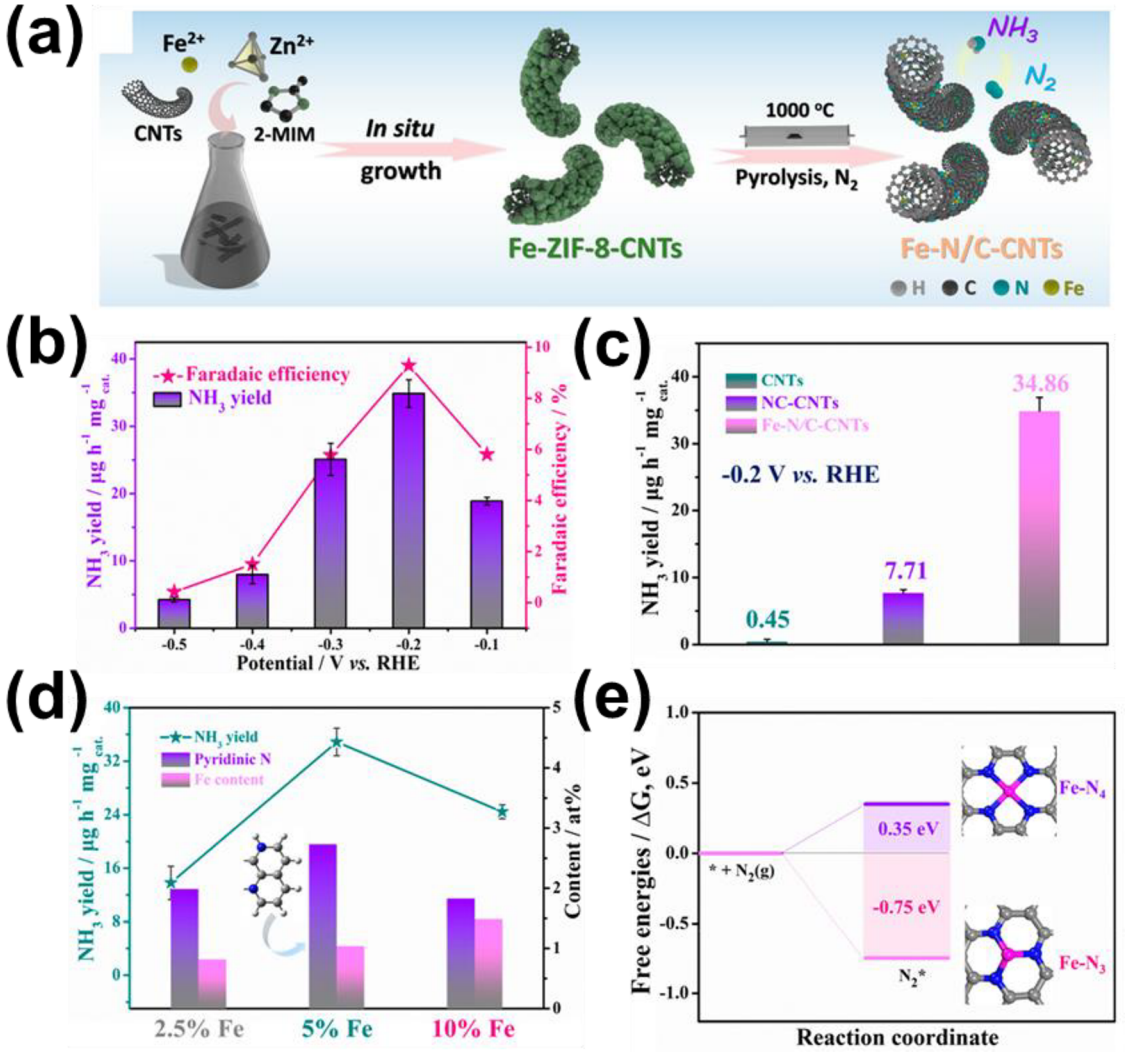

Figure 86. (a) Scheme illustration of the synthesis of Fe−N/C−CNTs. (b) Yield rate of NH_3 (blue) and the Faradaic efficiency (red) at each given potential. (c) Yield rate of NH_3 at −0.2 V vs RHE at room temperature and ambient pressure with different catalysts. (d) Correlation between the yield rate of NH_3 and different N contents with catalysts with different amounts of Fe. (e) Different free energy diagrams of the N_2 adsorption on the Fe−N_4 and Fe−N_3 structures. Reproduced with permission from ref 565. Copyright 2019 American Chemical Society.

NPC-750 was explained by its higher N content, especially pyridinic N (dominant N species with a content of 14.0 at%).

Metal−N_2 moiety was also proved to be active toward electrochemical NRR at ambient condition in the case of Cu/N−C system.[569] Cu-doped C_3N_4 was annealed to obtain Cu single-atom−N−C catalysts (NC-Cu SA) (Figure 87a). The NC-Cu SA is shown to exhibit an outstanding FE of 13.8% and 11.7%, high NH_3 yield rate of ∼53.3 and ∼49.3 $\mu g_{NH3} \cdot h^{-1} mg_{ca.}^{-1}$ in 0.1 M KOH and 0.1 M HCl electrolytes, respectively, surpassing the performance of Cu nanoparticles on nitrogen-doped carbon (NC-Cu NP) and pure nitrogen-doped carbon (N−C). According to XANES measurements, the structure of NC-Cu SA is a mixture of Cu−N_2 (20% ± 5%) and Cu−N_4/N_3C (80% ± 5%). DFT calculations demonstrate that Cu atoms in Cu−N_2 strongly adsorb N_2 and catalyze NRR through the alternating mechanism.

8.6. Perspectives about Single-Atom Electrocatalysts for Nitrogen Reduction Reaction

Despite the progress in past decades, the yield rate of ammonia in electrochemical NRR remains extremely low, hindering the practical prospect of such a technology. The development of NRR is still in its primary stage with many unanswered questions. First, the activation of inert N_2 molecules is still challenging on SAECs. The active sites on the SAECs need to be further explored to guide the design of highly efficient NRR catalysts. Second, the biggest challenge for NRR is the rapid side reaction, HER, which features a much lower activation barrier. Consequently, the FE for NRR is significantly compromised once HER takes off at high overpotentials. Inspired by the progress of catalyst design for CO2RR, researchers have explored several strategies to suppress HER. For instance, engineering of the surface hydrophilicity/hydrophobicity has been reported to effectively suppress HER.[570,571] Besides, some metal centers in SAECs have high overpotentials for HER, such as Bi, Sn, Sb, and In, and have potentials for catalyzing NRR. Lastly, the stability of single-atom catalysts requires further optimization. To date, most single-atom catalysts for NRR are based on the M−N−C sites. However, metal centers in M−N−C sites can be bonded with oxygen in aqueous media during NRR, leading to potential degradation of active sites. Precise control of synthesis, electrochemical test, and supporting environment is needed to improve the stability of SACEs for NRR (Table 6).

https://dx.doi.org/10.1021/acs.chemrev.0c00594
Chem. Rev. 2020, 120, 12217−12314

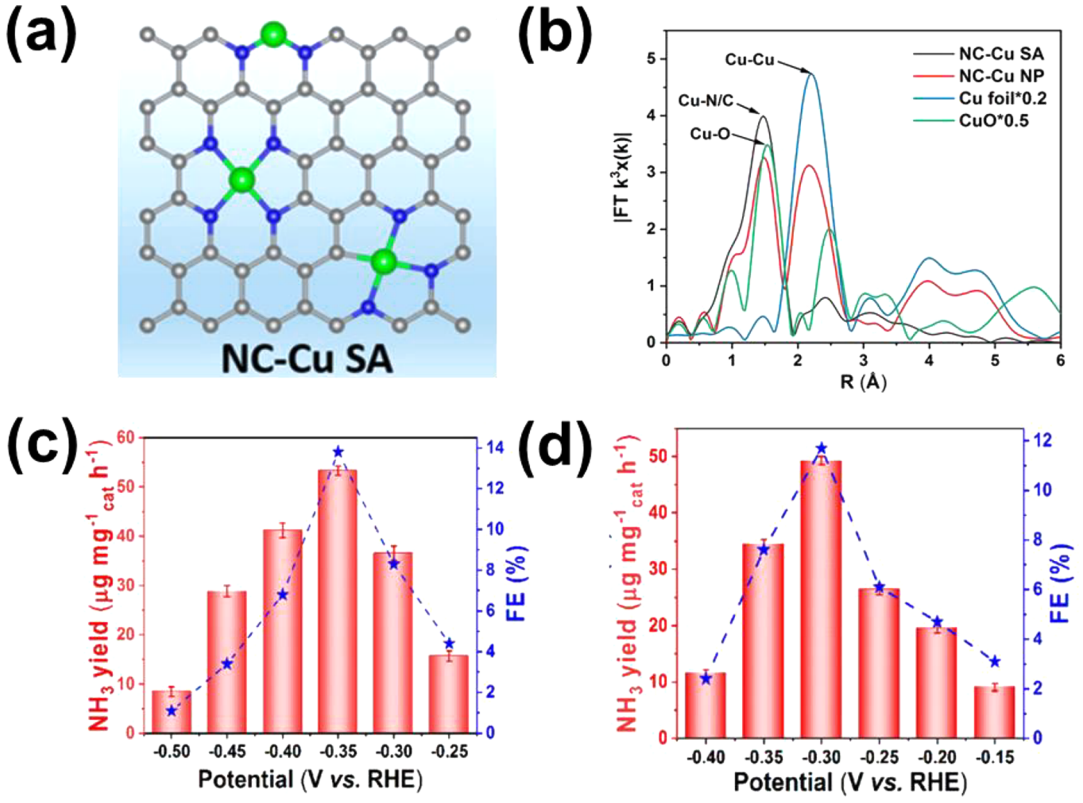

Figure 87. (a) Atomic structure of Cu single atom on N-doped C. (b) *k*-weighted $\chi(k)$ function of EXAFS spectra. (c,d) NH_3 yield rate and FE at different potentials in 0.1 M KOH (c) and 0.1 M HCl (d). Reproduced with permission from ref 569. Copyright 2019 American Chemical Society.

Table 6. Catalytic Performance of SAECs toward NRR

catalysts	electrolyte	FE (%)	NH_3 yield rate ($\mu g_{NH3} \cdot mg^{-1}\ h^{-1}$)	partial current density (mA cm^{-2})	ref
Ru SAs/N−C	0.05 M H_2SO_4	29.6	120.9	0.13	542
Ru_1−ZrO_2/N−C	0.1 M HCl	15	~1.8	0.21	543
Ru_1/N−C	0.1 M HCl	~7.5	3.665	0.15	543
CF-Ru SAs/g-C_3N_4	0.5 M NaOH	8.3	23.0		544
Au_1−NDPC	0.1 M HCl	12.3	2.32	~0.02	551
Au_1/C_3N_4	5 mM H_2SO_4	11.1	1.305		552
Mo_1/NPC	0.1 M KOH	14.6	34	~0.16	558
Mo^0/GDY	0.1 M Na_2SO_4	>21	145.4		559
Fe_{SA}−N−C	0.1 M KOH	56.55	~7.5		561
FePc/C	0.1 M Na_2SO_4	10.5	137.95	~0.05	564
Fe_1/N−C	0.1 M HCl	4.51	1.56×10^{-11}		562
ISAS-Fe/NC	0.1 M PBS	18.6	62.9	~0.3	563
Fe−N/C−CNTs	0.1 M KOH	9.28	34.83	~0.07	565
CSA/NPC-750	0.05 M Na_2SO_4	10.5	0.86	~0.06	568
NC-Cu SA	0.1 M KOH	13.8	~53.3	~0.083	569
NC-Cu SA	0.1 M HCl	11.7	~49.3	~0.076	569

9. OUTLOOK

Single-atom electrocatalysis has evolved to become a new frontier of electrochemical research.[572] The unique atomic structures and adsorption properties of SAECs make them compelling in improving the energy conversion and chemical transformation efficiencies of electrochemical reactions. Compared to conventional nanoparticulate catalysts that have various types of surface structures, SAECs are considered to be well-defined active site models; thus, the structure−property relationship can be precisely described and readily applied for rational design of advanced electrocatalysts. Superior catalytic activity and selectivity have been demonstrated in many scenarios, with the advanced catalytic performance typically originating from the exotic metal−substrate coordination and electronic interactions. SAECs also possess great potential for reducing the cost of electrochemical systems, owing to their high utilization efficiency of metal elements and stabilization of non-noble metals under harsh reaction conditions. Nevertheless, despite tremendous progress in recent years, further development in the following aspects is envisioned to be essential for advancing the practical implementation of SAECs:

https://dx.doi.org/10.1021/acs.chemrev.0c00594
Chem. Rev. 2020, 120, 12217−12314

9.1. Improved Stability

An inevitable concern with atomically dispersed metal atoms is their stability, especially under harsh electrochemical reaction conditions, such as in ORR and OER. The reported stability tests of SAECs in such reactions range from ∼10 to ∼100 h.[59,197,390,515] However, to bridge the gap between preliminary laboratory tests and industrial applications, the stability of SAECs needs to be substantially improved to meet the DOE goal of 8000 h.[64] Fundamental studies and understanding of the degradation mechanisms of SAECs are still limited. It remains elusive whether the degradation is triggered by the attack to the metal atoms, the heteroatomic ligand (e.g., N) or the conductive substrate. Because the metal atoms are usually in their cationic form (i.e., positively charged), their dissolution in acidic or alkaline electrolyte does not necessarily involve the oxidation step, distinct from the situation of metal nanoparticles. The metal atoms are typically anchored via doped N or other heterogeneous species. It is likely that stronger coordination to the metal atom would lead to enhanced stability, but such a trend has not been explicitly revealed. To understand the structure−property relationship governing the stability of SAECs, it is a prerequisite to examine the possible degradation mechanisms of the substrate (e.g., carbon). Under reaction conditions, the doped heteroatoms, such as N, may be leached out, and the defective sites for anchoring metal atoms may also experience structural changes, both of which can affect the stability of the metal centers. In this aspect, combination of operando spectroscopic studies and computational simulations will be a viable approach in unravelling the mechanistic origin, which can then be used to design SAECs with enhanced stability.

9.2. Implementation in Practical Devices

Despite the advantages and potential of SAECs, significant challenges remain for their implementation in practical devices. Owing to their different form factors and microscopic structures from conventional electrocatalysts based on metal nanoparticles supported on carbon, direct incorporation of SAECs into MEAs following established protocols has encountered challenges in water management[434] and gas/heat transfer.[74,573,574] This is primarily due to the low volumetric density of active sites in the SAECs, as compared to conventional nanoparticulate electrocatalysts. It may require a redesign of the MEAs, adoption of new ionomers that are compatible with SAECs, revision of the fabrication protocols, etc. to take full advantage of their superior electrocatalytic performance.

9.3. Engineering of Ensemble Size of Metal Sites

Our discussion of SAECs hitherto has illustrated the advantages of single-atom active sites. The isolated active sites may be a disadvantage in some electrocatalytic processes. For example, C−C coupling for the electroreduction of CO_2 to C_2 hydrocarbons generally require two adjacent adsorption sites.[432,433] Even though the coordinative atoms, such as N, O, S, P, and C, have been argued to play a synergetic role in the stabilization of certain intermediates, C_1 compounds (formate, CO, methane, or methanol) have been found to dominate the products of CO2RR catalyzed by SAECs. To enable such Langmuir−Hinshelwood (L−H) type of reaction mechanisms, it becomes imperative to explore an atomic-level control over the ensemble size of the active sites. Notably, metal dimers or trimers have been extensively studied in heterogeneous catalysis, as enabled by the confinement in zeolite channels[74] or supporting on metal oxides.[575] Electrocatalysts with dimeric metal sites have also been reported for CO2RR, albeit with CO being the dominant product.[33,576,577] The full potential of electrocatalysts with controlled ensemble sizes is yet to be discovered.

AUTHOR INFORMATION

Corresponding Authors

Chao Wang − *Department of Chemical and Biomolecular Engineering, Johns Hopkins University, Baltimore, Maryland 21218, United States;* orcid.org/0000-0001-7398-2090; Email: chaowang@jhu.edu

Minhua Shao − *Department of Chemical and Biological Engineering, Energy Institute, Hong Kong Branch of the Southern Marine Science and Engineering Guangdong Laboratory, and Chinese National Engineering Research Center for Control & Treatment of Heavy Metal Pollution, The Hong Kong University of Science and Technology, Kowloon, Hong Kong, P. R. China*; Email: kemshao@ust.hk

Shaowei Chen − *Department of Chemistry and Biochemistry, University of California, Santa Cruz, California 95064, United States;* orcid.org/0000-0002-3668-8551; Email: shaowei@ucsc.edu

Gang Wu − *Department of Chemical and Biological Engineering, University at Buffalo, The State University of New York, Buffalo, New York 14260, United States;* orcid.org/0000-0003-0885-6172; Email: gangwu@buffalo.edu

Jie Zeng − *Hefei National Laboratory for Physical Sciences at the Microscale, Key Laboratory of Strongly-Coupled Quantum Matter Physics of Chinese Academy of Sciences, Key Laboratory of Surface and Interface Chemistry and Energy Catalysis of Anhui Higher Education Institutes, Department of Chemical Physics, University of Science and Technology of China, Hefei, Anhui 230026, P. R. China*; Email: zengj@ustc.edu.cn

Authors

Yuxuan Wang − *Department of Chemical and Biomolecular Engineering, Johns Hopkins University, Baltimore, Maryland 21218, United States*

Hongyang Su − *Hefei National Laboratory for Physical Sciences at the Microscale, Key Laboratory of Strongly-Coupled Quantum Matter Physics of Chinese Academy of Sciences, Key Laboratory of Surface and Interface Chemistry and Energy Catalysis of Anhui Higher Education Institutes, Department of Chemical Physics, University of Science and Technology of China, Hefei, Anhui 230026, P. R. China*

Yanghua He − *Department of Chemical and Biological Engineering, University at Buffalo, The State University of New York, Buffalo, New York 14260, United States*

Ligui Li − *New Energy Research Institute, School of Environment and Energy, South China University of Technology, Guangzhou 510007, China*

Shangqian Zhu − *Department of Chemical and Biological Engineering, The Hong Kong University of Science and Technology, Kowloon, Hong Kong, P. R. China;* orcid.org/0000-0002-5813-9588

Hao Shen − *Department of Chemical and Biomolecular Engineering, Johns Hopkins University, Baltimore, Maryland 21218, United States*

Pengfei Xie − *Department of Chemical and Biomolecular Engineering, Johns Hopkins University, Baltimore, Maryland 21218, United States;* orcid.org/0000-0002-7644-9934

https://dx.doi.org/10.1021/acs.chemrev.0c00594
Chem. Rev. 2020, 120, 12217−12314

Xianbiao Fu − *Department of Chemical and Biomolecular Engineering, Johns Hopkins University, Baltimore, Maryland 21218, United States*

Guangye Zhou − *Department of Chemical and Biomolecular Engineering, Johns Hopkins University, Baltimore, Maryland 21218, United States*

Chen Feng − *Hefei National Laboratory for Physical Sciences at the Microscale, Key Laboratory of Strongly-Coupled Quantum Matter Physics of Chinese Academy of Sciences, Key Laboratory of Surface and Interface Chemistry and Energy Catalysis of Anhui Higher Education Institutes, Department of Chemical Physics, University of Science and Technology of China, Hefei, Anhui 230026, P. R. China*

Dengke Zhao − *New Energy Research Institute, School of Environment and Energy, South China University of Technology, Guangzhou 510007, China*

Fei Xiao − *Department of Chemical and Biological Engineering, The Hong Kong University of Science and Technology, Kowloon, Hong Kong, P. R. China*

Xiaojing Zhu − *New Energy Research Institute, School of Environment and Energy, South China University of Technology, Guangzhou 510007, China*

Yachao Zeng − *Department of Chemical and Biological Engineering, University at Buffalo, The State University of New York, Buffalo, New York 14260, United States*

Complete contact information is available at: https://pubs.acs.org/10.1021/acs.chemrev.0c00594

Author Contributions

[▽]Y. Wang, H. Su, Y. He, L. Li, and S. Zhu contributed equally to the work.

Notes

The authors declare no competing financial interest.

Biographies

Yuxuan Wang is a Ph.D. candidate in the Department of Chemical and Biomolecular Engineering, Johns Hopkins University. He received his B.S. degree in chemistry from Nankai University in 2017. After that, he has worked in Dr. Chao Wang's group at Johns Hopkins as a research assistant, with the interest focusing on electrocatalysis and electrochemical biosensors.

Hongyang Su is a Ph.D. candidate at National Laboratory for Physical Sciences at the Microscale, University of Science and Technology of China, Hefei. His advisor is Prof. Jie Zeng. He received his B.S. degree in chemistry from Shandong University in 2013. His current research interests include electrochemistry and operando characterizations on the heterogenous catalysis using X-ray spectroscopy.

Yanghua He is a Ph.D. student at the Department of Chemical and Biological Engineering, University at Buffalo (UB), SUNY. She received her B.S. in Chemistry at Sun Yat-Sen University (SYSU) in 2015, followed by research training at Dalian Institute of Chemical Physics, Chinese Academy of Sciences (2015−2016). Her research interests focus on the development of functional materials and their applications on electrochemical energy storage and conversion.

Ligui Li received his B.S. degree from Jilin University (China) in 2004 and his Ph.D. degree from Changchun Institute of Applied Chemistry (CIAC), Chinese Academy of Sciences (CAS) in January 2010. He then started postdoctoral research with Professor Hai-Feng Ji at Drexel University in 2010 and Professor Ling Zang at the University of Utah in 2011. In 2013, he became an associate professor in the School of Environment and Energy at South China University of Technology (SCUT). His recent research interests include the synthesis of nanomaterials for energy storage and the physics and chemistry of functional polymers.

Shangqian Zhu is a Research Grants Council Postdoctoral Fellow at the Department of Chemical and Biological Engineering, The Hong Kong University of Science and Technology, Hong Kong SAR, China. He obtained his Ph.D. degree in Chemical and Bimolecular Engineering from the same department in 2020 under the supervision of Prof. Minhua Shao, working on carbon dioxide electrochemical reduction reactions. His current research interests include in situ spectroscopy and advanced materials for energy conversion and storage.

Hao Shen is a Ph.D. candidate in the Department of Chemical and Biomolecular Engineering at Johns Hopkins University. He obtained his B.S. degree (2019) from Fudan University. His current research focuses on electrochemistry and its applications for energy conversion and storage.

Pengfei Xie is an Assistant Research Scientist in the Department of Chemical and Biomolecular Engineering, Johns Hopkins University. He works in Prof. Chao Wang's group on heterogeneous catalysis. He obtained his Ph.D. in Chemistry from Fudan University in 2016, with the thesis themed on the reduction of NO_x catalyzed by transitional metal-exchanged zeolites. His current research interests includes single-atom catalysts for chemical transformations.

Xianbiao Fu is a Ph.D. candidate at University of Electronic Science and Technology of China, under the supervision of Prof. Yijin Kang. He is currently a visiting Ph.D. student in Prof. Chao Wang's group at Department of Chemical and Biomolecular Engineering, Johns Hopkins University. He obtained his B.S. degree from Central South University in 2016. His research focuses on the catalysis science in electrochemical reduction of CO_2 and N_2.

Guangye Zhou is a graduate student in the Department of Chemical and Biomolecular Engineering, Johns Hopkins University. In 2019, he obtained his B.S. degree from the School of Chemical Engineering and Technology, Tianjin University. His current research interests focus on the advanced nanomaterials for energy storage and CO_2 reduction.

Chen Feng is a Ph.D. candidate at the National Laboratory for Physical Sciences at the Microscale, University of Science and Technology of China, Hefei. Her advisor is Prof. Jie Zeng. She received her B.S. degree in Materials Science and Engineering at Nanjing University of Aeronautics and Astronautics in 2016. Her current research interests include electrochemistry and single-atom catalysts for water splitting.

Dengke Zhao received his B.S. degree from Zhengzhou University of Light Industry in 2015. He is currently a Ph.D. candidate in South China University of Technology under the supervision of Prof. Ligui Li. His research interests focus on the design and synthesis of novel functional nanomaterials and their applications on electrochemical energy conversion and storage.

Fei Xiao is a Ph.D. candidate at the Department of Chemical and Biological Engineering, The Hong Kong University of Science and Technology, Hong Kong SAR, China. She is under the supervision of Prof. Minhua Shao, working on oxygen reduction reactions. Her current research interests include nonprecious metal and hybrid electrocatalysts for proton exchange membrane fuel cells.

Xiaojing Zhu is a Ph.D. candidate in the School of Environment and Energy, SCUT. He received his M.S. degree from Guangdong Pharmaceutical University in 2017. His research focuses on the design

https://dx.doi.org/10.1021/acs.chemrev.0c00594
Chem. Rev. 2020, 120, 12217−12314

and fabrication of functionalized carbon-based composite nanomaterials for efficient hydrogen/oxygen electrocatalysis.

Yachao Zeng is a postdoc research associate at the Department of Chemical and Biological Engineering, University at Buffalo, SUNY. He received his Ph.D. degree in 2018 from Dalian Institute of Chemical Physics, Chinese Academy of Sciences, majoring in chemical engineering. He continued his research as a postdoc at the University of New South Wales (Australia, 2018−2020). His research focuses on the development of advanced nanomaterials and devices for energy storage technologies.

Minhua Shao is a Professor at the Department of Chemical and Biological Engineering, Associate Director of Energy Institute and Director of Sustainable Energy Engineering Program of the Hong Kong University of Science and Technology, Hong Kong SAR, China. Prior to this appointment, he worked in UTC Power as a Technical Fellow on fuel cell and Ford Motor Company as Senior Battery Engineer on next-generation battery research. He earned a Ph.D. degree in Materials Science and Engineering from the State University of New York at Stony Brook in 2006, working on fuel cell reactions. His current research mainly focuses on electrocatalysis, fuel cells, and advanced batteries.

Shaowei Chen received his B.S. degree in Chemistry from the University of Science and Technology of China in 1991, and his M.S. and Ph.D. degrees from Cornell University in 1993 and 1996, respectively. Following a postdoctoral appointment at the University of North Carolina at Chapel Hill, he started his independent career in Southern Illinois University in 1998. In 2004, he moved to the University of California Santa Cruz and is currently a professor of chemistry. His research interests are primarily focused on high-performance catalysts for electrochemical energy conversion and storage, impacts of core−ligand interfacial bonding interactions on nanoparticle charge-transfer dynamics, Janus nanoparticles by interfacial engineering, and antimicrobial activity of functional nanocomposites.

Gang Wu is a professor at the Department of Chemical Engineering, University at Buffalo (UB), SUNY. He obtained his Ph.D. on Electrochemical Engineering at the Harbin Institute of Technology in 2004, followed by postdoctoral training at Tsinghua University, the University of South Carolina, and Los Alamos National Laboratory (LANL). Dr. Wu became a staff scientist at LANL in 2010. He joined UB as an assistant professor in 2014 and was promoted as a tenured associate professor in 2018 and a full professor in 2020. His research interests are electrochemical energy science and technology with an emphasis on catalysts for fuel cells and batteries.

Jie Zeng received his B.S. degree in Applied Chemistry at the University of Science and Technology of China in 2002 and his Ph.D. in Condensed Matter Physics (with Prof. Jianguo Hou) in 2007. He worked in Prof. Younan Xia's group as a postdoctoral fellow at Washington University in St. Louis from 2008 to 2011. Since 2012, he has held the position of Professor for Chemistry in the Hefei National Laboratory for Physical Sciences at the Microscale. His current research focuses on heterogeneous catalysis including atomic-level design of active sites and understanding of catalytic mechanisms.

Chao Wang received his B.S. degree in Physics from the University of Science and Technology of China in 2004 and Ph.D. in Engineering, with Prof. Shouheng Sun as the advisor, from Brown University in 2009. He worked as a postdoctoral fellow in Drs. Vojislav R. Stamenkovic and Nenad M. Markovic's group at Argonne National Laboratory up to 2012. After that he joined the Department of Chemical and Biomolecular Engineering at Johns Hopkins University as Assistant Professor and got promoted to Associate Professor in 2019. His current research focuses on heterogeneous catalysis for both electrochemical energy conversion and thermochemical molecular transformation reactions.

ACKNOWLEDGMENTS

C. Wang acknowledges the financial support from National Science Foundation (CBET-1803482 and CBET-1930013) and Department of Energy (DE-EE0008501). G. Wu appreciates the financial support from the U.S. Department of Energy, Office of Energy Efficiency and Renewable Energy (EERE), Fuel Cell Technology Office (DE-EE0008075, DE-EE0008076, and DE-EE0008417) along with National Science Foundation (CBET-1604392, 1804326). J. Zeng acknowledges the support from National Science Fund for Distinguished Young Scholars (21925204), NSFC (U19A2015), National Key Research and Development Program of China (2019YFA0405600), Key Research Program of Frontier Sciences of the CAS (QYZDB-SSW-SLH017), Fundamental Research Funds for the Central Universities, and USTC Research Funds of the Double First-Class Initiative (YD2340002002). M. Shao recognizes the support from National Key R&D Program of China (no. 2017YFB0102900), the Research Grant Council (16310419, 26206115, 16309418, N_HKUST610/17, T23-601/17-R) and Innovation and Technology Commission (ITC-CNER-C14EG03, ITC-CNERC14SC01) of the Hong Kong Special Administrative Region, the Shenzhen Science and Technology Innovation Commission (SGDX2019081623340748, JCYJ20180507183818040), and Foshan-HKUST Project (FSUST19-FYTRI07). S. Zhu was supported by the Research Grants Council Postdoctoral Fellowship Scheme (PDFS2021-6S08). S. Chen thanks the National Science Foundation for partial support of this work (CHE-2003685, CHE-1900235, and CBET-1848841).

REFERENCES

(1) Kulkarni, A.; Siahrostami, S.; Patel, A.; Nørskov, J. K. Understanding Catalytic Activity Trends in the Oxygen Reduction Reaction. *Chem. Rev.* **2018**, *118*, 2302−2312.
(2) Xie, C.; Niu, Z.; Kim, D.; Li, M.; Yang, P. Surface and Interface Control in Nanoparticle Catalysis. *Chem. Rev.* **2020**, *120*, 1184−1249.
(3) Hunt, S. T.; Román-Leshkov, Y. Principles and Methods for the Rational Design of Core−Shell Nanoparticle Catalysts with Ultralow Noble Metal Loadings. *Acc. Chem. Res.* **2018**, *51*, 1054−1062.
(4) Qiao, B.; Wang, A.; Yang, X.; Allard, L. F.; Jiang, Z.; Cui, Y.; Liu, J.; Li, J.; Zhang, T. Single-Atom Catalysis of CO Oxidation Using Pt_1/FeO_x. *Nat. Chem.* **2011**, *3*, 634−641.
(5) Wang, A.; Li, J.; Zhang, T. Heterogeneous Single-Atom Catalysis. *Nature Reviews Chemistry* **2018**, *2*, 65−81.
(6) Jones, J.; Xiong, H. F.; Delariva, A. T.; Peterson, E. J.; Pham, H.; Challa, S. R.; Qi, G. S.; Oh, S.; Wiebenga, M. H.; Pereira Hernandez, X. I.; Wang, Y.; Datye, A. K. Thermally Stable Single-Atom Platinum-on-Ceria Catalysts via Atom Trapping. *Science* **2016**, *353*, 150−154.
(7) Kyriakou, G.; Boucher, M. B.; Jewell, A. D.; Lewis, E. A.; Lawton, T. J.; Baber, A. E.; Tierney, H. L.; Flytzani-Stephanopoulos, M.; Sykes, E. C. H. Isolated Metal Atom Geometries as a Strategy for Selective Heterogeneous Hydrogenations. *Science* **2012**, *335*, 1209−1212.
(8) Liu, L.; Corma, A. Metal Catalysts for Heterogeneous Catalysis: From Single Atoms to Nanoclusters and Nanoparticles. *Chem. Rev.* **2018**, *118*, 4981−5079.
(9) Liu, J. Catalysis by Supported Single Metal Atoms. *ACS Catal.* **2017**, *7*, 34−59.
(10) Bashyam, R.; Zelenay, P. A Class of Non-Precious Metal Composite Catalysts for Fuel Cells. *Nature* **2006**, *443*, 63−66.

https://dx.doi.org/10.1021/acs.chemrev.0c00594
Chem. Rev. 2020, 120, 12217−12314

(11) Yang, X.-F.; Wang, A.; Qiao, B.; Li, J.; Liu, J.; Zhang, T. Single-Atom Catalysts: A New Frontier in Heterogeneous Catalysis. *Acc. Chem. Res.* **2013**, *46*, 1740−1748.
(12) Duchesne, P. N.; Li, Z.; Deming, C. P.; Fung, V.; Zhao, X.; Yuan, J.; Regier, T.; Aldalbahi, A.; Almarhoon, Z.; Chen, S.; et al. Golden Single-atomic-site Platinum Electrocatalysts. *Nat. Mater.* **2018**, *17*, 1033−1039.
(13) Zhu, C. Z.; Fu, S. F.; Shi, Q. R.; Du, D.; Lin, Y. H. Single-Atom Electrocatalysts. *Angew. Chem., Int. Ed.* **2017**, *56*, 13944−13960.
(14) Zhao, C.; Dai, X.; Yao, T.; Chen, W.; Wang, X.; Wang, J.; Yang, J.; Wei, S.; Wu, Y.; Li, Y. Ionic Exchange of Metal−Organic Frameworks to Access Single Nickel Sites for Efficient Electroreduction of CO_2. *J. Am. Chem. Soc.* **2017**, *139*, 8078−8081.
(15) Zhang, H.; Hwang, S.; Wang, M.; Feng, Z.; Karakalos, S.; Luo, L.; Qiao, Z.; Xie, X.; Wang, C.; Su, D.; et al. Single Atomic Iron Catalysts for Oxygen Reduction in Acidic Media: Particle Size Control and Thermal Activation. *J. Am. Chem. Soc.* **2017**, *139*, 14143−14149.
(16) Fei, H.; Dong, J.; Arellano-Jiménez, M. J.; Ye, G.; Kim, N. D.; Samuel, E. L.; Peng, Z.; Zhu, Z.; Qin, F.; Bao, J.; et al. Atomic Cobalt on Nitrogen-Doped Graphene for Hydrogen Generation. *Nat. Commun.* **2015**, *6*, 8668.
(17) Wang, Y.; Cao, L.; Libretto, N. J.; Li, X.; Li, C.; Wan, Y.; He, C.; Lee, J.; Gregg, J.; Zong, H.; Su, D.; Miller, J. T.; Mueller, T.; Wang, C. Ensemble Effect in Bimetallic Electrocatalysts for CO_2 Reduction. *J. Am. Chem. Soc.* **2019**, *141*, 16635−16642.
(18) Qiao, B.; Wang, A.; Yang, X.; Allard, L. F.; Jiang, Z.; Cui, Y.; Liu, J.; Li, J.; Zhang, T. Single-atom catalysis of CO oxidation using Pt1/FeOx. *Nat. Chem.* **2011**, *3*, 634−641.
(19) Lin, S.; Diercks, C. S.; Zhang, Y.-B.; Kornienko, N.; Nichols, E. M.; Zhao, Y.; Paris, A. R.; Kim, D.; Yang, P.; Yaghi, O. M.; Chang, C. J. Covalent Organic Frameworks Comprising Cobalt Porphyrins for Catalytic CO_2 Reduction in Water. *Science* **2015**, *349*, 1208−1213.
(20) Ren, S.; Joulié, D.; Salvatore, D.; Torbensen, K.; Wang, M.; Robert, M.; Berlinguette, C. P. Molecular Electrocatalysts Can Mediate Fast, Selective CO_2 Reduction in a Flow Cell. *Science* **2019**, *365*, 367−369.
(21) Su, X.; Yang, X. F.; Huang, Y.; Liu, B.; Zhang, T. Single-Atom Catalysis toward Efficient CO_2 Conversion to CO and Formate Products. *Acc. Chem. Res.* **2019**, *52*, 656−664.
(22) Zheng, N.; Zhang, T. Preface: single-atom catalysts as a new generation of heterogeneous catalysts. *Natl. Sci. Rev.* **2018**, *5*, 625−625.
(23) Ji, S.; Chen, Y.; Wang, X.; Zhang, Z.; Wang, D.; Li, Y., Chemical synthesis of single-atomic site catalysts. *Chem. Rev.* **2020**.*120* DOI: 10.1021/acs.chemrev.9b00818
(24) Flytzani-Stephanopoulos, M.; Gates, B. C. Atomically Dispersed Supported Metal Catalysts. *Annu. Rev. Chem. Biomol. Eng.* **2012**, *3*, 545−574.
(25) Hansen, T. W.; DeLaRiva, A. T.; Challa, S. R.; Datye, A. K. Sintering of Catalytic Nanoparticles: Particle Migration or Ostwald Ripening? *Acc. Chem. Res.* **2013**, *46*, 1720−1730.
(26) Pan, F.; Deng, W.; Justiniano, C.; Li, Y. Identification of Champion Transition Metals Centers in Metal and Nitrogen-Codoped Carbon Catalysts for CO_2 Reduction. *Appl. Catal., B* **2018**, *226*, 463−472.
(27) Wu, G.; More, K. L.; Johnston, C. M.; Zelenay, P. High-Performance Electrocatalysts for Oxygen Reduction Derived From Polyaniline, Iron, and Cobalt. *Science* **2011**, *332*, 443−447.
(28) Li, Y.; Zhou, W.; Wang, H.; Xie, L.; Liang, Y.; Wei, F.; Idrobo, J.-C.; Pennycook, S. J.; Dai, H. An Oxygen Reduction Electrocatalyst Based on Carbon Nanotube-Graphene Complexes. *Nat. Nanotechnol.* **2012**, *7*, 394−400.
(29) Guo, X.; Fang, G.; Li, G.; Ma, H.; Fan, H.; Yu, L.; Ma, C.; Wu, X.; Deng, D.; Wei, M.; Tan, D.; Si, R.; Zhang, S.; Li, J.; Sun, L.; Tang, Z.; Pan, X.; Bao, X. Direct, Nonoxidative Conversion of Methane to Ethylene, Aromatics, and Hydrogen. *Science* **2014**, *344*, 616.
(30) Liu, P.; Zhao, Y.; Qin, R.; Mo, S.; Chen, G.; Gu, L.; Chevrier, D. M.; Zhang, P.; Guo, Q.; Zang, D.; Wu, B.; Fu, G.; Zheng, N. Photochemical route for synthesizing atomically dispersed palladium catalysts. *Science* **2016**, *352*, 797.
(31) Kosinov, N.; Wijpkema, A. S. G.; Uslamin, E.; Rohling, R.; Coumans, F.; Mezari, B.; Parastaev, A.; Poryvaev, A. S.; Fedin, M. V.; Pidko, E. A.; Hensen, E. J. M. Confined Carbon Mediating Dehydroaromatization of Methane over Mo/ZSM-5. *Angew. Chem., Int. Ed.* **2018**, *57*, 1016−1020.
(32) Kistler, J. D.; Chotigkrai, N.; Xu, P. H.; Enderle, B.; Praserthdam, P.; Chen, C. Y.; Browning, N. D.; Gates, B. C. A Single-Site Platinum CO Oxidation Catalyst in Zeolite KLTL: Microscopic and Spectroscopic Determination of the Locations of the Platinum Atoms. *Angew. Chem., Int. Ed.* **2014**, *53*, 8904−8907.
(33) Jiao, J.; Lin, R.; Liu, S.; Cheong, W.-C.; Zhang, C.; Chen, Z.; Pan, Y.; Tang, J.; Wu, K.; Hung, S.-F.; Chen, H. M.; Zheng, L.; Lu, Q.; Yang, X.; Xu, B.; Xiao, H.; Li, J.; Wang, D.; Peng, Q.; Chen, C.; Li, Y. Copper Atom-Pair Catalyst Anchored on Alloy Nanowires for Selective and Efficient Electrochemical Reduction of CO_2. *Nat. Chem.* **2019**, *11*, 222−228.
(34) Fu, Q.; Saltsburg, H.; Flytzani-Stephanopoulos, M. Active Nonmetallic Au and Pt Species on Ceria-Based Water-Gas Shift Catalysts. *Science* **2003**, *301*, 935−938.
(35) Xie, P. F.; Pu, T. C.; Nie, A. M.; Hwang, S.; Purdy, S. C.; Yu, W. J.; Su, D.; Miller, J. T.; Wang, C. Nanoceria-Supported Single-Atom Platinum Catalysts for Direct Methane Conversion. *ACS Catal.* **2018**, *8*, 4044−4048.
(36) Chen, Y.; Ji, S.; Wang, Y.; Dong, J.; Chen, W.; Li, Z.; Shen, R.; Zheng, L.; Zhuang, Z.; Wang, D.; Li, Y. Isolated Single Iron Atoms Anchored on N-Doped Porous Carbon as an Efficient Electrocatalyst for the Oxygen Reduction Reaction. *Angew. Chem., Int. Ed.* **2017**, *56*, 6937−6941.
(37) Huang, Y.-B.; Liang, J.; Wang, X.-S.; Cao, R. Multifunctional Metal−Organic Framework Catalysts: Synergistic Catalysis and Tandem Reactions. *Chem. Soc. Rev.* **2017**, *46*, 126−157.
(38) Schoedel, A.; Li, M.; Li, D.; O'Keeffe, M.; Yaghi, O. M. Structures of Metal−Organic Frameworks with Rod Secondary Building Units. *Chem. Rev.* **2016**, *116*, 12466−12535.
(39) Li, F.; Han, G.-F.; Noh, H.-J.; Kim, S.-J.; Lu, Y.; Jeong, H. Y.; Fu, Z.; Baek, J.-B. Boosting Oxygen Reduction Catalysis with Abundant Copper Single Atom Active Sites. *Energy Environ. Sci.* **2018**, *11*, 2263−2269.
(40) Lu, Z.; Wang, B.; Hu, Y.; Liu, W.; Zhao, Y.; Yang, R.; Li, Z.; Luo, J.; Chi, B.; Jiang, Z.; Li, M.; Mu, S.; Liao, S.; Zhang, J.; Sun, X. An Isolated Zinc−Cobalt Atomic Pair for Highly Active and Durable Oxygen Reduction. *Angew. Chem., Int. Ed.* **2019**, *58*, 2622−2626.
(41) Zhao, L.; Zhang, Y.; Huang, L.-B.; Liu, X.-Z.; Zhang, Q.-H.; He, C.; Wu, Z.-Y.; Zhang, L.-J.; Wu, J.; Yang, W.; Gu, L.; Hu, J.-S.; Wan, L.-J. Cascade Anchoring Strategy for General Mass Production of High-Loading Single-Atomic Metal-Nitrogen Catalysts. *Nat. Commun.* **2019**, *10*, 1278.
(42) Li, J.; Chen, M.; Cullen, D. A.; Hwang, S.; Wang, M.; Li, B.; Liu, K.; Karakalos, S.; Lucero, M.; Zhang, H.; Lei, C.; Xu, H.; Sterbinsky, G. E.; Feng, Z.; Su, D.; More, K. L.; Wang, G.; Wang, Z.; Wu, G. Atomically Dispersed Manganese Catalysts for Oxygen Reduction in Proton-Exchange Membrane Fuel Cells. *Nat. Catal.* **2018**, *1*, 935−945.
(43) Kaneti, Y. V.; Dutta, S.; Hossain, M. S. A.; Shiddiky, M. J. A.; Tung, K.-L.; Shieh, F.-K.; Tsung, C.-K.; Wu, K. C. W.; Yamauchi, Y. Strategies for Improving the Functionality of Zeolitic Imidazolate Frameworks: Tailoring Nanoarchitectures for Functional Applications. *Adv. Mater.* **2017**, *29*, 1700213.
(44) Saliba, D.; Ammar, M.; Rammal, M.; Al-Ghoul, M.; Hmadeh, M. Crystal Growth of ZIF-8, ZIF-67, and Their Mixed-Metal Derivatives. *J. Am. Chem. Soc.* **2018**, *140*, 1812−1823.
(45) Torad, N. L.; Hu, M.; Kamachi, Y.; Takai, K.; Imura, M.; Naito, M.; Yamauchi, Y. Facile Synthesis of Nanoporous Carbons with Controlled Particle Sizes by Direct Carbonization of Monodispersed ZIF-8 Crystals. *Chem. Commun.* **2013**, *49*, 2521−2523.
(46) Chao, S.; Zou, F.; Wan, F.; Dong, X.; Wang, Y.; Wang, Y.; Guan, Q.; Wang, G.; Li, W. Nitrogen-doped Carbon Derived from

ZIF-8 as a High-performance Metal-free Catalyst for Acetylene Hydrochlorination. *Sci. Rep.* **2017**, *7*, 39789.
(47) Zheng, T.; Jiang, K.; Ta, N.; Hu, Y.; Zeng, J.; Liu, J.; Wang, H. Large-Scale and Highly Selective CO_2 Electrocatalytic Reduction on Nickel Single-Atom Catalyst. *Joule* **2019**, *3*, 265−278.
(48) Yang, H.; Shang, L.; Zhang, Q.; Shi, R.; Waterhouse, G. I.; Gu, L.; Zhang, T. A universal ligand mediated method for large scale synthesis of transition metal single atom catalysts. *Nat. Commun.* **2019**, *10*, 4585.
(49) Li, Q.; Chen, W.; Xiao, H.; Gong, Y.; Li, Z.; Zheng, L.; Zheng, X.; Yan, W.; Cheong, W.-C.; Shen, R.; Fu, N.; Gu, L.; Zhuang, Z.; Chen, C.; Wang, D.; Peng, Q.; Li, J.; Li, Y. Fe Isolated Single Atoms on S, N Codoped Carbon by Copolymer Pyrolysis Strategy for Highly Efficient Oxygen Reduction Reaction. *Adv. Mater.* **2018**, *30*, 1800588.
(50) Kim, D.; Xie, C.; Becknell, N.; Yu, Y.; Karamad, M.; Chan, K.; Crumlin, E. J.; Nørskov, J. K.; Yang, P. Electrochemical Activation of CO_2 through Atomic Ordering Transformations of AuCu Nanoparticles. *J. Am. Chem. Soc.* **2017**, *139*, 8329−8336.
(51) Liu, J.; Jiao, M.; Lu, L.; Barkholtz, H. M.; Li, Y.; Wang, Y.; Jiang, L.; Wu, Z.; Liu, D.-j.; Zhuang, L.; Ma, C.; Zeng, J.; Zhang, B.; Su, D.; Song, P.; Xing, W.; Xu, W.; Wang, Y.; Jiang, Z.; Sun, G. High performance platinum single atom electrocatalyst for oxygen reduction reaction. *Nat. Commun.* **2017**, *8*, 15938.
(52) Zheng, W.; Yang, J.; Chen, H.; Hou, Y.; Wang, Q.; Gu, M.; He, F.; Xia, Y.; Xia, Z.; Li, Z.; Yang, B.; Lei, L.; Yuan, C.; He, Q.; Qiu, M.; Feng, X. Atomically Defined Undercoordinated Active Sites for Highly Efficient CO_2 Electroreduction. *Adv. Funct. Mater.* **2020**, *30*, 1907658.
(53) Zhang, H.; Li, J.; Xi, S.; Du, Y.; Hai, X.; Wang, J.; Xu, H.; Wu, G.; Zhang, J.; Lu, J.; Wang, J. A Graphene-Supported Single-Atom FeN_5 Catalytic Site for Efficient Electrochemical CO_2 Reduction. *Angew. Chem., Int. Ed.* **2019**, *58*, 14871−14876.
(54) Beniya, A.; Higashi, S. Towards Dense Single-Atom Catalysts for Future Automotive Applications. *Nat. Catal.* **2019**, *2*, 590−602.
(55) Cui, X.; Li, W.; Ryabchuk, P.; Junge, K.; Beller, M. Bridging Homogeneous and Heterogeneous Catalysis by Heterogeneous Single-Metal-Site Catalysts. *Nat. Catal.* **2018**, *1*, 385−397.
(56) Wang, Y.; Chen, Z.; Han, P.; Du, Y.; Gu, Z.; Xu, X.; Zheng, G. Single-Atomic Cu with Multiple Oxygen Vacancies on Ceria for Electrocatalytic CO_2 Reduction to CH_4. *ACS Catal.* **2018**, *8*, 7113−7119.
(57) Higgins, D.; Zamani, P.; Yu, A.; Chen, Z. The application of graphene and its composites in oxygen reduction electrocatalysis: a perspective and review of recent progress. *Energy Environ. Sci.* **2016**, *9*, 357−390.
(58) Yoo, E.; Okata, T.; Akita, T.; Kohyama, M.; Nakamura, J.; Honma, I. Enhanced electrocatalytic activity of Pt subnanoclusters on graphene nanosheet surface. *Nano Lett.* **2009**, *9*, 2255−2259.
(59) Zhang, L.; Jia, Y.; Gao, G.; Yan, X.; Chen, N.; Chen, J.; Soo, M. T.; Wood, B.; Yang, D.; Du, A.; Yao, X. Graphene Defects Trap Atomic Ni Species for Hydrogen and Oxygen Evolution Reactions. *Chem* **2018**, *4*, 285−297.
(60) Zhang, X.; Guo, J.; Guan, P.; Liu, C.; Huang, H.; Xue, F.; Dong, X.; Pennycook, S. J.; Chisholm, M. F. Catalytically active single-atom niobium in graphitic layers. *Nat. Commun.* **2013**, *4*, 1924.
(61) Huang, F.; Deng, Y.; Chen, Y.; Cai, X.; Peng, M.; Jia, Z.; Ren, P.; Xiao, D.; Wen, X.; Wang, N.; Liu, H.; Ma, D. Atomically dispersed Pd on nanodiamond/graphene hybrid for selective hydrogenation of acetylene. *J. Am. Chem. Soc.* **2018**, *140*, 13142−13146.
(62) Huang, F.; Deng, Y.; Chen, Y.; Cai, X.; Peng, M.; Jia, Z.; Xie, J.; Xiao, D.; Wen, X.; Wang, N.; Jiang, Z.; Liu, H.; Ma, D. Anchoring Cu 1 species over nanodiamond-graphene for semi-hydrogenation of acetylene. *Nat. Commun.* **2019**, *10*, 4431.
(63) Clark, E. L.; Hahn, C.; Jaramillo, T. F.; Bell, A. T. Electrochemical CO_2 Reduction over Compressively Strained CuAg Surface Alloys with Enhanced Multi-Carbon Oxygenate Selectivity. *J. Am. Chem. Soc.* **2017**, *139*, 15848−15857.
(64) Gao, F.; Wang, Y.; Goodman, D. W. CO Oxidation over AuPd(100) from Ultrahigh Vacuum to Near-Atmospheric Pressures: The Critical Role of Contiguous Pd Atoms. *J. Am. Chem. Soc.* **2009**, *131*, 5734−5735.
(65) Slanac, D. A.; Hardin, W. G.; Johnston, K. P.; Stevenson, K. J. Atomic Ensemble and Electronic Effects in Ag-Rich AgPd Nanoalloy Catalysts for Oxygen Reduction in Alkaline Media. *J. Am. Chem. Soc.* **2012**, *134*, 9812−9819.
(66) Cheng, M.-J.; Clark, E. L.; Pham, H. H.; Bell, A. T.; Head-Gordon, M. Quantum Mechanical Screening of Single-Atom Bimetallic Alloys for the Selective Reduction of CO_2 to C_1 Hydrocarbons. *ACS Catal.* **2016**, *6*, 7769−7777.
(67) O'Neill, B. J.; Jackson, D. H. K.; Lee, J.; Canlas, C.; Stair, P. C.; Marshall, C. L.; Elam, J. W.; Kuech, T. F.; Dumesic, J. A.; Huber, G. W. Catalyst Design with Atomic Layer Deposition. *ACS Catal.* **2015**, *5*, 1804−1825.
(68) Sun, S.; Zhang, G.; Gauquelin, N.; Chen, N.; Zhou, J.; Yang, S.; Chen, W.; Meng, X.; Geng, D.; Banis, M. N.; Li, R.; Ye, S.; Knights, S.; Botton, G. A.; Sham, T.-K.; Sun, X. Single-atom Catalysis Using Pt/Graphene Achieved through Atomic Layer Deposition. *Sci. Rep.* **2013**, *3*, 1775.
(69) Zhang, C.; Yang, S.; Wu, J.; Liu, M.; Yazdi, S.; Ren, M.; Sha, J.; Zhong, J.; Nie, K.; Jalilov, A. S.; et al. Electrochemical CO_2 Reduction with Atomic Iron-Dispersed on Nitrogen-Doped Graphene. *Adv. Energy Mater.* **2018**, *8*, 1703487.
(70) Hou, Y.; Qiu, M.; Kim, M. G.; Liu, P.; Nam, G.; Zhang, T.; Zhuang, X.; Yang, B.; Cho, J.; Chen, M.; et al. Atomically Dispersed Nickel−Nitrogen−Sulfur Species Anchored on Porous Carbon Nanosheets for Efficient Water Oxidation. *Nat. Commun.* **2019**, *10*, 1392.
(71) Fei, H.; Dong, J.; Feng, Y.; Allen, C. S.; Wan, C.; Volosskiy, B.; Li, M.; Zhao, Z.; Wang, Y.; Sun, H.; et al. General Synthesis and Definitive Structural Identification of MN_4C_4 Single-Atom Catalysts with Tunable Electrocatalytic Activities. *Nat. Catal.* **2018**, *1*, 63.
(72) Cheng, N.; Stambula, S.; Wang, D.; Banis, M. N.; Liu, J.; Riese, A.; Xiao, B.; Li, R.; Sham, T.-K.; Liu, L.-M.; Botton, G. A.; Sun, X. Platinum single-atom and cluster catalysis of the hydrogen evolution reaction. *Nat. Commun.* **2016**, *7*, 13638.
(73) Kim, D.; Kley, C. S.; Li, Y.; Yang, P. Copper nanoparticle ensembles for selective electroreduction of CO_2 to C_2-C_3 products. *Proc. Natl. Acad. Sci. U. S. A.* **2017**, *114*, 10560−10565.
(74) Dinh, K. T.; Sullivan, M. M.; Narsimhan, K.; Serna, P.; Meyer, R. J.; Dincă, M.; Román-Leshkov, Y. Continuous Partial Oxidation of Methane to Methanol Catalyzed by Diffusion-Paired Copper Dimers in Copper-Exchanged Zeolites. *J. Am. Chem. Soc.* **2019**, *141*, 11641−11650.
(75) Greeley, J.; Stephens, I. E. L.; Bondarenko, A. S.; Johansson, T. P.; Hansen, H. A.; Jaramillo, T. F.; Rossmeisl, J.; Chorkendorff, I.; Nørskov, J. K. Alloys of platinum and early transition metals as oxygen reduction electrocatalysts. *Nat. Chem.* **2009**, *1*, 552−556.
(76) Cui, C.; Gan, L.; Heggen, M.; Rudi, S.; Strasser, P. Compositional segregation in shaped Pt alloy nanoparticles and their structural behaviour during electrocatalysis. *Nat. Mater.* **2013**, *12*, 765−771.
(77) Huang, X.; Zhao, Z.; Cao, L.; Chen, Y.; Zhu, E.; Lin, Z.; Li, M.; Yan, A.; Zettl, A.; Wang, Y. M.; Duan, X.; Mueller, T.; Huang, Y. High-performance transition metal−doped Pt_3Ni octahedra for oxygen reduction reaction. *Science* **2015**, *348*, 1230.
(78) Jiang, K.; Zhao, D.; Guo, S.; Zhang, X.; Zhu, X.; Guo, J.; Lu, G.; Huang, X. Efficient oxygen reduction catalysis by subnanometer Pt alloy nanowires. *Sci. Adv.* **2017**, *3*, No. e1601705.
(79) Tian, X.; Zhao, X.; Su, Y.-Q.; Wang, L.; Wang, H.; Dang, D.; Chi, B.; Liu, H.; Hensen, E. J. M.; Lou, X. W.; Xia, B. Y. Engineering bunched Pt-Ni alloy nanocages for efficient oxygen reduction in practical fuel cells. *Science* **2019**, *366*, 850−856.
(80) Francke, R.; Schille, B.; Roemelt, M. Homogeneously Catalyzed Electroreduction of Carbon Dioxide—Methods, Mechanisms, and Catalysts. *Chem. Rev.* **2018**, *118*, 4631−4701.
(81) Wu, Y.; Jiang, Z.; Lu, X.; Liang, Y.; Wang, H. Domino electroreduction of CO2 to methanol on a molecular catalyst. *Nature* **2019**, *575*, 639−642.

https://dx.doi.org/10.1021/acs.chemrev.0c00594
Chem. Rev. 2020, 120, 12217−12314

(82) Li, X.; Yang, X.; Zhang, J.; Huang, Y.; Liu, B. In Situ/Operando Techniques for Characterization of Single-Atom Catalysts. *ACS Catal.* **2019**, *9*, 2521−2531.
(83) Chen, C. J. Origin of atomic resolution on metal surfaces in scanning tunneling microscopy. *Phys. Rev. Lett.* **1990**, *65*, 448−451.
(84) Somorjai, G. A. The surface science of heterogeneous catalysis. *Surf. Sci.* **1994**, *299−300*, 849−866.
(85) Zambelli, T.; Barth, J. V.; Wintterlin, J.; Ertl, G. Complex pathways in dissociative adsorption of oxygen on platinum. *Nature* **1997**, *390*, 495−497.
(86) Boucher, M. B.; Zugic, B.; Cladaras, G.; Kammert, J.; Marcinkowski, M. D.; Lawton, T. J.; Sykes, E. C. H.; Flytzani-Stephanopoulos, M. Single Atom Alloy Surface Analogs in $Pd_{0.18}Cu_{15}$ Nanoparticles For Selective Hydrogenation Reactions. *Phys. Chem. Chem. Phys.* **2013**, *15*, 12187−12196.
(87) Crewe, A. V.; Wall, J.; Langmore, J. Visibility of Single Atoms. *Science* **1970**, *168*, 1338−1340.
(88) Liu, J. Aberration-Corrected Scanning Transmission Electron Microscopy in Single-Atom Catalysis: Probing the Catalytically Active Centers. *Chin. J. Catal.* **2017**, *38*, 1460−1472.
(89) Treacy, M. M. J.; Howie, A.; Wilson, C. J. Z-Contrast of Platinum and Palladium Catalysts. *Philos. Mag. A* **1978**, *38*, 569−585.
(90) Nellist, P. D.; Pennycook, S. J. Direct Imaging of the Atomic Configuration of Ultradispersed Catalysts. *Science* **1996**, *274*, 413−415.
(91) Fadley, C. S. X-ray photoelectron spectroscopy: Progress and perspectives. *J. Electron Spectrosc. Relat. Phenom.* **2010**, *178−179*, 2−32.
(92) Johansson, G.; Hedman, J.; Berndtsson, A.; Klasson, M.; Nilsson, R. Calibration of electron spectra. *J. Electron Spectrosc. Relat. Phenom.* **1973**, *2*, 295−317.
(93) Siegbahn, K.; Nordling, C. *ESCA, Atomic, Molecular and Solid State Structure Studied by Means of Electron Spectroscopy*; Nova Acta Regiae Societatis Scientiarum Upsaliensis, 1967.
(94) Peng, H.; Mo, Z.; Liao, S.; Liang, H.; Yang, L.; Luo, F.; Song, H.; Zhong, Y.; Zhang, B. High Performance Fe- and N- Doped Carbon Catalyst with Graphene Structure for Oxygen Reduction. *Sci. Rep.* **2013**, *3*, 1765.
(95) Yang, H. B.; Hung, S.-F.; Liu, S.; Yuan, K.; Miao, S.; Zhang, L.; Huang, X.; Wang, H.-Y.; Cai, W.; Chen, R.; Gao, J.; Yang, X.; Chen, W.; Huang, Y.; Chen, H.; Li, C.; Zhang, T.; Liu, B. Atomically Dispersed Ni(I) as the Active Site for Electrochemical CO_2 Reduction. *Nat. Energy* **2018**, *3*, 140.
(96) Greiner, M. T.; Jones, T.; Beeg, S.; Zwiener, L.; Scherzer, M.; Girgsdies, F.; Piccinin, S.; Armbrüster, M.; Knop-Gericke, A.; Schlögl, R. Free-atom-like d States in Single-atom Alloy Catalysts. *Nat. Chem.* **2018**, *10*, 1008−1015.
(97) Azároff, L. V. Studies of Alloys by X-ray Absorption Spectroscopy. *Science* **1966**, *151*, 785−789.
(98) de Groot, F. High-Resolution X-ray Emission and X-ray Absorption Spectroscopy. *Chem. Rev.* **2001**, *101*, 1779−1808.
(99) Ravel, B.; Newville, M. Data analysis for X-ray absorption spectroscopy using IFEFFIT. *J. Synchrotron Radiat.* **2005**, *12*, 537−41.
(100) Ogino, I. X-ray Absorption Spectroscopy for Single -Atom Catalysts: Critical Importance and Persistent Challenges. *Chin. J. Catal.* **2017**, *38*, 1481−1488.
(101) Koningsberger, D. C.; Gates, B. C. Nature of the metal-support interface in supported metal catalysts: Results from X-ray absorption spectroscopy. *Catal. Lett.* **1992**, *14*, 271−277.
(102) Yang, M.; Li, S.; Wang, Y.; Herron, J. A.; Xu, Y.; Allard, L. F.; Lee, S.; Huang, J.; Mavrikakis, M.; Flytzani-Stephanopoulos, M. Catalytically Aive Au-O(OH)$_{(x)}$-Species Sabilized by Akali Ions on Zeolites and Msoporous Oides. *Science* **2014**, *346*, 1498−1501.
(103) Zhang, H. B.; An, P. F.; Zhou, W.; Guan, B. Y.; Zhang, P.; Dong, J. C.; Lou, X. W. Dynamic traction of lattice-confined platinum atoms into mesoporous carbon matrix for hydrogen evolution reaction. *Sci. Adv.* **2018**, *4*, No. eaao6657.
(104) Funke, H.; Scheinost, A. C.; Chukalina, M. Wavelet analysis of extended x-ray absorption fine structure data. *Phys. Rev. B: Condens. Matter Mater. Phys.* **2005**, *71*, No. 094110.
(105) Shao, X. Z.; Yang, X. F.; Xu, J. M.; Liu, S.; Miao, S.; Liu, X. Y.; Su, X.; Duan, H. M.; Huang, Y. Q.; Zhang, T. Iridium Single-Atom Catalyst Performing a Quasi-homogeneous Hydrogenation Transformation of CO_2 to Formate. *Chem.* **2019**, *5*, 693−705.
(106) Kappers, M.; Van der Maas, J. Correlation between CO frequency and Pt coordination number. A DRIFT study on supported Pt catalysts. *Catal. Lett.* **1991**, *10*, 365−373.
(107) Vickerman, J.; Christmann, K.; Ertl, G. Model studies on bimetallic CuRu catalysts: III. Adsorption of carbon monoxide. *J. Catal.* **1981**, *71*, 175−191.
(108) Hoffman, A. S.; Fang, C. Y.; Gates, B. C. Homogeneity of Surface Sites in Supported Single-Site Metal Catalysts: Assessment with Band Widths of Metal Carbonyl Infrared Spectra. *J. Phys. Chem. Lett.* **2016**, *7*, 3854−3860.
(109) Ryczkowski, J. IR Spectroscopy in Catalysis. *Catal. Today* **2001**, *68*, 263−381.
(110) Miessner, H.; Burkhardt, I.; Gutschick, D.; Zecchina, A.; Morterra, C.; Spoto, G. The Formation of a Well Defined Rhodium Dicarbonyl in Highly Dealuminated Rhodium-Exchanged Zeolite-Y by Interaction with Co. *J. Chem. Soc., Faraday Trans. 1* **1989**, *85*, 2113−2126.
(111) Stakheev, A. Y.; Shpiro, E. S.; Tkachenko, O. P.; Jaeger, N. I.; SchulzEkloff, G. Evidence for Monatomic Platinum Species in H-ZSM-5 From Ftir Spectroscopy of Chemisorbed CO. *J. Catal.* **1997**, *169*, 382−388.
(112) Zholobenko, V. L.; Lei, G. D.; Carvill, B. T.; Lerner, B. A.; Sachtler, W. M. H. Identification of Isolated Pt Atoms in H-Mordenite. *J. Chem. Soc., Faraday Trans.* **1994**, *90*, 233−238.
(113) Avanesian, T.; Dai, S.; Kale, M. J.; Graham, G. W.; Pan, X. Q.; Christopher, P. Quantitative and Atomic-Scale View of CO-Induced Pt Nanoparticle Surface Reconstruction at Saturation Coverage via DFT Calculations Coupled with in Situ TEM and IR. *J. Am. Chem. Soc.* **2017**, *139*, 4551−4558.
(114) Kale, M. J.; Christopher, P. Utilizing Quantitative in Situ FTIR Spectroscopy To Identify Well-Coordinated Pt Atoms as the Active Site for CO Oxidation on Al_2O_3-Supported Pt Catalysts. *ACS Catal.* **2016**, *6*, 5599−5609.
(115) Marcinkowski, M. D.; Darby, M. T.; Liu, J. L.; Wimble, J. M.; Lucci, F. R.; Lee, S.; Michaelides, A.; Flytzani-Stephanopoulos, M.; Stamatakis, M.; Sykes, E. C. H. Pt/Cu Single-Atom Alloys as Coke-Resistant Catalysts for Efficient C-H Activation. *Nat. Chem.* **2018**, *10*, 325−332.
(116) Zhang, B.; Sun, G.; Ding, S. P.; Asakura, H.; Zhang, J.; Sautet, P.; Yan, N. Atomically Dispersed Pt-1-Polyoxometalate Catalysts: How Does Metal-Support Interaction Affect Stability and Hydrogenation Activity? *J. Am. Chem. Soc.* **2019**, *141*, 8185−8197.
(117) Nie, L.; Mei, D.; Xiong, H.; Peng, B.; Ren, Z.; Hernandez, X. I. P.; DeLaRiva, A.; Wang, M.; Engelhard, M. H.; Kovarik, L.; Datye, A. K.; Wang, Y. Activation of surface lattice oxygen in single-atom Pt/CeO_2 for low-temperature CO oxidation. *Science* **2017**, *358*, 1419.
(118) Mössbauer, R. L. Kernresonanzfluoreszenz von gammastrahlung in Ir 191. *Eur. Phys. J. A* **1958**, *151*, 124−143.
(119) Gütlich, P.; Bill, E.; Trautwein, A. X. *Mössbauer Spectroscopy and Transition Metal Chemistry: Fundamentals and Applications*; Springer Science & Business Media, 2010.
(120) Kramm, U. I.; Lefèvre, M.; Larouche, N.; Schmeisser, D.; Dodelet, J.-P. Correlations Between Mass Activity and Physicochemical Properties of Fe/N/C Catalysts for the ORR in PEM Fuel Cell via 57Fe Mossbauer Spectroscopy and Other Techniques. *J. Am. Chem. Soc.* **2014**, *136*, 978−985.
(121) Kramm, U. I.; Herranz, J.; Larouche, N.; Arruda, T. M.; Lefevre, M.; Jaouen, F.; Bogdanoff, P.; Fiechter, S.; Abs-Wurmbach, I.; Mukerjee, S.; Dodelet, J.-P. Structure of the Catalytic Sites in Fe/N/C-Catalysts for O_2-Reduction in PEM Fuel Cells. *Phys. Chem. Chem. Phys.* **2012**, *14*, 11673−11688.

https://dx.doi.org/10.1021/acs.chemrev.0c00594
Chem. Rev. 2020, 120, 12217−12314

(122) Xiao, M.; Zhu, J.; Ma, L.; Jin, Z.; Ge, J.; Deng, X.; Hou, Y.; He, Q.; Li, J.; Jia, Q.; Mukerjee, S.; Yang, R.; Jiang, Z.; Su, D.; Liu, C.; Xing, W. Microporous Framework Induced Synthesis of Single-Atom Dispersed Fe-NC Acidic ORR Catalyst and Its in Situ Reduced Fe-N_4 Active Site Identification Revealed by X-Ray Absorption Spectroscopy. *ACS Catal.* **2018**, *8*, 2824−2832.
(123) Zitolo, A.; Goellner, V.; Armel, V.; Sougrati, M.-T.; Mineva, T.; Stievano, L.; Fonda, E.; Jaouen, F. Identification of Catalytic Sites for Oxygen Reduction in Iron-and Nitrogen-Doped Graphene Materials. *Nat. Mater.* **2015**, *14*, 937−942.
(124) Kramm, U.; Abs-Wurmbach, I.; Herrmann-Geppert, I.; Radnik, J.; Fiechter, S.; Bogdanoff, P. Influence of the Electron-Density of FeN_4-Centers Towards the Catalytic Activity of Pyrolyzed FeTMPPCl-Based ORR-Electrocatalysts. *J. Electrochem. Soc.* **2011**, *158*, B69−B78.
(125) Bouwkamp-Wijnoltz, A.; Visscher, W.; Van Veen, J.; Boellaard, E.; Van der Kraan, A.; Tang, S. On Active-Site Heterogeneity in Pyrolyzed Carbon-Supported Iron Porphyrin Catalysts for the Electrochemical Reduction of Oxygen: An in Situ Mössbauer Study. *J. Phys. Chem. B* **2002**, *106*, 12993−13001.
(126) Schulenburg, H.; Stankov, S.; Schünemann, V.; Radnik, J.; Dorbandt, I.; Fiechter, S.; Bogdanoff, P.; Tributsch, H. Catalysts for the Oxygen Reduction from Heat-Treated Iron(III) Tetramethoxyphenylporphyrin Chloride: Structure and Stability of Active Sites. *J. Phys. Chem. B* **2003**, *107*, 9034−9041.
(127) Goellner, V.; Baldizzone, C.; Schuppert, A.; Sougrati, M. T.; Mayrhofer, K.; Jaouen, F. Degradation of Fe/N/C Catalysts Upon High Polarization in Acid Medium. *Phys. Chem. Chem. Phys.* **2014**, *16*, 18454−18462.
(128) Kramm, U. I.; Lefèvre, M.; Bogdanoff, P.; Schmeißer, D.; Dodelet, J.-P. Analyzing Structural Changes of Fe−N−C Cathode Catalysts in PEM Fuel Cell by Mößbauer Spectroscopy of Complete Membrane Electrode Assemblies. *J. Phys. Chem. Lett.* **2014**, *5*, 3750−3756.
(129) Jiang, K.; Siahrostami, S.; Zheng, T.; Hu, Y.; Hwang, S.; Stavitski, E.; Peng, Y.; Dynes, J.; Gangisetty, M.; Su, D.; Attenkofer, K.; Wang, H. Isolated Ni Single Atoms in Graphene Nanosheets for High-performance CO_2 Reduction. *Energy Environ. Sci.* **2018**, *11*, 893−903.
(130) Liu, S.; Yang, H. B.; Hung, S. F.; Ding, J.; Cai, W.; Liu, L.; Gao, J.; Li, X.; Ren, X.; Kuang, Z.; Kuang, Z.; Huang, Y.; Zhang, T.; Liu, B. Elucidating the Electrocatalytic CO_2 Reduction Reaction over a Model Single-Atom Nickel Catalyst. *Angew. Chem.* **2020**, *132*, 518.
(131) Gu, J.; Hsu, C.-S.; Bai, L.; Chen, H. M.; Hu, X. Atomically Dispersed Fe^{3+} Sites Catalyze Efficient CO_2 Electroreduction to CO. *Science* **2019**, *364*, 1091−1094.
(132) Karapinar, D.; Huan, N. T.; Ranjbar Sahraie, N.; Li, J.; Wakerley, D.; Touati, N.; Zanna, S.; Taverna, D.; Galvao Tizei, L. H.; Zitolo, A.; Jaouen, F.; Mougel, V.; Fontecave, M. Electroreduction of CO_2 on Single-Site Copper-Nitrogen-Doped Carbon Material: Selective Formation of Ethanol and Reversible Restructuration of the Metal Sites. *Angew. Chem., Int. Ed.* **2019**, *58*, 15098.
(133) Weng, Z.; Wu, Y.; Wang, M.; Jiang, J.; Yang, K.; Huo, S.; Wang, X.-F.; Ma, Q.; Brudvig, G. W.; Batista, V. S.; Liang, Y.; Feng, Z.; Wang, H. Active Sites of Copper-Complex Catalytic Materials for Electrochemical Carbon Dioxide Reduction. *Nat. Commun.* **2018**, *9*, 415.
(134) Cao, L.; Luo, Q.; Liu, W.; Lin, Y.; Liu, X.; Cao, Y.; Zhang, W.; Wu, Y.; Yang, J.; Yao, T.; Wei, S. Identification of Single-Atom Active Sites in Carbon-Based Cobalt Catalysts During Electrocatalytic Hydrogen Evolution. *Nat. Catal.* **2019**, *2*, 134−141.
(135) Jia, Q.; Ramaswamy, N.; Hafiz, H.; Tylus, U.; Strickland, K.; Wu, G.; Barbiellini, B.; Bansil, A.; Holby, E. F.; Zelenay, P.; Mukerjee, S. Experimental Observation of Redox-Induced Fe-N Switching Behavior as a Determinant Role for Oxygen Reduction Activity. *ACS Nano* **2015**, *9*, 12496−12505.
(136) Li, J.; Ghoshal, S.; Liang, W.; Sougrati, M.-T.; Jaouen, F.; Halevi, B.; McKinney, S.; McCool, G.; Ma, C.; Yuan, X.; Ma, Z.; Mukerjee, S.; Jia, Q. Structural and Mechanistic Basis for the High Activity of Fe−N−C Catalysts Toward Oxygen Reduction. *Energy Environ. Sci.* **2016**, *9*, 2418−2432.
(137) Jia, Q.; Liu, E.; Jiao, L.; Pann, S.; Pann, S.; Mukerjee, S. X-Ray Absorption Spectroscopy Characterizations on PGM-Free Electrocatalysts: Justification, Advantages, and Limitations. *Adv. Mater.* **2019**, *31*, 1805157.
(138) Zhu, S.; Li, T.; Cai, W.-B.; Shao, M. CO_2 Electrochemical Reduction as Probed Through Infrared Spectroscopy. *ACS Energy Lett.* **2019**, *4*, 682−689.
(139) Jiang, K.; Siahrostami, S.; Akey, A. J.; Li, Y.; Lu, Z.; Lattimer, J.; Hu, Y.; Stokes, C.; Gangishetty, M.; Chen, G.; Zhou, Y.; Hill, W.; Cai, W.-B.; Bell, D.; Chan, K.; Nørskov, J. K.; Cui, Y.; Wang, H. Transition-Metal Single Atoms in a Graphene Shell as Active Centers for Highly Efficient Artificial Photosynthesis. *Chem.* **2017**, *3*, 950−960.
(140) Qin, X.; Zhu, S.; Xiao, F.; Zhang, L.; Shao, M. Active Sites on Heterogeneous Single-Iron-Atom Electrocatalysts in CO2 Reduction Reaction. *ACS Energy Lett.* **2019**, *4*, 1778−1783.
(141) Cheng, W.; Zhao, X.; Su, H.; Tang, F.; Che, W.; Zhang, H.; Liu, Q. Lattice-Strained Metal−Organic-Framework Arrays for Bifunctional Oxygen Electrocatalysis. *Nat. Energy* **2019**, *4*, 115.
(142) Su, H.; Zhao, X.; Cheng, W.; Zhang, H.; Li, Y.; Zhou, W.; Liu, M.; Liu, Q. Hetero-N-Coordinated Co Single Sites with High Turnover Frequency for Efficient Electrocatalytic Oxygen Evolution in an Acidic Medium. *ACS Energy Lett.* **2019**, *4*, 1816−1822.
(143) Zheng, W.; Liu, M.; Lee, L. Y. S. Electrochemical Instability of Metal-Organic Frameworks: In Situ Spectroelectrochemical Investigation of the Real Active Sites. *ACS Catal.* **2020**, *10*, 81.
(144) Kumar, K.; Dubau, L.; Mermoux, M.; Li, J.; Zitolo, A.; Nelayah, J.; Jaouen, F.; Maillard, F. On the Influence of Oxygen On the Degradation of Fe-N-C Catalysts. *Angew. Chem., Int. Ed.* **2020**, *59*, 3235.
(145) Feng, K.; Zhang, H.; Gao, J.; Xu, J.; Dong, Y.; Kang, Z.; Zhong, J. Single atoms or not? *Appl. Phys. Lett.* **2020**, *116*, 191903.
(146) Chen, Y.; Ji, S.; Zhao, S.; Chen, W.; Dong, J.; Cheong, W.-C.; Shen, R.; Wen, X.; Zheng, L.; Rykov, A. I.; Cai, S.; Tang, H.; Zhuang, Z.; Chen, C.; Peng, Q.; Wang, D.; Li, Y. Enhanced oxygen reduction with single-atomic-site iron catalysts for a zinc-air battery and hydrogen-air fuel cell. *Nat. Commun.* **2018**, *9*, 5422.
(147) Wang, L.; Duan, X.; Liu, X.; Gu, J.; Si, R.; Qiu, Y.; Qiu, Y.; Shi, D.; Chen, F.; Sun, X.; Lin, J.; Sun, J. Atomically Dispersed Mo Supported on Metallic Co_9S_8 Nanoflakes as an Advanced Noble-Metal-Free Bifunctional Water Splitting Catalyst Working in Universal pH Conditions. *Adv. Energy Mater.* **2020**, *10*, 1903137.
(148) Seh, Z. W.; Kibsgaard, J.; Dickens, C. F.; Chorkendorff, I.; Nørskov, J. K.; Jaramillo, T. F. Combining Theory and Experiment in Electrocatalysis: Insights into Materials Design. *Science* **2017**, *355*, No. eaad4998.
(149) Subbaraman, R.; Tripkovic, D.; Chang, K.-C.; Strmcnik, D.; Paulikas, A. P.; Hirunsit, P.; Chan, M.; Greeley, J.; Stamenkovic, V.; Markovic, N. M. Trends in Activity for the Water Electrolyser Reactions on 3d M (Ni, Co, Fe, Mn) Hydr (oxy) Oxide Catalysts. *Nat. Mater.* **2012**, *11*, 550.
(150) Jamesh, M. I. Recent Progress on Earth Abundant Hydrogen Evolution Reaction and Oxygen Evolution Reaction Bifunctional Electrocatalyst for Overall Water Splitting in Alkaline Media. *J. Power Sources* **2016**, *333*, 213−236.
(151) Luo, J.; Im, J.-H.; Mayer, M. T.; Schreier, M.; Nazeeruddin, M. K.; Park, N.-G.; Tilley, S. D.; Fan, H. J.; Grätzel, M. Water Photolysis at 12.3% Efficiency via Perovskite Photovoltaics and Earth-Abundant Catalysts. *Science* **2014**, *345*, 1593−1596.
(152) Zheng, Y.; Jiao, Y.; Qiao, S. Z. Engineering of Carbon-Based Electrocatalysts for Emerging Energy Conversion: From Fundamentality to Functionality. *Adv. Mater.* **2015**, *27*, 5372−5378.
(153) Ramalingam, V.; Varadhan, P.; Fu, H. C.; Kim, H.; Zhang, D.; Chen, S.; Song, L.; Ma, D.; Wang, Y.; Alshareef, H. N.; He, H., Jr. Heteroatom-Mediated Interactions between Ruthenium Single Atoms and an MXene Support for Efficient Hydrogen Evolution. *Adv. Mater.* **2019**, *31*, 1903841.

https://dx.doi.org/10.1021/acs.chemrev.0c00594
Chem. Rev. 2020, 120, 12217−12314

(154) Tian, X.; Zhao, P.; Sheng, W. Hydrogen Evolution and Oxidation: Mechanistic Studies and Material Advances. *Adv. Mater.* **2019**, *31*, 1808066.
(155) Shang, L.; Bian, T.; Zhang, B.; Zhang, D.; Wu, L. Z.; Tung, C. H.; Yin, Y.; Zhang, T. Inside Cover: Graphene-Supported Ultrafine Metal Nanoparticles Encapsulated by Mesoporous Silica: Robust Catalysts for Oxidation and Reduction Reactions. *Angew. Chem., Int. Ed.* **2014**, *53*, 2−2.
(156) Wang, S.; Zhang, L.; Li, X.; Li, C.; Zhang, R.; Zhang, Y.; Zhu, H. Sponge-Like Nickel Phosphide−Carbon Nanotube Hybrid Electrodes for Efficient Hydrogen Evolution over a Wide pH Range. *Nano Res.* **2017**, *10*, 415−425.
(157) Yang, J.; Guo, D.; Zhao, S.; Lin, Y.; Yang, R.; Xu, D.; Shi, N.; Zhang, X.; Lu, L.; Lan, Y. Q.; Bao, J.; Han, M. Cobalt Phosphides Nanocrystals Encapsulated by P-Doped Carbon and Married with P-Doped Graphene for Overall Water Splitting. *Small* **2019**, *15*, 1804546.
(158) Zhou, Q.; Shen, Z.; Zhu, C.; Li, J.; Ding, Z.; Wang, P.; Pan, F.; Zhang, Z.; Ma, H.; Wang, S.; Zhang, H. Nitrogen-Doped CoP Electrocatalysts for Coupled Hydrogen Evolution and Sulfur Generation with Low Energy Consumption. *Adv. Mater.* **2018**, *30*, 1800140.
(159) Gupta, S.; Patel, N.; Fernandes, R.; Kadrekar, R.; Dashora, A.; Yadav, A.; Bhattacharyya, D.; Jha, S.; Miotello, A.; Kothari, D. Co−Ni−B Nanocatalyst for Efficient Hydrogen Evolution Reaction in Wide pH Range. *Appl. Catal., B* **2016**, *192*, 126−133.
(160) Mahmood, J.; Jung, S.-M.; Kim, S.-J.; Park, J.; Yoo, J.-W.; Baek, J.-B. Cobalt Oxide Encapsulated in C_2N-*h* 2D Network Polymer as a Catalyst for Hydrogen Evolution. *Chem. Mater.* **2015**, *27*, 4860−4864.
(161) Shen, J.; Yang, Z.; Ge, M.; Li, P.; Nie, H.; Cai, Q.; Gu, C.; Yang, K.; Huang, S. Neuron-Inspired Interpenetrative Network Composed of Cobalt−Phosphorus-Derived Nanoparticles Embedded within Porous Carbon Nanotubes for Efficient Hydrogen Production. *ACS Appl. Mater. Interfaces* **2016**, *8*, 17284−17291.
(162) Wu, H. B.; Xia, B. Y.; Yu, L.; Yu, X.-Y.; Lou, X. W. D. Porous Molybdenum Carbide Nano-Octahedrons Synthesized via Confined Carburization in Metal-Organic Frameworks for Efficient Hydrogen Production. *Nat. Commun.* **2015**, *6*, 6512.
(163) Yang, C.; Gao, M.; Zhang, Q.; Zeng, J.; Li, X.; Abbott, A. In-Situ Activation of Self-Supported 3D Hierarchically porous Ni_3S_2 Films Grown on Nanoporous Copper as Excellent pH-Universal Electrocatalysts for Hydrogen Evolution Reaction. *Nano Energy* **2017**, *36*, 85−94.
(164) Su, J.; Ge, R.; Dong, Y.; Hao, F.; Chen, L. Recent Progress in Single-Atom Electrocatalysts: Concept, Synthesis, and Applications in Clean Energy Conversion. *J. Mater. Chem. A* **2018**, *6*, 14025−14042.
(165) Peng, Y.; Pan, W.; Wang, N.; Lu, J.-E.; Chen, S. Ruthenium Ion-Complexed Graphitic Carbon Nitride Nanosheets Supported on Reduced Graphene Oxide as High-Performance Catalysts for Electrochemical Hydrogen Evolution. *ChemSusChem* **2018**, *11*, 130−136.
(166) Peng, Y.; Lu, B.; Chen, L.; Wang, N.; Lu, J. E.; Ping, Y.; Chen, S. Hydrogen evolution reaction catalyzed by ruthenium ion-complexed graphitic carbon nitride nanosheets. *J. Mater. Chem. A* **2017**, *5*, 18261−18269.
(167) Lu, B.; Guo, L.; Wu, F.; Peng, Y.; Lu, J. E.; Smart, T. J.; Wang, N.; Finfrock, Y. Z.; Morris, D.; Zhang, P.; et al. Ruthenium Atomically Dispersed in Carbon Outperforms Platinum Toward Hydrogen Evolution in Alkaline Media. *Nat. Commun.* **2019**, *10*, 631.
(168) Deng, J.; Li, H.; Xiao, J.; Tu, Y.; Deng, D.; Yang, H.; Tian, H.; Li, J.; Ren, P.; Bao, X. Triggering the Electrocatalytic Hydrogen Evolution Activity of the Inert Two-Dimensional MoS_2 Surface Via Single-Atom Metal Doping. *Energy Environ. Sci.* **2015**, *8*, 1594−1601.
(169) Fang, M.; Dong, G.; Wei, R.; Ho, J. C. Hierarchical Nanostructures: Hierarchical Nanostructures: Design for Sustainable Water Splitting. *Adv. Energy Mater.* **2017**, *7*, 1770135.
(170) Qu, Y.; Chen, B.; Li, Z.; Duan, X.; Wang, L.; Lin, Y.; Yuan, T.; Zhou, F.; Hu, Y.; Yang, Z.; Zhao, C.; Wang, J.; Zhao, C.; Hu, Y.; Wu, G.; Zhang, Q.; Xu, Q.; Liu, B.; Gao, P.; You, R.; Huang, W.; Zheng, L.; Gu, L.; Wu, Y.; Li, Y. Thermal Emitting Strategy to Synthesize Atomically Dispersed Pt Metal Sites from Bulk Pt Metal. *J. Am. Chem. Soc.* **2019**, *141*, 4505−4509.
(171) Ye, S.; Luo, F.; Zhang, Q.; Zhang, P.; Xu, T.; Wang, Q.; He, D.; Guo, L.; Zhang, Y.; He, C.; et al. Highly Stable Single Pt Atomic Sites Anchored on Aniline-Stacked Graphene for Hydrogen Evolution Reaction. *Energy Environ. Sci.* **2019**, *12*, 1000−1007.
(172) Nørskov, J. K.; Bligaard, T.; Rossmeisl, J.; Christensen, C. H. Towards the Computational Design of Solid Catalysts. *Nat. Chem.* **2009**, *1*, 37.
(173) Yin, X. P.; Wang, H. J.; Tang, S. F.; Lu, X. L.; Shu, M.; Si, R.; Lu, T. B. Engineering the Coordination Environment of Single-Atom Platinum Anchored on Graphdiyne for Optimizing Electrocatalytic Hydrogen Evolution. *Angew. Chem., Int. Ed.* **2018**, *57*, 9382−9386.
(174) Li, X.; Liu, H.; Chen, Z.; Wu, Q.; Yu, Z.; Yang, M.; Wang, X.; Cheng, Z.; Fu, Z.; Lu, Y. Enhancing Oxygen Evolution Efficiency of Multiferroic Oxides by Spintronic and Ferroelectric Polarization Regulation. *Nat. Commun.* **2019**, *10*, 1409.
(175) Zeiger, M.; Jäckel, N.; Mochalin, V. N.; Presser, V. Carbon Onions for Electrochemical Energy Storage. *J. Mater. Chem. A* **2016**, *4*, 3172−3196.
(176) Seitz, L. C.; Dickens, C. F.; Nishio, K.; Hikita, Y.; Montoya, J.; Doyle, A.; Kirk, C.; Vojvodic, A.; Hwang, H. Y.; Norskov, J. K.; Jaramillo, T. F. A Highly Active and stable $IrO_x/SrIrO_3$ Catalyst for the Oxygen Evolution Reaction. *Science* **2016**, *353*, 1011−1014.
(177) You, B.; Sun, Y. Chalcogenide and Phosphide Solid-State Electrocatalysts for Hydrogen Generation. *ChemPlusChem* **2016**, *81*, 1045−1055.
(178) Park, J.; Lee, S.; Kim, H. E.; Cho, A.; Kim, S.; Ye, Y.; Han, J. W.; Lee, H.; Jang, J. H.; Lee, J. Investigation of the Support Effect in Atomically Dispersed Pt on WO_{3-x} for Utilization of Pt in the Hydrogen Evolution Reaction. *Angew. Chem.* **2019**, *131*, 16184−16188.
(179) Niu, S.; Jiang, W.-J.; Wei, Z.; Tang, T.; Ma, J.; Hu, J.-S.; Wan, L.-J. Se-Doping Activates FeOOH for Cost-Effective and Efficient Electrochemical Water Oxidation. *J. Am. Chem. Soc.* **2019**, *141*, 7005−7013.
(180) Zhang, L.; Han, L.; Liu, H.; Liu, X.; Luo, J. Potential-Cycling Synthesis of Single Platinum Atoms for Efficient Hydrogen evolution in Neutral Media. *Angew. Chem., Int. Ed.* **2017**, *56*, 13694−13698.
(181) Gobbi, M.; Bonacchi, S.; Lian, J. X.; Liu, Y.; Wang, X.-Y.; Stoeckel, M.-A.; Squillaci, M. A.; D'avino, G.; Narita, A.; Müllen, K.; et al. Periodic Potentials in Hybrid Van der Waals Heterostructures Formed by Supramolecular Lattices on Graphene. *Nat. Commun.* **2017**, *8*, 14767.
(182) Qin, Q.; Jang, H.; Chen, L.; Nam, G.; Liu, X.; Cho, J. Low Loading of Rh_xP and RuP on N, P Codoped Carbon as Two Trifunctional Electrocatalysts for the Oxygen and Hydrogen Electrode Reactions. *Adv. Energy Mater.* **2018**, *8*, 1801478.
(183) Zhang, C.; Liu, Y.; Chang, Y.; Lu, Y.; Zhao, S.; Xu, D.; Dai, Z.; Han, M.; Bao, J. Component-Controlled Synthesis of Necklace-Like Hollow Ni_xRu_y Nanoalloys as Electrocatalysts for Hydrogen Evolution Reaction. *ACS Appl. Mater. Interfaces* **2017**, *9*, 17326−17336.
(184) Ye, S.; Luo, F.; Xu, T.; Zhang, P.; Shi, H.; Qin, S.; Wu, J.; He, C.; Ouyang, X.; Zhang, Q.; Liu, J.; Sun, X. Boosting the Alkaline Hydrogen Evolution of Ru Nanoclusters Anchored on B/N−Doped Graphene by Accelerating Water Dissociation. *Nano Energy* **2020**, *68*, 104301.
(185) Adeniyi, A. A.; Ajibade, P. A. Exploring the Ruthenium-Ligands Bond and Their Relative Properties at Different Computational Methods. *J. Chem.* **2016**, *2016*, 3672062.
(186) Zhang, W.; Zhao, H.; Wang, L. The Simple Cubic Structure of Ruthenium Clusters. *J. Phys. Chem. B* **2004**, *108*, 2140−2147.
(187) Fu, H. C.; Ramalingam, V.; Kim, H.; Lin, C. H.; Fang, X.; Alshareef, H. N.; He, J. H. MXene-Contacted Silicon Solar Cells with 11.5% Efficiency. *Adv. Energy Mater.* **2019**, *9*, 1900180.
(188) Pang, J.; Mendes, R. G.; Bachmatiuk, A.; Zhao, L.; Ta, H. Q.; Gemming, T.; Liu, H.; Liu, Z.; Rummeli, M. H. Applications of 2D

MXenes in Energy Conversion and Storage Systems. *Chem. Soc. Rev.* **2019**, *48*, 72−133.
(189) Zhang, J.; Xu, X.; Yang, L.; Cheng, D.; Cao, D. Single-Atom Ru Doping Induced Phase Transition of MoS_2 and S Vacancy for Hydrogen Evolution Reaction. *Small Methods* **2019**, *3*, 1900653.
(190) Luo, R.; Luo, M.; Wang, Z.; Liu, P.; Song, S.; Wang, X.; Chen, M. The Atomic Origin of Nickel-Doping-Induced catalytic Enhancement in MoS_2 for Electrochemical Hydrogen Production. *Nanoscale* **2019**, *11*, 7123−7128.
(191) Chi, J. Q.; Zeng, X. J.; Shang, X.; Dong, B.; Chai, Y. M.; Liu, C. G.; Marin, M.; Yin, Y. Embedding RhP_x in N, P Co-Doped Carbon Nanoshells Through Synergetic Phosphorization and Pyrolysis for Efficient Hydrogen Evolution. *Adv. Funct. Mater.* **2019**, *29*, 1901790.
(192) Pu, Z.; Zhao, J.; Amiinu, I. S.; Li, W.; Wang, M.; He, D.; Mu, S. A Universal Synthesis Strategy for P-rich Noble Metal Diphosphide-Based Electrocatalysts for the Hydrogen Evolution Reaction. *Energy Environ. Sci.* **2019**, *12*, 952−957.
(193) Yu, H.; Xue, Y.; Huang, B.; Hui, L.; Zhang, C.; Fang, Y.; Liu, Y.; Zhao, Y.; Li, Y.; Liu, H.; Li, Y. Ultrathin Nanosheet of Graphdiyne-Supported Palladium Atom Catalyst for Efficient Hydrogen Production. *iScience* **2019**, *11*, 31−41.
(194) Lai, W.; Zhang, L.; Hua, W.; Indris, S.; Yan, Z.; Hu, Z.; Zhang, B.; Liu, Y.; Wang, L.; Liu, M.; et al. General π-Electron-Assisted Strategy for Ir, Pt, Ru, Pd, Fe, Ni Single-Atom Electrocatalysts with Bifunctional Active Sites for Highly Efficient Water Splitting. *Angew. Chem., Int. Ed.* **2019**, *58*, 11868−11873.
(195) Feng, J.; Lv, F.; Zhang, W.; Li, P.; Wang, K.; Yang, C.; Wang, B.; Yang, Y.; Zhou, J.; Lin, F.; Wang, G.-C.; Guo, S. Iridium-Based Multimetallic Porous Hollow Nanocrystals for Efficient Overall-Water-Splitting Catalysis. *Adv. Mater.* **2017**, *29*, 1703798.
(196) Pan, Y.; Liu, S.; Sun, K.; Chen, X.; Wang, B.; Wu, K.; Cao, X.; Cheong, W. C.; Shen, R.; Han, A.; et al. A Bimetallic Zn/Fe Polyphthalocyanine-Derived Single-Atom Fe-N_4 Catalytic Site: A Superior Trifunctional Catalyst for Overall Water Splitting and Zn−Air Batteries. *Angew. Chem., Int. Ed.* **2018**, *57*, 8614−8618.
(197) Xue, Y.; Huang, B.; Yi, Y.; Guo, Y.; Zuo, Z.; Li, Y.; Jia, Z.; Liu, H.; Li, Y. Anchoring Zero Valence Single Atoms of Nickel and Iron on Graphdiyne for Hydrogen Evolution. *Nat. Commun.* **2018**, *9*, 1460.
(198) Zhang, J.; Liu, J.; Xi, L.; Yu, Y.; Chen, N.; Sun, S.; Wang, W.; Lange, K. M.; Zhang, B. Single-Atom Au/NiFe Layered Double Hydroxide Electrocatalyst: Probing the Origin of Activity for Oxygen Evolution Reaction. *J. Am. Chem. Soc.* **2018**, *140*, 3876−3879.
(199) Liang, H.-W.; Brüller, S.; Dong, R.; Zhang, J.; Feng, X.; Müllen, K. Molecular Metal−N_x Centres in Porous Carbon for Electrocatalytic Hydrogen Evolution. *Nat. Commun.* **2015**, *6*, 7992.
(200) Mao, J.; He, C.-T.; Pei, J.; Chen, W.; He, D.; He, Y.; Zhuang, Z.; Chen, C.; Peng, Q.; Wang, D.; Li, Y. Accelerating Water Dissociation Kinetics by Isolating Cobalt Atoms into Ruthenium Lattice. *Nat. Commun.* **2018**, *9*, 4958.
(201) Sun, T.; Zhao, S.; Chen, W.; Zhai, D.; Dong, J.; Wang, Y.; Zhang, S.; Han, A.; Gu, L.; Yu, R.; et al. Single-Atomic Cobalt Sites Embedded in Hierarchically Ordered Porous Nitrogen-Doped Carbon as a Superior Bifunctional Electrocatalyst. *Proc. Natl. Acad. Sci. U. S. A.* **2018**, *115*, 12692−12697.
(202) Wang, Z.-L.; Hao, X.-F.; Jiang, Z.; Sun, X.-P.; Xu, D.; Wang, J.; Zhong, H.-X.; Meng, F.-L.; Zhang, X.-B. C and N Hybrid Coordination Derived Co−C−N Complex as a Highly Efficient Electrocatalyst for Hydrogen Evolution Reaction. *J. Am. Chem. Soc.* **2015**, *137*, 15070−15073.
(203) Fan, L.; Liu, P. F.; Yan, X.; Gu, L.; Yang, Z. Z.; Yang, H. G.; Qiu, S.; Yao, X. Atomically Isolated Nickel Species Anchored on Graphitized Carbon for Efficient Hydrogen Evolution Electrocatalysis. *Nat. Commun.* **2016**, *7*, 10667.
(204) Ling, C.; Shi, L.; Ouyang, Y.; Zeng, X. C.; Wang, J. Nanosheet Supported Single-Metal Atom Bifunctional Catalyst for Overall Water Splitting. *Nano Lett.* **2017**, *17*, 5133−5139.
(205) Ouyang, T.; Chen, A.-N.; He, Z.-Z.; Liu, Z.-Q.; Tong, Y. Rational Design of Atomically Dispersed Nickel Active Sites in β-Mo_2C for the Hydrogen Evolution Reaction at all pH Values. *Chem. Commun.* **2018**, *54*, 9901−9904.
(206) Qiu, H. J.; Ito, Y.; Cong, W.; Tan, Y.; Liu, P.; Hirata, A.; Fujita, T.; Tang, Z.; Chen, M. Nanoporous Graphene with Single-Atom Nickel Dopants: An Efficient and Stable Catalyst for Electrochemical Hydrogen Production. *Angew. Chem., Int. Ed.* **2015**, *54*, 14031−14035.
(207) Zhang, Y.; Li, W.; Lu, L.; Song, W.; Wang, C.; Zhou, L.; Liu, J.; Chen, Y.; Jin, H.; Zhang, Y. Tuning Active Sites on Cobalt/Nitrogen Doped Graphene for Electrocatalytic Hydrogen and Oxygen Evolution. *Electrochim. Acta* **2018**, *265*, 497−506.
(208) Zhang, Z.; Liu, C.; Feng, C.; Gao, P.; Liu, Y.; Ren, F.; Zhu, Y.; Cao, C.; Yan, W.; Si, R.; Zhou, S.; Zeng, J. Breaking the local symmetry of $LiCoO_2$ via atomic doping for efficient oxygen evolution. *Nano Lett.* **2019**, *19*, 8774−8779.
(209) Liang, Z.; Guo, W.; Zhao, R.; Qiu, T.; Tabassum, H.; Zou, R. Engineering Atomically Dispersed Metal Sites for Electrocatalytic Energy Conversion. *Nano Energy* **2019**, *64*, 103917.
(210) Sultan, S.; Tiwari, J. N.; Singh, A. N.; Zhumagali, S.; Ha, M.; Myung, C. W.; Thangavel, P.; Kim, K. S. Single Atoms and Clusters Based Nanomaterials for Hydrogen Evolution, Oxygen Evolution Reactions, and Full Water Splitting. *Adv. Energy Mater.* **2019**, *9*, 1900624.
(211) Qiu, H. J.; Ito, Y.; Cong, W.; Tan, Y.; Liu, P.; Hirata, A.; Fujita, T.; Tang, Z.; Chen, M. Nanoporous Graphene with Single-Atom Nickel Dopants: An Efficient and Stable Catalyst for Electrochemical Hydrogen Production. *Angew. Chem., Int. Ed.* **2015**, *54*, 14031−14035.
(212) Chen, W.; Pei, J.; He, C. T.; Wan, J.; Ren, H.; Zhu, Y.; Wang, Y.; Dong, J.; Tian, S.; Cheong, W. C.; et al. Rational Design of Single Molybdenum Atoms Anchored on N-Doped Carbon for Effective Hydrogen Evolution Reaction. *Angew. Chem., Int. Ed.* **2017**, *56*, 16086−16090.
(213) Chen, W.; Pei, J.; He, C. T.; Wan, J.; Ren, H.; Wang, Y.; Dong, J.; Wu, K.; Cheong, W. C.; Mao, J.; et al. Single Tungsten Atoms Supported on MOF-Derived N-Doped Carbon for Robust Electrochemical Hydrogen Evolution. *Adv. Mater.* **2018**, *30*, 1800396.
(214) Qiao, Z.; Hwang, S.; Li, X.; Wang, C.; Samarakoon, W.; Karakalos, S.; Li, D.; Chen, M.; He, Y.; Wang, M.; Liu, Z.; Wang, G.; Zhou, H.; Feng, Z.; Su, D.; Spendelow, J. S.; Wu, G. 3D Porous Graphitic Nanocarbon for Enhancing the Performance and Durability of Pt Catalysts: a Balance between Graphitization and Hierarchical Porosity. *Energy Environ. Sci.* **2019**, *12*, 2830−2841.
(215) Birdja, Y. Y.; Pérez-Gallent, E.; Figueiredo, M. C.; Göttle, A. J.; Calle-Vallejo, F.; Koper, M. T. M. Advances and Challenges in Understanding the Electrocatalytic Conversion of Carbon Dioxide to Fuels. *Nat. Energy* **2019**, *4*, 732−745.
(216) Hwang, J.; Rao, R. R.; Giordano, L.; Katayama, Y.; Yu, Y.; Shao-Horn, Y. Perovskites in Catalysis and Electrocatalysis. *Science* **2017**, *358*, 751.
(217) McCalla, E.; Abakumov, A. M.; Saubanère, M.; Foix, D.; Berg, E. J.; Rousse, G.; Doublet, M.-L.; Gonbeau, D.; Novák, P.; Van Tendeloo, G.; Dominko, R.; Tarascon, J.-M. Visualization of O-O Peroxo-Like Dimers in High-capacity Layered Oxides for Li-ion Batteries. *Science* **2015**, *350*, 1516−1521.
(218) Risch, M.; Stoerzinger, K. A.; Maruyama, S.; Hong, W. T.; Takeuchi, I.; Shao-Horn, Y. $La_{0.8}Sr_{0.2}MnO_{3-\delta}$ Decorated with $Ba_{0.5}Sr_{0.5}Co_{0.8}Fe_{0.2}O_{3-\delta}$: A Bifunctional Surface for Oxygen Electrocatalysis with Enhanced Stability and Activity. *J. Am. Chem. Soc.* **2014**, *136*, 5229−5232.
(219) Sathiya, M.; Rousse, G.; Ramesha, K.; Laisa, C. P.; Vezin, H.; Sougrati, M. T.; Doublet, M. L.; Foix, D.; Gonbeau, D.; Walker, W.; Prakash, A. S.; Ben Hassine, M.; Dupont, L.; Tarascon, J. M. Reversible Anionic redox Chemistry in High-Capacity Layered-Oxide Electrodes. *Nat. Mater.* **2013**, *12*, 827−835.
(220) Xia, B. Y.; Yan, Y.; Li, N.; Wu, H. B.; Lou, X. W.; Wang, X. A Metal−Organic Framework-Derived Bifunctional Oxygen Electrocatalyst. *Nat. Energy* **2016**, *1*, 15006.

https://dx.doi.org/10.1021/acs.chemrev.0c00594
Chem. Rev. 2020, 120, 12217−12314

(221) Hong, W. T.; Risch, M.; Stoerzinger, K. A.; Grimaud, A.; Suntivich, J.; Shao-Horn, Y. Toward the Rational Design of Non-Precious Transition Metal Oxides for Oxygen Electrocatalysis. *Energy Environ. Sci.* **2015**, *8*, 1404−1427.
(222) Koper, M. T. M. Theory of Multiple Proton−Electron Transfer Reactions and its Implications for Electrocatalysis. *Chem. Sci.* **2013**, *4*, 2710−2723.
(223) Abild-Pedersen, F.; Greeley, J.; Studt, F.; Rossmeisl, J.; Munter, T. R.; Moses, P. G.; Skúlason, E.; Bligaard, T.; Nørskov, J. K. Scaling Properties of Adsorption Energies for Hydrogen-Containing Molecules on Transition-Metal Surfaces. *Phys. Rev. Lett.* **2007**, *99*, No. 016105.
(224) Man, I. C.; Su, H.-Y.; Calle-Vallejo, F.; Hansen, H. A.; Martínez, J. I.; Inoglu, N. G.; Kitchin, J.; Jaramillo, T. F.; Nørskov, J. K.; Rossmeisl, J. Universality in Oxygen Evolution Electrocatalysis on Oxide Surfaces. *ChemCatChem* **2011**, *3*, 1159−1165.
(225) Suntivich, J.; May, K. J.; Gasteiger, H. A.; Goodenough, J. B.; Shao-Horn, Y. A Perovskite Oxide Optimized for Oxygen Evolution Catalysis from Molecular Orbital Principles. *Science* **2011**, *334*, 1383.
(226) Hardin, W. G.; Mefford, J. T.; Slanac, D. A.; Patel, B. B.; Wang, X.; Dai, S.; Zhao, X.; Ruoff, R. S.; Johnston, K. P.; Stevenson, K. J. Tuning the Electrocatalytic Activity of Perovskites through Active Site Variation and Support Interactions. *Chem. Mater.* **2014**, *26*, 3368−3376.
(227) Hardin, W. G.; Slanac, D. A.; Wang, X.; Dai, S.; Johnston, K. P.; Stevenson, K. J. Highly Active, Nonprecious Metal Perovskite Electrocatalysts for Bifunctional Metal−Air Battery Electrodes. *J. Phys. Chem. Lett.* **2013**, *4*, 1254−1259.
(228) Diaz-Morales, O.; Raaijman, S.; Kortlever, R.; Kooyman, P. J.; Wezendonk, T.; Gascon, J.; Fu, W. T.; Koper, M. T. M. Iridium-Based Double Perovskites for Efficient Water Oxidation in Acid Media. *Nat. Commun.* **2016**, *7*, 12363.
(229) Grimaud, A.; Diaz-Morales, O.; Han, B.; Hong, W. T.; Lee, Y.-L.; Giordano, L.; Stoerzinger, K. A.; Koper, M. T. M.; Shao-Horn, Y. Activating Lattice Oxygen Redox Reactions in Metal Oxides to Catalyse Oxygen Evolution. *Nat. Chem.* **2017**, *9*, 457−465.
(230) Grimaud, A.; Hong, W. T.; Shao-Horn, Y.; Tarascon, J.-M. Anionic Redox Processes for Electrochemical Devices. *Nat. Mater.* **2016**, *15*, 121.
(231) Grimaud, A.; May, K. J.; Carlton, C. E.; Lee, Y.-L.; Risch, M.; Hong, W. T.; Zhou, J.; Shao-Horn, Y. Double Perovskites as a Family of Highly Active Catalysts for Oxygen Evolution in Alkaline Solution. *Nat. Commun.* **2013**, *4*, 2439.
(232) Huang, Z.-F.; Song, J.; Du, Y.; Xi, S.; Dou, S.; Nsanzimana, J. M. V.; Wang, C.; Xu, Z. J.; Wang, X. Chemical and Structural Origin of Lattice Oxygen Oxidation in Co−Zn Oxyhydroxide Oxygen Evolution Electrocatalysts. *Nat. Energy* **2019**, *4*, 329−338.
(233) Mefford, J. T.; Rong, X.; Abakumov, A. M.; Hardin, W. G.; Dai, S.; Kolpak, A. M.; Johnston, K. P.; Stevenson, K. J. Water Electrolysis on La_{1-x} $Sr_xCoO_{3-\delta}$ Perovskite Electrocatalysts. *Nat. Commun.* **2016**, *7*, 11053.
(234) Maiyalagan, T.; Jarvis, K. A.; Therese, S.; Ferreira, P. J.; Manthiram, A. Spinel-Type Lithium Cobalt Oxide as a Bifunctional Electrocatalyst for the Oxygen Evolution and Oxygen Reduction Reactions. *Nat. Commun.* **2014**, *5*, 3949.
(235) Nong, H. N.; Reier, T.; Oh, H.-S.; Gliech, M.; Paciok, P.; Vu, T. H. T.; Teschner, D.; Heggen, M.; Petkov, V.; Schlögl, R.; Jones, T.; Strasser, P. A Unique Oxygen Ligand Environment Facilitates Wter Oidation in Hole-Dped $IrNiO_x$ Core−Shell Electrocatalysts. *Nat. Catal.* **2018**, *1*, 841−851.
(236) Yang, L.; Yu, G.; Ai, X.; Yan, W.; Duan, H.; Chen, W.; Li, X.; Wang, T.; Zhang, C.; Huang, X.; Chen, J.-S.; Zou, X. Efficient Oxygen Evolution Electrocatalysis in Acid by a Perovskite with Face-Sharing IrO_6 Octahedral Dimers. *Nat. Commun.* **2018**, *9*, 5236.
(237) Bergmann, A.; Jones, T. E.; Martinez Moreno, E.; Teschner, D.; Chernev, P.; Gliech, M.; Reier, T.; Dau, H.; Strasser, P. Unified Structural Motifs of the Catalytically Active State of Co (Oxyhydr) Oxides During the Electrochemical Oxygen Evolution Reaction. *Nat. Catal.* **2018**, *1*, 711−719.
(238) Wu, T.; Sun, S.; Song, J.; Xi, S.; Du, Y.; Chen, B.; Sasangka, W. A.; Liao, H.; Gan, C. L.; Scherer, G. G.; et al. Iron-Facilitated dynamic Active-site generation on Spinel $CoAl_2O_4$ with Self-Termination of Surface Reconstruction for Water Oxidation. *Nat. Catal.* **2019**, *2*, 763−772.
(239) Hu, C.; Zhang, L.; Zhao, Z. J.; Li, A.; Chang, X.; Gong, J. Synergism of Geometric Construction and Electronic Regulation: 3D Se-$(NiCo)S_x/(OH)_x$ Nanosheets for Highly Efficient Overall Water Splitting. *Adv. Mater.* **2018**, *30*, 1705538.
(240) Zhang, J.-Y.; Lv, L.; Tian, Y.; Li, Z.; Ao, X.; Lan, Y.; Jiang, J.; Wang, C. Rational Design of Cobalt−Iron Selenides for Highly Efficient Electrochemical Water Oxidation. *ACS Appl. Mater. Interfaces* **2017**, *9*, 33833−33840.
(241) Xu, X.; Song, F.; Hu, X. J. N. c. A Nickel Iron Diselenide-Derived Efficient Oxygen-Evolution Catalyst. *Nat. Commun.* **2016**, *7*, 12324.
(242) Fabbri, E.; Nachtegaal, M.; Binninger, T.; Cheng, X.; Kim, B.-J.; Durst, J.; Bozza, F.; Graule, T.; Schäublin, R.; Wiles, L.; et al. Dynamic Surface Self-Reconstruction is the Key of Highly Active Perovskite Nano-Electrocatalysts for Water Splitting. *Nat. Mater.* **2017**, *16*, 925−931.
(243) Kim, B.-J.; Fabbri, E.; Abbott, D. F.; Cheng, X.; Clark, A. H.; Nachtegaal, M.; Borlaf, M.; Castelli, I. E.; Graule, T.; Schmidt, T. J. Functional Role of Fe-Doping in Co-based Perovskite Oxide Catalysts for Oxygen Evolution Reaction. *J. Am. Chem. Soc.* **2019**, *141*, 5231−5240.
(244) Baran, J. D.; Grönbeck, H.; Hellman, A. Analysis of Porphyrines as Catalysts for Electrochemical Reduction of O_2 and Oxidation of H_2O. *J. Am. Chem. Soc.* **2014**, *136*, 1320−1326.
(245) Liu, Y.; Han, Y.; Zhang, Z.; Zhang, W.; Lai, W.; Wang, Y.; Cao, R. Low Overpotential Water Oxidation at Neutral pH Catalyzed by a Copper (II) Porphyrin. *Chem. Sci.* **2019**, *10*, 2613−2622.
(246) Schöfberger, W.; Faschinger, F.; Chattopadhyay, S.; Bhakta, S.; Mondal, B.; Elemans, J. A.; Müllegger, S.; Tebi, S.; Koch, R.; Klappenberger, F.; et al. A Bifunctional Electrocatalyst for Oxygen Evolution and Oxygen Reduction Reactions in Water. *Angew. Chem., Int. Ed.* **2016**, *55*, 2350−2355.
(247) Zhang, Y.; Wu, C.; Jiang, H.; Lin, Y.; Liu, H.; He, Q.; Chen, S.; Duan, T.; Song, L. Atomic Iridium Incorporated in Cobalt Hydroxide for Efficient Oxygen Evolution Catalysis in Neutral Electrolyte. *Adv. Mater.* **2018**, *30*, 1707522.
(248) Wang, D.; Li, Q.; Han, C.; Lu, Q.; Xing, Z.; Yang, X. Atomic and Electronic Modulation of Self-Supported Nickel-Vanadium Layered double Hydroxide to Accelerate Water Splitting Kinetics. *Nat. Commun.* **2019**, *10*, 3899.
(249) Li, P.; Wang, M.; Duan, X.; Zheng, L.; Cheng, X.; Zhang, Y.; Kuang, Y.; Li, Y.; Ma, Q.; Feng, Z.; Liu, W.; Sun, X. Boosting Oxygen Evolution of Single-Atomic Ruthenium Through Electronic Coupling with Cobalt-Iron Layered Double Hydroxides. *Nat. Commun.* **2019**, *10*, 1711.
(250) Zhuang, L.; Jia, Y.; Liu, H.; Wang, X.; Hocking, R. K.; Liu, H.; Chen, J.; Ge, L.; Zhang, L.; Li, M.; et al. Defect-Induced Pt−Co−Se Coordinated Sites with Highly Asymmetrical Electronic Distribution for Boosting Oxygen-Involving Electrocatalysis. *Adv. Mater.* **2019**, *31*, 1805581.
(251) Cao, L.; Luo, Q.; Chen, J.; Wang, L.; Lin, Y.; Wang, H.; Liu, X.; Shen, X.; Zhang, W.; Liu, W. Dynamic Oxygen Adsorption on Single-Atomic Ruthenium Catalyst with High Performance for Acidic Oxygen Evolution Reaction. *Nat. Commun.* **2019**, *10*, 4849.
(252) Yao, Y.; Hu, S.; Chen, W.; Huang, Z.-Q.; Wei, W.; Yao, T.; Liu, R.; Zang, K.; Wang, X.; Wu, G.; et al. Engineering the Electronic Structure of Single Atom Ru Sites via Compressive Strain Boosts Acidic Water Oxidation Electrocatalysis. *Nat. Catal.* **2019**, *2*, 304−313.
(253) Zhang, H.; Liu, Y.; Chen, T.; Zhang, J.; Zhang, J.; Lou, X. W. Unveiling the Activity Origin of Electrocatalytic Oxygen Evolution over Isolated Ni Atoms Supported on a N-Doped Carbon Matrix. *Adv. Mater.* **2019**, *31*, 1904548.

https://dx.doi.org/10.1021/acs.chemrev.0c00594
Chem. Rev. 2020, 120, 12217−12314

(254) Lei, C.; Chen, H.; Cao, J.; Yang, J.; Qiu, M.; Xia, Y.; Yuan, C.; Yang, B.; Li, Z.; Zhang, X.; et al. Fe-N_4 Sites Embedded into Carbon Nanofiber Integrated with Electrochemically Exfoliated Graphene for Oxygen Evolution in Acidic Medium. *Adv. Energy Mater.* **2018**, *8*, 1801912.
(255) Guan, J.; Duan, Z.; Zhang, F.; Kelly, S. D.; Si, R.; Dupuis, M.; Huang, Q.; Chen, J. Q.; Tang, C.; Li, C. Water Oxidation on a Mononuclear Manganese Heterogeneous Catalyst. *Nat. Catal.* **2018**, *1*, 870−877.
(256) Chen, P.; Zhou, T.; Xing, L.; Xu, K.; Tong, Y.; Xie, H.; Zhang, L.; Yan, W.; Chu, W.; Wu, C.; Xie, Y. Atomically Dispersed Iron−Nitrogen Species as Electrocatalysts for Bifunctional Oxygen Evolution and Reduction Reactions. *Angew. Chem., Int. Ed.* **2017**, *56*, 610−614.
(257) Zheng, Y.; Jiao, Y.; Zhu, Y.; Cai, Q.; Vasileff, A.; Li, L. H.; Han, Y.; Chen, Y.; Qiao, S.-Z. Molecule-level g-C3N4 coordinated transition metals as a new class of electrocatalysts for oxygen electrode reactions. *J. Am. Chem. Soc.* **2017**, *139*, 3336−3339.
(258) Shen, G.; Zhang, R.; Pan, L.; Hou, F.; Zhao, Y.; Shen, Z.; Mi, W.; Shi, C.; Wang, Q.; Zhang, X.; Zou, J.-J. Regulating the Spin State of FeIII by Atomically Anchoring on Ultrathin Titanium Dioxide for Efficient Oxygen Evolution Electrocatalysis. *Angew. Chem., Int. Ed.* **2020**, *59*, 2313−2317.
(259) Yan, J.; Kong, L.; Ji, Y.; White, J.; Li, Y.; Zhang, J.; An, P.; Liu, S.; Lee, S.-T.; Ma, T. Single Atom Tungsten Doped Ultrathin α-Ni$(OH)_2$ for Enhanced Electrocatalytic Water Oxidation. *Nat. Commun.* **2019**, *10*, 2149.
(260) Che, G.; Lakshmi, B. B.; Fisher, E. R.; Martin, C. R. Carbon nanotubule membranes for electrochemical energy storage and production. *Nature* **1998**, *393*, 346−349.
(261) Yang, Z.; Zhang, J.; Kintner-Meyer, M. C.; Lu, X.; Choi, D.; Lemmon, J. P.; Liu, J. Electrochemical Energy Storage for Green Grid. *Chem. Rev.* **2011**, *111*, 3577−3613.
(262) Rabis, A.; Rodriguez, P.; Schmidt, T. J. Electrocatalysis for Polymer Electrolyte Fuel Cells: Recent Achievements and Future Challenges. *ACS Catal.* **2012**, *2*, 864−890.
(263) Debe, M. K. Electrocatalyst Approaches and Challenges for Automotive Fuel Cells. *Nature* **2012**, *486*, 43−51.
(264) Proietti, E.; Jaouen, F.; Lefèvre, M.; Larouche, N.; Tian, J.; Herranz, J.; Dodelet, J.-P. Iron-Based Cathode Catalyst With Enhanced Power Density in Polymer Electrolyte Membrane Fuel Cells. *Nat. Commun.* **2011**, *2*, 416.
(265) Hou, J.; Yang, M.; Ke, C.; Wei, G.; Priest, C.; Qiao, Z.; Wu, G.; Zhang, J. Platinum-Group-Metal Catalysts for Proton Exchange Membrane Fuel Cells: From Catalyst Design to Electrode Structure Optimization. *EnergyChem.* **2020**, *2*, 100023.
(266) Ren, X.; Lv, Q.; Liu, L.; Liu, B.; Wang, Y.; Liu, A.; Wu, G. Current Progress of Pt and Pt-Based Electrocatalysts Used for Fuel Cells. *Sustain. Energy Fuels* **2020**, *4*, 15−30.
(267) Wang, X. X.; Hwang, S.; Pan, Y.-T.; Chen, K.; He, Y.; Karakalos, S.; Zhang, H.; Spendelow, J. S.; Su, D.; Wu, G. Ordered Pt_3Co Intermetallic Nanoparticles Derived from Metal−Organic Frameworks for Oxygen Reduction. *Nano Lett.* **2018**, *18*, 4163−4171.
(268) Chong, L.; Wen, J.; Kubal, J.; Sen, F. G.; Zou, J.; Greeley, J.; Chan, M.; Barkholtz, H.; Ding, W.; Liu, D.-J. Ultralow-Loading Platinum-Cobalt Fuel Cell Catalysts Derived From Imidazolate Frameworks. *Science* **2018**, *362*, 1276−1281.
(269) Liang, J.; Ma, F.; Hwang, S.; Wang, X.; Sokolowski, J.; Li, Q.; Wu, G.; Su, D. Atomic Arrangement Engineering of Metallic Nanocrystals for Energy-Conversion Electrocatalysis. *Joule* **2019**, *3*, 956−991.
(270) Shao, M.; Chang, Q.; Dodelet, J.-P.; Chenitz, R. Recent Advances in Electrocatalysts for Oxygen Reduction Reaction. *Chem. Rev.* **2016**, *116*, 3594−3657.
(271) Li, C.; Tan, H.; Lin, J.; Luo, X.; Wang, S.; You, J.; Kang, Y.-M.; Bando, Y.; Yamauchi, Y.; Kim, J. Emerging Pt-based electrocatalysts with highly open nanoarchitectures for boosting oxygen reduction reaction. *Nano Today* **2018**, *21*, 91−105.
(272) Chung, D. Y.; Yoo, J. M.; Sung, Y.-E. Highly Durable and Active Pt-Based Nanoscale Design for Fuel-Cell Oxygen-Reduction Electrocatalysts. *Adv. Mater.* **2018**, *30*, 1704123.
(273) Wang, L.; Zeng, Z.; Ma, C.; Liu, Y.; Giroux, M.; Chi, M.; Jin, J.; Greeley, J.; Wang, C. Plating Precious Metals on Nonprecious Metal Nanoparticles for Sustainable Electrocatalysts. *Nano Lett.* **2017**, *17*, 3391−3395.
(274) Escudero-Escribano, M.; Malacrida, P.; Hansen, M. H.; Vej-Hansen, U. G.; Velázquez-Palenzuela, A.; Tripkovic, V.; Schiøtz, J.; Rossmeisl, J.; Stephens, I. E. L.; Chorkendorff, I. Tuning the activity of Pt alloy electrocatalysts by means of the lanthanide contraction. *Science* **2016**, *352*, 73−76.
(275) Kongkanand, A.; Subramanian, N. P.; Yu, Y.; Liu, Z.; Igarashi, H.; Muller, D. A. Achieving High-Power PEM Fuel Cell Performance with an Ultralow-Pt-Content Core−Shell Catalyst. *ACS Catal.* **2016**, *6*, 1578−1583.
(276) Zhang, S.; Hao, Y.; Su, D.; Doan-Nguyen, V. V. T.; Wu, Y.; Li, J.; Sun, S.; Murray, C. B. Monodisperse Core/Shell Ni/FePt Nanoparticles and Their Conversion to Ni/Pt to Catalyze Oxygen Reduction. *J. Am. Chem. Soc.* **2014**, *136*, 15921−15924.
(277) Tian, X. L.; Xu, Y. Y.; Zhang, W.; Wu, T.; Xia, B. Y.; Wang, X. Unsupported Platinum-Based Electrocatalysts for Oxygen Reduction Reaction. *ACS Energy Lett.* **2017**, *2*, 2035−2043.
(278) Yu, T.; Kim, D. Y.; Zhang, H.; Xia, Y. Platinum Concave Nanocubes with High-Index Facets and Their Enhanced Activity for Oxygen Reduction Reaction. *Angew. Chem., Int. Ed.* **2011**, *50*, 2773−2777.
(279) Meier, J. C.; Galeano, C.; Katsounaros, I.; Topalov, A. A.; Kostka, A.; Schüth, F.; Mayrhofer, K. J. J. Degradation Mechanisms of Pt/C Fuel Cell Catalysts under Simulated Start−Stop Conditions. *ACS Catal.* **2012**, *2*, 832−843.
(280) Lefèvre, M.; Proietti, E.; Jaouen, F.; Dodelet, J.-P. Iron-Based Catalysts With Improved Oxygen Reduction Activity in Polymer Electrolyte Fuel Cells. *Science* **2009**, *324*, 71−74.
(281) Gong, K.; Du, F.; Xia, Z.; Durstock, M.; Dai, L. Nitrogen-Doped Carbon Nanotube Arrays With High Electrocatalytic Activity for Oxygen Reduction. *Science* **2009**, *323*, 760−764.
(282) Chung, H. T.; Cullen, D. A.; Higgins, D.; Sneed, B. T.; Holby, E. F.; More, K. L.; Zelenay, P. Direct Atomic-Level Insight Into the Active Sites of a High-Performance PGM-Free ORR Catalyst. *Science* **2017**, *357*, 479−484.
(283) Wang, X. X.; Prabhakaran, V.; He, Y.; Shao, Y.; Wu, G. Iron-Free Cathode Catalysts for Proton-Exchange-Membrane Fuel Cells: Cobalt Catalysts and the Peroxide Mitigation Approach. *Adv. Mater.* **2019**, *31*, 1805126.
(284) Wu, G. Current Challenge and Perspective of PGM-Free Cathode Catalysts for PEM Fuel Cells. *Front. Energy Res.* **2017**, *11*, 286−298.
(285) Chen, M.; He, Y.; Spendelow, J. S.; Wu, G. Atomically Dispersed Metal Catalysts for Oxygen Reduction. *ACS Energy Lett.* **2019**, *4*, 1619−1633.
(286) Han, G.; Zheng, Y.; Zhang, X.; Wang, Z.; Gong, Y.; Du, C.; Banis, M. N.; Yiu, Y.-M.; Sham, T.-K.; Gu, L.; et al. High Loading Single-Atom Cu Dispersed on Graphene for Efficient Oxygen Reduction Reaction. *Nano Energy* **2019**, *66*, 104088.
(287) Zhang, H.; Osgood, H.; Xie, X.; Shao, Y.; Wu, G. Engineering Nanostructures of PGM-Free Oxygen-Reduction Catalysts Using Metal-Organic Frameworks. *Nano Energy* **2017**, *31*, 331−350.
(288) Zhang, H.; Li, J.; Tan, Q.; Lu, L.; Wang, Z.; Wu, G. Metal−Organic Frameworks and Their Derived Materials as Electrocatalysts and Photocatalysts for CO2 Reduction: Progress, Challenges, and Perspectives. *Chem. - Eur. J.* **2018**, *24*, 18137−18157.
(289) Barkholtz, H. M.; Liu, D.-J. Advancements in Rationally Designed PGM-Free Fuel Cell Catalysts Derived From Metal−Organic Frameworks. *Mater. Horiz.* **2017**, *4*, 20−37.
(290) Zhang, H. G.; Chung, H. T.; Cullen, D. A.; Wagner, S.; Kramm, U. I.; More, K. L.; Zelenay, P.; Wu, G. High-Performance Fuel Cell Cathodes Exclusively Containing Atomically Dispersed Iron Active Sites. *Energy Environ. Sci.* **2019**, *12*, 2548−2558.

https://dx.doi.org/10.1021/acs.chemrev.0c00594
Chem. Rev. 2020, 120, 12217−12314

(291) He, Y.; Tan, Q.; Lu, L.; Sokolowski, J.; Wu, G. Metal-Nitrogen-Carbon Catalysts for Oxygen Reduction in PEM Fuel Cells: Self-Template Synthesis Approach to Enhancing Catalytic Activity and Stability. *Electrochem. Energy Rev.* **2019**, *2*, 231−251.
(292) Kim, J.; Kim, H.-E.; Lee, H. Single-Atom Catalysts of Precious Metals for Electrochemical Reactions. *ChemSusChem* **2018**, *11*, 104−113.
(293) Dutczak, J. Issues related to fuel cells application to small drones propulsion. *IOP Conf. Ser.: Mater. Sci. Eng.* **2018**, *421*, No. 042014.
(294) Zhang, H.; Liu, G.; Shi, L.; Ye, J. Single-Atom Catalysts: Emerging Multifunctional Materials in Heterogeneous Catalysis. *Adv. Energy Mater.* **2018**, *8*, 1701343.
(295) Liu, J.; Jiao, M.; Mei, B.; Tong, Y.; Li, Y.; Ruan, M.; Song, P.; Sun, G.; Jiang, L.; Wang, Y.; Jiang, Z.; Gu, L.; Zhou, Z.; Xu, W. Carbon-Supported Divacancy-Anchored Platinum Single-Atom Electrocatalysts with Superhigh Pt Utilization for the Oxygen Reduction Reaction. *Angew. Chem., Int. Ed.* **2019**, *58*, 1163−1167.
(296) Calle-Vallejo, F.; Martinez, J. I.; Rossmeisl, J. Density Functional Studies of Functionalized Graphitic Materials With Late Transition Metals for Oxygen Reduction Reactions. *Phys. Chem. Chem. Phys.* **2011**, *13*, 15639−15643.
(297) van Veen, J. A. R.; van Baar, J. F.; Kroese, C. J.; Coolegem, J. G. F.; De Wit, N.; Colijn, H. A. Oxygen Reduction on Transition-Metal Porphyrins in Acid Electrolyte I. Activity. *Ber. Bunsenges. Phys. Chem.* **1981**, *85*, 693−700.
(298) Xiao, M.; Zhu, J.; Li, G.; Li, N.; Li, S.; Cano, Z. P.; Ma, L.; Cui, P.; Xu, P.; Jiang, G.; Jin, H.; Wang, S.; Wu, T.; Lu, J.; Yu, A.; Su, D.; Chen, Z. A Single-Atom Iridium Heterogeneous Catalyst in Oxygen Reduction Reaction. *Angew. Chem., Int. Ed.* **2019**, *58*, 9640−9645.
(299) He, F.; Li, K.; Yin, C.; Wang, Y.; Tang, H.; Wu, Z. Single Pd atoms supported by graphitic carbon nitride, a potential oxygen reduction reaction catalyst from theoretical perspective. *Carbon* **2017**, *114*, 619−627.
(300) Jahnke, H.; Schoenborn, M.; Zimmermann, G. In *N_4 Chelates as Catalysts in Fuel Cells*; Thieme, 1973; pp 71−89.
(301) Jahnke, H.; Schoenborn, M. In *Cathodic Reduction of Oxygen on Phthalocyanine−Carbon Catalysts*; Presses Academies Europeennes, 1969; pp 60−65.
(302) Beck, F.; Dammert, W.; Heiss, J.; Hiller, H.; Polster, R. Electrocatalysis of the Oxygen Cathode by Metal-Phthalocyanines and -Dibenzotetraazaannulenes. *Z. Naturforsch., A: Phys. Sci.* **1973**, *28*, 1009−21.
(303) Alt, H.; Binder, H.; Sandstede, G. Mechanism of the Electrocatalytic Reduction of Oxygen on Metal Chelates. *J. Catal.* **1973**, *28*, 8−19.
(304) Kattel, S.; Wang, G. A Density Functional Theory Study of Oxygen Reduction Reaction on Me−N_4 (Me = Fe, Co, or Ni) Clusters Between Graphitic Pores. *J. Mater. Chem. A* **2013**, *1*, 10790−10797.
(305) Holby, E. F.; Wu, G.; Zelenay, P.; Taylor, C. D. Structure of Fe−Nx−C Defects in Oxygen Reduction Reaction Catalysts from First-Principles Modeling. *J. Phys. Chem. C* **2014**, *118*, 14388−14393.
(306) Kattel, S.; Wang, G. Reaction Pathway for Oxygen Reduction on FeN4 Embedded Graphene. *J. Phys. Chem. Lett.* **2014**, *5*, 452−456.
(307) Liu, J.; Zhu, D.; Guo, C.; Vasileff, A.; Qiao, S.-Z. Design Strategies toward Advanced MOF-Derived Electrocatalysts for Energy-Conversion Reactions. *Adv. Energy Mater.* **2017**, *7*, 1700518.
(308) Zhao, D.; Shui, J.-L.; Grabstanowicz, L. R.; Chen, C.; Commet, S. M.; Xu, T.; Lu, J.; Liu, D.-J. Highly Efficient Non-Precious Metal Electrocatalysts Prepared from One-Pot Synthesized Zeolitic Imidazolate Frameworks. *Adv. Mater.* **2014**, *26*, 1093−1097.
(309) Wang, X.; Zhang, H.; Lin, H.; Gupta, S.; Wang, C.; Tao, Z.; Fu, H.; Wang, T.; Zheng, J.; Wu, G.; Li, X. Directly converting Fe-doped metal−organic frameworks into highly active and stable Fe-N-C catalysts for oxygen reduction in acid. *Nano Energy* **2016**, *25*, 110−119.
(310) Ye, Y.; Cai, F.; Li, H.; Wu, H.; Wang, G.; Li, Y.; Miao, S.; Xie, S.; Si, R.; Wang, J.; Bao, X. Surface functionalization of ZIF-8 with ammonium ferric citrate toward high exposure of Fe-N active sites for efficient oxygen and carbon dioxide electroreduction. *Nano Energy* **2017**, *38*, 281−289.
(311) Peng, P.; Shi, L.; Huo, F.; Mi, C.; Wu, X.; Zhang, S.; Xiang, Z. A pyrolysis-free path toward superiorly catalytic nitrogen-coordinated single atom. *Sci. Adv.* **2019**, *5*, No. eaaw2322.
(312) Lai, Q.; Zheng, L.; Liang, Y.; He, J.; Zhao, J.; Chen, J. Metal−Organic-Framework-Derived Fe-N/C Electrocatalyst with Five-Coordinated Fe-Nx Sites for Advanced Oxygen Reduction in Acid Media. *ACS Catal.* **2017**, *7*, 1655−1663.
(313) Serov, A.; Artyushkova, K.; Atanassov, P. Fe-N-C Oxygen Reduction Fuel Cell Catalyst Derived from Carbendazim: Synthesis, Structure, and Reactivity. *Adv. Energy Mater.* **2014**, *4*, 1301735.
(314) Sa, Y. J.; Seo, D.-J.; Woo, J.; Lim, J. T.; Cheon, J. Y.; Yang, S. Y.; Lee, J. M.; Kang, D.; Shin, T. J.; Shin, H. S.; et al. A General Approach to Preferential Formation of Active Fe−N_x Sites in Fe−N/C Electrocatalysts for Efficient Oxygen Reduction Reaction. *J. Am. Chem. Soc.* **2016**, *138*, 15046−15056.
(315) Qiao, Z.; Zhang, H.; Karakalos, S.; Hwang, S.; Xue, J.; Chen, M.; Su, D.; Wu, G. 3D Polymer Hydrogel for High-Performance Atomic Iron-Rich Catalysts for Oxygen Reduction in Acidic Media. *Appl. Catal., B* **2017**, *219*, 629−639.
(316) Li, J.; Zhang, H.; Samarakoon, W.; Shan, W.; Cullen, D. A.; Karakalos, S.; Chen, M.; Gu, D.; More, K. L.; Wang, G.; Feng, Z.; Wang, Z.; Wu, G. Thermally Driven Structure and Performance Evolution of Atomically Dispersed FeN4 Sites for Oxygen Reduction. *Angew. Chem., Int. Ed.* **2019**, *58*, 18971−18980.
(317) Wang, C.; Kim, J.; Tang, J.; Kim, M.; Lim, H.; Malgras, V.; You, J.; Xu, Q.; Li, J.; Yamauchi, Y. New Strategies for Novel MOF-Derived Carbon Materials Based on Nanoarchitectures. *Chem.* **2020**, *6*, 19−40.
(318) Shang, L.; Yu, H.; Huang, X.; Bian, T.; Shi, R.; Zhao, Y.; Waterhouse, G. I. N.; Wu, L.-Z.; Tung, C.-H.; Zhang, T. Well-Dispersed ZIF-Derived Co,N-Co-doped Carbon Nanoframes through Mesoporous-Silica-Protected Calcination as Efficient Oxygen Reduction Electrocatalysts. *Adv. Mater.* **2016**, *28*, 1668−1674.
(319) Fu, X.; Li, N.; Ren, B.; Jiang, G.; Liu, Y.; Hassan, F. M.; Su, D.; Zhu, J.; Yang, L.; Bai, Z.; et al. Tailoring FeN4 Sites with Edge Enrichment for Boosted Oxygen Reduction Performance in Proton Exchange Membrane Fuel Cell. *Adv. Energy Mater.* **2019**, *9*, 1803737.
(320) Wang, X. X.; Prabhakaran, V.; He, Y.; Shao, Y.; Wu, G. Iron-Free Cathode Catalysts for Proton-Exchange-Membrane Fuel Cells: Cobalt Catalysts and the Peroxide Mitigation Approach. *Adv. Mater.* **2019**, *31*, 1805126.
(321) Yin, P.; Yao, T.; Wu, Y.; Zheng, L.; Lin, Y.; Liu, W.; Ju, H.; Zhu, J.; Hong, X.; Deng, Z.; Zhou, G.; Wei, S.; Li, Y. Single Cobalt Atoms with Precise N-Coordination as Superior Oxygen Reduction Reaction Catalysts. *Angew. Chem., Int. Ed.* **2016**, *55*, 10800−10805.
(322) He, Y.; Hwang, S.; Cullen, D. A.; Uddin, M. A.; Langhorst, L.; Li, B.; Karakalos, S.; Kropf, A. J.; Wegener, E. C.; Sokolowski, J.; Chen, M.; Myers, D.; Su, D.; More, K. L.; Wang, G.; Litster, S.; Wu, G. Highly Active Atomically Dispersed CoN_4 Fuel Cell Cathode Catalysts Derived From Surfactant-Assisted MOFs: Carbon-Shell Confinement Strategy. *Energy Environ. Sci.* **2019**, *12*, 250−260.
(323) Wu, G.; Santandreu, A.; Kellogg, W.; Gupta, S.; Ogoke, O.; Zhang, H.; Wang, H.-L.; Dai, L. Carbon Nanocomposite Catalysts for Oxygen Reduction and Evolution Reactions: From Nitrogen Doping to Transition-Metal Addition. *Nano Energy* **2016**, *29*, 83−110.
(324) Xiong, X.; Li, Y.; Jia, Y.; Meng, Y.; Sun, K.; Zheng, L.; Zhang, G.; Li, Y.; Sun, X. Ultrathin atomic Mn-decorated formamide-converted N-doped carbon for efficient oxygen reduction reaction. *Nanoscale* **2019**, *11*, 15900−15906.
(325) Bai, L.; Duan, Z.; Wen, X.; Si, R.; Guan, J. Atomically dispersed manganese-based catalysts for efficient catalysis of oxygen reduction reaction. *Appl. Catal., B* **2019**, *257*, 117930.
(326) Yang, Y.; Mao, K.; Gao, S.; Huang, H.; Xia, G.; Lin, Z.; Jiang, P.; Wang, C.; Wang, H.; Chen, Q. O-, N-Atoms-Coordinated Mn

https://dx.doi.org/10.1021/acs.chemrev.0c00594
Chem. Rev. 2020, 120, 12217−12314

Cofactors within a Graphene Framework as Bioinspired Oxygen Reduction Reaction Electrocatalysts. *Adv. Mater.* **2018**, *30*, 1801732.
(327) Xiao, M.; Zhang, H.; Chen, Y.; Zhu, J.; Gao, L.; Jin, Z.; Ge, J.; Jiang, Z.; Chen, S.; Liu, C.; Xing, W. Identification of Binuclear Co_2N_5 Active Sites for Oxygen Reduction Reaction With More Than One Magnitude Higher Activity Than Single Atom CoN_4 Site. *Nano Energy* **2018**, *46*, 396−403.
(328) Sahraie, N. R.; Kramm, U. I.; Steinberg, J.; Zhang, Y.; Thomas, A.; Reier, T.; Paraknowitsch, J.-P.; Strasser, P. Quantifying the density and utilization of active sites in non-precious metal oxygen electroreduction catalysts. *Nat. Commun.* **2015**, *6*, 8618.
(329) Tarasevich, M. R.; Radiyschkina, K. A.; Androuseva, S. I. Electrocatalysis of Oxygen Reduction on Organic Metallic Complexes. *Bioelectrochem. Bioenerg.* **1977**, *4*, 18−29.
(330) Kadish, K. M., Smith, K. M., Guilard, R., Eds. *The Porphyrin Handbook; Applications: Past, Present and Future*; Academic Press, 2000; Vol. *6*, p 346.
(331) Yamanaka, I.; Onizawa, T.; Suzuki, H.; Hanaizumi, N.; Nishimura, N.; Takenaka, S. Study of Direct Synthesis of Hydrogen Peroxide Acid Solutions at a Heat-Treated MnCl-Porphyrin/Activated Carbon Cathode from H_2 and O_2. *J. Phys. Chem. C* **2012**, *116*, 4572−4583.
(332) Parvez, K.; Yang, S.; Hernandez, Y.; Winter, A.; Turchanin, A.; Feng, X.; Müllen, K. Nitrogen-Doped Graphene and Its Iron-Based Composite as Efficient Electrocatalysts for Oxygen Reduction Reaction. *ACS Nano* **2012**, *6*, 9541.
(333) Qu, L.; Liu, Y.; Baek, J.-B.; Dai, L. Nitrogen-Doped Graphene as Efficient Metal-Free Electrocatalyst for Oxygen Reduction in Fuel Cells. *ACS Nano* **2010**, *4*, 1321−1326.
(334) Byon, H. R.; Suntivich, J.; Shao-Horn, Y. Graphene-Based Non-Noble-Metal Catalysts for Oxygen Reduction Reaction in Acid. *Chem. Mater.* **2011**, *23*, 3421−3428.
(335) Lai, L.; Potts, J. R.; Zhan, D.; Wang, L.; Poh, C. K.; Tang, C.; Gong, H.; Shen, Z.; Lin, J.; Ruoff, R. S. Exploration of the Active Center Structure of Nitrogen-Doped Graphene-Based Catalysts for Oxygen Reduction Reaction. *Energy Environ. Sci.* **2012**, *5*, 7936−7942.
(336) Xiao, J.; Mei, D.; Li, X.; Xu, W.; Wang, D.; Graff, G. L.; Bennett, W. D.; Nie, Z.; Saraf, L. V.; Aksay, I. A.; Liu, J.; Zhang, J.-G. Hierarchically Porous Graphene as a Lithium−Air Battery Electrode. *Nano Lett.* **2011**, *11*, 5071−5078.
(337) Shui, J. L.; Karan, N. K.; Balasubramanian, M.; Li, S. Y.; Liu, D. J. Fe/N/C Composite in LI-O_2 Battery: Studies of Catalytic Structure and Activity Toward Oxygen Evolution Reaction. *J. Am. Chem. Soc.* **2012**, *134*, 16654−16661.
(338) Pylypenko, S.; Mukherjee, S.; Olson, T. S.; Atanassov, P. Non-Platinum Oxygen Reduction Electrocatalysts Based on Pyrolyzed Transition Metal Macrocycles. *Electrochim. Acta* **2008**, *53*, 7875−7883.
(339) Niwa, H.; Horiba, K.; Harada, Y.; Oshima, M.; Ikeda, T.; Terakura, K.; Ozaki, J.-i.; Miyata, S. X-Ray Absorption Analysis of Nitrogen Contribution to Oxygen Reduction Reaction in Carbon Alloy Cathode Catalysts for Polymer Electrolyte Fuel Cells. *J. Power Sources* **2009**, *187*, 93−97.
(340) Mamtani, K.; Ozkan, U. S. Heteroatom-Doped Carbon Nanostructures as Oxygen Reduction Reaction Catalysts in Acidic Media: An Overview. *Catal. Lett.* **2015**, *145*, 436−450.
(341) Wiggins-Camacho, J. D.; Stevenson, K. J. Mechanistic Discussion of the Oxygen Reduction Reaction at Nitrogen-Doped Carbon Nanotubes. *J. Phys. Chem. C* **2011**, *115*, 20002−20010.
(342) Jaouen, F.; Goellner, V.; Lefèvre, M.; Herranz, J.; Proietti, E.; Dodelet, J. Oxygen Reduction Activities Compared in Rotating-Disk Electrode and Proton Exchange Membrane Fuel Cells for Highly Active Fe-N-C Catalysts. *Electrochim. Acta* **2013**, *87*, 619−628.
(343) Nallathambi, V.; Leonard, N.; Kothandaraman, R.; Barton, S. C. Nitrogen Precursor Effects in Iron-Nitrogen-Carbon Oxygen Reduction Catalysts. *Electrochem. Solid-State Lett.* **2011**, *14*, B55−B58.
(344) Liang, H. W.; Wei, W.; Wu, Z. S.; Feng, X.; Mullen, K. Mesoporous Metal-Nitrogen-Doped Carbon Electrocatalysts for Highly Efficient Oxygen Reduction Reaction. *J. Am. Chem. Soc.* **2013**, *135*, 16002−5.
(345) Ramaswamy, N.; Tylus, U.; Jia, Q.; Mukerjee, S. Activity Descriptor Identification for Oxygen Reduction on Nonprecious Electrocatalysts: Linking Surface Science to Coordination Chemistry. *J. Am. Chem. Soc.* **2013**, *135*, 15443−9.
(346) Jaouen, F.; Herranz, J.; Lefevre, M.; Dodelet, J.-P.; Kramm, U. I.; Herrmann, I.; Bogdanoff, P.; Maruyama, J.; Nagaoka, T.; Garsuch, A.; et al. Cross-Laboratory Experimental Study of Non-Noble-Metal Electrocatalysts for the Oxygen Reduction Reaction. *ACS Appl. Mater. Interfaces* **2009**, *1*, 1623−1639.
(347) Jiao, Y.; Zheng, Y.; Jaroniec, M.; Qiao, S. Z. Origin of the Electrocatalytic Oxygen Reduction Activity of Graphene-Based Catalysts: A Roadmap to Achieve the Best Performance. *J. Am. Chem. Soc.* **2014**, *136*, 4394−403.
(348) Ganesan, S.; Leonard, N.; Barton, S. C. Impact of Transition Metal on Nitrogen Retention and Activity of Iron−Nitrogen−Carbon Oxygen Reduction Catalysts. *Phys. Chem. Chem. Phys.* **2014**, *16*, 4576−4585.
(349) Gong, Y.; Fei, H.; Zou, X.; Zhou, W.; Yang, S.; Ye, G.; Liu, Z.; Peng, Z.; Lou, J.; Vajtai, R.; Yakobson, B. I.; Tour, J. M.; Ajayan, P. M. Boron- and Nitrogen-Substituted Graphene Nanoribbons as Efficient Catalysts for Oxygen Reduction Reaction. *Chem. Mater.* **2015**, *27*, 1181−1186.
(350) Strickland, K.; Miner, E.; Jia, Q.; Tylus, U.; Ramaswamy, N.; Liang, W.; Sougrati, M.-T.; Jaouen, F.; Mukerjee, S. Highly Active Oxygen Reduction Non-Platinum Group Metal Electrocatalyst Without Direct Metal-Nitrogen Coordination. *Nat. Commun.* **2015**, *6*, 7343.
(351) Wu, G.; Nelson, M. A.; Mack, N. H.; Ma, S. G.; Sekhar, P.; Garzon, F. H.; Zelenay, P. Titanium Dioxide-Supported Non-Precious Metal Oxygen Reduction Electrocatalyst. *Chem. Commun.* **2010**, *46*, 7489−7491.
(352) Li, Q.; Xu, P.; Gao, W.; Ma, S. G.; Zhang, G. Q.; Cao, R. G.; Cho, J.; Wang, H. L.; Wu, G. Graphene/Graphene Tube Nanocomposites Templated from Cage-Containing Metal-Organic Frameworks for Oxygen Reduction in Li-O2 Batteries. *Adv. Mater.* **2014**, *26*, 1378−1386.
(353) Wu, G.; Chung, H. T.; Nelson, M.; Artyushkova, K.; More, K. L.; Johnston, C. M.; Zelenay, P. Graphene-Enriched Co_9S_8-N-C Non-Precious Metal Catalyst for Oxygen Reduction in Alkaline Media. *ECS Trans.* **2011**, *41*, 1709−1717.
(354) Wu, G.; More, K. L.; Xu, P.; Wang, H.-L.; Ferrandon, M.; Kropf, A. J.; Myers, D. J.; Ma, S.; Johnston, C. M.; Zelenay, P. A Carbon-Nanotube-Supported Graphene-Rich Non-Precious Metal Oxygen Reduction Catalyst With Enhanced Performance Durability. *Chem. Commun.* **2013**, *49*, 3291−3293.
(355) Li, Q.; Wu, G.; Cullen, D. A.; More, K. L.; Mack, N. H.; Chung, H. T.; Zelenay, P. Phosphate-Tolerant Oxygen Reduction Catalysts. *ACS Catal.* **2014**, *4*, 3193−3200.
(356) He, Q.; Li, Q.; Khene, S.; Ren, X.; López-Suárez, F. E.; Lozano-Castelló, D.; Bueno-López, A.; Wu, G. High-Loading Cobalt Oxide Coupled with Nitrogen-Doped Graphene for Oxygen Reduction in Anion-Exchange-Membrane Alkaline Fuel Cells. *J. Phys. Chem. C* **2013**, *117*, 8697−8707.
(357) Wu, G.; Mack, N. H.; Gao, W.; Ma, S.; Zhong, R.; Han, J.; Baldwin, J. K.; Zelenay, P. Nitrogen-Doped Graphene-Rich Catalysts Derived From Heteroatom Polymers for Oxygen Reduction in Nonaqueous Lithium−O_2 Battery Cathodes. *ACS Nano* **2012**, *6*, 9764−9776.
(358) Nallathambi, V.; Lee, J.-W.; Kumaraguru, S. P.; Wu, G.; Popov, B. N. Development of High Performance Carbon Composite Catalyst for Oxygen Reduction Reaction in PEM Proton Exchange Membrane Fuel Cells. *J. Power Sources* **2008**, *183*, 34−42.
(359) Matter, P. H.; Zhang, L.; Ozkan, U. S. The Role of Nanostructure in Nitrogen-Containing Carbon Catalysts for the Oxygen Reduction Reaction. *J. Catal.* **2006**, *239*, 83−96.
(360) Sahraie, N. R.; Kramm, U. I.; Steinberg, J.; Zhang, Y.; Thomas, A.; Reier, T.; Paraknowitsch, J.-P.; Strasser, P. Quantifying the

https://dx.doi.org/10.1021/acs.chemrev.0c00594
Chem. Rev. 2020, 120, 12217−12314

Density and Utilization of Active Sites in Non-Precious Metal Oxygen Electroreduction Catalysts. *Nat. Commun.* **2015**, *6*, 8618.
(361) Wu, G.; Zelenay, P. Nanostructured Non-Precious Metal Catalysts for Oxygen Reduction Reaction. *Acc. Chem. Res.* **2013**, *46*, 1878−1889.
(362) Weng, L. T.; Bertrand, P.; Lalande, G.; Dodelet, J. P. In *Characterization of Electrocatalysts for Oxygen Reduction by ToF SIMS*; Wiley, 1994; pp 442−445.
(363) Wu, G.; Nelson, M.; Ma, S.; Meng, H.; Cui, G.; Shen, P. K. Synthesis of Nitrogen-Doped Onion-Like Carbon and Its Use in Carbon-Based CoFe Binary Non-Precious-Metal Catalysts for Oxygen-Reduction. *Carbon* **2011**, *49*, 3972−3982.
(364) Lin, Z.; Chu, H.; Shen, Y.; Wei, L.; Liu, H.; Li, Y. Rational Preparation of Faceted Platinum Nanocrystals Supported on Carbon Nanotubes With Remarkably Enhanced Catalytic Performance. *Chem. Commun.* **2009**, 7167−7169.
(365) Li, Q.; Wu, L.; Wu, G.; Su, D.; Lv, H.; Zhang, S.; Zhu, W.; Casimir, A.; Zhu, H.; Mendoza-Garcia, A.; Sun, S. New Approach to Fully-Ordered fct-FePt Nanoparticles for Much Enhanced Electrocatalysis in Acid. *Nano Lett.* **2015**, *15*, 2468−2473.
(366) Zhao, D.; Shui, J.-L.; Grabstanowicz, L. R.; Chen, C.; Commet, S. M.; Xu, T.; Lu, J.; Liu, D.-J. Highly Efficient Non-Precious Metal Electrocatalysts Prepared from One-Pot Synthesized Zeolitic Imidazolate Frameworks. *Adv. Mater.* **2014**, *26*, 1093−1097.
(367) Wu, G.; Artyushkova, K.; Ferrandon, M.; Kropf, A. J.; Myers, D.; Zelenay, P. Performance Durability of Polyaniline-derived Non-precious Cathode Catalysts. *ECS Trans.* **2009**, *25*, 1299−1311.
(368) Wang, Y. C.; Lai, Y. J.; Song, L.; Zhou, Z. Y.; Liu, J. G.; Wang, Q.; Yang, X. D.; Chen, C.; Shi, W.; Zheng, Y. P.; Rauf, M.; Sun, S. G. S-Doping of an Fe/N/C ORR Catalyst for Polymer Electrolyte Membrane Fuel Cells with High Power Density. *Angew. Chem., Int. Ed.* **2015**, *54*, 9907−10.
(369) Wang, X.-J.; Zhang, H.; Lin, H.; Gupta, S.; Wang, C.; Tao, Z.; Fu, H.; Wang, T.; Zheng, J.; Wu, G.; Li, X. Directly Converting Fe-Doped Metal-Organic Frameworks Into Highly Active and Stable Fe-N-C Catalysts for Oxygen Reduction in Acid. *Nano Energy* **2016**, *25*, 110−119.
(370) Serov, A.; Artyushkova, K.; Niangar, E.; Wang, C.; Dale, N.; Jaouen, F.; Sougrati, M.-T.; Jia, Q.; Mukerjee, S.; Atanassov, P. Nano-Structured Non-Platinum Catalysts for Automotive Fuel Cell Application. *Nano Energy* **2015**, *16*, 293−300.
(371) Zhu, Y.; Sokolowski, J.; Song, X.; He, Y.; Mei, Y.; Wu, G. Engineering Local Coordination Environments of Atomically Dispersed and Heteroatom-Coordinated Single Metal Site Electrocatalysts for Clean Energy-Conversion. *Adv. Energy Mater.* **2020**, *10*, 1902844.
(372) Holby, E. F.; Zelenay, P. Linking Structure to Function: The Search for Active Sites in Non-Platinum Group Metal Oxygen Reduction Reaction Catalysts. *Nano Energy* **2016**, *29*, 54−64.
(373) Liu, K.; Wu, G.; Wang, G. Role of Local Carbon Structure Surrounding FeN4 Sites in Boosting Catalytic Activity for Oxygen Reduction. *J. Phys. Chem. C* **2017**, *121*, 11319−11324.
(374) Liu, K.; Lei, Y.; Wang, G. Correlation Between Oxygen Adsorption Energy and Electronic Structure of Transition Metal Macrocyclic Complexes. *J. Chem. Phys.* **2013**, *139*, 204306.
(375) Liu, K.; Kattel, S.; Mao, V.; Wang, G. Electrochemical and Computational Study of Oxygen Reduction Reaction on Nonprecious Transition Metal/Nitrogen Doped Carbon Nanofibers in Acid Medium. *J. Phys. Chem. C* **2016**, *120*, 1586−1596.
(376) Liu, K.; Qiao, Z.; Hwang, S.; Liu, Z.; Zhang, H.; Su, D.; Xu, H.; Wu, G.; Wang, G. Mn- and N- Doped Carbon as Promising Catalysts for Oxygen Reduction Reaction: Theoretical Prediction and Experimental Validation. *Appl. Catal., B* **2019**, *243*, 195−203.
(377) Wu, G.; Johnston, C. M.; Mack, N. H.; Artyushkova, K.; Ferrandon, M.; Nelson, M.; Lezama-Pacheco, J. S.; Conradson, S. D.; More, K. L.; Myers, D. J.; Zelenay, P. Synthesis−Structure−Performance Correlation for Polyaniline−Me−C Non-Precious Metal Cathode Catalysts for Oxygen Reduction in Fuel Cells. *J. Mater. Chem.* **2011**, *21*, 11392−11405.
(378) Li, J.; Zhang, H.; Samarakoon, W.; Shan, W.; Cullen, D. A.; Karakalos, S.; Chen, M.; Gu, D.; More, K. L.; Wang, G.; Feng, Z.; Wang, Z.; Wu, G. Thermally Driven Structure and Performance Evolution of Atomically Dispersed FeN_4 Sites for Oxygen Reduction. *Angew. Chem., Int. Ed.* **2019**, *58*, 18971.
(379) Shao, Y.; Dodelet, J.-P.; Wu, G.; Zelenay, P. PGM-Free Cathode Catalysts for PEM Fuel Cells: A Mini-Review on Stability Challenges. *Adv. Mater.* **2019**, *31*, 1807615.
(380) von Deak, D.; Biddinger, E. J.; Ozkan, U. S. Carbon Corrosion Characteristics of CN_x Nanostructures in Acidic Media and Implications for ORR Performance. *J. Appl. Electrochem.* **2011**, *41*, 757−763.
(381) Lee, J. S.; Kim, S. T.; Cao, R.; Choi, N. S.; Liu, M.; Lee, K. T.; Cho, J. Metal-Air Batteries With High Energy Density: Li-Air Versus Zn-Air. *Adv. Energy Mater.* **2011**, *1*, 34−50.
(382) Martinez, U.; Komini Babu, S.; Holby, E. F.; Zelenay, P. Durability challenges and perspective in the development of PGM-free electrocatalysts for the oxygen reduction reaction. *Curr. Opin. Electrochem.* **2018**, *9*, 224−232.
(383) Zhang, B. W.; Wang, Y. X.; Chou, S. L.; Liu, H. K.; Dou, S. X. Fabrication of Superior Single-Atom Catalysts toward Diverse Electrochemical Reactions. *Small Methods* **2019**, *3*, 1800497.
(384) Zhang, H.; Liu, G.; Shi, L.; Ye, J. Single-Atom Catalysts: Emerging Multifunctional Materials in Heterogeneous Catalysis. *Adv. Energy Mater.* **2018**, *8*, 1701343.
(385) Cheng, N.; Zhang, L.; Doyle-Davis, K.; Sun, X. Single-Atom Catalysts: From Design to Application. *Electrochem. Energy Rev.* **2019**, *2*, 539−573.
(386) Scofield, M. E.; Liu, H.; Wong, S. S. A Concise Guide to Sustainable PEMFCS: Recent Advances in Improving Both Oxygen Reduction Catalysts and Proton Exchange Membranes. *Chem. Soc. Rev.* **2015**, *44*, 5836−5860.
(387) Dombrovskis, J. K.; Palmqvist, A. E. C. Recent Progress in Synthesis, Characterization and Evaluation of Non-Precious Metal Catalysts for the Oxygen Reduction Reaction. *Fuel Cells* **2016**, *16*, 4−22.
(388) Yang, L.; Cheng, D.; Xu, H.; Zeng, X.; Wan, X.; Shui, J.; Xiang, Z.; Cao, D. Unveiling the High-Activity Origin of Single-Atom Iron Catalysts for Oxygen Reduction Reaction. *Proc. Natl. Acad. Sci. U. S. A.* **2018**, *115*, 6626−6631.
(389) Uddin, A.; Dunsmore, L.; Zhang, H.; Hu, L.; Wu, G.; Litster, S. High Power Density PGM-Free Cathodes for Polymer Electrolyte Fuel Cells. *ACS Appl. Mater. Interfaces* **2020**, *12*, 2216.
(390) Wang, J.; Huang, Z.; Liu, W.; Chang, C.; Tang, H.; Li, Z.; Chen, W.; Jia, C.; Yao, T.; Wei, S.; Wu, Y.; Li, Y. Design of N-Coordinated Dual-Metal Sites: A Stable and Active Pt-Free Catalyst for Acidic Oxygen Reduction Reaction. *J. Am. Chem. Soc.* **2017**, *139*, 17281−17284.
(391) Palaniselvam, T.; Kashyap, V.; Bhange, S. N.; Baek, J. B.; Kurungot, S. Nanoporous Graphene Enriched With Fe/Co-N Active Sites as a Promising Oxygen Reduction Electrocatalyst for Anion Exchange Membrane Fuel Cells. *Adv. Funct. Mater.* **2016**, *26*, 2150−2162.
(392) Wang, X. X.; Cullen, D. A.; Pan, Y. T.; Hwang, S.; Wang, M.; Feng, Z.; Wang, J.; Engelhard, M. H.; Zhang, H.; He, Y.; et al. Nitrogen-Coordinated Single Cobalt Atom Catalysts for Oxygen Reduction in Proton Exchange Membrane Fuel Cells. *Adv. Mater.* **2018**, *30*, 1706758.
(393) Li, Q.; Wang, T.; Havas, D.; Zhang, H.; Xu, P.; Han, J.; Cho, J.; Wu, G. High-Performance Direct Methanol Fuel Cells with Precious-Metal-Free Cathode. *Advanced Science* **2016**, *3*, 1600140.
(394) Osmieri, L.; Escudero-Cid, R.; MOnteverde Videla, A. H.; Ocón, P.; Specchia, S. Application of a Non-Noble Fe-NC Catalyst for Oxygen Reduction Reaction in an Alkaline Direct Ethanol Fuel Cell. *Renewable Energy* **2018**, *115*, 226−237.
(395) Sebastián, D.; Serov, A.; Artyushkova, K.; Gordon, J.; Atanassov, P.; Aricò, A. S.; Baglio, V. High Performance and Cost-Effective Direct Methanol Fuel Cells: Fe-N-C Methanol-Tolerant

https://dx.doi.org/10.1021/acs.chemrev.0c00594
Chem. Rev. 2020, 120, 12217−12314

Oxygen Reduction Reaction Catalysts. *ChemSusChem* **2016**, *9*, 1986−1995.
(396) Gu, L.; Jiang, L.; Li, X.; Jin, J.; Wang, J.; Sun, G. A Fe-NC Catalyst With Highly Dispersed Iron in Carbon for Oxygen Reduction Reaction and Its Application in Direct Methanol Fuel Cells. *Chin. J. Catal.* **2016**, *37*, 539−548.
(397) Sebastian, D.; Serov, A.; Matanovic, I.; Artyushkova, K.; Atanassov, P.; Aricò, A. S.; Baglio, V. Insights on the Extraordinary Tolerance to Alcohols of Fe-Nc Cathode Catalysts in Highly Performing Direct Alcohol Fuel Cells. *Nano Energy* **2017**, *34*, 195−204.
(398) Lo Vecchio, C.; Sebastián, D.; Lázaro, M. J.; Aricò, A. S.; Baglio, V. Methanol-Tolerant M−N−C Catalysts for Oxygen Reduction Reactions in Acidic Media and Their Application in Direct Methanol Fuel Cells. *Catalysts* **2018**, *8*, 650.
(399) Osmieri, L.; Escudero-Cid, R.; Armandi, M.; Ocón, P.; Monteverde Videla, A. H.; Specchia, S. Effects of Using Two Transition Metals in the Synthesis of Non-Noble Electrocatalysts for Oxygen Reduction Reaction in Direct Methanol Fuel Cell. *Electrochim. Acta* **2018**, *266*, 220−232.
(400) Yang, L.; Larouche, N.; Chenitz, R.; Zhang, G.; Lefèvre, M.; Dodelet, J.-P. Activity, Performance, and Durability for the Reduction of Oxygen in PEM Fuel Cells, of Fe/N/C electrocatalysts Obtained from the Pyrolysis of Metal-Organic-Framework and Iron Porphyrin Precursors. *Electrochim. Acta* **2015**, *159*, 184−197.
(401) Zhang, G.; Chenitz, R.; Lefèvre, M.; Sun, S.; Dodelet, J.-P. Is IRON Involved in the Lack of Stability of Fe/N/C Electrocatalysts Used to Reduce Oxygen at the Cathode of PEM Fuel Cells? *Nano Energy* **2016**, *29*, 111−125.
(402) Setzler, B. P.; Zhuang, Z.; Wittkopf, J. A.; Yan, Y. Activity Targets for Nanostructured Platinum-Group-Metal-Free Catalysts in Hydroxide Exchange Membrane Fuel Cells. *Nat. Nanotechnol.* **2016**, *11*, 1020−1025.
(403) Ratso, S.; Kruusenberg, I.; Käärik, M.; Kook, M.; Puust, L.; Saar, R.; Leis, J.; Tammeveski, K. Highly Efficient Transition Metal and Nitrogen Co-Doped Carbide-Derived Carbon Electrocatalysts for Anion Exchange Membrane Fuel Cells. *J. Power Sources* **2018**, *375*, 233−243.
(404) Adabi Firouzjaie, H.; Mustain, W. E. Catalytic Advantages, Challenges and Priorities in Alkaline Membrane Fuel Cells. *ACS Catal.* **2020**, *10*, 225−234.
(405) Omasta, T. J.; Park, A. M.; LaManna, J. M.; Zhang, Y.; Peng, X.; Wang, L.; Jacobson, D. L.; Varcoe, J. R.; Hussey, D. S.; Pivovar, B. S.; Mustain, W. E. Beyond Catalysis and Membranes: Visualizing and Solving the Challenge of Electrode Water Accumulation and Flooding in AEMFCs. *Energy Environ. Sci.* **2018**, *11*, 551−558.
(406) Cheng, F.; Chen, J. Metal−Air Batteries: From Oxygen Reduction Electrochemistry to Cathode Catalysts. *Chem. Soc. Rev.* **2012**, *41*, 2172−2192.
(407) Pan, J.; Xu, Y. Y.; Yang, H.; Dong, Z.; Liu, H.; Xia, B. Y. Advanced Architectures and Relatives of Air Electrodes in Zn−Air Batteries. *Advanced Science* **2018**, *5*, 1700691.
(408) Zheng, X.; Wu, J.; Cao, X.; Abbott, J.; Jin, C.; Wang, H.; Strasser, P.; Yang, R.; Chen, X.; Wu, G. N-, P-, and S-Doped Graphene-Like Carbon Catalysts Derived From Onium Salts With Enhanced Oxygen Chemisorption for Zn-Air Battery Cathodes. *Appl. Catal., B* **2019**, *241*, 442−451.
(409) Wang, Y.; Yu, B.; Liu, K.; Yang, X.; Liu, M.; Chan, T.-s.; Qiu, X.; Li, J.; Li, W. Co Single-Atoms on Ultrathin N-Doped Porous Carbon by Biomass Complexation Strategy for High Performance Metal-Air Batteries. *J. Mater. Chem. A* **2020**, *8*, 2131−2139.
(410) Shen, H.; Thomas, T.; Rasaki, S. A.; Saad, A.; Hu, C.; Wang, J.; Yang, M. Oxygen Reduction Reactions of Fe-N-C Catalysts: Current Status and the Way Forward. *Electrochem. Energy Rev.* **2019**, *2*, 252−276.
(411) Yang, Z. K.; Yuan, C.-Z.; Xu, A.-W. Confined Pyrolysis within a Nanochannel to Form a Highly Efficient Single Iron Site Catalyst for Zn−Air Batteries. *ACS Energy Lett.* **2018**, *3*, 2383−2389.
(412) Li, S.; Cheng, C.; Zhao, X.; Schmidt, J.; Thomas, A. Active Salt/Silica-Templated 2D Mesoporous FeCo-Nx-Carbon as Bifunctional Oxygen Electrodes for Zinc−Air Batteries. *Angew. Chem., Int. Ed.* **2018**, *57*, 1856−1862.
(413) Gabardo, C. M.; O'Brien, C. P.; Edwards, J. P.; McCallum, C.; Xu, Y.; Dinh, C.-T.; Li, J.; Sargent, E. H.; Sinton, D. Continuous Carbon Dioxide Electroreduction to Concentrated Multi-carbon Products Using a Membrane Electrode Assembly. *Joule* **2019**, *3*, 2777−2791.
(414) Ma, L.; Chen, S.; Pei, Z.; Huang, Y.; Liang, G.; Mo, F.; Yang, Q.; Su, J.; Gao, Y.; Zapien, J. A.; Zhi, C. Single-Site Active Iron-Based Bifunctional Oxygen Catalyst for a Compressible and Rechargeable Zinc−Air Battery. *ACS Nano* **2018**, *12*, 1949−1958.
(415) Olah, G. A.; Prakash, G. K. S.; Goeppert, A. Anthropogenic Chemical Carbon Cycle for a Sustainable Future. *J. Am. Chem. Soc.* **2011**, *133*, 12881−12898.
(416) De Luna, P.; Hahn, C.; Higgins, D.; Jaffer, S. A.; Jaramillo, T. F.; Sargent, E. H. What Would It Take for Renewably Powered Electrosynthesis to Displace Petrochemical Processes? *Science* **2019**, *364*, No. eaav3506.
(417) Hori, Y.; Wakebe, H.; Tsukamoto, T.; Koga, O. Electrocatalytic Process of CO Selectivity in Electrochemical Reduction of CO2 at Metal Electrodes in Aqueous Media. *Electrochim. Acta* **1994**, *39*, 1833−1839.
(418) Kuhl, K. P.; Cave, E. R.; Abram, D. N.; Jaramillo, T. F. New Insights into the Electrochemical Reduction of Carbon Dioxide on Metallic Copper Surfaces. *Energy Environ. Sci.* **2012**, *5*, 7050−7059.
(419) Zhu, W.; Michalsky, R.; Metin, O. n.; Lv, H.; Guo, S.; Wright, C. J.; Sun, X.; Peterson, A. A.; Sun, S. Monodisperse Au Nanoparticles for Selective Electrocatalytic Reduction of CO_2 to CO. *J. Am. Chem. Soc.* **2013**, *135*, 16833−16836.
(420) Lu, Q.; Rosen, J.; Zhou, Y.; Hutchings, G. S.; Kimmel, Y. C.; Chen, J. G.; Jiao, F. A Selective and Efficient Electrocatalyst for Carbon Dioxide Reduction. *Nat. Commun.* **2014**, *5*, 3242.
(421) Liu, M.; Pang, Y.; Zhang, B.; De Luna, P.; Voznyy, O.; Xu, J.; Zheng, X.; Dinh, C. T.; Fan, F.; Cao, C.; et al. Enhanced Electrocatalytic CO_2 Reduction via Field-induced Reagent Concentration. *Nature* **2016**, *537*, 382−386.
(422) Hall, A. S.; Yoon, Y.; Wuttig, A.; Surendranath, Y. Mesostructure-Induced Selectivity in CO_2 Reduction Catalysis. *J. Am. Chem. Soc.* **2015**, *137*, 14834−14837.
(423) Kwok, K. S.; Wang, Y.; Cao, M. C.; Shen, H.; He, Z.; Poirier, G.; McCandless, B. E.; Livi, K. J.; Muller, D. A.; Wang, C.; Gracias, D. H. Nano-folded Gold Catalysts for Electroreduction of Carbon Dioxide. *Nano Lett.* **2019**, *19*, 9154−9159.
(424) Schouten, K.; Kwon, Y.; Van der Ham, C.; Qin, Z.; Koper, M. A New Mechanism for the Selectivity to C_1 and C_2 Species in the Electrochemical Reduction of Carbon Dioxide on Copper Electrodes. *Chem. Sci.* **2011**, *2*, 1902−1909.
(425) Reske, R.; Mistry, H.; Behafarid, F.; Roldan Cuenya, B.; Strasser, P. Particle Size Effects in the Catalytic Electroreduction of CO_2 on Cu Nanoparticles. *J. Am. Chem. Soc.* **2014**, *136*, 6978−6986.
(426) Thiel, G. P.; Kumar, A.; Gómez-González, A.; Lienhard, J. H. Utilization of Desalination Brine for Sodium Hydroxide Production: Technologies, Engineering Principles, Recovery Limits, and Future Directions. *ACS Sustainable Chem. Eng.* **2017**, *5*, 11147−11162.
(427) Luc, W.; Fu, X.; Shi, J.; Lv, J.-J.; Jouny, M.; Ko, B. H.; Xu, Y.; Tu, Q.; Hu, X.; Wu, J.; et al. Two-dimensional Copper Nanosheets for Electrochemical Reduction of Carbon Monoxide to Acetate. *Nat. Catal.* **2019**, *2*, 423−430.
(428) Gao, L.; Li, X.; Yao, Z.; Bai, H.; Lu, Y.; Ma, C.; Lu, S.; Peng, Z.; Yang, J.; Pan, A.; Huang, H. Unconventional p-d Hybridization Interaction in PtGa Ultrathin Nanowires Boosts Oxygen Reduction Electrocatalysis. *J. Am. Chem. Soc.* **2019**, *141*, 18083−18090.
(429) Hori, Y.; Murata, A.; Takahashi, R. Formation of Hydrocarbons in the Electrochemical Reduction of Carbon-Dioxide at a Copper Electrode in Aqueous-Solution. *J. Chem. Soc., Faraday Trans. 1* **1989**, *85*, 2309−2326.

https://dx.doi.org/10.1021/acs.chemrev.0c00594
Chem. Rev. 2020, 120, 12217−12314

(430) Chen, Y.; Li, C. W.; Kanan, M. W. Aqueous CO_2 Reduction at Very Low Overpotential on Oxide-Derived Au Nanoparticles. *J. Am. Chem. Soc.* **2012**, *134*, 19969−19972.
(431) Liu, X.; Schlexer, P.; Xiao, J.; Ji, Y.; Wang, L.; Sandberg, R. B.; Tang, M.; Brown, K. S.; Peng, H.; Ringe, S.; et al. pH Effects on the Electrochemical Reduction of $CO_{(2)}$ towards C_2 Products on Stepped Copper. *Nat. Commun.* **2019**, *10*, 32.
(432) Schouten, K. J. P.; Qin, Z.; Pérez Gallent, E.; Koper, M. T. M. Two Pathways for the Formation of Ethylene in CO Reduction on Single-Crystal Copper Electrodes. *J. Am. Chem. Soc.* **2012**, *134*, 9864−9867.
(433) Calle-Vallejo, F.; Koper, M. T. M. Theoretical Considerations on the Electroreduction of CO to C_2 Species on Cu(100) Electrodes. *Angew. Chem., Int. Ed.* **2013**, *52*, 7282−7285.
(434) Weng, L.-C.; Bell, A. T.; Weber, A. Z. Modeling gas-diffusion electrodes for CO_2 reduction. *Phys. Chem. Chem. Phys.* **2018**, *20*, 16973−16984.
(435) Sung, S.; Kumar, D.; Gil-Sepulcre, M.; Nippe, M. Electrocatalytic CO_2 Reduction by Imidazolium-functionalized Molecular Catalysts. *J. Am. Chem. Soc.* **2017**, *139*, 13993−13996.
(436) Johnson, B. A.; Maji, S.; Agarwala, H.; White, T. A.; Mijangos, E.; Ott, S. Activating a Low Overpotential CO_2 Reduction Mechanism by a Strategic Ligand Modification on a Ruthenium Polypyridyl Catalyst. *Angew. Chem., Int. Ed.* **2016**, *55*, 1825−1829.
(437) Rosser, T. E.; Windle, C. D.; Reisner, E. Electrocatalytic and Solar-Driven CO_2 Reduction to CO with a Molecular Manganese Catalyst Immobilized on Mesoporous TiO_2. *Angew. Chem., Int. Ed.* **2016**, *55*, 7388−7392.
(438) Sun, Y.; Bigi, J. P.; Piro, N. A.; Tang, M. L.; Long, J. R.; Chang, C. J. Molecular Cobalt Pentapyridine Catalysts for Generating Hydrogen from Water. *J. Am. Chem. Soc.* **2011**, *133*, 9212−9215.
(439) Barlow, J. M.; Yang, J. Y. Thermodynamic Considerations for Optimizing Selective CO_2 Reduction by Molecular Catalysts. *ACS Cent. Sci.* **2019**, *5*, 580−588.
(440) Fleischer, E. B.; Palmer, J. M.; Srivastava, T.; Chatterjee, A. Thermodyamic and Kinetic Properties of an Iron-porphyrin System. *J. Am. Chem. Soc.* **1971**, *93*, 3162−3167.
(441) Dhanasekaran, T.; Grodkowski, J.; Neta, P.; Hambright, P.; Fujita, E. p-Terphenyl-sensitized Photoreduction of CO_2 with Cobalt and Iron Porphyrins. Interaction Between CO and Reduced Metalloporphyrins. *J. Phys. Chem. A* **1999**, *103*, 7742−7748.
(442) Takahashi, K.; Hiratsuka, K.; Sasaki, H.; Toshima, S. Electrocatalytic Behavior of Metal Porphyrins in the Reduction of Carbon Dioxide. *Chem. Lett.* **1979**, *8*, 305−308.
(443) Shen, J.; Kolb, M. J.; Gottle, A. J.; Koper, M. T. DFT Study on the Mechanism of the Electrochemical Reduction of CO_2 Catalyzed by Cobalt Porphyrins. *J. Phys. Chem. C* **2016**, *120*, 15714−15721.
(444) Hu, X. M.; Rønne, M. H.; Pedersen, S. U.; Skrydstrup, T.; Daasbjerg, K. Enhanced Catalytic Activity of Cobalt Porphyrin in CO_2 Electroreduction upon Immobilization on Carbon Materials. *Angew. Chem., Int. Ed.* **2017**, *56*, 6468−6472.
(445) Li, J.; Wang, Z.; McCallum, C.; Xu, Y.; Li, F.; Wang, Y.; Gabardo, C. M.; Dinh, C.-T.; Zhuang, T.-T.; Wang, L.; et al. Constraining CO Coverage on Copper Promotes High-efficiency Ethylene Electroproduction. *Nat. Catal.* **2019**, *2*, 1124−1131.
(446) Zhu, G.; Li, Y.; Zhu, H.; Su, H.; Chan, S. H.; Sun, Q. Curvature-dependent Selectivity of CO_2 Electrocatalytic Reduction on Cobalt Porphyrin Nanotubes. *ACS Catal.* **2016**, *6*, 6294−6301.
(447) Shen, J.; Kortlever, R.; Kas, R.; Birdja, Y. Y.; Diaz-Morales, O.; Kwon, Y.; Ledezma-Yanez, I.; Schouten, K. J. P.; Mul, G.; Koper, M. T. Electrocatalytic Reduction of Carbon Dioxide to Carbon Monoxide and Methane at an Immobilized Cobalt Protoporphyrin. *Nat. Commun.* **2015**, *6*, 8177.
(448) Diercks, C. S.; Lin, S.; Kornienko, N.; Kapustin, E. A.; Nichols, E. M.; Zhu, C.; Zhao, Y.; Chang, C. J.; Yaghi, O. M. Reticular Electronic Tuning of Porphyrin Active Sites in Covalent Organic Frameworks for Electrocatalytic Carbon Dioxide Reduction. *J. Am. Chem. Soc.* **2018**, *140*, 1116−1122.
(449) Azcarate, I.; Costentin, C.; Robert, M.; Savéant, J.-M. Through-space Charge Interaction Substituent Effects in Molecular Catalysis Leading to the Design of the Most Efficient Catalyst of CO_2-to-CO Electrochemical Conversion. *J. Am. Chem. Soc.* **2016**, *138*, 16639−16644.
(450) Mondal, B.; Sen, P.; Rana, A.; Saha, D.; Das, P.; Dey, A. Reduction of CO_2 to CO by an Iron Porphyrin Catalyst in the Presence of Oxygen. *ACS Catal.* **2019**, *9*, 3895−3899.
(451) Li, Y. C.; Lee, G.; Yuan, T.; Wang, Y.; Nam, D.-H.; Wang, Z.; García de Arquer, F. P.; Lum, Y.; Dinh, C.-T.; Voznyy, O.; Sargent, E. H. CO_2 Electroreduction from Carbonate Electrolyte. *ACS Energy Lett.* **2019**, *4*, 1427−1431.
(452) Xu, Y.; Edwards, J. P.; Zhong, J.; O'Brien, C.; Gabardo, C. M.; McCallum, C.; Li, J.; Dinh, T. C.; Sargent, E. H.; Sinton, D. Oxygen-tolerant Electroproduction of C_2 Products from Simulated Flue Gas. *Energy Environ. Sci.* **2020**, *13*, 554−561.
(453) Cao, R.; Thapa, R.; Kim, H.; Xu, X.; Kim, M. G.; Li, Q.; Park, N.; Liu, M.; Cho, J. Promotion of Oxygen Reduction by a Bio-inspired Tethered Iron Phthalocyanine Carbon Nanotube-based Catalyst. *Nat. Commun.* **2013**, *4*, 2076.
(454) Hiratsuka, K.; Takahashi, K.; Sasaki, H.; Toshima, S. Electrocatalytic Behavior of Tetrasulfonated Metal Phthalocyanines in the Reduction of Carbon Dioxide. *Chem. Lett.* **1977**, *6*, 1137−1140.
(455) Lieber, C. M.; Lewis, N. S. Catalytic Reduction of Carbon Dioxide at Carbon Electrodes Modified with Cobalt Phthalocyanine. *J. Am. Chem. Soc.* **1984**, *106*, 5033−5034.
(456) Li, J.; Wang, Z.; McCallum, C.; Xu, Y.; Li, F.; Wang, Y.; Gabardo, C. M.; Dinh, C.-T.; Zhuang, T.-T.; Wang, L.; Howe, J. Y.; Ren, Y.; Sargent, E. H.; Sinton, D. Constraining CO coverage on copper promotes high-efficiency ethylene electroproduction. *Nat. Catal.* **2019**, *2*, 1124−1131.
(457) Morlanés, N.; Takanabe, K.; Rodionov, V. Simultaneous Reduction of CO_2 and Splitting of H_2O by a Single Immobilized Cobalt Phthalocyanine Electrocatalyst. *ACS Catal.* **2016**, *6*, 3092−3095.
(458) Han, N.; Wang, Y.; Ma, L.; Wen, J.; Li, J.; Zheng, H.; Nie, K.; Wang, X.; Zhao, F.; Li, Y.; et al. Supported Cobalt Polyphthalocyanine for High-performance Electrocatalytic CO_2 Reduction. *Chem* **2017**, *3*, 652−664.
(459) Boutin, E.; Wang, M.; Lin, J. C.; Mesnage, M.; Mendoza, D.; Lassalle-Kaiser, B.; Hahn, C.; Jaramillo, T. F.; Robert, M. Aqueous Electrochemical Reduction of Carbon Dioxide and Carbon Monoxide into Methanol with Cobalt Phthalocyanine. *Angew. Chem., Int. Ed.* **2019**, *58*, 16172−16176.
(460) Reuillard, B.; Ly, K. H.; Rosser, T. E.; Kuehnel, M. F.; Zebger, I.; Reisner, E. Tuning Product Selectivity for Aqueous CO_2 Reduction with a Mn (bipyridine)-pyrene Catalyst Immobilized on a Carbon Nanotube Electrode. *J. Am. Chem. Soc.* **2017**, *139*, 14425−14435.
(461) Hori, Y.; Kikuchi, K.; Suzuki, S. Production of CO and CH_4 in Electrochemical Reduction of CO_2 at Metal-Electrodes in Aqueous Hydrogencarbonate Solution. *Chem. Lett.* **1985**, *14*, 1695−1698.
(462) Hori, Y. i., Electrochemical CO_2 Reduction on Metal Electrodes. In *Modern Aspects of Electrochemistry*; Springer, 2008; pp 89−189.
(463) Varela, A. S.; Ranjbar Sahraie, N.; Steinberg, J.; Ju, W.; Oh, H. S.; Strasser, P. Metal-Doped Nitrogenated Carbon as an Efficient Catalyst for Direct CO_2 Electroreduction to CO and Hydrocarbons. *Angew. Chem., Int. Ed.* **2015**, *54*, 10758−10762.
(464) Huan, T. N.; Ranjbar, N.; Rousse, G.; Sougrati, M.; Zitolo, A.; Mougel, V.; Jaouen, F.; Fontecave, M. Electrochemical Reduction of CO_2 Catalyzed by Fe-N-C Materials: A Structure−Selectivity Study. *ACS Catal.* **2017**, *7*, 1520−1525.
(465) Zhang, Z.; Ma, C.; Tu, Y.; Si, R.; Wei, J.; Zhang, S.; Wang, Z.; Li, J.-F.; Wang, Y.; Deng, D. Multiscale Carbon Foam Confining Single Iron Atoms for Efficient Electrocatalytic CO_2 Reduction to CO. *Nano Res.* **2019**, *12*, 2313−2317.
(466) Varela, A. S.; Ju, W.; Bagger, A.; Franco, P.; Rossmeisl, J.; Strasser, P. Electrochemical Reduction of CO_2 on Metal-Nitrogen-Doped Carbon Catalysts. *ACS Catal.* **2019**, *9*, 7270−7284.

https://dx.doi.org/10.1021/acs.chemrev.0c00594
Chem. Rev. 2020, 120, 12217−12314

(467) Leonard, N.; Ju, W.; Sinev, I.; Steinberg, J.; Luo, F.; Varela, A. S.; Roldan Cuenya, B.; Strasser, P. The Chemical Identity, State and Structure of Catalytically Active Centers during the Electrochemical CO_2 Reduction on Porous Fe−nitrogen−carbon (Fe−N−C) Materials. *Chem. Sci.* **2018**, *9*, 5064−5073.
(468) Ju, W.; Bagger, A.; Wang, X.; Tsai, Y.; Luo, F.; Möller, T.; Wang, H.; Rossmeisl, J.; Varela, A. S.; Strasser, P. Unraveling Mechanistic Reaction Pathways of the Electrochemical CO_2 Reduction on Fe−N−C Single-Site Catalysts. *ACS Energy Lett.* **2019**, *4*, 1663−1671.
(469) Kornienko, N.; Zhao, Y.; Kley, C. S.; Zhu, C.; Kim, D.; Lin, S.; Chang, C. J.; Yaghi, O. M.; Yang, P. Metal−organic Frameworks for Electrocatalytic Reduction of Carbon Dioxide. *J. Am. Chem. Soc.* **2015**, *137*, 14129−14135.
(470) Zhou, Y.; Che, F.; Liu, M.; Zou, C.; Liang, Z.; De Luna, P.; Yuan, H.; Li, J.; Wang, Z.; Xie, H.; Li, H.; Chen, P.; Bladt, E.; Quintero-Bermudez, R.; Sham, T. K.; Bals, S.; Hofkens, J.; Sinton, D.; Chen, G.; Sargent, E. H. Dopant-induced electron localization drives CO2 reduction to C2 hydrocarbons. *Nat. Chem.* **2018**, *10*, 974−980.
(471) Di, J.; Chen, C.; Yang, S.-Z.; Chen, S.; Duan, M.; Xiong, J.; Zhu, C.; Long, R.; Hao, W.; Chi, Z.; et al. Isolated Single Atom Cobalt in Bi_3O_4Br Atomic Layers to Trigger Efficient CO_2 Photoreduction. *Nat. Commun.* **2019**, *10*, 2840.
(472) Zheng, T.; Jiang, K.; Wang, H. Recent Advances in Electrochemical CO_2-to-CO Conversion on Heterogeneous Catalysts. *Adv. Mater.* **2018**, *30*, 1802066.
(473) Hu, X.-M.; Hval, H. H.; Bjerglund, E. T.; Dalgaard, K. J.; Madsen, M. R.; Pohl, M.-M.; Welter, E.; Lamagni, P.; Buhl, K. B.; Bremholm, M.; et al. Selective CO_2 Reduction to CO in Water using Earth-abundant Metal and Nitrogen-doped Carbon Electrocatalysts. *ACS Catal.* **2018**, *8*, 6255−6264.
(474) Zhang, Z.; Xiao, J.; Chen, X. J.; Yu, S.; Yu, L.; Si, R.; Wang, Y.; Wang, S.; Meng, X.; Wang, Y.; Tian, Z. Q.; Deng, D. Reaction Mechanisms of Well-Defined Metal−N_4 Sites in Electrocatalytic CO_2 Reduction. *Angew. Chem., Int. Ed.* **2018**, *57*, 16339−16342.
(475) Guo, Z.; Cheng, S.; Cometto, C.; Anxolabéhère-Mallart, E.; Ng, S.-M.; Ko, C.-C.; Liu, G.; Chen, L.; Robert, M.; Lau, T.-C. Highly Efficient and Selective Photocatalytic CO_2 Reduction by Iron and Cobalt Quaterpyridine Complexes. *J. Am. Chem. Soc.* **2016**, *138*, 9413−9416.
(476) Wang, X.; Chen, Z.; Zhao, X.; Yao, T.; Chen, W.; You, R.; Zhao, C.; Wu, G.; Wang, J.; Huang, W.; et al. Regulation of Coordination Number over Single Co Sites: Triggering the Efficient Electroreduction of CO_2. *Angew. Chem., Int. Ed.* **2018**, *57*, 1944−1948.
(477) Pan, Y.; Lin, R.; Chen, Y.; Liu, S.; Zhu, W.; Cao, X.; Chen, W.; Wu, K.; Cheong, W.-C.; Wang, Y.; et al. Design of Single-atom Co−N_5 Catalytic Site: A Robust Electrocatalyst for CO_2 Reduction with Nearly 100% CO Selectivity and Remarkable Stability. *J. Am. Chem. Soc.* **2018**, *140*, 4218−4221.
(478) Han, J.; An, P.; Liu, S.; Zhang, X.; Wang, D.; Yuan, Y.; Guo, J.; Qiu, X.; Hou, K.; Shi, L.; Zhang, Y.; Zhao, S.; Long, C.; Tang, Z. Reordering d Orbital Energies of Single-Site Catalysts for CO2 Electroreduction. *Angew. Chem., Int. Ed.* **2019**, *58*, 12711−12716.
(479) Gong, M.; Wang, D.-Y.; Chen, C.-C.; Hwang, B.-J.; Dai, H. A Mini Review on Nickel-based Electrocatalysts for Alkaline Hydrogen Evolution Reaction. *Nano Res.* **2016**, *9*, 28−46.
(480) Mou, K.; Chen, Z.; Zhang, X.; Jiao, M.; Zhang, X.; Ge, X.; Zhang, W.; Liu, L. Highly Efficient Electroreduction of CO_2 on Nickel Single-Atom Catalysts: Atom Trapping and Nitrogen Anchoring. *Small* **2019**, *15*, 1903668.
(481) Li, X.; Bi, W.; Chen, M.; Sun, Y.; Ju, H.; Yan, W.; Zhu, J.; Wu, X.; Chu, W.; Wu, C.; Xie, Y. Exclusive Ni−N4 Sites Realize Near-unity CO Selectivity for Electrochemical CO_2 Reduction. *J. Am. Chem. Soc.* **2017**, *139*, 14889−14892.
(482) Song, Y.; Johnson, D.; Peng, R.; Hensley, D. K.; Bonnesen, P. V.; Liang, L.; Huang, J.; Yang, F.; Zhang, F.; Qiao, R.; et al. A Physical Catalyst for the Electrolysis of Nitrogen to Ammonia. *Sci. Adv.* **2018**, *4*, No. e1700336.
(483) Su, P.; Iwase, K.; Harada, T.; Kamiya, K.; Nakanishi, S. Covalent Triazine Framework Modified With Coordinatively-Unsaturated Co or Ni Atoms for CO_2 Electrochemical Reduction. *Chem. Sci.* **2018**, *9*, 3941−3947.
(484) Burdyny, T.; Smith, W. A. CO_2 reduction on gas-diffusion electrodes and why catalytic performance must be assessed at commercially-relevant conditions. *Energy Environ. Sci.* **2019**, *12*, 1442−1453.
(485) Cheng, T.; Xiao, H.; Goddard, W. A. Nature of the Active Sites for CO Reduction on Copper Nanoparticles; Suggestions for Optimizing Performance. *J. Am. Chem. Soc.* **2017**, *139*, 11642−11645.
(486) Jiao, Y.; Zheng, Y.; Chen, P.; Jaroniec, M.; Qiao, S.-Z. Molecular Scaffolding Strategy with Synergistic Active Centers To Facilitate Electrocatalytic CO_2 Reduction to Hydrocarbon/Alcohol. *J. Am. Chem. Soc.* **2017**, *139*, 18093−18100.
(487) Yang, H.; Wu, Y.; Li, G.; Lin, Q.; Hu, Q.; Zhang, Q.; Liu, J.; He, C. Scalable Production of Efficient Single-Atom Copper Decorated Carbon Membranes for CO_2 Electroreduction to Methanol. *J. Am. Chem. Soc.* **2019**, *141*, 12717−12723.
(488) Chen, Y.; Kanan, M. W. Tin Oxide Dependence of the CO_2 Reduction Efficiency on Tin Electrodes and Enhanced Activity for Tin/Tin Oxide Thin-Film Catalysts. *J. Am. Chem. Soc.* **2012**, *134*, 1986−1989.
(489) Zhao, Y.; Liang, J.; Wang, C.; Ma, J.; Wallace, G. G. Tunable and Efficient Tin Modified Nitrogen-Doped Carbon Nanofibers for Electrochemical Reduction of Aqueous Carbon Dioxide. *Adv. Energy Mater.* **2018**, *8*, 1702524.
(490) Zu, X.; Li, X.; Liu, W.; Sun, Y.; Xu, J.; Yao, T.; Yan, W.; Gao, S.; Wang, C.; Wei, S.; Xie, Y. Efficient and Robust Carbon Dioxide Electroreduction Enabled by Atomically Dispersed $Sn^{\delta+}$ Sites. *Adv. Mater.* **2019**, *31*, 1808135.
(491) Huang, P.; Cheng, M.; Zhang, H.; Zuo, M.; Xiao, C.; Xie, Y. Single Mo Atom Realized Enhanced CO_2 Electro-reduction into Formate on N-doped Graphene. *Nano Energy* **2019**, *61*, 428−434.
(492) Yan, C.; Li, H.; Ye, Y.; Wu, H.; Cai, F.; Si, R.; Xiao, J.; Miao, S.; Xie, S.; Yang, F.; et al. Coordinatively unsaturated nickel−nitrogen sites towards selective and high-rate CO 2 electroreduction. *Energy Environ. Sci.* **2018**, *11*, 1204−1210.
(493) Yang, F.; Song, P.; Liu, X.; Mei, B.; Xing, W.; Jiang, Z.; Gu, L.; Xu, W. Highly Efficient CO_2 Electroreduction on ZnN_4-based Single-Atom Catalyst. *Angew. Chem., Int. Ed.* **2018**, *57*, 12303−12307.
(494) Zhang, E.; Wang, T.; Yu, K.; Liu, J.; Chen, W.; Li, A.; Rong, H.; Lin, R.; Ji, S.; Zheng, X.; et al. Bismuth Single Atoms Resulting from Transformation of Metal−Organic Frameworks and Their Use as Electrocatalysts for CO_2 Reduction. *J. Am. Chem. Soc.* **2019**, *141*, 16569−16573.
(495) Wuttig, A.; Yoon, Y.; Ryu, J.; Surendranath, Y. Bicarbonate Is Not a General Acid in Au-Catalyzed CO_2 Electroreduction. *J. Am. Chem. Soc.* **2017**, *139*, 17109−17113.
(496) Xiao, H.; Cheng, T.; Goddard, W. A., III; Sundararaman, R. Mechanistic Explanation of the pH Dependence and Onset Potentials for Hydrocarbon Products from Electrochemical Reduction of CO on Cu (111). *J. Am. Chem. Soc.* **2016**, *138*, 483−486.
(497) Clemo, G.; Swan, G. The Nitrogen Cycle in Nature. *Nature* **1949**, *164*, 811−813.
(498) Gruber, N.; Galloway, J. N. An Earth-System Perspective of the Global Nitrogen Cycle. *Nature* **2008**, *451*, 293−296.
(499) Stevens, C. J. Nitrogen in the Environment. *Science* **2019**, *363*, 578−580.
(500) Desch, C. The Nitrogen Industry. *Nature* **1922**, *110*, 670−671.
(501) Fajen, J.; Carson, G.; Rounbehler, D.; Fan, T.; Vita, R.; Goff, U.; Wolf, M.; Edwards, G.; Fine, D.; Reinhold, V.; Biemann, K. N-Nitrosamines in the Rubber and Tire Industry. *Science* **1979**, *205*, 1262−1264.
(502) Mowry, D. T. The Preparation of Nitriles. *Chem. Rev.* **1948**, *42*, 189−283.
(503) Slade, R. The Nitrogen Industry and Our Food Supply. *Nature* **1930**, *126*, 569−572.

https://dx.doi.org/10.1021/acs.chemrev.0c00594
Chem. Rev. 2020, 120, 12217−12314

(504) Darwent, B. *Bond Dissociation Energies in Simple Molecules*; National Standard Reference Data Series, No. 31. National Bureau of Standards: Washington, DC, 1970.
(505) Chatt, J.; Dilworth, J. R.; Richards, R. L. Recent Advances in the Chemistry of Nitrogen Fixation. *Chem. Rev.* **1978**, *78*, 589−625.
(506) Dixon, R.; Kahn, D. Genetic Regulation of Biological Nitrogen Fixation. *Nat. Rev. Microbiol.* **2004**, *2*, 621.
(507) Hoffman, B. M.; Lukoyanov, D.; Yang, Z.-Y.; Dean, D. R.; Seefeldt, L. C. Mechanism of Nitrogen Fixation by Nitrogenase: The Next Stage. *Chem. Rev.* **2014**, *114*, 4041−4062.
(508) The Haber Process. *Nature* **1923**, *111*, 101−102.
(509) Haber, F.; Le Rossignol, R. Über Die Technische Darstellung Von Ammoniak Aus Den Elementen. *Z. Elektrochem. Angew. Phys. Chem.* **1913**, *19*, 53−72.
(510) Erisman, J. W.; Sutton, M. A.; Galloway, J.; Klimont, Z.; Winiwarter, W. How a Century of Ammonia Synthesis Changed the World. *Nat. Geosci.* **2008**, *1*, 636−639.
(511) Liu, H. Ammonia Synthesis Catalyst 100 Years: Practice, Enlightenment and Challenge. *Chin. J. Catal.* **2014**, *35*, 1619−1640.
(512) Andersen, S. Z.; Čolić, V.; Yang, S.; Schwalbe, J. A.; Nielander, A. C.; McEnaney, J. M.; Enemark-Rasmussen, K.; Baker, J. G.; Singh, A. R.; Rohr, B. A.; et al. A Rigorous Electrochemical Ammonia Synthesis Protocol With Quantitative Isotope Measurements. *Nature* **2019**, *570*, 504−508.
(513) Cao, N.; Chen, Z.; Zang, K.; Xu, J.; Zhong, J.; Luo, J.; Xu, X.; Zheng, G. Doping Strain Induced Bi-Ti^{3+} Pairs for Efficient N_2 Activation and Electrocatalytic Fixation. *Nat. Commun.* **2019**, *10*, 2877.
(514) Cheng, H.; Cui, P.; Wang, F.; Ding, L. X.; Wang, H. High Efficiency Electrochemical Nitrogen Fixation Achieved with a Lower Pressure Reaction System by Changing the Chemical Equilibrium. *Angew. Chem., Int. Ed.* **2019**, *58*, 15541−15547.
(515) Qi, K.; Cui, X.; Gu, L.; Yu, S.; Fan, X.; Luo, M.; Xu, S.; Li, N.; Zheng, L.; Zhang, Q.; et al. Single-Atom Cobalt Array Bound to Distorted 1T MoS_2 with Ensemble Effect for Hydrogen Evolution catalysis. *Nat. Commun.* **2019**, *10*, 5231.
(516) Jiao, F.; Xu, B. Electrochemical Ammonia Synthesis and Ammonia Fuel Cells. *Adv. Mater.* **2019**, *31*, 1805173.
(517) Li, L.; Tang, C.; Xia, B.; Jin, H.; Zheng, Y.; Qiao, S.-Z. Two-Dimensional Mosaic Bismuth Nanosheets for Highly Selective Ambient Electrocatalytic Nitrogen Reduction. *ACS Catal.* **2019**, *9*, 2902−2908.
(518) Qin, Q.; Zhao, Y.; Schmallegger, M.; Heil, T.; Schmidt, J.; Walczak, R.; Gescheidt-Demner, G.; Jiao, H.; Oschatz, M. Enhanced Electrocatalytic N_2 Reduction via Partial Anion Substitution in Titanium Oxide−Carbon Composites. *Angew. Chem., Int. Ed.* **2019**, *58*, 13101−13106.
(519) Suryanto, B. H.; Du, H.-L.; Wang, D.; Chen, J.; Simonov, A. N.; MacFarlane, D. R. Challenges and Prospects in the Catalysis of Electroreduction of Nitrogen to Ammonia. *Nat. Catal.* **2019**, *2*, 290−296.
(520) Wu, T.; Zhu, X.; Xing, Z.; Mou, S.; Li, C.; Qiao, Y.; Liu, Q.; Luo, Y.; Shi, X.; Zhang, Y.; Sun, X. Greatly Improving Electrochemical N_2 Reduction Over TiO_2 Nanoparticles by Iron Doping. *Angew. Chem., Int. Ed.* **2019**, *58*, 18449−18453.
(521) Wang, S.; Jiang, S. P. Prospects of Fuel Cell Technologies. *Natl. Sci. Rev.* **2017**, *4*, 163−166.
(522) Winter, M.; Brodd, R. J. What Are Batteries, Fuel Cells, and Supercapacitors? *Chem. Rev.* **2004**, *104*, 4245−4270.
(523) Bauer, N. Theoretical Pathways for the Reduction of N_2 Molecules in Aqueous Media: Thermodynamics of N_2H_n[1]. *J. Phys. Chem.* **1960**, *64*, 833−837.
(524) Shilov, A. Catalytic Reduction of Molecular Nitrogen in Solutions. *Russ. Chem. Bull.* **2003**, *52*, 2555−2562.
(525) Bratsch, S. G. Standard Electrode Potentials and Temperature Coefficients in Water at 298.15 K. *J. Phys. Chem. Ref. Data* **1989**, *18*, 1−21.
(526) Guo, W.; Zhang, K.; Liang, Z.; Zou, R.; Xu, Q. Electrochemical Nitrogen Fixation and Utilization: Theories, Advanced Catalyst Materials and System Design. *Chem. Soc. Rev.* **2019**, *48*, 5658−5716.
(527) Cao, N.; Zheng, G. Aqueous Electrocatalytic N_2 Reduction Under Ambient Conditions. *Nano Res.* **2018**, *11*, 2992−3008.
(528) Cui, X.; Tang, C.; Zhang, Q. A Review of Electrocatalytic Reduction of Dinitrogen to Ammonia Under Ambient Conditions. *Adv. Energy Mater.* **2018**, *8*, 1800369.
(529) Foster, S. L.; Bakovic, S. I. P.; Duda, R. D.; Maheshwari, S.; Milton, R. D.; Minteer, S. D.; Janik, M. J.; Renner, J. N.; Greenlee, L. F. Catalysts for Nitrogen Reduction to Ammonia. *Nat. Catal.* **2018**, *1*, 490−500.
(530) Höskuldsson, A. r. B.; Abghoui, Y.; Gunnarsdóttir, A. B.; Skúlason, E. Computational Screening of Rutile Oxides for Electrochemical Ammonia Formation. *ACS Sustainable Chem. Eng.* **2017**, *5*, 10327−10333.
(531) Howalt, J. G.; Bligaard, T.; Rossmeisl, J.; Vegge, T. DFT Based Study of Transition Metal Nano-Clusters for Electrochemical NH_3 Production. *Phys. Chem. Chem. Phys.* **2013**, *15*, 7785−7795.
(532) Logadottir, A.; Rod, T. H.; Nørskov, J. K.; Hammer, B.; Dahl, S.; Jacobsen, C. The Brønsted−Evans−Polanyi Relation and the Volcano Plot for Ammonia Synthesis Over Transition Metal Catalysts. *J. Catal.* **2001**, *197*, 229−231.
(533) Montoya, J. H.; Tsai, C.; Vojvodic, A.; Nørskov, J. K. The Challenge of Electrochemical Ammonia Synthesis: A New Perspective on the Role of Nitrogen Scaling Relations. *ChemSusChem* **2015**, *8*, 2180−2186.
(534) Skulason, E.; Bligaard, T.; Gudmundsdóttir, S.; Studt, F.; Rossmeisl, J.; Abild-Pedersen, F.; Vegge, T.; Jonsson, H.; Nørskov, J. K. A Theoretical Evaluation of Possible Transition Metal Electro-Catalysts for N_2 Reduction. *Phys. Chem. Chem. Phys.* **2012**, *14*, 1235−1245.
(535) Choi, C.; Back, S.; Kim, N.-Y.; Lim, J.; Kim, Y.-H.; Jung, Y. Suppression of Hydrogen Evolution Reaction in Electrochemical N_2 Reduction Using Single-Atom Catalysts: A Computational Guideline. *ACS Catal.* **2018**, *8*, 7517−7525.
(536) Zhao, W.; Zhang, L.; Luo, Q.; Hu, Z.; Zhang, W.; Smith, S.; Yang, J. Single $Mo_1(Cr_1)$ Atom on Nitrogen-Doped Graphene Enables Highly Selective Electroreduction of Nitrogen Into Ammonia. *ACS Catal.* **2019**, *9*, 3419−3425.
(537) Chen, X.; Zhao, X.; Kong, Z.; Ong, W.-J.; Li, N. Unravelling the Electrochemical Mechanisms for Nitrogen Fixation on Single Transition Metal Atoms Embedded in Defective Graphitic Carbon Nitride. *J. Mater. Chem. A* **2018**, *6*, 21941−21948.
(538) Zhang, L.; Zhao, W.; Zhang, W.; Chen, J.; Hu, Z. gt-C_3N_4 Coordinated Single Atom as an Efficient Electrocatalyst for Nitrogen Reduction Reaction. *Nano Res.* **2019**, *12*, 1181−1186.
(539) Kitano, M.; Kanbara, S.; Inoue, Y.; Kuganathan, N.; Sushko, P. V.; Yokoyama, T.; Hara, M.; Hosono, H. Electride Support Boosts Nitrogen Dissociation Over Ruthenium Catalyst and Shifts the Bottleneck in Ammonia Synthesis. *Nat. Commun.* **2015**, *6*, 6731.
(540) Ozaki, A. Development of Alkali-Promoted Ruthenium as a Novel Catalyst for Ammonia Synthesis. *Acc. Chem. Res.* **1981**, *14*, 16−21.
(541) Zheng, J.; Liao, F.; Wu, S.; Jones, G.; Chen, T. Y.; Fellowes, J.; Sudmeier, T.; McPherson, I. J.; Wilkinson, I.; Tsang, S. C. E. Efficient Non-dissociative Activation of Dinitrogen to Ammonia over Lithium-Promoted Ruthenium Nanoparticles at Low Pressure. *Angew. Chem., Int. Ed.* **2019**, *58*, 17335−17341.
(542) Geng, Z.; Liu, Y.; Kong, X.; Li, P.; Li, K.; Liu, Z.; Du, J.; Shu, M.; Si, R.; Zeng, J. Achieving a Record-High Yield Rate of 120.9 $\mu g_{NH3} \cdot mg^{-1}_{cat.}{}^{-1} h^{-1}$ for N_2 Electrochemical Reduction over Ru Single-Atom Catalysts. *Adv. Mater.* **2018**, *30*, 1803498.
(543) Tao, H.; Choi, C.; Ding, L.-X.; Jiang, Z.; Han, Z.; Jia, M.; Fan, Q.; Gao, Y.; Wang, H.; Robertson, A. W.; et al. Nitrogen Fixation by Ru Single-Atom Electrocatalytic Reduction. *Chem* **2019**, *5*, 204−214.
(544) Yu, B.; Li, H.; White, J.; Donne, S.; Yi, J.; Xi, S.; Fu, Y.; Henkelman, G.; Yu, H.; Chen, Z.; Ma, T. Tuning the catalytic preference of ruthenium catalysts for nitrogen reduction by atomic dispersion. *Adv. Funct. Mater.* **2020**, *30*, 1905665.

https://dx.doi.org/10.1021/acs.chemrev.0c00594
Chem. Rev. 2020, 120, 12217−12314

(545) Yao, Y.; Zhu, S.; Wang, H.; Li, H.; Shao, M. A Spectroscopic Study on the Nitrogen Electrochemical Reduction Reaction on Gold and Platinum Surfaces. *J. Am. Chem. Soc.* **2018**, *140*, 1496−1501.
(546) Li, S. J.; Bao, D.; Shi, M. M.; Wulan, B. R.; Yan, J. M.; Jiang, Q. Amorphizing of Au Nanoparticles by CeO_x−RGO Hybrid Support Towards Highly Efficient Electrocatalyst for N_2 Reduction Under Ambient Conditions. *Adv. Mater.* **2017**, *29*, 1700001.
(547) Nazemi, M.; Panikkanvalappil, S. R.; El-Sayed, M. A. Enhancing the Rate of Electrochemical Nitrogen Reduction Reaction for Ammonia Synthesis Under Ambient Conditions Using Hollow Gold Nanocages. *Nano Energy* **2018**, *49*, 316−323.
(548) Shi, M. M.; Bao, D.; Wulan, B. R.; Li, Y. H.; Zhang, Y. F.; Yan, J. M.; Jiang, Q. Au Sub-Nanoclusters on TiO_2 Toward Highly Efficient and Selective Electrocatalyst for N_2 Conversion to NH_3 at Ambient Conditions. *Adv. Mater.* **2017**, *29*, 1606550.
(549) Xue, Z.-H.; Zhang, S.-N.; Lin, Y.-X.; Su, H.; Zhai, G.-Y.; Han, J.-T.; Yu, Q.-Y.; Li, X.-H.; Antonietti, M.; Chen, J.-S. Electrochemical Reduction of N_2 Into NH_3 by Donor−Acceptor Couples of Ni and Au Nanoparticles With a 67.8% Faradaic Efficiency. *J. Am. Chem. Soc.* **2019**, *141*, 14976−14980.
(550) Zheng, J.; Lyu, Y.; Qiao, M.; Veder, J. P.; Marco, R. D.; Bradley, J.; Wang, R.; Li, Y.; Huang, A.; Jiang, S. P.; Wang, S. Tuning the Electron Localization of Gold Enables the Control of Nitrogen-to-Ammonia Fixation. *Angew. Chem., Int. Ed.* **2019**, *58*, 18604−18609.
(551) Qin, Q.; Heil, T.; Antonietti, M.; Oschatz, M. Single-Site Gold Catalysts on Hierarchical N-Doped Porous Noble Carbon for Enhanced Electrochemical Reduction of Nitrogen. *Small Methods* **2018**, *2*, 1800202.
(552) Wang, X.; Wang, W.; Qiao, M.; Wu, G.; Chen, W.; Yuan, T.; Xu, Q.; Chen, M.; Zhang, Y.; Wang, X.; et al. Atomically Dispersed Au_1 Catalyst Towards Efficient Electrochemical Synthesis of Ammonia. *Sci. Bull.* **2018**, *63*, 1246−1253.
(553) McKenna, C. E.; Jones, J. B.; Eran, H.; Huang, C. W. Reduction of Cyclopropene as Criterion of Active-Site Homology Between Nitrogenase and Its Fe−Mo Cofactor. *Nature* **1979**, *280*, 611−612.
(554) Guo, R.; Hu, M.; Zhang, W.; He, J. Boosting Electrochemical Nitrogen Reduction Performance over Binuclear Mo Atoms on N-Doped Nanoporous Graphene: A Theoretical Investigation. *Molecules* **2019**, *24*, 1777.
(555) Le, Y.-Q.; Gu, J.; Tian, W. Q. Nitrogen-Fixation Catalyst Based on Graphene: Every Part Counts. *Chem. Commun.* **2014**, *50*, 13319−13322.
(556) Zhao, J.; Chen, Z. Single Mo Atom Supported on Defective Boron Nitride Monolayer as an Efficient Electrocatalyst for Nitrogen Fixation: A Computational Study. *J. Am. Chem. Soc.* **2017**, *139*, 12480−12487.
(557) Zhao, J.; Zhao, J.; Cai, Q. Single Transition Metal Atom Embedded Into a MoS_2 Nanosheet as a Promising Catalyst for Electrochemical Ammonia Synthesis. *Phys. Chem. Chem. Phys.* **2018**, *20*, 9248−9255.
(558) Han, L.; Liu, X.; Chen, J.; Lin, R.; Liu, H.; Lü, F.; Bak, S.; Liang, Z.; Zhao, S.; Stavitski, E.; et al. Atomically Dispersed Molybdenum Catalysts for Efficient Ambient Nitrogen Fixation. *Angew. Chem., Int. Ed.* **2019**, *58*, 2321−2325.
(559) Hui, L.; Xue, Y.; Yu, H.; Liu, Y.; Fang, Y.; Xing, C.; Huang, B.; Li, Y. Highly Efficient and Selective Generation of Ammonia and Hydrogen on a Graphdiyne-based Catalyst. *J. Am. Chem. Soc.* **2019**, *141*, 10677−10683.
(560) Sclafani, A.; Augugliaro, V.; Schiavello, M. Dinitrogen Electrochemical Reduction to Ammonia Over Iron Cathode in Aqueous Medium. *J. Electrochem. Soc.* **1983**, *130*, 734−736.
(561) Wang, M.; Liu, S.; Qian, T.; Liu, J.; Zhou, J.; Ji, H.; Xiong, J.; Zhong, J.; Yan, C. Over 56.55% Faradaic efficiency of ambient ammonia synthesis enabled by positively shifting the reaction potential. *Nat. Commun.* **2019**, *10*, 341.
(562) Zhang, R.; Jiao, L.; Yang, W.; Wan, G.; Jiang, H.-L. Single-Atom Catalysts Templated by Metal−Organic Frameworks for Electrochemical Nitrogen Reduction. *J. Mater. Chem. A* **2019**, *7*, 26371−26377.
(563) Lü, F.; Zhao, S.; Guo, R.; He, J.; Peng, X.; Bao, H.; Fu, J.; Han, L.; Qi, G.; Luo, J.; Tang, X.; Liu, X. Nitrogen-Coordinated Single Fe Sites for Efficient Electrocatalytic N_2 Fixation in Neutral Media. *Nano Energy* **2019**, *61*, 420−427.
(564) He, C.; Wu, Z.-Y.; Zhao, L.; Ming, M.; Zhang, Y.; Yi, Y.; Hu, J.-S. Identification of FeN_4 as an Efficient Active Site for Electrochemical N_2 Reduction. *ACS Catal.* **2019**, *9*, 7311−7317.
(565) Wang, Y.; Cui, X.; Zhao, J.; Jia, G.; Gu, L.; Zhang, Q.; Meng, L.; Shi, Z.; Zheng, L.; Wang, C.; Zhang, Z.; Zheng, W. Rational Design of Fe−N/C Hybrid for Enhanced Nitrogen Reduction Electrocatalysis under Ambient Conditions in Aqueous Solution. *ACS Catal.* **2019**, *9*, 336−344.
(566) Guo, X.; Gu, J.; Hu, X.; Zhang, S.; Chen, Z.; Huang, S. Coordination Tailoring Towards Efficient Single-Atom Catalysts for N2Fixation: A Case Study of Iron-Nitrogen-Carbon (Fe@ NC) Systems. *Catal. Today* **2020**, *350*, 91−99.
(567) Li, X.-F.; Li, Q.-K.; Cheng, J.; Liu, L.; Yan, Q.; Wu, Y.; Zhang, X.-H.; Wang, Z.-Y.; Qiu, Q.; Luo, Y. Conversion of Dinitrogen to Ammonia by FeN_3-Embedded Graphene. *J. Am. Chem. Soc.* **2016**, *138*, 8706−8709.
(568) Liu, Y.; Xu, Q.; Fan, X.; Quan, X.; Su, Y.; Chen, S.; Yu, H.; Cai, Z. Electrochemical Reduction of N_2 to Ammonia on Co Single Atom Embedded N-Doped Porous Carbon Under Ambient Conditions. *J. Mater. Chem. A* **2019**, *7*, 26358−26363.
(569) Zang, W.; Yang, T.; Zou, H.; Xi, S.; Zhang, H.; Liu, X.; Kou, Z.; Du, Y.; Feng, Y. P.; Shen, L.; et al. Copper Single Atoms Anchored in Porous Nitrogen-Doped Carbon as Efficient pH-Universal Catalysts for the Nitrogen Reduction Reaction. *ACS Catal.* **2019**, *9*, 10166−10173.
(570) Cheng, H.; Ding, L. X.; Chen, G. F.; Zhang, L.; Xue, J.; Wang, H. J. A. m. Molybdenum Carbide Nanodots Enable Efficient Electrocatalytic Nitrogen Fixation Under Ambient Conditions. *Adv. Mater.* **2018**, *30*, 1803694.
(571) Lee, H. K.; Koh, C. S. L.; Lee, Y. H.; Liu, C.; Phang, I. Y.; Han, X.; Tsung, C.-K.; Ling, X. Y. J. S. a. Favoring the Unfavored: Selective Electrochemical Nitrogen Fixation Using a Reticular Chemistry Approach. *Sci. Adv.* **2018**, *4*, No. eaar3208.
(572) Wei, S.; Li, A.; Liu, J.-C.; Li, Z.; Chen, W.; Gong, Y.; Zhang, Q.; Cheong, W.-C.; Wang, Y.; Zheng, L.; Xiao, H.; Chen, C.; Wang, D.; Peng, Q.; Gu, L.; Han, X.; Li, J.; Li, Y. Direct observation of noble metal nanoparticles transforming to thermally stable single atoms. *Nat. Nanotechnol.* **2018**, *13*, 856−861.
(573) Ji, M.; Wei, Z. A review of water management in polymer electrolyte membrane fuel cells. *Energies* **2009**, *2*, 1057−1106.
(574) Huang, Q.; Liu, H.; An, W.; Wang, Y.; Feng, Y.; Men, Y. Synergy of a Metallic NiCo Dimer Anchored on a C_2N−Graphene Matrix Promotes the Electrochemical CO_2 Reduction Reaction. *ACS Sustainable Chem. Eng.* **2019**, *7*, 19113−19121.
(575) Zhao, Y.; Yang, K. R.; Wang, Z.; Yan, X.; Cao, S.; Ye, Y.; Dong, Q.; Zhang, X.; Thorne, J. E.; Jin, L.; Materna, K. L.; Trimpalis, A.; Bai, H.; Fakra, S. C.; Zhong, X.; Wang, P.; Pan, X.; Guo, J.; Flytzani-Stephanopoulos, M.; Brudvig, G. W.; Batista, V. S.; Wang, D. Stable iridium dinuclear heterogeneous catalysts supported on metal-oxide substrate for solar water oxidation. *Proc. Natl. Acad. Sci. U. S. A.* **2018**, *115*, 2902−2907.
(576) Li, Y.; Su, H.; Chan, S. H.; Sun, Q. CO_2 Electroreduction Performance of Transition Metal Dimers Supported on Graphene: A Theoretical Study. *ACS Catal.* **2015**, *5*, 6658−6664.
(577) He, H.; Morrissey, C.; Curtiss, L. A.; Zapol, P. Graphene-Supported Monometallic and Bimetallic Dimers for Electrochemical CO_2 Reduction. *J. Phys. Chem. C* **2018**, *122*, 28629−28636.

https://dx.doi.org/10.1021/acs.chemrev.0c00594
Chem. Rev. 2020, 120, 12217−12314